Solar powered motorized blinds: A case study on using energy harvesting to power internet of things applications

SOLAR POWERED MOTORIZED BLINDS: A CASE STUDY ON USING ENERGY HARVESTING TO POWER INTERNET OF THINGS APPLICATIONS

BY

DAVID DRAKE, B.Eng., (Electrical Engineering)

McMaster University, Hamilton, Canada

A THESIS

SUBMITTED TO THE DEPARTMENT OF ENGINEERING PHYSICS

AND THE SCHOOL OF GRADUATE STUDIES

OF MCMASTER UNIVERSITY

IN PARTIAL FULFILMENT OF THE REQUIREMENTS

FOR THE DEGREE OF

MASTER OF APPLIED SCIENCE

Master of Applied Science (2016) McMaster University

(Engineering Physics) Hamilton, Ontario, Canada

TITLE:	Solar powered motorized blinds: A case study on using energy harvesting to power internet of things applications
AUTHOR:	David Drake B.Eng., (Electrical Engineering) McMaster University, Hamilton, Canada
SUPERVISOR:	Dr. Preston
NUMBER OF PAGES:	xxxiv, 255

Abstract

Smart devices capable of harvesting their own energy have advantages over their wired or battery-powered alternatives including improved portability, simplified installation, and reduced maintenance and operating costs. This thesis studies energy harvesting technology through a case study of a solar-powered motorized window shade. An analytical and experimental evaluation of window attenuation found that windows reduced the ability of solar cells to produce photocurrent by 30%-70%. This still allows significant potential to power small electronics so a prototype motorized window blind was designed and assembled. The solar array was mounted to the roller blind's bottom rail and power is conveyed to the control electronics and motor in the unit's top cylinder through wires embedded in the shade's fabric. A simple battery system was implemented to ensure the prototype could remain powered in the absence of light.

Various forms of powerflow in the prototype were evaluated. Experimental evaluation of joule heating within the conductive textile indicates that a temperature gradient that is less than 10 °C develops, meaning it is safe for use. The prototype was designed with artificial friction to prevent the blinds from slipping when not in use. An experimentally validated motor model was developed and used to determine that the system could use up to 46% less energy if the artificial friction was removed.

A pseudo-empirical system model was developed to simulate the interaction between system electronics. Simulation results indicate that the system would remain consistently powered if placed behind a south-facing window that receives a consistent supply of direct sunlight and attenuates that light by less than 75%. These results also indicate that the unit would remain powered in the absence of light for 13 days. Similar methods could be used to evaluate future energy harvesting systems.

Acknowledgements

This work would not be possible without the help of many individuals who have helped me along the way. I'd like to quickly acknowledge their help, though this brief summary really won't do justice to their contributions:

- Dr. John Preston who gave me an amazing opportunity to explore such exciting research. He allowed me to freely explore a wide breadth of topics that's reflected in the diversity of content of this thesis. The hundred pages I've written isn't enough to put down everything I've learned thanks to you.

- Stephen Jovanovic, Mike Cino, Tahereh Majdi, and the rest of my peers who've always helped me when I've needed it. Whether you've taught me how to use measurement equipment, taught me how to design my own testing equipment or helped me interpret results, I wouldn't understand nearly as much without your help.

- Peter Jonasson, Glen Leinweber and Clealand Berwick who helped me design and build. Over the course of this work I have had to use a mill, lathe, 3D print, program and network various components to make a cohesive prototype. Not only do I owe you gratitude for teaching me how to build, but for teaching me how to design systems with manufacturing in mind.

- My family who have always supported me and never refused me help. I would like to highlight my Aunt Heather and cousin Justine who gave me a place to live on short notice in the middle of this degree.

- Financial support of this project was made possible through the National Science and Engineering Research Council of Canada and the Ontario Graduate Scholarship Program.

Notation and Abbreviations

SYMBOL/ ACRONYM	DESCRIPTION	APPLICABLE CONSTANT /UNITS
API	**Application Programming Interface**	
A_s	Surface area of thermal interface	[m^2]
A_{uc}	Unshaded area of unit cell	[m^2]
A_{usd}	Unshaded area of double grid pattern	[m^2]
A_{uss}	Unshaded area of single grid pattern	[m^2]
AWG	**American Wire Gauge**	
a-Si:H	**Hydrogenated Amorphous Silicon**	
$\bar{B}$	Magnetic field strength vector	[T]
BOM	**Bill Of Materials**	
c	Speed of light constant	[3.00×10^8 ms^{-1}]
C	Capacitance	[F]
CAD	**Computer Aided Design**	
CCS	**Code Composer Suite**	
c_{tm}	Heat capacity of a thermal mass	[JK^{-1}]
C_1	RC capacitance in battery circuit model	[F]

DAQ	**Data Acquisition**	
DSC	**Dye-sensitized Solar Cells**	
E	Energy	[J], [eV]
E_F	Fermi energy	[J], [eV]
E_{Field}	Built in electric field	[NC^{-1}], [Vm^{-1}]
$E_{0,Oxidation}$	Oxidation potential	[V]
$E_{0,Reduction}$	Reduction potential	[V]
$E_{0,Standard}$	Battery standard potential	[V]
EHP	**Electron Hole Pairs**	
EMF	**Electromotive Force**	
EQE	**External Quantum Efficiency**	
e-textile	**Electronic Textile**	
F	Force	[N]
G	Rate of photogenerated carriers	[s^{-1}]
g	gravitational acceleration constant	[9.81 ms^{-2}]
GA	**Genetic Algorithm**	
g_r	gear ratio	
GUI	Graphical User Interface	
h	Plank's constant	[6.63×10^{-34} Js]
h_t	Heat transfer coefficient	[$Wm^{-2}K$]
HQP	**High Quality Polycrystalline**	
HVAC	**Heating Ventilation and Air Conditioning**	
I	Current	[A]
$\bar{I}$	Vector of electrical current	[A]

I_A	Armature current	[A]
I_d	Diode current	[A]
I_{gas}	Battery gassing current	[A]
I_{mp}	Current at maximum power point	[A]
IoT	**Internet of Things**	
IR	**Infrared**	
I_{ph}	Photocurrent source	[A]
I_s	Diode reverse saturation current	[A]
I_{SC}	Short circuit current	[A]
I_{sh}	Shunt current	[A]
I_t	Terminal current	[A]
ITO	**Indium Tin Oxide**	
I_0	Battery gassing model parameter	[A]
k_b	Boltzmann constant	$[1.38 \times 10^{-23}$J/K]
k_τ	Lumped motor torque coefficient	[NmA^{-1}]
k_U	Lumped motor EMF coefficient	[Vs rad^{-1}]
l_c	length of motor's armature coil	[m]
LQP	**Low Quality Polycrystalline**	
m	Mass	[kg]
M	**Metal Alloy**	
MH	**Metal Hydride**	
n	Diode ideality factor	
NEC	**National Electric Code**	
NI	**National Instruments**	

NIMH	**Nickel Metal Hydride**	
NREL	**National Renewable Energy Lab**	
OCT	**Open Circuit Test**	
OCV	**Open Circuit Voltage**	
P	Power	[W]
PCB	**Printed Circuit Board**	
P_{env}	Thermal power transfer, environment	[W]
P_{ex}	Thermal power transfer, external source	[W]
pfatfs	**Petite FAT File system**	
PHP	**PHP: Hypertext Preprocessor (PHP)**	
P_{jl}	Joule heating power loss	[W]
P_{max}	Maximum power point	[W]
PSU	**Power Supply Unit**	
P_{tm}	Thermal power transfer to a thermal mass	[W]
q	Charge on an electron constant	[e], [1.60×10^{-19} C]
Q	Thermal energy	[J]
Q_{hyst}	Observer of recent battery charging history	[Ahr]
Q_{max}	Max value of Q_{hyst}	[Ahr]
r_c	Radius of motor's armature coil	[m]
R_{elec}	Electrical resistance	[Ω]
R_I	Current measuring resistance	[Ω]
RMSE	**Root Mean Square Error**	
R_s	Series resistance	[Ω]
R_{sh}	Shunt resistance	[Ω]

R_{th}	Thermal resistance	[KW^{-1}], [$^{\circ}CW^{-1}$]
R_0	Series resistance in battery circuit model	[Ω]
R_1	RC resistance in battery circuit model	[Ω]
SCT	**Short Circuit Test**	
stc	**Standard Test Conditions**	
SD	**Secure Digital**	
SOC	**State of Charge**	
T	Temperature	[K], [$^{\circ}$C]
$\dot{T}$	Change in ΔT over time	[Ks^{-1}], [$^{\circ}Cs^{-1}$]
T_{env}	Temperature of ambient environment	[K], [$^{\circ}$C]
T_{enc}	Period of motor encoder's output wave	[s]
TI	**Texas Instruments**	
T_{stc}	Temperature at standard testing conditions	[K], [$^{\circ}$C]
T_{tm}	Temperature of thermal mass	[K], [$^{\circ}$C]
U	EMF of motor	[V]
U_{hyst}	Percent of upper voltage bound added	[%]
UV	**Ultraviolet**	
$\bar{v}$	Velocity vector	[ms^{-1}]
VDCL	**Variable DC Load**	
V_H	Hysteresis voltage	[V]
V_{int}	Internal battery voltage	[V]
$V_{int,cell}$	Internal voltage of a single cell	[V]
V_{lb}	Internal battery voltage lower bound	[V]
V_{meas}	Measured voltage	[V]

V_{mp}	Voltage at maximum power point	[V]
V_{OC}	Open circuit voltage	[V]
V_t	Terminal voltage	[V]
V_{th}	Thermal voltage, $V_{th} = k_b T/q$	[V]
V_{ub}	Internal battery voltage upper bound	[V]
α	Battery gassing model parameter	
β	Decrease in I_{ph} from attenuated light	[%]
$\gamma_w(\lambda)$	Window light transmission profile	[%]
δ	Error	
ΔT	Temperature gradient	[K], [°C]
ΔU_{hyst}^{charge}	Stretching factor for U_{hyst} during charge	
$\Delta U_{hyst}^{discharge}$	Stretching factor for U_{hyst} during discharge	
λ	Wavelength	[nm], [μm]
σ	Standard deviation	
τ	Exponential time constant	[s]
Φ	Irradiance, Insolation	[Wm^{-2}]
$\Phi_{AM}(\lambda)$	AM1.5 flux spectrum	[Wm^{-2}]
Φ_{max}	Maximum daily irradiance	[Wm^{-2}]
Φ_{ph}	Photon flux	[$m^{-2}s^{-1}$]
Φ_{stc}	Irradiance at standard testing conditions	[Wm^{-2}]
ω	Rotational velocity	[m s^{-1}]

Contents

List of Figures

Chapter 1

Introduction

1.1 Introduction

From self driving cars to smart watches, companies are increasingly integrating cheap, network-compatible electronics into their products. When such devices work together as part of the Internet of Things (IoT), they are capable of providing coordinated, intelligent services to users. For example, by using smart tags and advanced analytics to optimize patient flow, a leading Florida-based hospital was able to reduce wait times by 68% [1]. Alternatively, companies can avoid up to 70% of breakdowns by using a predictive maintenance schedule developed using real-time sensor data from industrial assets [1]. IoT has huge market potential that has lead large, established companies like Cisco to estimate the market value of this technology to be worth $14.4 trillion from 2013-2022 [2].

One major system that could see a huge improvement with the integration of IoT is the home. By integrating electronics into household objects, chores like cleaning,

locking doors, or adjusting window blinds can be automated, making home maintenance easier, more convenient and less time consuming. Home automation can help the elderly continue living independently by providing emergency assistance systems or additional security. Building managers can reduce operating costs by automatically shutting down HVAC and lighting in unoccupied regions.

Window blinds provides an interesting case study for the design and integration of home automation. O'Brian et al. [3] conducted a comprehensive review of studies exploring occupant use of window shades over the past 35 years. Multiple studies indicate that users will adjust their window dressings more frequently when the controls are convenient and user-friendly; one study noted that use increased by a factor of three. Users will get more utility out of automated devices because they are easier to operate than fussy, mechanical, conventional, window blinds. Rather than modifying the position of shades in anticipation of future thermal loads, occupants adjust window dressings to address immediate goals such as glare reduction or improved privacy. This problem is exacerbated in public spaces like hallways, waiting areas, or shared offices. In these spots, people are wary of disturbing other occupants or will not be present long enough to be bothered by the thermal conditions. Window blinds in these spaces are typically left undisturbed in a suboptimal configuration. Automated window shades could predictively optimize a building's passive thermal performance while also offering inhabitants more utility by being easier to use.

One technical challenge of home automation devices, especially motorized window blinds, is the design of their power system. Like many home devices, window dressings contribute to the aesthetic of a space and are more visually appealing when power wires are hidden in walls. The cost of permanently wiring sensors in a building

has been estimated to be $200 per installation [4]. Doing so in a hidden manner could increase the cost while also being a more time-consuming and invasive process. Alternatively, battery-powered system can have reduced installation costs by avoiding wires. However, these solutions have finite lifetimes and require periodic maintenance in the form of battery replacement or recharging. Maintenance can be particularly challenging for motorized blinds because batteries are typically installed near the top of the unit where they are hard to access. These challenges can be avoided by designing a power system that converts ambient energy into electricity. Motorized blinds are always installed behind a window that typically has good access to external sunlight. Some newer motorized blind products use this source of energy to produce electricity. There is little publicly available information on the design and optimization of such devices. This thesis addresses this shortcoming by presenting a case study on the design and operation of a novel, solar-energy harvesting, motorized blind prototype.

1.2 Thesis Outline

This thesis is a case study of the design and operation of a novel motorized window blind. The feasibility of energy harvesting is addressed by discussing modern technologies that can convert light into electricity in Chapter 2 and the available light from the inside of a window in Chapter 3. A motorized blind design that is expected to operate within the previously discussed energy bounds is described in Chapter 4. The following chapters analyze the performance of various subsystems within this design. Chapter 5 discusses the thermal losses from the novel electronic-textile power transmission system. Chapter 6 quantifies the power savings that could be expected with an improved mechanical design. Chapter 7 models the system powerflow to

determine the minimum amount of irradiance needed to ensure continuous operation and the device's expected operating time in the absence of input solar insolation.

Chapter 2

Harvesting Solar Energy

This section reviews the operating physics of several photovoltaic technologies capable of generating useful electricity. Their use in a solar powered motorized blind application is discussed. Empirical equivalent circuit models are discussed that can be used to estimate power flow from these devices.

2.1 Solar Cell Operating Physics

2.1.1 Semiconductor Physics

A single atom is composed of a positively charged core and orbiting electrons. Each electron can be characterized by a set of quantum numbers which give acceptable solutions to the Schrödinger wave equation. The principle quantum number is an integral value starting at unity (ie. 1, 2, ..., n) that relates the distance of its respective electron to the nucleus. The second quantum number describes the subshell, the shape of volume where the electron is most likely to exist. This is denoted with a letter,

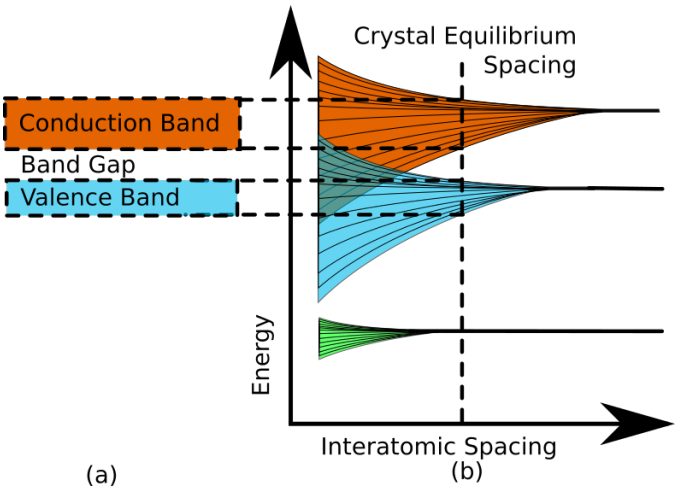

Figure 2.1: (a) The typical depiction of a crystal band structure that forms after atoms reach a stable spacing. (b) The divergence of electron energy vs interatomic spacing of the component atoms. Illustrations based on [5].

s, p, d or f. Subshells may have more than one states of energy where an electron can exist. The third quantum number tracks this state. Each state can house two electrons but in order to satisfy the Pauli exclusion principle, these electrons must have opposite spins. The fourth quantum number represents the spin of the electron. Typically, electrons inhabit the shells with the lowest energy [5].

Imagine a large number of atoms that are spaced infinitely apart. Consider the situation where these atoms are gradually moved together to form a periodic, crystalline structure. According to the Pauli exclusion principle, multiple close electrons cannot exist with the same energy. The set of allowed energy states of nearby atoms shifts to ensure all electrons in the system have a unique energy. Rather than tracking all the discrete levels, only the maximum and minimum energy are considered. These bounding values define a range of energies called a band. Figure 2.1 illustrates how an atom's discrete energy levels diverge as atoms are brought into close proximity of each other in a lattice forming bands [5].

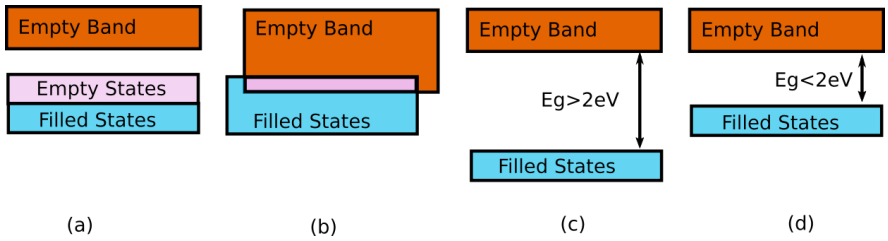

Figure 2.2: Band diagrams of various materials. (a) and (b) are distinct band configurations of conductive metals, (c) is an insulator and (d) is a semiconductor. Illustration based on [5].

Figure 2.2 shows different band structures for materials with various electrical qualities. In a typical crystal structure, there is band that is empty or only partially populated with electrons. An electron in this band can trade places with adjacent atoms due to the excessive number of vacancies. This mechanism allows for conduction lending, itself to the name "conduction band". Conductive metals have band structures where there is a direct path from the filled states to empty states, like Figure 2.2 (a) and (b). In contrast, insulators have a large gap between the conduction and valance band requiring electrons to have prohibitively high energy before they can be easily conducted as shown in Figure 2.2 (d). Figure 2.2 (c) is an intermediary case with a small band gap less than 2 eV. This material is called a semiconductor because thermal or optical energy can reasonably provide the energy needed to promote electrons into the conduction band [5].

Most electrons exist within the valence band in room temperature semiconductors. A few have received enough thermal energy to be promoted into the conduction band. When this occurs, they leave a "hole", an empty valence state that adjacent electrons can hop into. Every time an electron jumps into an adjacent hole, it leaves a vacancy. Rather than track the hopping electrons, it is easier to consider the absence of an electron as a positively charged particle called a hole. The movement of electrons in

the conduction band and holes in the valence band allow semiconductors to conduct charge [6]. The number of electrons and holes available are temperature dependent and are described by the Fermi Dirac distribution in (2.1).

$$f(E) = \frac{1}{1 + e^{\frac{E - E_F}{k_B T}}} \tag{2.1}$$

In this function f is the probability of an electron occupying a state with a given energy E. This function requires the Boltzmann's constant k_B as well as semiconductor specific parameters such as its temperature T and its specific Fermi energy E_F. The Fermi energy is a reference value that separates energy states according to their probability of being filled. States above the Fermi energy have a probability of being full that is less than 50% while states below the Fermi energy are more than 50% likely to be full [6].

Doping is the process of incorporating a small concentration of defects into a pure, intrinsic semiconductor. The resulting extrinsic semiconductor has different, useful, electrical properties. If a group V element, such as phosphorous, is integrated into a silicon crystal, this dopant will have an additional valence electron that is unable to bond within the tetrahedral crystal lattice. This electron is loosely bonded to the impurity and requires a small amount of energy to be promoted to the conduction band. This type of impurity is therefore called a donor; a semiconductor with many donors is called n-type. If a type III element, like boron, is introduced, this impurity can only form three local bonds within the silicon crystal structure, leaving the fourth empty. With a little additional energy, this impurity can accept an electron from an adjacent silicon atom, acting as a hole. This type of impurity is called an acceptor

and a semiconductor with many acceptors is called p-type. The term majority carrier refers to the more common charge carrier present in an extrinsic semiconductor. Electrons are the majority carrier in n-type semiconductors and holes are the majority carrier in p-type semiconductors. Minority carriers are the opposite charge of a semiconductor's majority carrier and are rarer in that material [6].

The introduction of dopants changes the Fermi energy. The loosely bonded extra electron in an n-type impurity introduces a spatially localized energy level near the conduction band energy, but still in the band gap. This increases the probability of states near the conduction band being full and the Fermi level must be increased accordingly. Conversely, a p-type semiconductor has vacancies, lowering the probability of occupied states in the valence band and thus lowering the Fermi energy [6].

2.1.2 The P-N Junction

A p-n junction is a variable-doped, silicon wafer that transitions from n-type to p-type. The simplest junction is a step junction where a uniformly doped p-type semiconductor sharply transitions into a uniformly doped n-type semiconductor. The majority carriers diffuse away from their respective halves leaving uncompensated donors in the n-type semiconductor and acceptors in the p-type semiconductor. These uncompensated charges establish a built-in electric field E_{field} that creates a drift current to balances the diffusion of charges. The region where E_{field} is present is depleted of mobile charges and is called the depletion region. At equilibrium this structure has no net current flow as depicted in Figure 2.3 [7].

The equilibrium behavior of the p-n junction can be understood in terms of its band structure. Since no current flows, the Fermi energy must be maintained at a

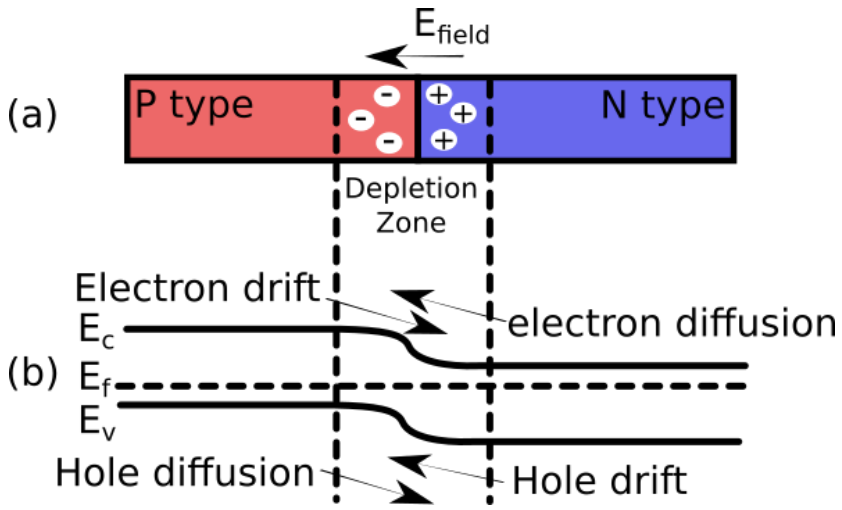

Figure 2.3: (a) Graphical illustration of p-n junction assembly and the resulting built in electric field. (b) The semiconductor band diagram that maintains E_f at a constant value when drift and diffusion currents are equal and opposite. Diagram based on [7].

constant level throughout this structure. The doping of the semiconductor forces the Fermi level to be closer to the valance band in the p-type and closer to the conduction band in the n-type [7]. Within the depletion region, the bands bend to ensure consistency as illustrated in Figure 2.3 (b).

This structure can be used as a one-way current switch. In forward bias, an external voltage is applied with positive connected to the p-type semiconductor, diminishing the built in electric field. The drift current will no longer counter the diffusion current and the device becomes an effective conductor. The opposite situation is reverse bias, when the polarity of the applied voltage is switched. A reverse bias increases the built in electric field. This field is effective at sweeping minority carriers from one side of the junction to the other. Despite the increased drift efficiency, the net improvement in current flow is negligible because a well designed p-n junction lacks minority carriers. This makes a useful device called a diode that can

only conduct when in forward bias [5].

2.1.3 Solar Cell Construction

Typical solar cells operate as a forward biased p-n junctions with one notable discrepancy, current flows in the opposite direction of a conventional diode. Light enters a p-n junction and is absorbed forming an electron-hole pair (EHP). Each EHP produces a minority and majority carrier. The minority carrier is separated by drift forces from the built in electric field. If successfully swept away, the minority carrier ends in the opposite side of the junction where it is now a majority carrier. Majority carriers diffuse to a metal contact. Solar cells are engineered to reduce EHP recombination so that the maximum number of carriers are collected at the external terminals [6].

2.1.3.1 Crystalline Silicon

The conventional crystalline silicon solar cell is built as a thin, flat, p-n junction with a large surface area as shown in Figure 2.4 (a). This produces a depletion plane that is parallel with the illuminated surface that is optimized for separating EHP. The goal in a solar cell is to keep the minority carriers from recombining with a majority carrier before they are swept away in the depletion region. In n-type semiconductors, the minority carriers are holes, while in p-type semiconductors, the minority carriers are electrons. If the minority charge carrier has a greater mobility, it is less likely to recombine before being swept away by E_{field}. For this reason, the bulk of the solar cell is typically selected to be p-type since the mobility of the minority electrons is greater than holes. The total device thickness is engineered to ensure a minimal amount of

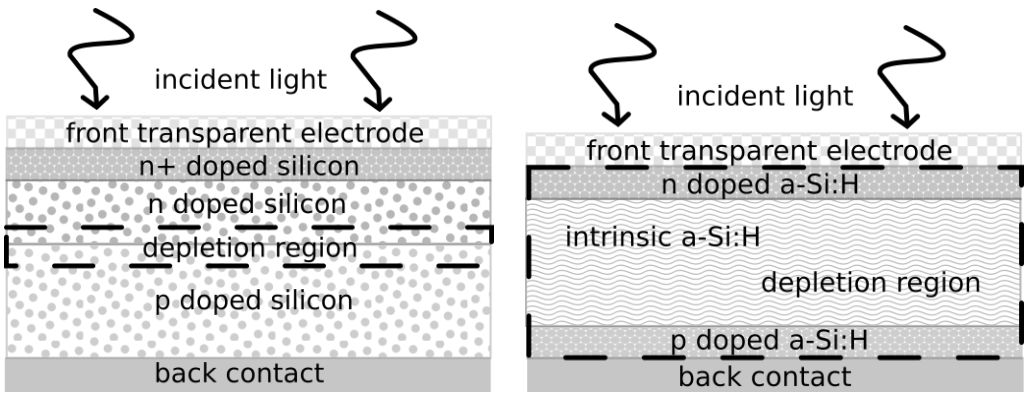

Figure 2.4: (a) Cross section of conventional crystalline silicon solar cell. (b) A p-i-n configuration that is commonly implemented with amorphous materials. Illustrations based on [6].

material is used while the solar cell can effectively absorb light. Optimal thicknesses for crystalline devices are usually around a couple hundred microns.

Charges are collected from the top using a thin metal grid with a combination of conductive metal oxide (like indium tin oxide (ITO)), and highly doped silicon (n+ or p+ doping). This contact must be developed carefully to ensure the conductive portion doesn't absorb or reflect light before it enters the active region of the device. The back contact can be made with a conventional metal since shading isn't a concern. The materials of both contact sides are developed to form an ohmic contact with minimal losses [6].

The bulk semiconducting material can be monocrystalline or polycrystalline. Typically single crystal solar cells are more efficient (on the order of 16-24%) as they lack the large number of defects associated with grain boundaries. Extra processing is required to grow large, defect-free wafers, meaning there are cost advantages to making polycrystalline silicon solar cells with efficiencies in the 14-18% range. Silicon solar cells currently dominate the market [6].

At a depth of a couple hundred microns, these devices are rigid, making them difficult to integrate into a moving system such as a roller blind. An advantage of this technology is that it is quite mature and can be easily and affordably sourced.

2.1.3.2 Amorphous Silicon

An amorphous material has no long range crystal structure and is inherently disordered. Amorphous silicon will exhibit short range order where neighboring atoms will bond in a tetrahedral fashion, but several bonds will be left dangling since the material is inherently disordered. The dangling bonds would normally act as traps that would inhibit the flow of charge carriers, but these can be passivated with the introduction of hydrogen to terminate the positions. When terminated by hydrogen, the material is referred to as hydrogenated amorphous silicon (a-Si:H) [6].

Solar cells made of a-Si:H have interesting characteristics that are distinct from conventional crystalline silicon solar cells. While there is a larger effective bandgap around 1.9 eV, its absorption coefficient for light with this energy is an order of magnitude greater than crystalline silicon. A thin film of around 1 μm of a-Si:H can absorb a considerable amount of light [6].

There are challenges associated with this material. While conventional doping techniques are applied, the success of doping is limited. Integrating phosphorous dopants does not produce the same magnitude of free electron concentration as an equivalently doped crystalline silicon wafer. A possible explanation is that the large amount of disorder opens up the possibility that phosphorous dopants only form three bonds with silicon, leaving the remaining two valence electrons tightly bound. Another side effect of this situation is poor minority carrier conduction. Holes in

n-doped silicon are likely to get caught in these phosphorous electron pairs [6].

To deal with the challenges of a-Si:H, a different solar cell structure must be employed. A common choice is the p-i-n structure shown in Figure 2.4 (b) where a thick intrinsic layer (∼500 nm) is sandwiched between thin n-type (∼20 nm) and p-type (∼20 nm) layers. A built in electric field is established over the entire intrinsic region. EHP drift across the bulk intrinsic region, limiting the distance charges have to travel through poorly conductive, doped regions [6].

The resulting devices have efficiencies that average around 7% new, decreasing to 5% as the solar cell ages [6]. Despite its low efficiency, a-Si:H is a mature technology that requires less material and less energy to process making it available at competitive prices.

2.1.3.3 Flexible Solar Cells

This case study examines the design and operation of various sub systems within a solar powered motorized blind. Integrating a flexible solar cell as part of the roller blind fabric is an attractive choice due to the large surface area when the blind is rolled down.

In 2008, Pagliaro et al. reviewed several different commercial flexible device architectures [8]. Some of these devices used alternative photovoltaic mechanisms such as organics or dye sensitized solar cells (DSC). Some were based on inorganic semiconductors such as the copper indium gallium diselenide or the previously discussed amorphous silicon p-i-n structure deposited on a flexible substrate. While this field appears promising, two of the companies discussed in [8] have filed for bankruptcy

since the paper was written highlighting the challenges faced by this emerging industry. Sourcing flexible solar cells is possible but is challenging with slow lead times and poor device efficiencies.

Another promising device architecture are solar cells in flexible wire format. Photovoltaic fibers could be woven directly into a roller blind maintaining the look and feel of a conventional fabric while being capable of generating power. Chen et al. reviews several methods of fabricating DSC and polymer wire solar cells [9]. While the best DSC experimental wires can achieve an efficiency of 7%, they require expensive materials and have limited flexibility. More robust designs have lower conversion efficiencies. A recent alternative are inorganic polycrystalline silicon wires. The first experimentally produced cells have limited efficiencies near 0.5% [10]. Appendix A simulates similar configurations of inorganic photovoltaic wires. This work suggest that improved material quality and changes to the doping structure could improve device efficiency to a magnitude around 4%, however these results have not been experimentally verified. The best photovoltaic wires are currently not scalable, reliable or efficient enough to be integrated with other products yet.

Existing flexible, photovoltaics are not appropriate to be integrated into a motorized blind prototype.

2.1.4 Five Parameter Model

A single solar cell's behavior can be described with the five parameter diode model shown in Figure 2.5 and is described by (2.2) [11]. For easier algebraic manipulation of (2.2), the thermal voltage is defined as $V_{th} = k_b T/q$ where q is the charge of an electron. Illuminated solar cells behave like constant current sources I_{ph}, that have

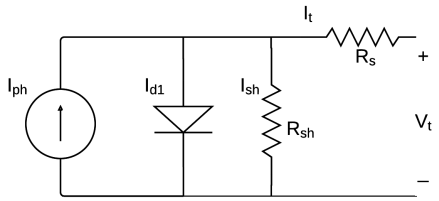

Figure 2.5: Photovoltaic solar cell equivalent circuit [11].

EHP recombination losses I_d, and losses through high conductivity shunts I_{sh} [11]. The recombination of EHP is described by Shockley's diffusion theory [11] and is exponentially dependent on V_{th}, the reverse saturation current I_s and the diode's ideality factor n. The ideality factor is unitless and describes how much the exponential deviates from an ideal diode. For a single junction device, n is typically between 1 and 1.5 [11]. Losses across the shunt resistance R_{sh} are calculated using Ohm's law and the internal voltage. When current I_t is flowing, there is a loss of voltage due to internal, series resistances modeled by R_s. Some authors suggest improving model accuracy by including a second parallel diode term. This second term describes the recombination effect that dominate at low voltages and low illumination levels. This behaviour is not relevant when simulating solar cells that are well-illuminated and operating at higher voltages for power generation applications [12].

$$\begin{aligned} I_t &= I_{ph} - I_d - I_{sh} \\ &= I_{ph} - I_s(\exp(\frac{q(V_t + R_s I_t)}{n k_b T}) - 1) - \frac{(V_t + R_s I_t)}{R_{sh}} \\ &= I_{ph} - I_s(\exp(\frac{(V_t + R_s I_T)}{n V_{th}}) - 1) - \frac{(V_t + R_s I_t)}{R_{sh}} \end{aligned} \tag{2.2}$$

These five parameters vary according to external conditions such as the change between the test temperature or the test irradiance, Φ. The dependencies are summarized in (2.3)-(2.7) where the subscript "stc" is used to indicate the reference parameters calculated at standard test conditions [13].

$$I_s(T,\Phi) = I_{s,stc}(\frac{T}{T_{stc}})^3 \exp(\frac{E_g}{k_b}(\frac{1}{T_{stc}} - \frac{1}{T})) \tag{2.3}$$

$$R_s(T,\Phi) = R_{s,stc}\frac{T}{T_{stc}}(1 - 00217ln(\frac{\Phi}{\Phi_{stc}})) \tag{2.4}$$

$$R_{sh}(\Phi) = R_{sh,stc}\frac{\Phi_{stc}}{\Phi} \tag{2.5}$$

$$n(T) = n_{stc}\frac{T}{T_{stc}} \tag{2.6}$$

$$I_{ph}(\Phi) = I_{ph,stc}(\frac{\Phi}{\Phi_{stc}}) \tag{2.7}$$

2.2 Applications

Silicon photovoltaics is a mature technology that is accessible and affordable making it a good choice for applications that need an independent source of electricity and have a strong source of ambient light available. The five parameter model simplifies the quantum operating physics of the solar cells into an equivalent circuit. This model can be used to determine useful parameters when the solar cells are integrated into larger optical or electronic systems.

Chapter 3

Window Light Attenuation

A goal of this project was to harness light entering through a window and convert it into electrical energy that can power a motorized blind. Modern glazings are designed to optimize building illumination and thermal performance. They employ special treatments and construction to ensure visible light is transmitted while solar irradiation of wavelengths that cause material fading or excessive building heating are rejected. By selectively blocking wavelengths of light, windows block some of the fuel that powers photovoltaics. This section quantifies the impact windows have on available solar power.

Recall the five parameter model discussed in Chapter 2.1.4 which can model solar cell's output current and voltage characteristics. Equation (2.7) shows that the photocurrent I_{ph} is significantly impacted when available light is attenuated. While the resistance parameters R_s and R_{sh} also vary, their impact on the output power is negligible. This chapter discusses methods to quantify the amount I_{ph} varies due to attenuating mediums present in common windows.

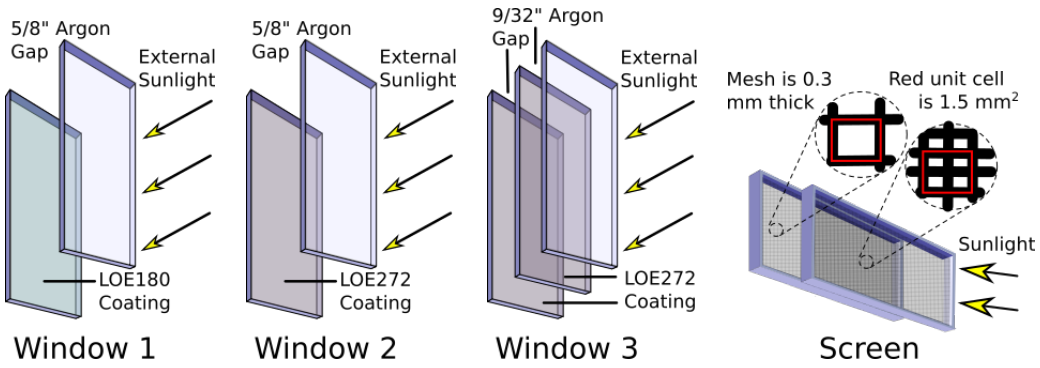

Figure 3.1: Exploded representations of the attenuating media evaluated.

3.1 Window Technology

Windows can employ a variety of different coatings for different purposes. Thin coatings of silver can prevent infrared (IR) wavelengths of light from entering and leaving the building or ultraviolet (UV) wavelengths from fading materials. Other coatings can be used to improve various performance parameters like indium tin oxide (ITO) which can improve the IR reflectance of windows or titanium dioxide which reduces water condensation [14].

Window samples were obtained from Cardinal Glass Industries to evaluate. These windows are recommended for residential use in Canadian homes. All windows are a series of 1/8" glass panes separated by an air gap of inactive argon. The test windows are pictured in Figure 3.1 and will be referred to according to their labels in that diagram. The LOE180 is a single layer of Cardinal's proprietary silver coating while the LOE272 is two layers of proprietary silver coating. A mesh bug screen was also obtained so that its impact on solar performance could be evaluated.

3.2 Fundamental Interaction

Equation (2.7) shows that the photocurrent I_{ph} varies linearly with changing irradiance G. The impact of all attenuating media are quantified using the relative photocurrent measurement represented by β in (3.1). This calculation compares the change in photocurent between the case where the solar cell is mounted behind an attenuating medium and the case where it is outside exposed to natural sunlight. The following sections present different methods of calculating the ratio β.

$$\beta = \frac{G_{inside}}{G_{outside}} = \frac{I_{ph,inside}}{I_{ph,outside}} \tag{3.1}$$

3.3 Analytical Evaluation of Window's Impact on Performance

A solar cell's ability to produce electrical power is constrained by the wavelength of photons impinging the device and the cell's ability to convert those particular photons into usable electricity. This section reviews an analytical approximation that estimates the relative change in photogenerated current between a solar cell mounted outdoors to one that is mounted on the inside of a conventional window.

The available sunlight in a conventional, outdoor, terrestrial system, is not a perfect blackbody function as would be expected from the sun because the earth's atmosphere absorbs certain wavelengths of light. The industry standard AM1.5 spectrum $\Phi_{AM}(\lambda)$ is drawn as the solid black curve in Figure 3.2 and considers the impact of the earth's atmosphere on the solar spectrum [15]. Typical windows reject UV and IR wavelengths, further modifying the spectrum that interacts with an indoor solar

cell. The transmission profile $\gamma_w(\lambda)$ of various windows can be obtained using industrial software Optics6. Multiplying $\Phi_{AM}(\lambda)$ by the $\gamma_w(\lambda)$, yields the spectrum of light available from the inside of a particular window. The expected irradiance spectrum from the inside of the analyzed windows are shown by the grey curves in Figure 3.2.

In order to perform a useful analysis, a given irradiance spectrum $\Phi(\lambda)$ (units of Wm^{-2}) must be converted to a photon flux $\Phi_{ph}(\lambda)$ (units of $m^{-2}s^{-1}$) using (3.2). This conversion is necessary because a solar cell converts individual photons into useful charges rather than a direct power conversion. The efficiency that a solar cell converts a photon to a useful electron is stored in a commonly available function called the the external quantum efficiency (EQE). The dashed curve of Figure 3.2 shows the approximate EQE of the solar cell used in the prototype.

Considering that EQE and $\Phi_{ph}(\lambda)$ vary given wavelength of photon, the rate of at which a solar cell generates charge carriers G can be estimated by summing the product of these two values across an appropriate wavelength range as expressed in (3.3). Since solar cell's photocurrent I_{ph} is dependent on the number of photons converted, $I_{ph} \propto G$ and β can be used to describe the expected change in I_{ph} caused by the attenuating media. The error propagation is included in Appendix B.2.1 and the resulting measured values of β are shown in Table 3.1.

$$\Phi_{ph}(\lambda) = \frac{\Phi(\lambda)}{E_{ph}(\lambda)} = \frac{\Phi(\lambda) \cdot \lambda}{hc} \tag{3.2}$$

$$G = \sum^{\lambda} \Phi_{ph}(\lambda) \cdot EQE(\lambda) \tag{3.3}$$

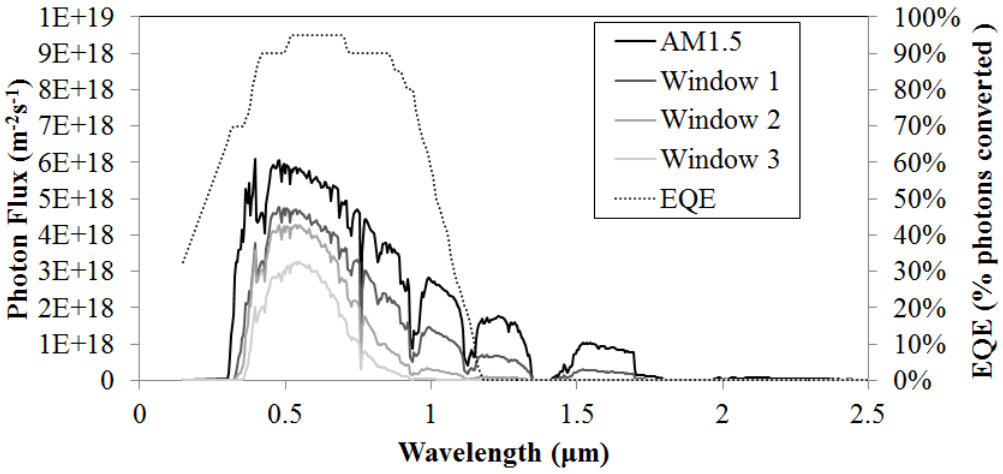

Figure 3.2: The unattenuated photon flux compared to the photon flux through various windows. The solar cell's EQE is also shown to demonstrate which wavelengths of light are effectively absorbed by the solar cell.

Table 3.1: Theoretical and experimental relative photocurrent (β) values for the different glazing attenuation media.

Window	Analytical Manufacturer Relative Photocurrent	Experimental Relative Photocurrent
Window 1	0.68 ± 0.09	0.7205 ± 0.0010
Window 2	0.48 ± 0.06	0.4929 ± 0.0007
Window 3	0.32 ± 0.04	0.3327 ± 0.0005
Single Screen	0.64 ± 0.06	0.6044 ± 0.0009
Double Screen	0.36 ± 0.10	0.3184 ± 0.0005

$$\beta = \frac{\sum^{\lambda} \Phi_{ph,window}(\lambda) \cdot \gamma_w \cdot EQE(\lambda)}{\sum^{\lambda} \Phi_{ph,AM}(\lambda) \cdot EQE(\lambda)} \tag{3.4}$$

3.4 Analytical Evaluation of Screen's Impact on Performance

Unlike windows that selectively transmit light, a screen does not discriminate and evenly shades the AM1.5 spectrum. The light intensity impinging on the solar cell, and the resulting photocurrent is directly proportional to the unshaded area of the screen. By determining the percentage area shaded by the screen, an estimate of the reduction in photocurrent can be calculated.

The investigated bug screen is composed of two square meshes which can overlap and adjust to various window widths as dimensioned and pictured in Figure 3.1. The dimensions shown in that image were evaluated using vernier calipers. Depending on the configuration of screen, a single grid shadow pattern may emerge or a double interlocking grid pattern may block the light. The shadow cast by this screen may vary depending on the angle of incident light but only light that was normal to the screen was investigated. The screen pattern can be thought of as a repeating 2D sequence of the red unit cell pictured in Figure 3.1 with area A_{uc}. A ratio β can be calculated by comparing the change in shaded area to the unit cell before and after the unit is shaded. β is calculated using the unshaded area of the single cell A_{uss} in (3.5) and the double pattern A_{usd} in (3.6). The results are included in Table 3.1 while a detailed calculation of the value with an error analysis is included in Appendix B.2.2.

$$\beta = \frac{A_{uss}}{A_{uc}} = \frac{1.2^2}{1.5^2} = 0.64 \tag{3.5}$$

$$\beta = \frac{A_{usd}}{A_{uc}} = \frac{4 \cdot 0.45^2}{1.5^2} = 0.36 \tag{3.6}$$

3.5 Experimental Evaluation of Media's Impact on Performance

3.5.1 Experimental Setup

A 150 W xenon arc lamp in conjunction with an ND03 neutral density filter was used to simulate the solar spectrum. The output of the simulator was checked against a calibrated PVM 298 solar cell to ensure operation at a consistent 1 sun power. A KXOB22-12X1L solar bit solar cell was placed within the calibrated beam and a Keithley 2400 source meter measured the output current of the cell given different voltage biases, tracing the solar cell's IV curve. This process was repeated with each of the attenuating mediums placed between the simulator and the solar cell. The outside glazing was always oriented towards the simulator.

3.5.2 Analysis

The five parameter model was fit to the collected experimental data using Bouzidi's method, a process outlined in Appendix C and [16]. A MATLAB script was written to automate this process considering the 20 datapoints surrounding the x and y intercept of the experimentally measured IV curve. The script would return the five solar cell model parameters, including I_{ph}, that accurately model the input dataset.

Attenuation was determined by taking the ratio of the solved I_{ph} parameters between the data collected when there was an attenuating medium $I_{ph_{attenuated}}$ and when there was no attenuating medium $I_{ph_{unattenuated}}$as shown in (3.7). The resulting ratios are included in Table 3.1 and error calculations are discussed in Appendix B.2.3.

$$\beta = \frac{I_{ph_{attenuated}}}{I_{ph_{unattenuated}}} \tag{3.7}$$

3.6 Discussion

The two discussed methods are consistent with each other. The analytical method is versatile because it uses freely available industrial data and presents a method of estimating a solar cell's EQE from a datasheet when it is not possible to obtain that information through other means. The experimental data is more precise and reflects the actual observed attenuation.

This determination did not consider the effect of temperature. A window will not transmit much of the higher frequency wavelengths or infrared wavelengths that are poorly converted to electrical energy but are readily converted to heat in a solar cell. Solar cells indoors are expected to run cooler and exhibit slightly improved voltage characteristics.

This work indicates that the amount a window will attenuate light and therefore, a solar cell's photogenerated current is highly dependent on which type of window is placed in front of it. This attenuation factor can be estimated analytically using the AM1.5 spectrum, the window's transmission profile and the solar cell's EQE. The windows evaluated appear to attenuate the photocurrent by 30-70%.

Chapter 4

Design Overview

Many motorized blind products are available on the market and many prominent design features of blinds are protected with patents [17]. Despite its availability, there are several areas where this technology can be improved, such as its power system. While power cables can be run directly to the electronics, an invasive and costly installation must take place to hide the cables in adjacent walls. Alternatively, the cables could be left exposed but this reduces the visual appeal of the device. Some products deal with this by introducing a portable power supply like disposable or rechargeable batteries. The batteries are typically installed near the top of the blind making it difficult to access them when they need to be replaced or recharged.

A few products address this challenge by taking advantage of the available solar power shining through the window. The Somfy WireFree solar pack or the solar panel add-on to the automation kit from MySmartBlinds use stationary photovoltaic panels that are secured to the inside of a window using clips or tape. This design typically requires more space because the batteries must be mounted outside of the cylinder that the blind fabric wraps around. Additional installation steps are also required to

secure the solar array to the window or to install more mounting brackets for external circuitry.

This section discusses a novel motorized blind that uses energy harvesting. Solar panels, control circuitry and the system's actuator are included within the prototype with the goal of reducing the use of space compared to other energy harvesting systems. The blinds can be inserted into conventional brackets without extra steps like securing solar panels to windows or mounting external electronics. Like other energy harvesting systems, this prototype removes the need to install wiring or perform difficult maintenance by replacing or recharging inaccessible batteries.

4.1 Design Overview

A conventional roller blind was modified to introduce automatic functionality using power harvested from a local solar array. Key features of the original blind like the fabric, mounting brackets and top cylinder were maintained to ensure it behaves in a similar fashion to a non-motorized counterpart. Additional electronics were integrated to make the system capable of autonomous operation.

The built prototype is pictured in Figure 4.1 (a) and can be grouped according to the three modules: A, B and C shown in Figure 4.1 (b). A bottom rail is necessary in a roller shade to keep the shade fabric flat. Module A consists of a redesigned bottom rail with a built-in solar array. As a backup measure, this bottom rail was built with a connector capable of accepting DC power from a wall adapter. The wall adapter connection can be used to quickly recharge the prototype's battery if it was used in the absence of light; a possibility while operating as a demo. Module C consists of the power electronics that were inserted in the top cylinder of the blind, where they are

hidden from view and save space. During operation, they keep track of the system's schedule, store excess energy in a battery pack and control a motor that rotates the unit to change the position of the blind. Module B is a conductive electronic textile (e-textile) that connects the power supplies of module A to the power loads in module C. To install the unit in the window, the prototype only needs to be mounted to the two brackets that came with the original unit. Since all circuitry and solar cells are self-contained in the unit, no further steps are needed to setup the physical installation.

The unit requires certain information in order to operate correctly such as which direction the motor must spin to move the fabric up or down and what Wi-Fi credentials will allow it access to the internet. To convey this information to the unit, the user must configure a secure digital (SD) card that the prototype reads on bootup. After bootup, the unit will operate on its own power, periodically checking its schedule by connecting to a server through the local Wi-Fi network. The user can update their blind's schedule by accessing a website from any device with a web browser. If the user would prefer an immediate change, they can pull the bead chain or send commands through the unit's included button box to send commands to the control electronics. LEDs and an emergency stop switch were mounted at the end of the top cylinder where they are visible and accessible.

The goal of the project was to successfully integrate a functional energy harvesting system. The remainder of this chapter reviews the design of power system in more depth because the following chapters evaluate the performance of this system in various contexts. Other information such as: rational for certain design choices, operation of the unit's communication system, and assembly instructions are included

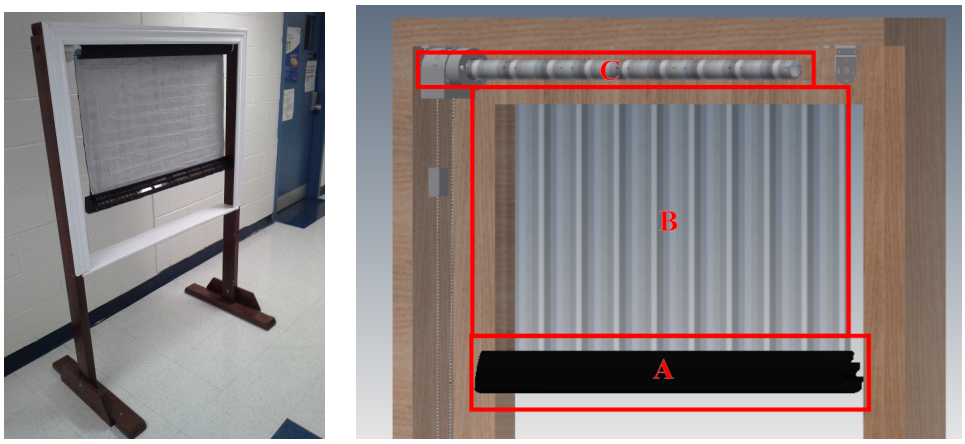

(a) (b)

Figure 4.1: (a) Photo of the assembled prototype in a mock window stand (outside view). (b) CAD model of the assembly (inside view). The top cylinder and fabric are transparent in (b) to highlight the built-in electronics.

in Appendix D.

4.2 Energy System

4.2.1 Solar Array

Prior to this thesis, four stacks of solar cells were built. Each stack is made of thirty-two solar cells wired in series as shown in Figure 4.2. Each individual solar cell is an IXOLAR SolarBIT and eight of these in series form a SLMD121H08 assembly (see red dashed circle in Figure 4.2). Bypass diodes were placed across each SLMD121H08 assembly allowing current flow when the unit is shaded. A blocking diode was placed in series to prevent current from running in the wrong direction. Each series stack was packaged using a foam backing that has a machined slot to fit the solar cells and diodes.

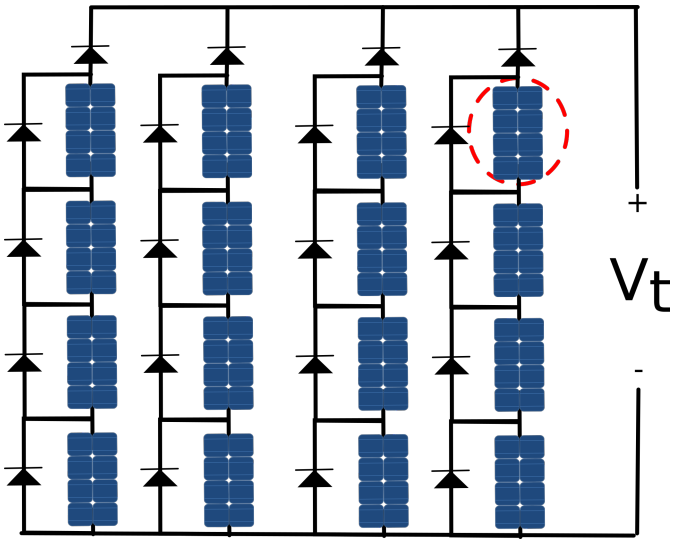

Figure 4.2: Wiring diagram of the prototype's solar array. The unit in the red dash represents a single SLMD121H08 product that is made of eight individual cells.

When the impinging irradiance is normal to the surface of the solar cells, photo-generation is optimized. This lends itself to tracking, a technique where solar arrays are physically manoeuvred to be normal to ambient irradiance. Costs of actuators and control systems can be avoided if solar panels are mounted at a static angle that maximizes their yearly generation potential. North American solar farms typically orient their panels due south at a static angle equal to the location's latitude [18]. Studies have shown that the maximum yearly output of these installations are insensitive to panel tilt [18][19]. One study in particular concludes that if a panel is tilted within $\pm 10^{\circ}$ of the optimal, it will only suffer a maximum loss of 2% generation over the course of a year [20]. The bottom rail was redesigned to take advantage of this trait through the inclusion of grooves capable of holding two rows of solar panels tilted at angles 25° and 45° from the horizontal as shown in Figure 4.3. One of the two rows will be mounted at near its optimal static angle for the large population of potential users who live in latitudes of 15° N to 55° N. There are additional advantages to this

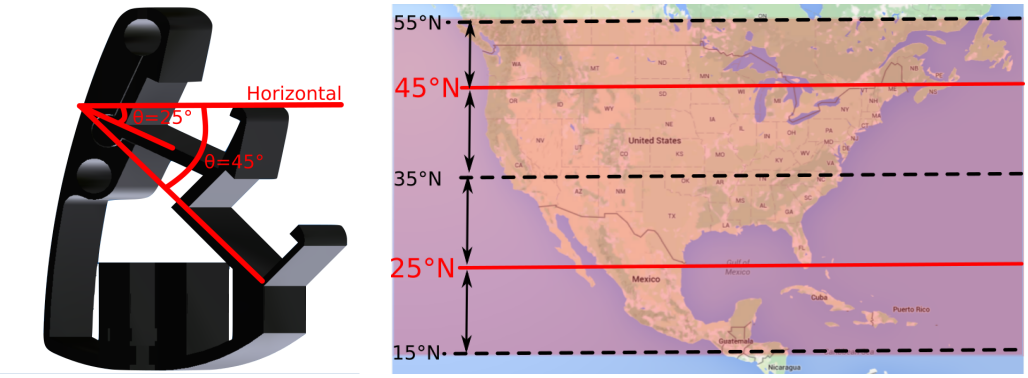

(a) (b)

Figure 4.3: (a) Bottom rail design with optimized solar array angles. (b) The red lines indicate the optimal latitudes for each of these angles while the red region indicates the latitude where one of the two array collects near optimal solar energy (red overlay).

configuration such as a smoother overall power generation profile. For example, in a southern location, the shallow tilt should produce more power overall, but at certain times, like sunrise or sunset, the sun may be low in the sky allowing the steeper tilted array to pick up the slack.

Several other design features were included in the bottom rail. The rail was designed to be hollow to include space for hidden wiring and other power electronics. Fabrication was limited to an available RepRap Huxley 3D printer, so parts were printed in 7.6 cm (3") pieces that slot together like puzzle pieces and can be secured with screws. When the screws are tightened, teeth in the bottom of the design are pushed together forming a strong mechanical connection. This connection is capable of contacting metal terminals from the power supplies to the embedded wires in the electronic textile so that power can be relayed to the electronics in the top cylinder.

4.2.2 Battery Pack

The prototype's nickel metal hydride (NIMH) battery pack was connected directly to the solar array to expedite the assembly. The voltage of the battery dictates the operating conditions of the solar array. The pack was designed using twelve series battery cells so that its general operating voltage would range between 10.9 V and 17.5 V so that the solar array would be operating near its optimal point as shown in Figure 4.4. A direct connection between the battery pack and the solar array is possible because a fully charged NIMH battery is tolerant to low rate overcharge it may experience from the solar array [21]. This system can be quickly assembled and tested without a mechanism to disconnect the array from the battery when the battery is fully charged.

Another notable design feature is the addition of a backup recharging mechanism. Power from an external wall adapter can be used by a fast-charging circuit to completely recharge the battery pack in under 2 hours. This was included in anticipation of suboptimal operating conditions while using this prototype as a demo.

In the future, the integration of peak power trackers should be explored to improve the energy extracted from the solar array.

4.2.3 Electrical Load

An MSP430 microcontroller was chosen to control the system because of its simple code and easy installation in a finished printed circuit board (PCB). During regular operation, it controls various peripheral electronics including the motor that moves the unit and the Wi-Fi chip that allows the circuit to communicate with the schedule server.

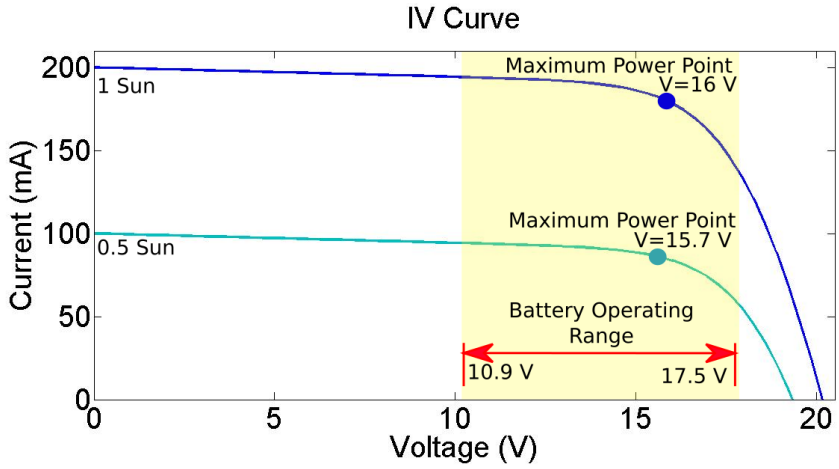

Figure 4.4: Solar array's IV curve with battery operating range overlaid in yellow. The battery pack biases the solar array near its optimal region given variable lighting conditions.

To ensure a robust energy harvesting system, the load power had to be minimized. A major source of power loss can be the buffer system that ensures the voltage remains within tolerance of system components. An efficient DCDC buck converter was used as a buffer for the low voltage (3.3 V) standby electronics. Ideally the high voltage components would also be buffered by DCDC converters. However, due to space constraints, these components had to be buffered by smaller, less-efficient, voltage regulators. A switching circuit was included in the final PCB design to disconnect the voltage regulators when not in use to avoid excessive standby power loss.

4.2.4 E-Textile Power Transmission

Most electrical interconnects in this system are short, thick cables with negligible power losses. The e-textile requires the use of long, thin wires in order to ensure blind flexibility and length requirements. Conductors that are thin and long are inherently resistive and may be subject to Joule heating power loss P_{jl} according to (4.1). Not

only does this prevent power from being used by the prototype, but the waste power is heat which could cause large temperature gradients to build that could damage electronics or hurt users.

$$P_{jl} = I^2 R \tag{4.1}$$

When designing an e-textile, steps can be taken to minimize failure risk and heat production. Using many fibers in parallel with small spacing between them can avoid the creation of localized hotspots in the material [22]. It also reduces the network resistance and increases redundancy. A redundant network is good because the entire system doesn't fail if a few conductors stop working. Using a higher DC voltage can improve power transfer while reducing necessary current.

Thin enamel wire with a conductor diameter of 0.16 mm (34 American Wire Gauge (AWG)) was chosen for the e-textile because with an assumed 0.05 mm coating of insulation, the wire is still smaller than the measured threads woven in the blind (diameter of 0.33 mm). This thin diameter limited the wires' impact on the blind's flexibility. The wire is an excellent conductor as it is a metal, however many wires were still connected in parallel to reduce network resistance to an acceptable level. These wires were sandwiched between a Hunter Douglas, woven blind and a white, unwoven, back material as shown in Figure 4.5. The entire assembly was secured using strips of thermally activated Heat'n Bond adhesive.

Figure 4.5 shows that the wires were grouped into three buses A, B and C made of 250, 100 and 250 parallel wires, respectively. Three buses were chosen to keep the positive connection of the wall adapter and solar array separate, while maintaining a shared ground. This setup requires one less bus than maintaining a separate ground

for both the wall adapter and the solar array. The size difference of the arrays is due to the possible currents that could be supplied. Bus A was designed to be the positive connection for the wall adapter and was designed with 250 wires to handle large currents (up to 3 A) from the wall adapter. Bus B was designed for the solar array's positive connection and uses less wires because the solar array can only supply a maximum of 200 mA. The shared ground bus, bus C was designed with 250 wires so it could handle current from both power adapter and solar array.

The number of parallel wires for the high current circuit was chosen according to the conservative 1 A for every 700 circular mils (0.355 mm^2) rule [23]. Given 3 A of current and 34 AWG cables, 71 conductors are needed when the current is evenly divided. The total number of wires should be increased (derated) to compensate for wire defects and imperfect contacts that cause resistance imbalance in the network. According to the national electric code 2005, when an excess of 41 conductors are used, the derating factor should be 0.35 [24] meaning 203 parallel wires would be needed for the high current buses. Buses A and C were actually made using 250 wires as this was easier to construct than 203.

The solar bus B was designed using 100 wires which is far in excess of the derated circular mill rule. This was done to reduce the path resistance to minimize solar losses because this is the primary method of recharging the unit. A round number like 100 was also easy to construct.

The ends of individual wires were stripped of insulation by exposure to a flame. They were connected into a single network using crimped copper tape and conductive adhesive. The copper tape was connected to the electronics by a crimp connection on the bottom rail. At the top cylinder, wires were soldered to the copper bus.

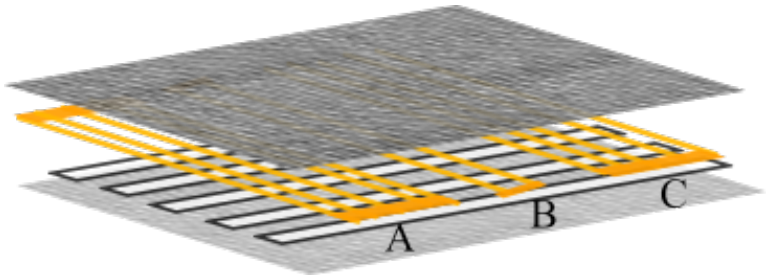

Figure 4.5: Prototype blind fabric. From top down is the finished blind surface, conductive wires (shown as yellow), strips of heat'n bond and white backing material. The wires are grouped into buses A, B and C each single yellow wire in the diagram represents 50 wires in the actual prototype.

Resistive losses were further reduced by increasing the voltage of the systems. The solar array is composed of 32 series cells adding voltage rather than current. A DCDC boost converter was included in the bottom rail to convert power from the wall adapter to 30 V so that less current is needed to transmit power.

4.2.5 Mechanical Load

One challenge while designing this system was to ensure the blind height wouldn't slip after being adjusted. The bottom rail is heavier than the equivalent rail for a manual system. Without an opposing force, the blind unit would unravel due to the weight of this new rail.

A simple friction brake was introduced by installing an adjustable screw to rub between a few of the PLA plastic enclosure pieces mounted at the top cylinder. This brake provides enough static friction to prevent the blinds from lowering by themselves, but the force of the friction must be overcome when the blinds are moved. This additional torque means more energy must be supplied to the motor during operation.

Chapter 5

Electronic Textile Thermal Considerations

The power supplies in the bottom rail were connected to the battery and load in the top cylinder through a custom built electronic textile (e-textile). While transmitting power, the e-textile loses a small portion of power through Joule heating according to (5.1). This power loss could cause a temperature gradient to build. Temperature gradients can cause component failure and safety concerns for the end user. This chapter reviews basic thermal models and the available literature on textile heating. This is used to evaluate the performance of the prototype e-textile in a worst-case configuration to show that the expected temperature gradients are safe.

$$P_{jl} = I^2 R \tag{5.1}$$

5.1 Literature Review and Theory

5.1.1 Thermal Lumped Parameter Model

The following section reviews the simplified lumped parameter thermal model as derived in [25]. A lumped thermal mass approximates a material at a uniform temperature. Good thermal masses include well mixed fluids, like a cup of tea, or masses that conduct heat within their bulk faster than to the external environment, like a block of metal. The change in temperature ΔT of the thermal mass T_{tm} with respect to its environment T_{env} is defined in (5.2). The thermal element has a mass m that requires additional thermal energy Q to increase the measured temperature gradient. The variable that describes the amount of energy needed to raise the temperature of the material is the heat capacity, c_{tm}.

$$\Delta T = T_{tm} - T_{env} = \frac{Q}{mc_{tm}} \tag{5.2}$$

It is impossible to instantaneously dump thermal energy into a thermal mass. Instead, thermal energy can be provided over time $\frac{dQ}{dt}$, which is the definition of power $P_{tm}(t)$. By taking the derivative of (5.2), a differential equation is obtained that describes the time derivative of temperature gradient $\dot{T}$ as a function of thermal power input. All following calculations consider power positive when flowing into the thermal mass.

$$\frac{d\Delta T(t)}{dt} = \dot{T} = \frac{P_{tm}(t)}{mc_{tm}} \tag{5.3}$$

Consider the example of an object at a given temperature T(t) that is placed in

an ambient environment at a different temperature, T_{env}. The thermal interactions between the object and the environment involve complex gradients due to multiple different heat exchange mechanisms (conduction, convection, radiation, material transport) which may occur with different interfaces. Given the example of a hot cup of coffee, heat can transfer to the external environment through convection at the surface of the liquid or by conduction through the insulating cup. This complex situation is often simplified by lumping the entire exchange into a single variable called the heat transfer coefficient h_t with units $W^2m^{-2}K^{-1}$. Equation (5.4) uses h_t to determine the thermal power flow between the environment and thermal mass $P_{env}(t)$, given a shared interface surface area A_s. A thermal element with a large h_tA_s product effectively transfers heat from itself to the external environment. For that reason, h_tA_s is often referred to as thermal conductance. The inverse, $\frac{1}{h_tA_s}$, is a measure of how much the element resists heat exchange and is called the thermal resistance, R_{th}.

$$P_{env}(t) = h_tA_s(T_{env}(t) - T(t)) \tag{5.4}$$

Now consider a thermal element that shares an interface with the external environment and is initially at the same ambient temperature. At some point, an external source of power begins heating the thermal element. For example, consider a kettle of water. Power from the kettle's element heats the water with P_{ex}, but some of that power leaks to the environment though conduction of the kettle enclosure P_{env}. The power that is being used to heat the thermal mass is the sum of thermal power exchanges in (5.5).

$$P_{tm}(t) = P_{ex}(t) + P_{env}(t) \tag{5.5}$$

Equations (5.3), (5.4) and (5.5) can be combined to make (5.6).

$$mc_{tm}\dot{T} = h_t A_s(T_{env}(t) - T(t)) + P_{ex}(t) \tag{5.6}$$

Equation (5.7) can be derived using Laplace transforms to solve (5.6) [25].

$$T(t) = T_{env} + \frac{P_{ex}}{h_t A_s}(1 - e^{-\frac{h_t A_s}{mc_{tm}}t}) \tag{5.7}$$

If this formula is solved for the temperature difference between the thermal mass and the ambient environment it can be further simplified to (5.8) by considering the final temperature difference $\Delta T_f = \frac{P_{ex}}{h_t A_s}$ and the time constant of the system $\tau = \frac{mc_{tm}}{h_t A_s}$.

$$\Delta T(t) = \Delta T_f(1 - e^{-\frac{t}{\tau}}) \tag{5.8}$$

5.1.2 Thermal Circuit Model

These equations are analogous to the behaviour of an electrical circuit. Equation (5.3) resembles the differential equation describing the voltage and current relationship of an electrical capacitor while (5.4) resembles Ohm's law. Drawing direct comparisons between both systems each parameter has an analog as described in Table 5.1.

A complex thermal system can be approximated as an electrical circuit. The solution to a heated element in an external environment (5.8) is analogous to the response of parallel resistor capacitor network when a constant electrical current is injected. When considering novel thermal systems, a first order approximation of its

Table 5.1: Analogous parameters between electrical and lumped thermal systems.

Electrical Parameter	Thermal Parameter
Voltage Difference, ΔV	Temperature Difference, ΔT
Electrical Current, I	Thermal Power, P
Electrical Resistance, R	Thermal Resistance, $\frac{1}{h_t A_s}$
Electrical Capacitance, C	Thermal Capacitance, $\mathrm{mc_{tm}}$

behaviour is to consider where heat could be transferred to the environment through a thermal resistor and where it could be stored in a thermal capacitor. An equivalent electrical network can approximate the response of an equivalent thermal system.

5.1.3 Electronic Textiles

E-textiles are an exciting field attracting much attention with advances in functional fibers, flexible electronics, microelectronics and sensors. Research has mostly focused on how to make such fabrics from electro-active threads [26] [10], fabrication methods [27] [28] or summarizing advances in the field [29] [30] [31]. Less research has been done on the operating considerations of electronic textiles such as Joule heating effects.

Heating effects of conventional textiles is a well understood field of research. Many techniques exist to evaluate thermal conductivity such as mathematical models [32], experimental simulation of skin contact [33] [34] or evaluation of thermal conductivity through the plane of a flat textile [34] [35] [36] [37]. These models are inapplicable to the modeling of e-textile waste heat since the source of thermal flux is integrated within the fabric rather than being on one side of the fabric.

A few studies discuss the purposeful addition of electrically resistive elements to create a heating fabric. The underlying concept is Joule heating which involves

controlling the e-textile network resistance and current injection according to (5.1) to create thermal power output. One report has found that laying electric textiles flat and allowing them to heat up will see the temperature rise according to an exponential approach according to (5.8). The paper reports the exponential time constant τ to range from 100-1000 seconds depending on the fabric tested [38]. Sezgin et al. investigated the impact of textile weave on thermal resistance and found that plain weaves have a greater thermal conductivity than twill or sateen [39]. Other factors can impact the thermal resistance of e-textiles such as strain, which has been shown to improve thermal conductivity by making the fabric's surface area more porous [38]. Another variable parameter is the fabric's electrical resistance which may change with temperature. Increasing temperature can change the electrical resistance of individual fibers or may cause fiber expansion improving inter-fiber contact [22]. This expanded contact can improve or degrade system resistance causing the e-textile to consume a different amount of power as it operates and heats [22]. Under these variable conditions, it is imperative that the fabric is designed conservatively because if conductors produce too much heat, they are liable to fail [22][38].

5.2 Conductive Window Blind Prototype

In the investigated motorized blind prototype, wires were integrated into the shade fabric in order to conduct electrical current from the bottom rail to the control electronics in the top cylinder. The detail design of the conductive window blind is discussed in Chapter 4.2.4. Briefly, the electrical network was designed using wires with a similar diameter to the fabric. Many were electrically connected in parallel. The network was designed to exceed the 700 circular mils per amp rule [23] and

national electric code (NEC) 2005 derating factors [24].

Two sources of power can provide the current used to recharge the battery pack. A low current solar array with a short circuit current rating of 200 mA can continuously trickle charge the battery pack. An alternative power source is an external wall adapter. When a wall adapter is plugged in, the fast charger circuit consumes a large amount of current to recharge the battery. When operating, the value of electrical current has been measured to reach values as high as 1.8 A. Charge times have been calculated to take a maximum time of 1.5 hours to fully recharge the battery.

5.3 Experimental Design

Modeling the e-textile as a lumped thermal mass that is receiving heat from Joule heating of the embedded wires while losing heat to the external environment, it would be expected to heat according to (5.8). This type of behaviour has been observed in heating e-textiles [38]. In this model, larger thermal resistances lead to larger temperature gradients. When the blind is fully wrapped around the top cylinder, the thermal resistance should be maximized because there is minimal surface area contacting the system with the ambient environment and therefore a larger thermal resistance. The outside surface should be the coolest getting progressively warmer near the core because heat from this center would have to travel through the thermal resistance of several layers of fabric.

The experiment was designed to measure the temperature gradients that develop under fast charging conditions while the blind is fully wrapped. Recall (5.1) which shows that Joule heating is proportional to the square of electrical current while only directly proportional to the network resistance. Less wires were used for the solar

array implying that it may have a slightly higher network resistance. However, the magnitude of current during a fast recharge is ten times larger than during the solar array's trickle charge. Therefore Joule heating is likely on the order of a hundred times larger between a fast recharge and a solar trickle charge. Investigation was limited to this worst case situation.

An experiment was designed to measure these temperature gradients. The fabric was laid flat and five Dallas 18B20 digital thermometers were secured to the blind using copper tape according to the layout in Figure 5.1 (a). An additional thermometer was left to measure the uncontrolled changes to ambient temperature. Wires connected the thermometers to an Arduino Mega which was remotely controlled by a LabVIEW program to collect temperature measurements. The blind was subsequently wrapped around the top cylinder as shown in Figure 5.1 (b).

The operating conditions of the conductive network was designed to mimic similar conditions to a charging battery. An Agilent E3646A power supply unit was configured to provide a constant current through the conductive blind network to observe the heating effects. The value for current was varied between 1 A and 2 A, a range appropriate to recharge the battery pack. The test was run for two hours, a time that is longer than the expected 1.5 hours needed to recharge an empty battery pack.

5.4 Analysis Method

The raw measured temperature of the blind when 2 A were passed through the e-textile are shown in Figure 5.2 (a). To further develop this model, the measured temperature values were converted into a ΔT gradient between the point of measurement and the ambient temperature. The ΔT value was calculated by subtracting

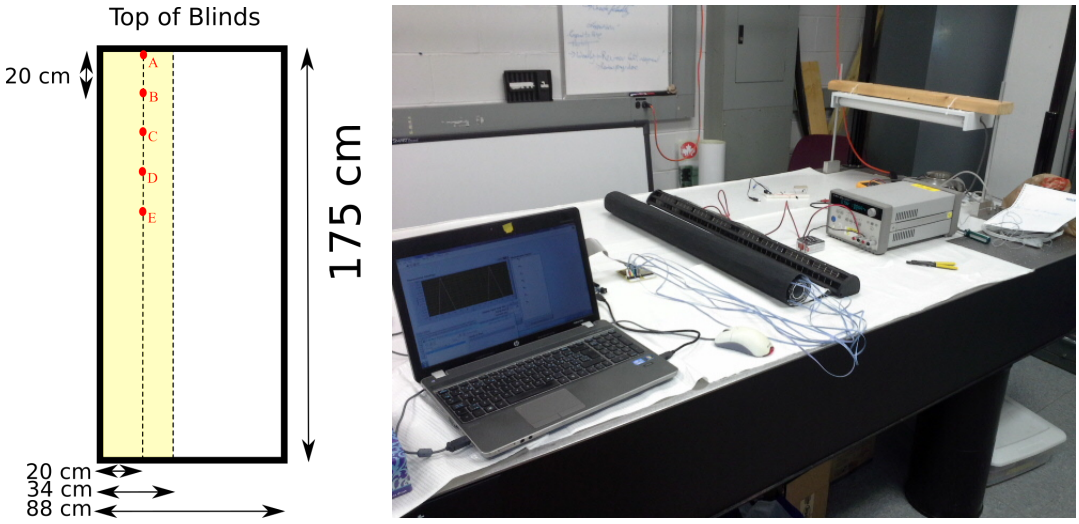

(a) (b)

Figure 5.1: (a) The yellow overlay displays the region occupied by the e-textile wire network and the red dots indicate the location of thermometers. (b) The fabric is wrapped around the top cylinder and a computer monitors temperature change as current is passed through the e-textile wire network.

the ambient temperature from the e-textile temperature and correcting it to ensure ΔT is 0 at t=0 because the system was initially at the same temperature. Details on the ΔT calculation and its error propagation are included in Appendix B.3. The resulting trend is shown in Figure 5.2 (b) and behaves according to (5.8). This behaviour is defined by two variables, ΔT_f and τ. MATLAB's fminsolve function was used to iteratively solve the value of ΔT_f, and τ that resulted in the lowest root mean square error (RMSE) between the model and the measured data. The solved model parameters for each experiment are recorded in Table 5.2 and examples of fit datasets are shown in Figure 5.2 (b).

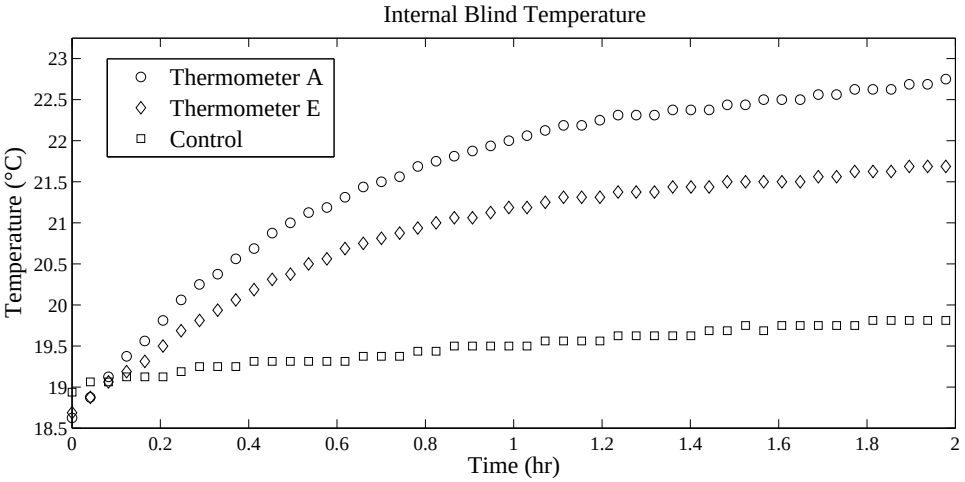

(a)

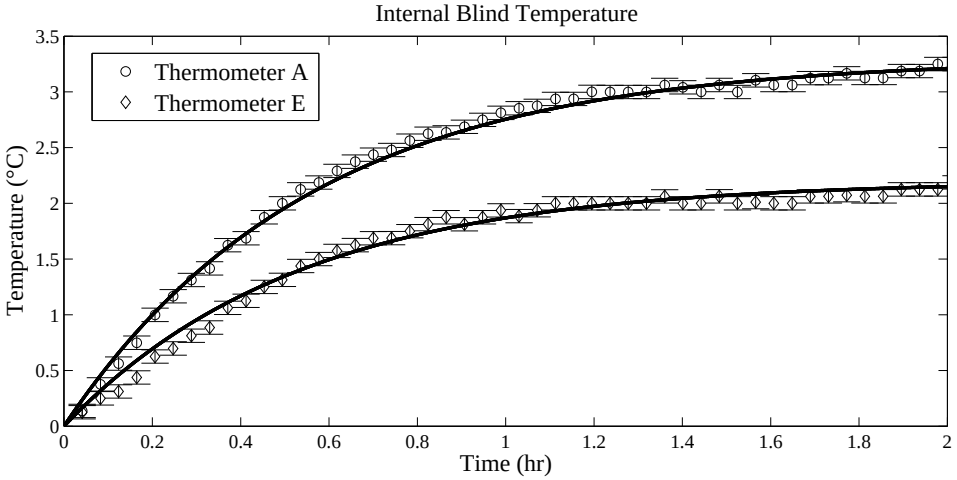

(b)

Figure 5.2: Temperature at different thermometer locations when 2 A are conducted through the e-textile. (a) Raw results. (b) The temperature difference between the thermometer location and ambient.

Table 5.2: Solved thermal analysis parameters.

Wire Current (A)	Location	ΔT_f (°C)	τ (s)	Model RMSE (°C)
1	A	1.1	1400	0.10
	B	0.88	1700	0.06
	C	0.80	1600	0.06
	D	0.69	1700	0.06
	E	0.61	1800	0.07
1.25	A	1.3	2100	0.09
	B	1.1	2500	0.09
	C	1.0	2500	0.08
	D	0.94	2400	0.06
	E	0.85	2400	0.07
1.5	A	2.1	2100	0.09
	B	1.9	1900	0.10
	C	1.7	1700	0.09
	D	1.6	1600	0.07
	E	1.4	1400	0.09
1.75	A	3.1	3100	0.06
	B	2.9	3700	0.07
	C	2.9	4400	0.07
	D	2.9	5000	0.07
	E	2.8	5700	0.07
2	A	3.3	2000	0.13
	B	2.9	2100	0.15
	C	2.7	2000	0.14
	D	2.4	1900	0.14
	E	2.2	1900	0.15

5.5 Discussion

The general shape of the blind's heating behaviour is an exponential approach, leading model to fit the data with and RMSE between 0.06 °C and 0.15 °C. However, the absolute uncertainty in the ΔT measurements is only 0.06 °C implying that small non-linearities exist in the data that prevent the model from predicting temperature within consistency bounds. This makes sense because this is a complicated system with many interfaces and an uncontrolled ambient environment which add complexity to its thermal response.

The repeatability of this test is limited. Recall thermal time constant τ is the product of the thermal resistance and the thermal capacitance. The time constants displayed in Table 5.2 vary significantly indicating that one or both of these parameters are changing between tests. This is further supported by (5.9), an expression that considers the ratio of ΔT_f at the same thermometer between different tests. The electrical resistance R_{elec} does not vary between tests. If the thermal resistance, R_{th}, were held constant, this ratio would be determined only by the squared current. This relationship is not observed in the data in Table 5.2 indicating that the thermal resistance also varies between tests.

$$\frac{\Delta T_{f,I_2}}{\Delta T_{f,I_1}} = \frac{I_2^2 R_{elec} R_{th}}{I_1^2 R_{elec} R_{th}} \tag{5.9}$$

Lessons can be learned from this first-order model of system thermal behaviour. Current conduction through the e-textile is needed as long as the battery is charging, which could take as long as 1.5 hours (5400 s). The modeled time constant for this heating behaviour is consistently in the thousands of seconds. During a long battery

recharge it is possible that the blinds could reach the steady state ΔT_f. Even if this occurs, the steady state temperature gradient is safe. The hottest temperature difference was 3.3 °C and was observed near the center of the wrapped e-textile while 2 A of current was conducted. This is a small temperature gradient that will not damage any electronics or pose any safety risk to a user. This test was done in the expected worst case situation. Conduction from the low current solar array or when the e-textile is unraveled and has a greater interface with the external environment are expected to produce even smaller temperature gradients.

5.6 Conclusion

A roller blind was made conductive by sandwiching thin magnet wires between two sheets of fabric. The wires were selected to have a similar diameter to the fabric and enough were placed in parallel to meet the 700 circular mils per amp rule and stringent NEC derating factors. The unit was tested in a worst-case situation by rolling the fabric in bundle then passing a similar amount of electrical current as could be expected in regular use, 1-2 A for 2 hours. Measurements from embedded temperature sensors exhibit behaviour similar to an exponential approach with additional nonlinearities. Fitting the data to an exponential approach model indicates that while the blinds may reach their maximum temperature while the battery pack is being recharged, that maximum temperature is of a magnitude less than 5 °C. This is an acceptable temperature rise and will not hurt any users or electronics.

Chapter 6

Motor Losses

Without a brake, the heavy bottom rail would cause the roller blind to unravel by itself. A source of friction was introduced between the rotating blinds and the mounting bracket to prevent unintentional slipping from occurring. A side effect of this solution is that the motor must overcome this friction brake when raising and lowering the blinds, requiring more power. This chapter develops an analytical model for the DC motor and uses it to quantify the electrical power wasted in overcoming the friction brake.

6.1 DC Motor Physics

The basic physical interactions between electric charges, wires and magnetic fields are discussed in [40] and certain principles of interest are summarized here. Note that in the previous sections, the value of q has been a scalar quantity. For these calculations it is important to determine the velocity of positive charge. When discussing the velocity of electrons, direction vectors must be flipped to represent the velocity

of positive charge.

Consider a single charge flowing through a magnetic field as pictured in Figure 6.1 (a). This charge experiences a force according to (6.1). When this fundamental interaction is considered in a larger system it becomes useful. Consider the case in Figure 6.1 (b) where electrical current is put through a conductor in a magnetic field. This conductor feels a force according to (6.2).

$$F = q\bar{v} \times \bar{B} \tag{6.1}$$

$$F = \bar{I}l_c \times \bar{B} \tag{6.2}$$

The same principle causes a voltage or induced electromotive force (EMF) to appear across the moving wire in Figure 6.1 (c). In this case, all the charges in the wire feel a force causing them to move in the system. The electrons can only move the length of the wire l so the work done by the magnetic field moving these charges is (6.3) which corresponds to the development of a voltage in (6.4).

$$W = F \cdot d = (q\bar{v} \times \bar{B}) \cdot (l) \tag{6.3}$$

$$V = W/q = (\bar{v} \times \bar{B}) \cdot (l) \tag{6.4}$$

The principle motor diagram (Figure 6.2) shows a device that takes advantage of these physical interactions to provide constant mechanical rotation when provided with electrical power. In this idealized model, the light blue portion represents the motor's stator, the stationary part of the motor made of a permanent magnet. The

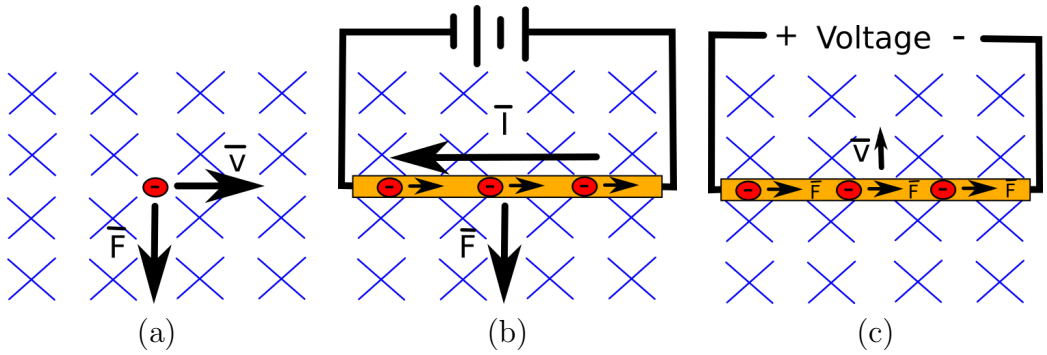

Figure 6.1: Electromagnetic interaction of charges and wires in a magnetic field (going into page). (a) Force felt by a single moving charge. (b) Force felt by a wire conducting current. (c) Voltage is induced by a wire moving through the field. Based on [40].

permanent magnet's field interacts with the current-carrying conductor loop called the armature, (or rotor). The armature is designed with a specific radius r_c and length l_c. The key to this motor's construction is the commutator which ensures current always flows in such a direction that the rotor spins continuously. A running, non-stalled motor has a current carrying armature loop that moves according to the vector $\bar{\nu}$, with a rotational velocity ω. This loop experience an EMF represented by the symbol U and defined by (6.5) [41]. It is possible to simplify this to (6.6) because the stator is designed to ensure that the magnetic field is maintained perpendicular to the rotor's length for the majority of the coil's rotation. Many of the design specific details of this motor can be lumped together into a single coefficient k_U in (6.7) which clearly shows that the motor's EMF is proportional to the speed at which it rotates.

$$U = -\oint(\bar{\nu} \times \bar{B})d\bar{l} \tag{6.5}$$

$$U = 2|B|\nu l_c = 2|B|\omega r_c l_c \tag{6.6}$$

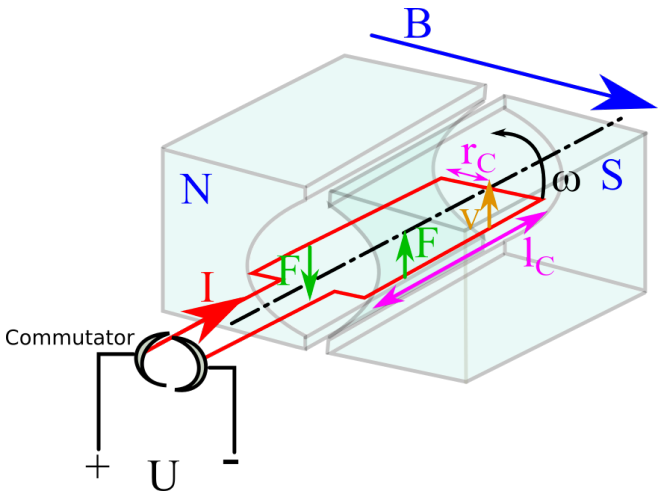

Figure 6.2: Principle diagram of a DC motor. Based on [41].

$$U = k_U \omega \tag{6.7}$$

By considering the geometry of the rotor the motor's magnetic field and the terminal current, equation (6.2) can be used to calculate the rotor torque in (6.8) [41]. By lumping all motor construction details into a coefficient k_τ the equation simplifies to (6.9). The output torque is linearly proportional to the motor's electrical current.

$$\tau = 2IBl_c r_c \tag{6.8}$$

$$\tau = k_\tau I \tag{6.9}$$

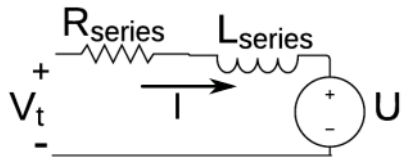

Figure 6.3: Motor equivalent circuit model. Based on figures in [41].

6.2 DC Motor Model

The previously derived formulas only relate to an idealized motor where all electrical inputs are perfectly converted into mechanical energy. Figure 6.7 shows an equivalent circuit model that considers electrical losses experienced by a real motor [41]. Electrical power that is converted into mechanical power is represented by the voltage source U while a series resistance R_s and inductance L model extra losses. The terminal voltage V_t of this machine can be represented by (6.10) which simplifies to (6.11) in the steady state.

$$V_t = U + RI + L\frac{dI}{dt} \tag{6.10}$$

$$V_t = U + RI \tag{6.11}$$

If R_s, k_U and k_τ are known, then measurements of terminal voltage and current can be used to solve for the motor's mechanical performance. Alternatively, measurements of the motor's rotating speed and torque can be used to solve the electrical characteristics.

It is important to note that not all mechanical power contributes to useful work. The motor rotor has a base level of friction that must be overcome while it spins,

which means some mechanical power is always being wasted. If an intermediary system of components manipulate the mechanical power, like a series of pulleys or a gear set, additional friction losses can be expected.

6.3 Motorized Blind Model Development

The motor used in the automatic window blind prototype was a Phidgets 3264E_1. This motor comes with a built-in optical encoder that outputs a square wave whose period T_{enc} is proportional to the motor's speed of rotation. The wave's period corresponds to the time needed to complete $\frac{1}{360}$ of a rotor revolution. The DC motor's armature is connected to an orbital gear set that scales the rotating speed down and the torque up by a factor of $139\frac{184}{1221}$.

A series of tests were developed in order to measure motor behaviour. A National Instruments (NI) MyDAQ was used to monitor the operating conditions of the motor. Since the MyDAQ is limited to sensing voltages less than 10 V, a voltage divider was used to step down motor terminal voltage by a factor of three. While the MyDAQ has a built in ammeter, it takes time to measure current. Instead, a 1 Ω resistor was inserted into the circuit where electrical current was to be measured. The MyDAQ monitored the voltage across this resistor and Ohm's law was used to calculate current. The MyDAQ is capable of making timing measurements of a switching input. This was used to read the period of the motor's encoder T_{enc} so that the rotation speed was measured. These measurements were used to develop an electrical model based on Figure 6.2 and governed by equations (6.7), (6.9) and (6.11).

6.3.1 Open Circuit Voltage Test

Equation (6.7) shows that the internal EMF is proportional to armature rotational speed. When electrical power is fed to the machine, this EMF is observed as a load that converts the electrical energy to mechanical energy. Conversely, a spinning rotor converts that input mechanical power into an electrical output. If no load is connected to the motor, then the EMF will be measurable from the motor's terminals. Measurements of the rotor speed and EMF can be used to determine the constant k_U.

Two Phidgets 3264E_1 motors were mounted facing each other in 3D printed brackets. Their rotors were secured together using a 3D printed sleeve secured with set screws. This setup is shown in Figure 6.4. A voltage limited power supply would drive one motor to rotate the second motor's armature at a constant speed. The second motor's connections were left in the open circuit condition and its terminal voltage V_t and the encoder period were measured. The results from this tests were used in (6.12) to determine k_U.

$$k_U = \frac{360}{2\pi} V_t T_{enc} \tag{6.12}$$

6.3.2 Short Circuit Current Test

With the short circuit test, the motor terminals are shorted while the motor armature is spun by an external force. This forces the internal EMF to be dropped across the motor's internal series resistance R_s. If k_U is known and the motor's rotational speed is measured, (6.7) can be used to determine the motor's EMF. Further, if the

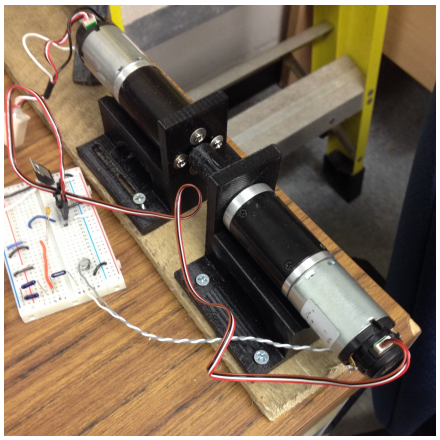

Figure 6.4: Two motors are mounted in 3D printed brackets with their rotor's connected by a 3D printed sleeve. One is energized to rotate the second at a constant speed.

current flowing through the shorted terminals I_t is measured, Ohm's law can be used with the previously solved EMF to determine the motor's internal resistance R_s.

Similar to the previous test, the armatures of two identical motors were connected so that the first motor drove the second. The second motor's terminals were placed across a 1 Ω current measuring resistor R_I. The NI MyDAQ measured this resistor's voltage to determine current. The MyDAQ also monitored T_{enc}. The final Ohm's law calculation must adjust for this extra resistance when used to calculate R_s.

$$R_s = \frac{2\pi k_U R_I}{360 T_{enc} \cdot V_t} - R_I = 13.69 \tag{6.13}$$

6.3.3 Power Test

Power relationships were used to develop a test to solve the parameter k_τ introduced in (6.9). Mechanical power is the product of rotational speed and torque. By subtracting the electrical losses from the input electrical power, the remainder is

known to be converted into mechanical rotation. These two equations are equated in (6.14) and reduced to a useful equation in (6.15).

$$P_{mech} = \tau \cdot \omega = P_{in} - P_{elec} = I_A V_t - I_A^2 R_s \tag{6.14}$$

$$k_\tau = \frac{V_T - I_A R_s}{\omega} = \frac{360 T_{enc}}{2\pi} \cdot (V_t - \frac{V_{meas}}{R_I} R_s) \tag{6.15}$$

This test was run by allowing one Phidgets 3264E_1 to spin freely while monitoring the current flowing in, the motor terminal voltage and the encoder period. The voltage across R_I was measured V_{meas} and used to determine the armature current I_A. The motor was run at high voltages and currents so that it would run faster because this was found to produced less noisy results.

6.3.4 Baseline Test

The motor was removed from its usual mounting position within the top cylinder and installed on a temporary jig outside of the unit as shown in Figure 6.5. From this position, current, voltage and encoder output from the motor could easily be monitored as the motor raised and lowered the fully assembled blind prototype. A voltage limited power supply unit (PSU) provided 14 V of power, similar to the nominal voltage of the prototype's battery pack. Power from the PSU went through a series current measuring resistor before going through a 12 V regulator similar to the one within the prototype. Measurements from the series resistor were used to monitor current while the regulator was used to feed a similar voltage input to the motor as it would get from the prototype control circuitry. This data was used to

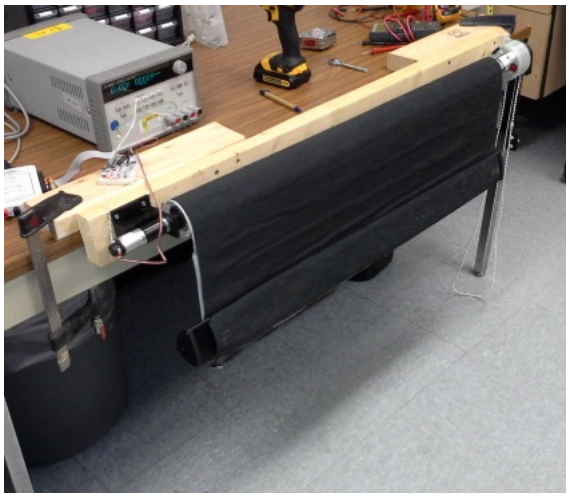

Figure 6.5: The motor was mounted outside the unit and used to drive the blind prototype up and down. Current, voltage and encoder period measurements were used to determine the power needed for this operation.

ensure consistency from the model and to quantify efficiency improvements.

6.4 Results

After running the previously developed experiments and collecting measurements, the motor model parameters were calculated and are presented in Table 6.1. These calculations and their corresponding error are included in Appendix B.4 while Appendix B.4.4 uses these parameters and the observations from the baseline test to show model consistency. Using the measured current and rotational speed of the blind while moving the unit up, the model's terminal voltage was calculated to be 13±2 V which is consistent with the measured value of 12.1±0.1 V.

Using the calculated model parameters in Table 6.1, it is estimated that when the motor is mounted in the test jig for the baseline test, it exerts 1.6 ± 0.5 Nm of torque to raise the blinds and 0.2 ± 0.3 Nm to lower the blinds. The uncertainty of

Table 6.1: Calculated motor model parameters.

Test	Parameter	Value
Open Circuit Voltage	k_U	$(21.4 \pm 1.1) \times 10^{-2} V \cdot s/rad$
Short Circuit Current	R_s	$(14.0 \pm 1.8)\Omega$
Power Test	k_τ	$(21 \pm 2) \times 10^{-2} Nm/A$

these calculations is rather high because of the large uncertainty in both the model parameters and the baseline test data. In particular, the measured electrical current going into the motor as it lowered the blinds was very noisy and had an uncertainty of 127%. The ability to collect many sets of data was limited because the jig was only a meter high which doesn't take long for the blind prototype to traverse. Additionally, while spinning, it is likely that the friction brake was imperfect and didn't apply an even amount of friction throughout the rotation. The motor need to provide varying torque to overcome this varying friction and would be expected to require a variable current draw. The high uncertainty in the current measurements is consistent with an imperfect friction brake.

Despite the uncertainty, the calculated torque is consistent with experimental observations. A different motor with a smaller gearbox that stalls at 1.8 Nm was found to be incapable of raising the blinds. This observation is consistent with the calculation that indicates the torque needed to raise the blinds is 1.6 ± 0.5 Nm.

When the bottom rail is weighed and the top cylinder's dimensions are taken, the minimum torque needed to lift the unit can be calculated to be 0.4±0.2 Nm. Assuming the voltage is held constant and the motor uses the same orbital gear set, the power needed to lift an idealized blind without the friction brake is 46% lower than the power observed in the baseline test. These calculations are provided in Appendix B.4.5. Replacing the friction brake with an alternative system could result

in significant power savings. A simple improvement from this design change is that the system would consume less battery power leading to a longer life.

6.5 Conclusion

The built-in friction brake that prevents the blinds from falling by themselves causes the motor to need twice as much power as a frictionless system. Replacing the friction brake with an improved mechanical system can lead to reduced power loss and increase prototype run-time.

Chapter 7

System Power Flow

The power sources and loads during typical operation are illustrated in Figure 7.1. A battery stores energy during times of excess solar generation and provides power during solar shortages. This is necessary because factors like solar altitude, time of day and obstructions cause the available solar power to vary. It is conceivable that the system could be placed in a sub-optimal configuration like a north-facing window or behind a heavily tinted glazing. Worse yet, it could be completely shaded by an awning or a tree. As long as there is charge in the battery, the system can maintain operation even with inadequate lighting.

The nonlinear current and voltage characteristics of the battery, solar array and electrical load are discussed in this chapter. A numerical, pseudo-empirical, equivalent-circuit, system model was developed to simulate the interaction of these separate systems. The simulation was used to quantify the minimum light needed for continuous operation and the time it would take to completely lose power if no sunlight was available.

7.1 Modeling Solar Cell Behaviour

Solar cell operating physics and the five parameter equivalent-circuit model of solar cells are discussed in Chapter 2. When the five parameters are fully defined, an iterative numerical method can solve the harvested terminal current I_t given an input voltage V_t according to (7.1). This section reviews a method that solves for the values of the parameters such that the equivalent circuit behaviour is consistent with the parameters described on the manufacturer's datasheet.

$$I = I_{ph} - I_d - I_{sh} = I_{ph} - I_s(\exp\frac{(V_t + R_s I_t)}{nV_{th}} - 1) - \frac{(V_t + R_s I_t)}{R_{sh}} \tag{7.1}$$

7.1.1 Cubas' Parameter Estimation Method

In [11], Cubas, Pindado and Victoria develop a method of estimating the five equivalent circuit parameters using numerical techniques and boundary conditions. In order for the model to be consistent with datasheet values the following boundary conditions must be met:

- When the terminal is shorted and no external voltage is applied, $V_t = 0$, the

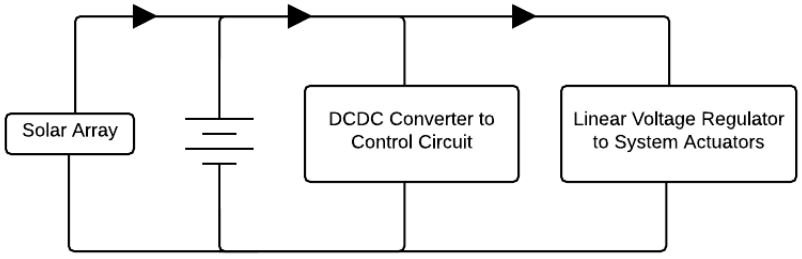

Figure 7.1: Block diagram showing system power sources and load.

model's predicted current must equal the datasheet's reported short circuit current, I_{sc}.

- When the terminal is left open and no current is allowed to flow, $I_t = 0$, the model's predicted voltage must equal the datasheet's reported open circuit voltage, V_{oc}.

- The value of the model's maximum power, $V_{mp} \cdot I_{mp}$, must be equal to the datasheet's reported maximum power, P_{max}.

- When the model's power function is considered, the derivative at the maximum power point must be 0, $\frac{\delta P(V_{mp})}{\delta V} = 0$.

To completely solve a system of five parameters, five bounding conditions are needed. This method ignores the fifth constraint by recognizing that the ideality factor n of the diode lies along a small range [1, 1.5] from which a value is arbitrarily selected. With a value for n, an iterative numerical method such as MATLAB's fminsolve can solve for the implicitly defined R_s value in (7.2). The remaining parameters can be obtained by solving (7.3) to (7.5) sequentially. The derivation of these equations are described in detail in [11].

$$\frac{nV_{th}V_{mp}(2I_{mp} - I_{sc})}{(V_{mp}I_{sc} + V_{oc}(I_{mp} - I_{sc}))(V_{mp} - I_{mp}R_s) - nV_{th}(V_{mp}I_{sc} - V_{oc}I_{mp})} = \exp(\frac{V_{mp} + I_{mp}R_s - V_{oc}}{nV_{th}}) \tag{7.2}$$

$$R_{sh} = \frac{(V_{mp} - I_{mp}R_s)(V_{mp} - R_s(I_{sc} - I_{mp}) - nV_{th})}{(V_{mp} - I_{mp}R_s)(I_{sc} - I_{mp}) - nV_{th}I_{mp}} \tag{7.3}$$

$$I_0 = \frac{(R_{sh} + R_s)I_{sc} - V_{oc}}{R_{sh}\exp(\frac{V_{oc}}{nV_{th}})} \tag{7.4}$$

$$I_{pv} = \frac{R_{sh} + R_s}{R_{sh}} I_{sc} \tag{7.5}$$

7.1.2 Improved Parameter Estimation Method

The parameter with the greatest impact on solar cell performance is irradiance. Some datasheets provide information describing the change in open circuit voltage as a function of solar cell illumination. By following Cubas' method, the developed model will match the open circuit, short circuit and max power conditions under standard illumination (1000 W/m^2), but may not match the datasheet values when the light is attenuated. A numerical method can be implemented which iterates through values of n until a model that is consistent with the datasheet's expected light dimming performance is defined. The algorithm for this estimation technique is summarized in the flow chart in Figure 7.2.

7.1.3 Implemented Irradiance Model

As the intensity of irradiance varies, so does the photocurrent generated by the solar cell according to (7.6) [13]. Daily irradiance is a complex subject. Over the course of a day, irradiance can vary because of: changing intensity of components of light (direct or diffuse), geometry of the system (path of the sun and its relationship to the solar panel), the local weather and many other variables.

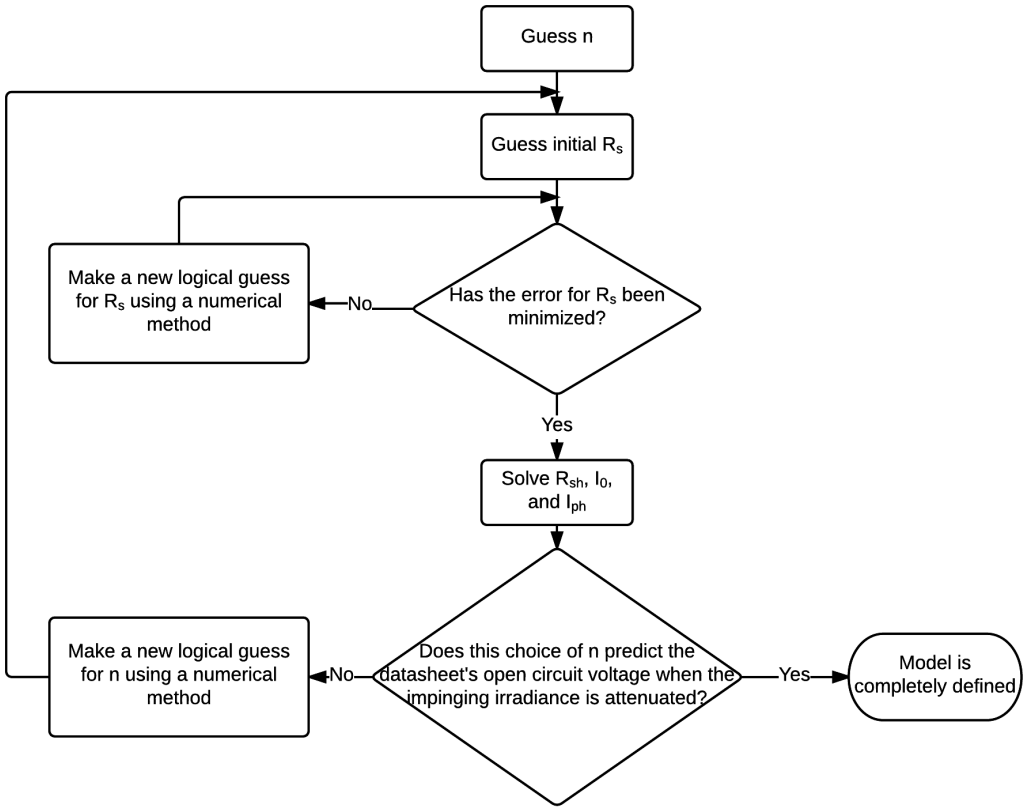

Figure 7.2: Algorithm that is used to define a solar cell model that is consistent with datasheet values.

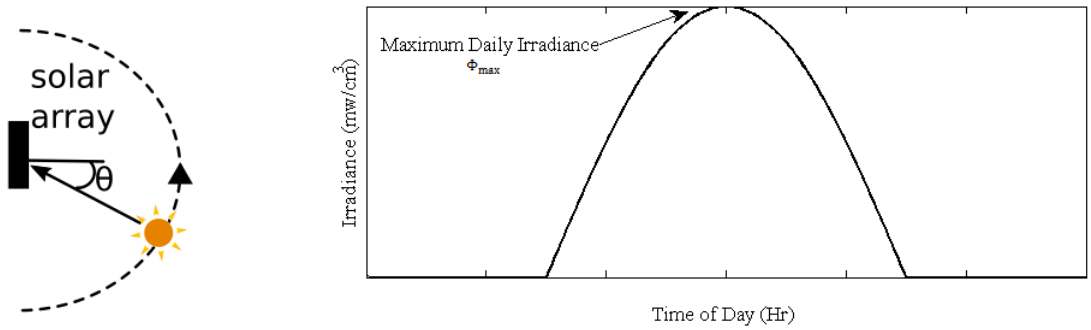

(a) (b)

Figure 7.3: (a) Simple irradiance model considers the sun following a perfect arc around an appropriately angled solar array. (b) The resulting half sinusoid irradiance profile.

$$I_{ph}(\Phi) = I_{ph,stc}(\frac{\Phi}{\Phi_{stc}}) \tag{7.6}$$

A simple first order model approximation was employed that assumes the sun follows a perfect arc around an appropriately oriented solar array as shown in Figure 7.3 (a). If only the direct component of light is considered, it can be calculated by considering the angle made between the incident light and the normal of the solar array according to (7.7). This produces the half sinusoid profile in Figure 7.3 (b). This model provides the opportunity to explore the impacts of changing attenuating medium by varying Φ_{max} or different lengths of days by varying the period of the sinusoid.

$$\Phi(t) = \begin{cases} \Phi_{max} cos(\theta(t)) & -90 \leq \theta(t) \leq 90 \\ 0 & \theta(t) < -0, \theta(t) > 90 \end{cases} \tag{7.7}$$

Table 7.1: Parameters to model IXOLAR SolarBIT using the five parameter, equivalent circuit model

Parameter	Value
n	1.34
R_s	0.821Ω
R_{sh}	222Ω
I_0	5.64×10^{-10}A
I_{ph}	0.0502 A

7.1.4 Implemented Solar Cell Model

A MATLAB script was written to solve the parameters according to the algorithm in Figure 7.2. The numerical method used to solve for R_s and n was fminsolve. The boundary conditions were solved for a single IXOLAR KXOB22-12X1L SolarBIT's defining parameters that are included in Appendix E. For the expanded method, n was chosen such that the open circuit voltage of the model was 0.56 V when the irradiance was 100 W/m^2. The parameters that fit these constraints are shown in Table 7.1.

The implemented solar array is composed of individual solarBITs that are wired according to Figure 4.2 in Chapter 4.2.1. Thirty-two solarBITs are wired in series to form a stack whose terminal voltage is the sum of the individual cells. This stack is connected to the battery pack, and the terminal voltage is determined by the battery's voltage. If the voltage is assumed to fall evenly across all cells in a series stack, each solar cell's bias can be calculated by dividing the voltage applied to the stack by thirty two.

Additionally, there are four separate stacks wired in parallel to form the system's solar array. Whatever value of current is produced by a single solar stack must be scaled by four in the simulation.

The implemented irradiance model was varied depending on the simulation. Typically Φ_{max} was chosen to be consistent with the attenuation of a residential window. The day length was also varied and was chosen to be similar to the day length observed in Hamilton Ontario.

7.2 Control Circuit Load

7.2.1 Types of Loads

The prototype's control circuit can run several different tasks each requiring a variable amount of power. Typically, the system operates in standby where the microcontroller is energized but overall power consumption is low as it is only keeping track of time. Every five minutes, the system turns on the XBee Wi-Fi peripheral chip to check if its schedule has been updated. This action requires additional power for the duration of the message exchange. While this time varies, it is typically short. When the prototype physically moves the blinds, a high power circuit is energized to provide the motor with the appropriate voltage to power the motor. The power demands of the motor vary depending on whether it is fighting gravity to lift the blind or letting the fabric fall.

The low power microcontroller and XBee chip operate at 3.3 V. These components are powered by a DCDC converter that efficiently converts high voltage battery power to this lower voltage. Since DCDC converters transfer power, P=VI, the rate of current drain from the battery is dependent on the voltage of the battery.

A linear voltage regulator ensures that the voltage supplied to the motor remains at the rated 12 V. This device acts as a variable resistor that burns the extra voltage

across a variable internal resistance. This means that the current required by the load at 12 V is the current taken from the battery at a higher voltage. The particular voltage regulator used (LM1085) requires the voltage supply be 1.3 V greater than the supplied 12 V to ensure operation. When the battery pack reaches a voltage of 13.3 V, the circuit may fail. A voltage regulator is also used to power the 5 V optical encoder.

7.2.2 Voltage-Power Relationship

An experiment was designed to verify the voltage-current behaviour of the load. The prototype circuitry was removed and programmed to do one of the following tasks: stay in standby, energize Wi-Fi or power a free-spinning motor. Instead of providing power from the battery pack, an Agilent E3646A power supply unit (PSU) was manually set to provide power at a known voltage and a Fluke 179 multimeter was used to measure the current flowing into the control circuit.

The current needed by the standby circuit is shown in Figure 7.4 (a) and the current of the system while operating the Wi-Fi chip is shown in Figure 7.4 (b). As the input voltage is increased, the required current to power the load decreases. This behaviour is consistent with the expected behaviour of the DCDC converter.

The same test was performed while the load powered a free spinning motor. Figure 7.4 (c) shows the results that vary from the the previous tests. The current flowing into the motor varies with significant error as denoted by the displayed error bars. This behaviour is similar to previous observations made in the motor analysis in Chapter 6. The dashed line is the mean current which is consistent with most measured values. This voltage invariant current demand is expected for a load that is buffered by a

linear voltage regulator.

7.2.3 Baseline Test

A baseline test is discussed in Chapter 6.3.4 where the prototype was operated to raise and lower the blinds and the voltage, current and motor period were monitored. These results show that 0.490 ± 0.13 A are necessary to raise the blinds while 0.060 ± 0.08 A are needed to lower the blinds.

7.3 Battery

7.3.1 Battery Physics

There are three major components in a NIMH cell. The anode is the negative electrode which gives up electrons during discharge [42]. Complex metal hydrides (MH) like AB_5 (LaCePrNdNiCoMnAl) are used for anode materials in NIMH batteries [21]. The cathode is the positive electrode made of nickel hydroxide [21] which accepts electrons during discharge [42]. The last component is the electrolyte which allows ions to be transferred between the electrodes [42]. It is typically made of 30% potassium hydroxide water solution [21].

A complete description of the battery reactions is provided in [21] and briefly summarized here. When discharging, a reduction reaction occurs at the nickel electrode while the metal hydride (MH) anode is oxidized. These reactions are called half-cell reactions and a byproduct of these reactions is a potential difference E_0 that forms between the electrode and electrolyte.

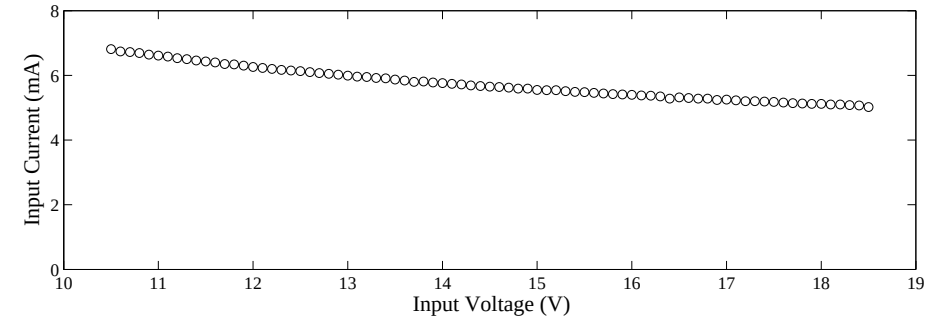

(a)

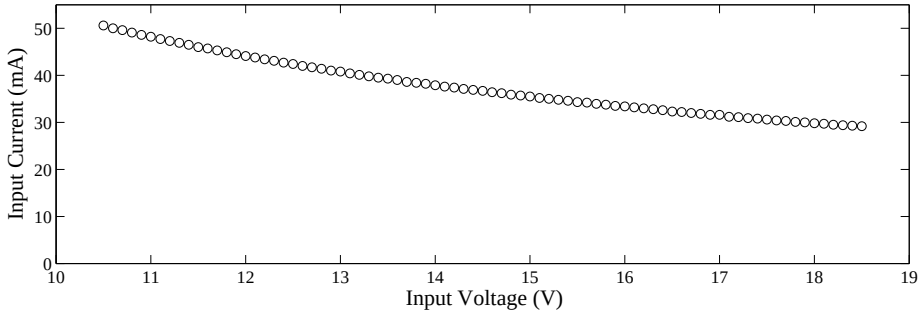

(b)

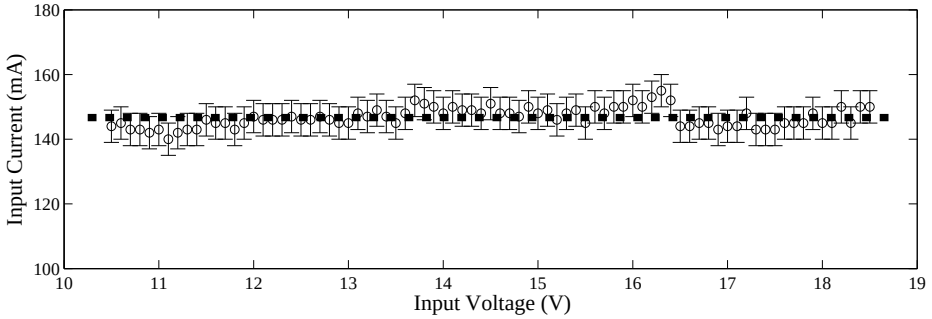

(c)

Figure 7.4: (a) Control circuit standby current as a function of voltage. (b) Control circuit current when Wi-Fi circuit is active. (c) Measured current for motor with the mean measured terminal current overlaid using the dashed line.

$$NiOOH + H_2O + e \rightarrow Ni(OH)_2 + OH^- \quad E_{0,Reduction} = 0.52V$$

$$MH + OH^- \rightarrow M + H_2O + e \quad E_{0,Oxidation} = 0.83V$$

The sum of the potential differences resulting from the two half cell reactions form the basis for the cell's voltage, the standard cell potential $E_{0,standard}$. The two half cell reactions can be summarized as a single reaction below:

$$MH + NiOOH \rightarrow M + Ni(OH)_2 \quad E_{0,Standard} = 1.35V$$

$$E_{0,Standard} = E_{0,Oxidation} + E_{0,Reduction}$$

The opposite reaction occurs during recharge. There is a range where a given cell can continue to reversibly experience these reactions to store energy. This is called the battery's capacity. If more charge is added to the battery than its capacity, or more charge is removed than its entire capacity, the cell could be damaged. A battery's capacity is typically defined using the unit "ampere-hour". This unit communicates the battery's C rate, the rate a battery must be continuously discharged to be completely empty after an hour of use. The C rate is used to estimate a battery's lifetime. For example, a battery that is discharged at 0.5 C will be empty after 2 hours. Simulations and battery management systems often try to track the battery's remaining charge using a variable called the state-of-charge (SOC). SOC is the ratio of a battery's remaining capacity to its capacity when fully charged [43]. SOC is not directly measurable, rather a battery's operating conditions are tracked and used to estimate SOC in a model. A simple way of tracking would be to initialize the battery to a known state, then integrate the current that is added or removed from the cell.

A risk in electrochemical storage devices is the effect of overcharging and overdischarging. NIMH batteries are designed so a side reaction can absorb excess energy without damaging the cell. The nickel cathode has a lower capacity than the anode. At the end of a charge, the cathode begins evolving oxygen [21].

$$2OH^- \rightarrow H_2O + \frac{1}{2}O_2 + 2e^-$$

The oxygen diffuses to the anode where it is forms water with the metal hydride according to:

$$2MH + \frac{1}{2}O_2 + 2e^- \rightarrow 2M + 1H_2O$$

When overcharged at low rates, the oxygen gassing reaction allows the battery to handle the extra energy without being damaged. The low capacity of the cathode forces the electrons to be used in the gassing side reaction rather than continuing to charge the anode. This is good because an overcharged anode can form hydrogen gas which can build up without being reabsorbed causing high internal cell pressure, venting and deterioration of cell performance. The oxygen gassing reaction becomes noticeable when the cell has around 80% of its charge capacity. This makes the final part of the recharge less efficient [21].

7.3.2 Battery Model

An equivalent circuit model shown in Figure 7.5 and developed by [44] was used to approximate the battery's behaviour. The equivalent circuit model is composed of an internal voltage source V_{int} that is dependent on the battery's SOC and recent

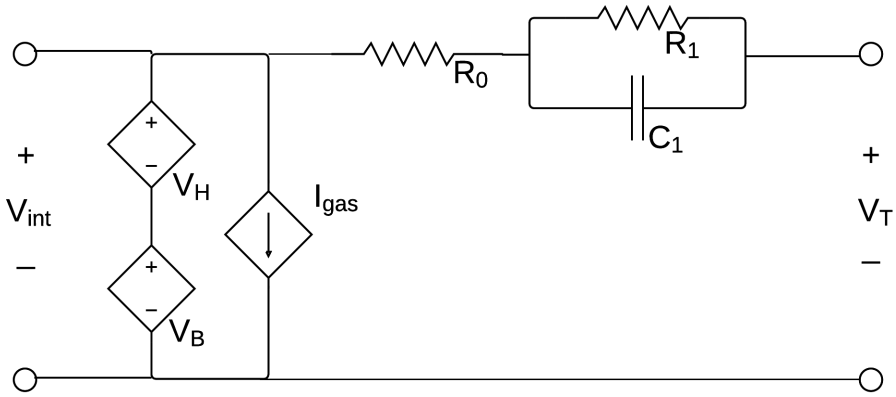

Figure 7.5: Equivalent circuit model used to represent the NIMH battery pack studied in this case study. Model discussed in [44].

charge history. There is a continuous current loss due to the gassing reaction. A series impedance branch of R_0, R_1, and C_1 causes terminal nonlinearities such as voltage drops, sags and swells.

To simplify the development of this model a few assumptions were made. With the exception of the internal voltage, the model parameters were assumed to be invariant to the battery's SOC. The impacts of battery's age and the system temperature were neglected. Instead of applying this equivalent circuit model to each individual cell, the entire pack was modeled by a single equivalent circuit.

7.3.2.1 Internal Voltage

Consider a battery that has been resting for a long time. According to the discussed model, this battery would have no voltage across the series impedance and the terminal voltage would be equal to its internal voltage, $V_t = V_{int}$. By taking a resting battery and measuring its terminal voltage at different values of SOC, a trend similar

to Figure 7.6 (a) can be plotted. This trend illustrates how the battery's internal voltage varies nonlinearly with stored charge. It also shows hysteresis. Two exact same batteries at the same SOC may exhibit different internal voltages depending on whether they were recently charged or discharged as shown by the boundary curves in Figure 7.6 (a). If the battery operates with shallow cycles, its internal voltage can reach intermediary regions such as those along AB [44].

This internal voltage is modeled by cotaking the lower bound V_{lb} of Figure 7.6 (a) and adding a hysteresis term V_H which is nonzero if the battery was charged recently as shown in (7.8) [44]. V_{lb} can be modeled using empirical data that is fit with a fifth order polynomial [44].

$$V_{int} = V_{lb}(SOC) + V_H(SOC, Q_{hyst}) \tag{7.8}$$

V_H is modeled with a state observer based algorithm. A state variable Q_{hyst} tracks the recent charging history of the battery and is defined by (7.9) [44]. Q_{hyst} is 0 when the battery has been discharged continuously. Conversely, a battery that has been continuously charged will have Q_{hyst} clipped at a maximum value Q_{max}.

$$Q_{hyst} = \int Idt \quad \text{with } 0 \leq Q_{hyst} \leq Q_{max} \tag{7.9}$$

The spacing between the internal voltage's lower bound V_{lb} and upper bound V_{ub} vary according to the battery's SOC. U_{hyst} is calculated using Q_{hyst} in (7.10) and represents the percentage of the upper bound voltage that hysteresis is adding to the battery's terminal voltage.

$$V_H(SOC, Q_{hyst}) = U_{hyst}(Q_{hyst}) \cdot [V_{ub}(SOC) - V_{lb}(SOC)] \tag{7.10}$$

The method outlined in [44] approximates the relationship between U_{hyst} and Q_{hyst} with a quadratic function that is recalculated every time charge direction is switched. To explain the function of the observer, consider Figure 7.6 (b) where a battery that has been discharging recently and has an initial Q_{hyst} and U_{hyst} of 0 (point A on the figure). The instant a recharge is started, a straight line from the observer's current value A to its destination B is drawn. The point C is calculated by taking the midpoint of AB and adding a stretch term ΔU_{hyst}^{charge} defined by (7.11). A second order polynomial is fit to these three points as shown by the curve ACB. While the battery is being charged, Q_{hyst} tracks the charge stored in the battery and the value of U_{hyst} varies according to ACB. U_{hyst} is used to calculate the hysteresis component according to (7.10).

If, at point C, the direction of current is reversed and the battery starts being discharged, the process must be restarted. Point D is calculated by subtracting $\Delta U_{hyst}^{discharge}$, calculated with (7.12), from the midpoint of line CA. A new quadratic is fit to define CDA which describes the position of is fit to these three points that will define U_{hyst} as the battery is discharged.

$$\Delta U_{hyst}^{charge} = \Delta U_{hyst\_max}^{charge} \frac{Q_{hyst\_max} - Q_{hyst}}{Q_{hyst\_max}} \tag{7.11}$$

$$\Delta U_{hyst}^{discharge} = \Delta U_{hyst\_max}^{discharge} \frac{Q_{hyst}}{Q_{hyst\_max}} \tag{7.12}$$

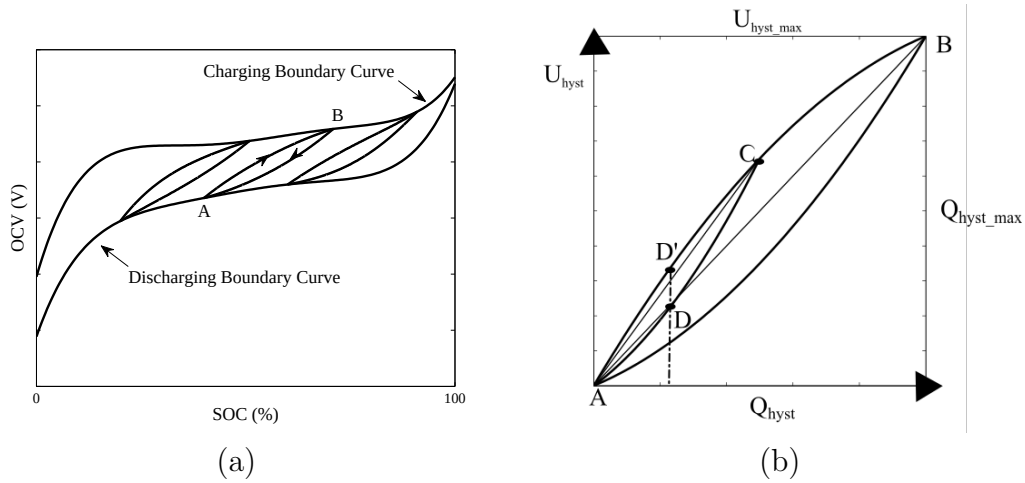

Figure 7.6: (a) Representation of the hysteresis phenomena of NIMH batteries. V_{int} is not solely dependent on SOC, but also on the battery's recent charge history. (b) Illustration used to describe the method outlined in [44] to model $U_{hyst}(Q_{hyst})$ to track the OCV when in the intermediate region of hysteresis. Illustrations based on [44].

7.3.2.2 Gassing Current

Even when charge is not being removed by an external circuit, gassing reactions are still occurring within the cell. I_{gas} is exponentially dependent on the internal voltage of an individual cell $V_{int,cell}$ and can be described by (7.13). Since the model represents the behaviour of twelve series cells, a single cell's voltage can be calculated through $V_{int,cell} = \frac{V_{int}}{12}$. This is an empirical model that requires two parameters I_0 and α to be defined for behaviour to be fully described [44].

$$I_{gas} = I_o \exp(\alpha(V_{int,cell} - 1.23)) = I_o \exp(\alpha(\frac{V_{int}}{12} - 1.23)) \tag{7.13}$$

7.3.2.3 Impedance Core

The instant a resting battery begins being discharged, the terminal voltage will immediately lower and over time it will continue to sag. The instant drop is caused

by an internal resistance R_0 that is observed because current must pass through electrolyte, contact resistances and other variable conductive paths within the cell [45]. The voltage sag is modeled by a series impedance path (R_1 and C_1) and occurs because of the limited rate of mass transfer that can occur in the electrochemical cell [45].

7.3.3 Parameterizing the Model

7.3.3.1 Initializing Battery to 100% SOC

Many of the experiments used to parameterize the model require a fully charged battery pack. This can be challenging because a fully charged battery is likely to experience an increased rate of self discharge due to the gassing reaction discussed in Section 7.3.1. Finishing a recharge procedure with a small trickle current will replace the charge that is lost to the gassing reaction and will ensure the battery remains at 100% SOC.

A three step recharge procedure is developed in [21] that quickly recharges a NIMH battery to a fully charged state and ends the procedure with a trickle charge. This procedure was implemented using a remotely controlled Agilent E3646A PSU with series diode protection. The PSU was programmed with the following steps:

1. Recharge the batteries at 0.5 C (1.15 A). While higher currents would recharge the battery more quickly, hardware constraints of the PSU limited this recharge rate. As the battery nears the end of the charge routine, the monitored voltage will reach a local maximum. Typical NIMH battery rechargers use a measured terminal voltage drop ($-\Delta V_t$) of 10 mV per cell to indicate the end of the charge. With multiple series cells and the relatively low recharge rate of 0.5

C, the measured $-\Delta V_t$ is likely to be smaller. To be conservative, a $-\Delta V_t$ condition of 5 mV per cell was selected to terminate this step.

2. Top off the batteries at 0.1 C (230 mA) for one hour. This slower charge allows some of the extra energy to be absorbed without damaging the battery [21]. It also serves as a balancing charge for cells in series, as undercharged cells will absorb the current while overcharged cells will use the excess energy in the gassing reaction [46].

3. Finish with a small trickle charge of C/40 (57.5 mA) until the battery is removed from the recharger.

For consistency, the recharge procedure was always run from a completely depleted battery. An example of the current and voltage profile of this method is shown in Figure 7.7 (a).

7.3.3.2 Measuring Stored Battery Charge

If the electrical current is integrated as a battery is discharged to an empty state, the resulting sum is the charge that was stored in the battery at the start of the test. This method was used to determine the battery's fully charged capacity and was used while parameterizing other aspects of the battery's behaviour.

In order to discuss this method further, the battery's empty state must be defined. The amount of charge in a battery can be inferred from its voltage because the battery's potential decreases as charge is removed. The manufacturer of the batteries recommends cutting off discharge when a single cell reaches a voltage of 0.9 V [47]. It is good practice to raise the cutoff voltage when a large number of cells are in series to

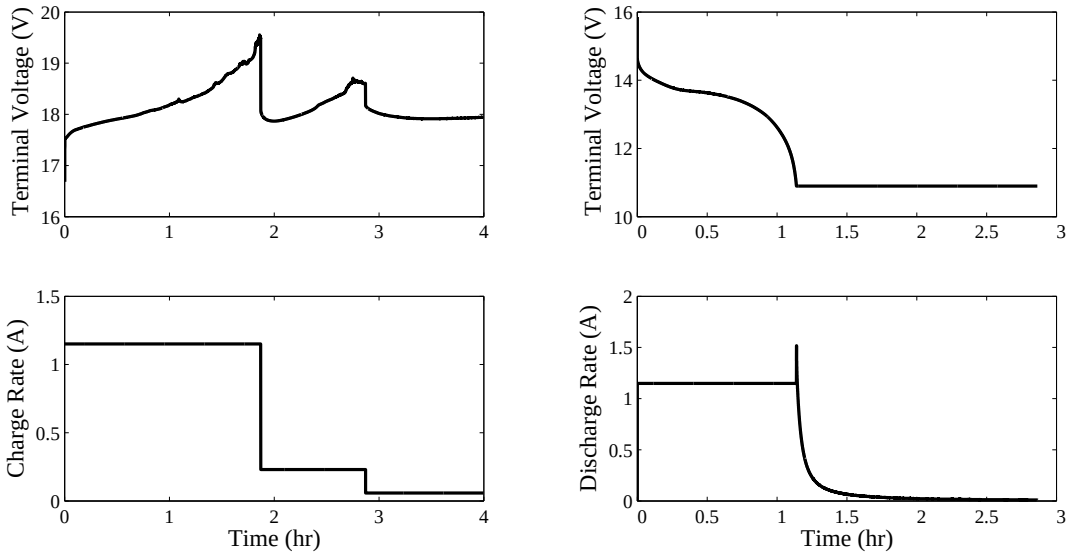

(a) (b)

Figure 7.7: Current and voltage profiles to (a) bring the pack to 100% SOC and (b) measure a battery's capacity and bring the pack to 0% SOC. The top trend is the terminal voltage and the bottom trend shows the rate of charge exchange.

avoid the situation where one battery discharges to an excessively low voltage before the rest of the series stack. For this reason a pack cutoff of 10.9 V was selected.

Consider a battery pack discharging at a high current rate. This battery's terminal voltage will reach the cutoff faster than the internal voltage because of the potential drop across its internal series resistance. To ensure an accurate capacity measurement, once the terminal voltage reaches 10.9 V, it should be held at this potential while the remaining charge is allowed to drain out.

To accomplish the capacity discharge test, the following procedure was implemented using a remotely controlled BK Precision 8500 Variable DC Load (VDCL).

- Discharge the battery at a rate of C/2 (1.15 A) until a terminal voltage of 10.9 V is reached.
- Hold the voltage at 10.9 V and allow the remaining charge to drain out. End the test when the rate of discharge falls below 10 mA. This value was chosen because at discharge rates lower than this, the error of the VDCL's ammeter becomes significant.

The current and voltage profile from this test is shown in Figure 7.7 (b). This data was taken from a battery pack that was initially at about 50% SOC.

This method was used to determine the capacity of a fully charged battery. While the manufacturer reports the battery's capacity to be 2.3 Ahr, this test indicates that the capacity is 2.35 ± 0.03 Ahr. The evaluation of error for this value is discussed in Appendix B.5.

7.3.3.3 Internal Battery Voltage

The battery's internal voltage is fundamentally dependent on SOC. Hysteresis effects cause the internal voltage to experience an upper and lower bound, V_{ub} and V_{lb}, depending on whether the battery was charged or discharged. To measure the internal voltage, the battery must be at a resting state to remove the impact of a potential drop across the impedance core. V_{ub} can be measured by taking a completely discharged battery and stepwise recharging it as shown in Figure 7.8 (a). Similarly, the discharge curve can be determined by stepwise discharging a battery that is initially at 100% SOC as shown in Figure 7.8 (b).

For consistency, both tests allowed charge transfer at 0.5 C (1.15 A) for 720 seconds (12 minutes) followed by 2700 seconds (45 minutes) of rest. The batteries were recharged using a remotely controlled Agilent E3646A PSU with series diode protection. During the recharge test, the battery's voltage was measured using a National Instrument's (NI) MyDAQ and a voltage divider. The discharge test was run using a remotely controlled BK Precision 8500 VDCL, which also made voltage measurements.

The battery's resting terminal voltage was taken and plotted against the battery's remaining charge capacity in Figure 7.8 (c). A fifth order polynomial was fit to the data and is shown in the dashed line to determine the curves for V_{ub} and V_{lb}. This methodology is consistent with similar empirical models in the literature [44][48].

7.3.3.4 Gassing Parameters

Self discharge data was collected by fully charging the battery pack then allowing the pack to rest for varying periods of time. The test was terminated by performing

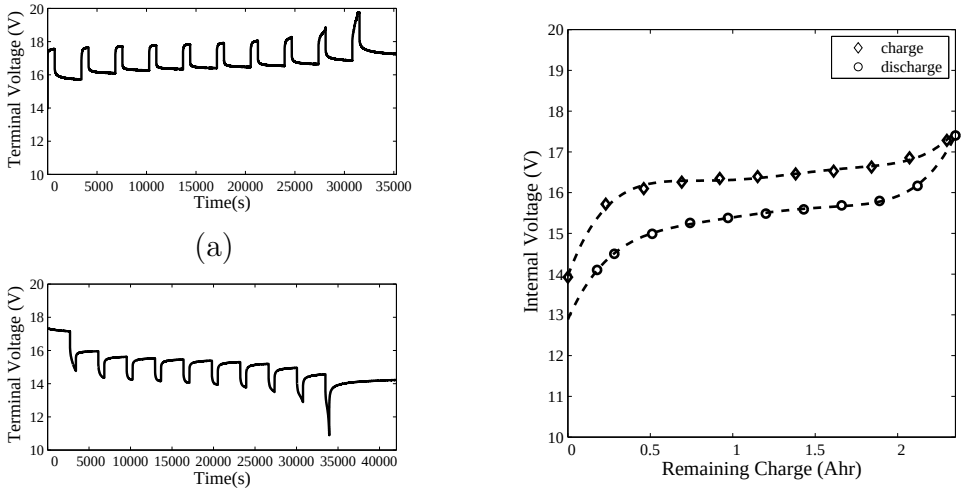

Figure 7.8: (a) Stepwise recharge of a battery. (b) Stepwise discharge of battery. (c) The battery's internal voltage vs remaining charge for both recharge and discharge conditions. A dashed fifth order polynomial fit is superimposed on both datasets.

a capacity test as discussed in Section 7.3.3.1 to determine the remaining charge.

When a fully charged battery is allowed to rest, the only mechanism for charge loss is through internal gassing reactions. SOC, as a function of time, can be described by integrating the gassing losses and dividing them by the battery's maximum capacity C_{bat} as shown in (7.14). Since a fifth order polynomial is used to describe V_{lb}, (7.14) has no analytical solution.

$$SOC(t) = 100\% - \frac{\int_0^t I_0 \exp(\alpha(\frac{V_{lb}(SOC(t))}{12} - 1.23))}{C_{bat}} \tag{7.14}$$

Instead, a numerical model was developed to describe the battery's self discharge behaviour. An iterative numerical method, MATLAB's fminsolve, was used to loop through potential combinations of I_0 and α to find a combination that minimized the error between the simulated battery's capacity and the measured results. This

is represented by the external loop of the flowchart in Figure 7.9. This method was used to estimate the value of I_0 to be 1.11×10^{-11} A and α to be 111. The dashed line in Figure 7.10 (a) shows the remaining capacity of a resting battery according to the developed gassing model and shows this model is consistent with the measured data.

The importance of this work is to highlight where gassing is non-negligible. Due to hysteresis, V_{int} can be higher or lower depending on its recent charge history. This impacts the cell's internal voltage and therefore its rate of self discharge. Figure 7.10 (b) illustrates the modeled self discharge given the two voltage boundary curves. A charging battery at 65% SOC is expected to experience self discharge with the magnitude of a fraction of a mA. This self discharge is similar to the rate at which the idle control circuit consumes power and is not negligible.

7.3.3.5 Hysteresis and Impedance Parameters

The remaining undefined parameters are the impedance core parameters: R_0, R_1, and C_1 as well as the hysteresis tracking variables: $Q_{max,}$ $\Delta U_{hyst}^{discharge}$, and ΔU_{hyst}^{charge}. Reference [44] describes how impedance spectra can be used to define the impedance core parameters and it also describes a novel method of fitting the hysteresis tracking variables. Due to problems with timing and equipment, these tests were not possible. Instead, a dataset was collected by monitoring the battery's terminal voltage and current as it powered the prototype over a rigorous schedule. A fitting procedure was used to parameterize the remaining variables.

The battery pack was initialized to 50% SOC before being connected to the control circuit. The battery voltage and current draw were monitored as it powered the

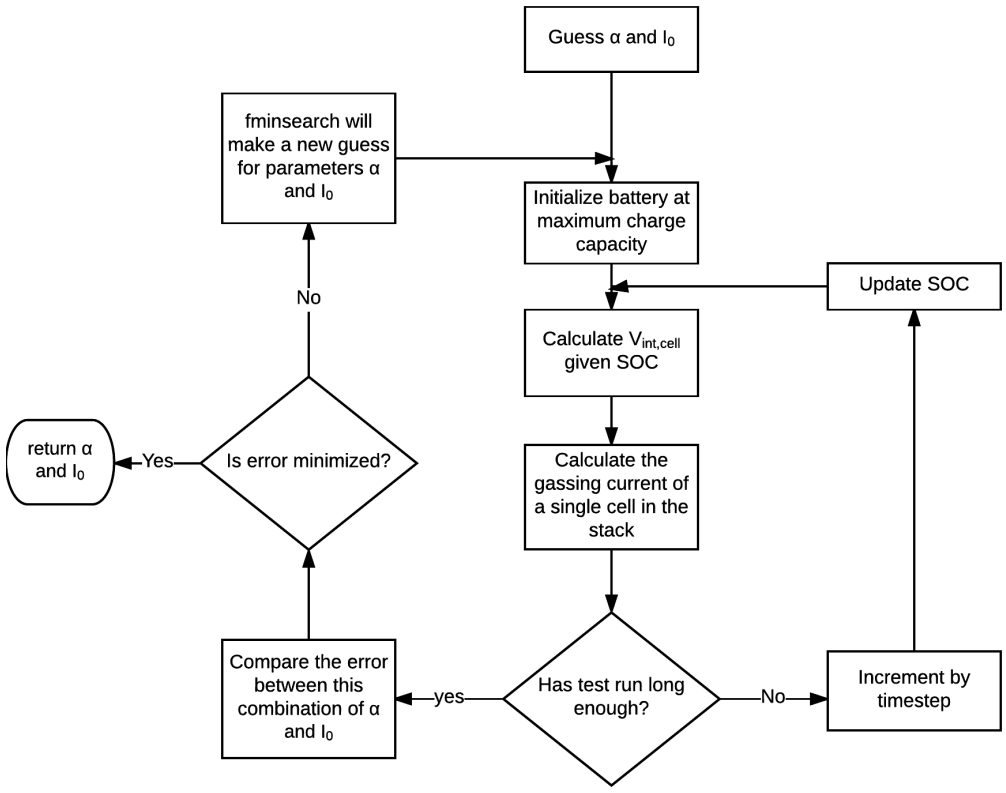

Figure 7.9: Algorithm to determine gassing model of best fit. An iterative solving function, fminsearch, is used to evaluate the gassing model parameters that best predict the observed self discharge.

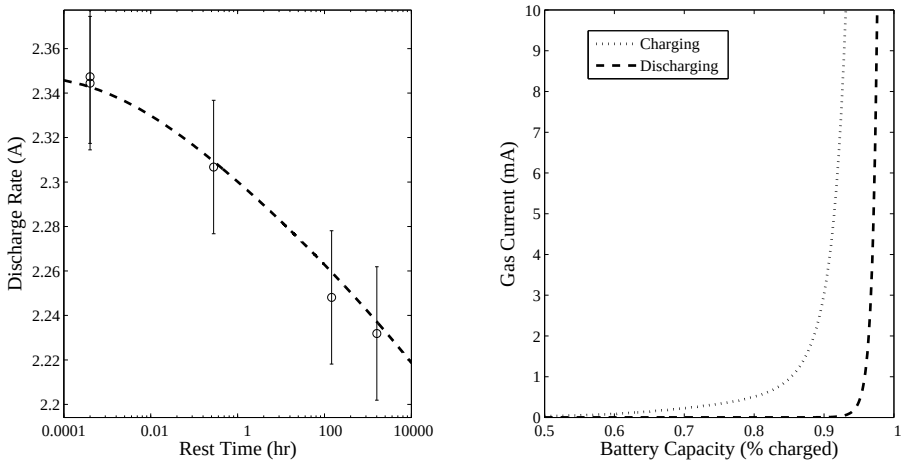

(a) (b)

Figure 7.10: (a) Battery capacity predicted by the gassing model (dashed line) corresponds well with the measured experimental data. (b) The magnitude of gassing current predicted by this model. NIMH hysteresis causes the internal voltage to be higher when the battery was recently charged, causing a higher rate of self discharge.

prototype electronics including a simulated solar array for 24 hours. At the end of the test, the battery pack was disconnected and the remaining charge was determined by performing a capacity test.

The control circuit was programmed with a more rigorous schedule than usual to ensure that a significant amount of charge would be removed from the battery. This was accomplished by scheduling the circuit to run a free-spinning motor for one minute every half hour. In a regular schedule, the motor would only be infrequently energized to move the blinds. The Wi-Fi schedule was also more rigorous than usual. Typically, the Wi-Fi communication occurs every five minutes and lasts five seconds or less. In this schedule, the Wi-Fi circuit was programmed to be energized for 30 seconds every five minutes. The remainder of time the circuit stayed in standby.

A remotely controlled Agilent E3646A PSU was connected to the prototype circuitry (and battery) as if it were the solar array. Every time the DAQ measured the battery's terminal voltage, this measurement was used to calculate a reasonable value for solar array current. The battery voltage measurement was fed into the five parameter model developed in Section 7.1.4 along with a value for irradiance. Irradiance was modeled as a 12 hour half sinusoid shown in Figure 7.3 (b) with a maximum irradiance of 500 W/m^2. This is a simple first order representation of irradiance model is consistent with the light available through a moderately tinted, south facing window, near the spring equinox in Hamilton, Ontario.

The measured current profile is shown in Figure 7.11 (a). It shows that every five minutes the control circuit activated the XBee Wi-Fi chip and every half hour the motor was activated. It is these events that cause the instant spikes in demanded current and the associated drop in battery terminal voltage in the blue voltage trend in Figure 7.11 (b). The twelve hour sag in negative current indicates the time when the PSU injected current into the system. The sag is sinusoidal because the photocurrent is proportional to the sinusoidal irradiance profile that was used.

A genetic algorithm (GA) is a robust technique used to identify optimum solutions to an engineering problem [49] and was used to determine appropriate values for the six remaining parameters: R_0, R_1, C_1, Q_{max}, $\Delta U_{hyst}^{discharge}$, and ΔU_{hyst}^{charge}. The GA randomly initiated a series of guesses for the parameters within user-specified upper and lower bounds. Each set of parameters is called a "child". For each child, the GA simulated the terminal voltage of that child's battery model considering the input current profile in Figure 7.11 (a). Each simulation produced a simulated battery terminal voltage and the GA calculated the error between the modeled voltage and

Table 7.2: Parameters for implemented battery model

Parameter	Symbol	Value
Series Resistance	R_0	1.42 Ω
Impedance Resistance	R_1	3.00 Ω
Capacitance	C	255 F
Maximum charge tracker	$Q_{hyst,max}$	731 mAh
Hysteresis charge stretching coefficient	ΔU_{hyst}^{charge}	0.131
Hysteresis discharge stretching coefficient	$\Delta U_{hyst}^{discharge}$	0.207

the measured voltage. The child with the lowest error was classified as elite and copied into the next generation. The algorithm used techniques such as selection, crossover and mutation to generate a new population of children and repeated this process for a number of generations. After 50 generations of 50 children, the GA converged on a parameter set in Table 7.2 that produced the red curve in Figure 7.11 (b). This model predicts the battery pack's terminal voltage with a root mean square error of 50 mV when compared to the measured dataset.

7.4 System Simulation

7.4.1 Simulation Setup

A numerical simulation was developed to investigate the interactions between the solar array, the battery and the loads to calculate useful parameters. The solar array and battery were modeled according to the equivalent circuit models discussed in this chapter. The load was modeled with time-dependent lookup tables.

During usual operation, the amount of current consumed by the load varies according to the blind's schedule and the system voltage. The usual system state is standby. Standby current can be found by referring to a lookup table of the data

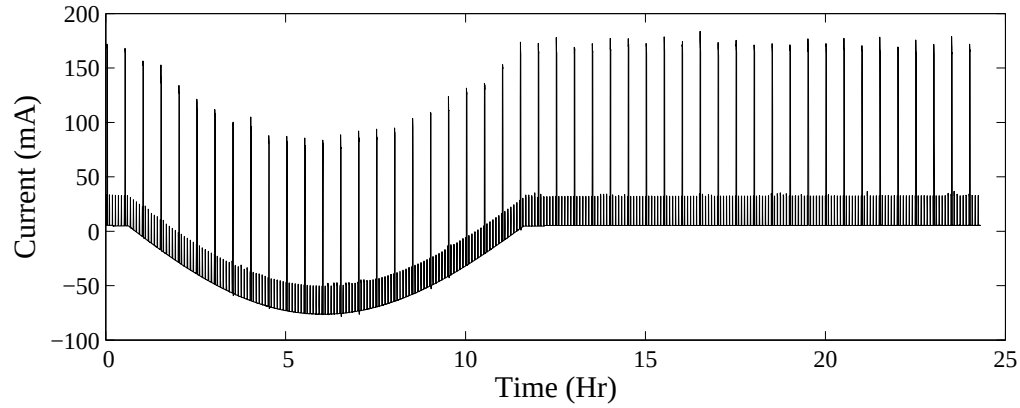

(a)

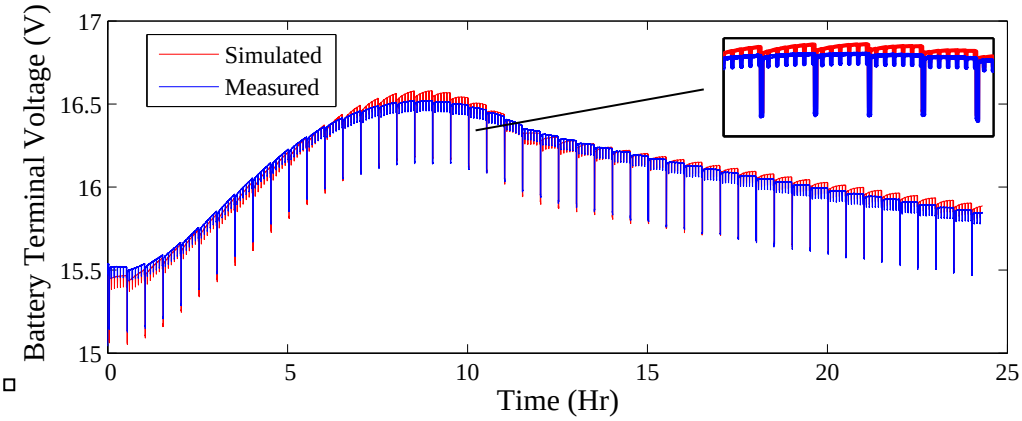

(b)

Figure 7.11: (a) The current removed from the battery. Positive current indicates that current was removed, while negative indicates the battery was recharged. (b) Measured and simulated terminal voltage of the battery.

in Figure 7.4 (a). Every five minutes, a five second Wi-Fi communication occurs. This requires more power, the exact amount can be found using a lookup table of data from Figure 7.4 (b). Figure 7.4 (c) shows that the motor current demands are insensitive to voltage. However, this particular dataset is inappropriate for the model because it was taken when the motor had no load. Instead, the motor load is modeled as a constant current source that is consistent with worst case measurements from the the motor baseline test discussed in Section 7.2.3. Specifically, this is modeled as a 140 mA current draw that lasts one minute and occurs once in a 24 hour simulation to model lowering the blinds. A 620 mA current draw lasting one minute but offset from the last event by 12 hours, was used to simulate raising the blinds.

The output of the solar array is also time dependent according to the variance in $\Phi(t)$. The half sinusoid model discussed in Section 7.1.3 was used and requires two parameters, a value for day length and a value for Φ_{max}.

The time increment that was chosen for this simulation is five seconds to ensure that Wi-Fi events were captured. At each time interval, the terminal voltage of the battery was calculated. This voltage was used as an input to the load current and solar array current calculations. Battery SOC was tracked through the simulation.

7.4.2 Energy Balance Simulation

One of the goals of this model was to quantify the minimum irradiance profile that would allow this system to operate continuously without needing to be recharged by the user. This was investigated by running several simulations with different values for: initial battery SOC, number of sunlight hours, and Φ_{max}. The simulation was run for 24 hours and the difference between the initial battery SOC and the final

battery SOC was evaluated with the goal of determining what value of Φ_{max} would cause this difference to be zero. A single simulation requires many iterative solutions and takes about two minutes to run making it prohibitively slow to use a numerical algorithm such as newton's method to solve Φ_{max}. Instead, 10 simulations were run where Φ_{max} was varied but initial battery SOC and number of sunlight hours were maintained constant. Linear interpolation was used to determine an approximation of the value of Φ_{max} that kept the system balanced.

The initial values for sunlight hours were chosen to correspond to the day lengths of Hamilton, Ontario during the 8.97 hour the winter solstice, 12.2 hour spring/fall equinox and the 15.4 hour summer solstice. The battery was initialized to a variety of different SOC values. The value of Φ_{max} that balances these different systems is shown in Figure 7.12.

These results show that batteries with greater charge require more sunlight to maintain their SOC. This behaviour is consistent with the expected system interactions. As a battery's SOC increases, so does its terminal voltage. This larger voltage is placed across the solar array causing a decrease in extracted current. This decrease in current is especially pronounced when the voltage is near the peak power point voltage of the solar array. To produce the same current when the terminal voltage is increased, the impinging irradiance must also increase.

The increase in Φ_{max} is more pronounced at the extremely low or high values of SOC. The voltage-SOC curve illustrated in Figure 7.8 (c) shows that the battery's terminal voltage has a steeper derivative when nearly depleted or fully charged. This faster change in voltage can lead to an increased change in extracted solar current

as the initial SOC is varied. Additionally, a fully charged battery experiences a non-negligible source of current loss through its secondary gassing reaction. More solar flux is needed for the solar cells to replace the current lost through this mechanism.

As the day length decreases, the value of Φ_{max} increases. To balance the system on a short day, Φ_{max} must be larger to make up for the hours that the sun isn't shining.

In Chapter 3, attenuation factors of 30%-70% were observed for different windows. The triple pane tinted window that rejected the most amount of light would still let approximately 300 W/m^2 through which is more than the 210 W/m^2 needed to balance the system during a winter's day. This suggests that the system would work continuously if placed behind a single window that has reliable access to consistent direct energy source. If additional attenuating factors are placed in front of the solar panels, such as a bug screen or a tree, the system may not receive the minimum irradiance necessary. Additionally, if the quality of outdoor light is low, like the diffuse light in a north facing window or the dim light that from consistently cloudy weather, this system may not receive enough ambient energy to continue operating.

7.4.3 Time to Failure Simulation

To address the question of run-time in the absence of ambient light, the model was simulated as running for several days without a solar array. The simulation was discontinued if the battery's terminal voltage reached the voltage regulator's cutoff of 13.3 V and would fail to power the circuit. The simulation was also set to end if all charge was removed from the battery.

The battery's SOC over the course of this simulation is shown in Figure 7.13 (a)

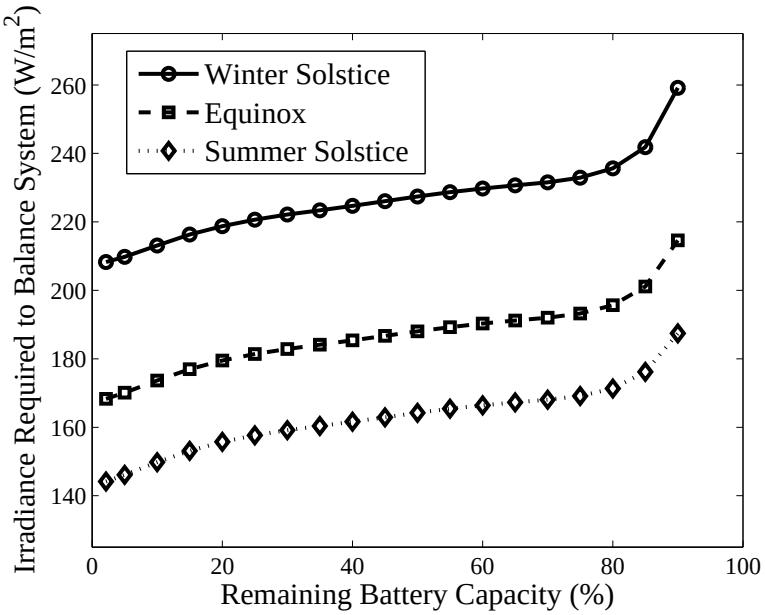

Figure 7.12: The estimated value of Φ_{max} needed to ensure the battery maintains a consistent level of charge over 24 hours according to the developed numerical model.

and is mostly linear. At the start of the test an initial rapid discharge can be observed, likely due to gassing current. Throughout the test, small step decreases in SOC can be observed which correspond with the time the motor is engaged.

The battery's voltage trend is shown in Figure 7.13 (b) and follows the same shape as the battery's discharge curve in Figure 7.8 (c). The spike decreases indicate times when the motor is engaged and there are increased voltage drops across the battery's internal resistance. These voltage sags are more pronounced when the motor is lifting the blind unit and requires more current.

The test was terminated when the battery had about 15% capacity remaining and was simulating a raise blind event. The increased demand caused the terminal voltage to lower because of voltage drops across the battery's series resistance and

impedance components. This simulation indicates that the system could operate on battery power alone for about 13 days.

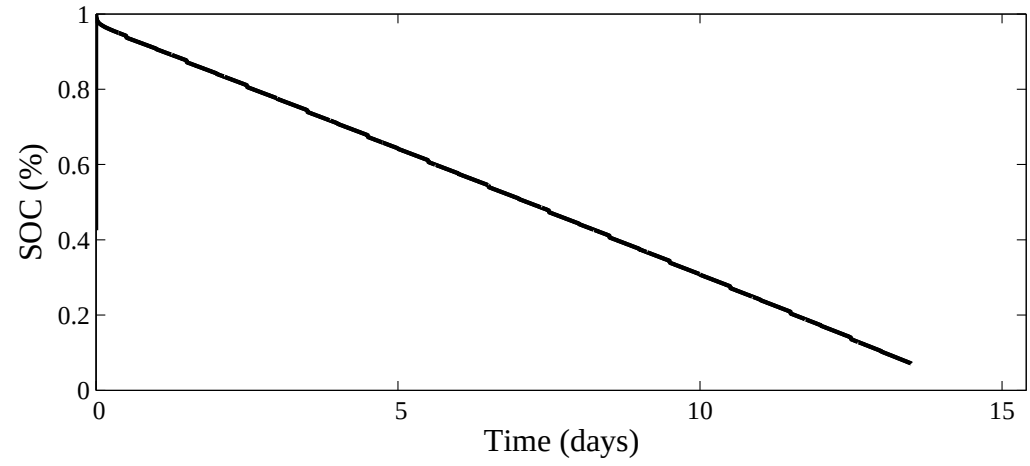

(a)

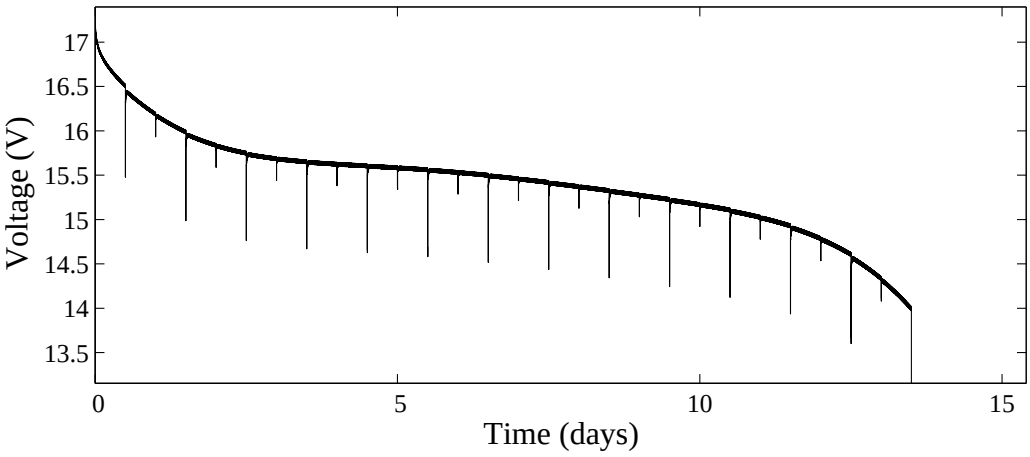

(b)

Figure 7.13: Results of simulating a battery continuously operating the load without a recharge. (a) The decline in charge capacity. (b) The terminal voltage cutting off when a minimum of 13.3 V is reached.

Chapter 8

Conclusion

This thesis examines the feasibility, design and operation of a novel, solar-powered motorized blind from a powerflow perspective. This particular design can be built, can operate safely and can function on its own power when installed in an area with an appropriate amount of light. Lessons from this prototype can be applied to various fields of study.

8.1 Interdisciplinary Relevance

8.1.1 Solar Energy Harvesting

The accessibility and wealth of knowledge surrounding silicon photovoltaics makes this type of technology a good choice for energy harvesting devices. New developments in the field of flexible photovoltaics will make solar energy harvesting available for even more novel applications.

The work in Chapter 5 has shown a significant amount of light flux is transmitted

through modern windows. While windows are designed to reject wavelengths that cause heating loads on buildings, they transmit much of the visible light that is effectively converted by silicon solar cells. An experimentally validated method of approximating the useful light transmission was presented in this thesis and can be used to approximate the available ambient energy in different conditions. In general, if the only attenuating medium is a window, this work indicates that the amount of useful transmitted light can vary between 30% and 70% depending on the type of window.

A novel mounting configuration was proposed in Chapter 4. By convention, static solar arrays are mounted at an angle that corresponds to the geographic latitude where the system will be deployed. Research indicates that this mounting angle is insensitive to changes within $\pm 10^{\circ}$ of mounting angle. Using two mounting angles of 25° and 45°, one array should be optimized for a large geographic region encompassing the latitudes 15°N to 55°N. A single design can create a device that is optimized for a large geographic region.

The five parameter model can be used to approximate the solar cell's behaviour in a complex electrical circuit. The work in Chapter 7 extends Cubas' method of parameterizing the five parameter model to ensure the model is consistent with datasheet values in variable irradiance conditions. This model can be used in numerical simulations of other system components to determine useful parameters like minimum insolation required for continuous operation of solar energy harvesting systems.

8.1.2 Internet of Things

The Internet of Things is growing. At an estimated cost of $200 per installation, the cost of running wiring to individual sensors could be excessive [4]. Battery powered solutions may avoid the costs of wiring, but they have periodic maintenance costs associated with recharging or replacing batteries. A device that takes advantage of local energy harvesting can have reduced costs by removing the need for costly installation procedures or periodic maintenance. The power system that is described in Chapter 4 can be adapted for future energy harvesting IoT systems. Likewise the methods discussed in Chapter 7 can be used to evaluate system run-time or the required input energy for energy harvesting IoT systems.

8.1.3 Electronic Textiles

Embedding power transmission wires within the blind fabric is a novel design feature. This technique could be used in other applications to hide power cables in aesthetically pleasing fabrics (carpet, clothes). This topic is especially relevant as the popularity of wearable technology increases.

Similar applications must consider the safety of their design choices. The work in Chapter 5 developed a method of evaluating order of magnitude temperature rise for e-textiles that are transmitting power. This test could be modified to evaluate the safety of other novel e-textiles.

The results of this experiment on the e-textile proposed in this thesis indicate that only a small temperature rise (less than 5 °C) is experienced while it transmits power. This validates the design methodology as appropriate to this specific case. In particular, the blind e-textile was designed using the 1 amp per 700 circular mill rule

and derated using NEC standards.

8.2 Continued Work

The analyzed prototype is a novel realization of a motorized blind. The work analyzing this system has identified some short-comings that could be improved upon in future iterations.

The total active photovoltaic area is limited to solar cells mounted in the bottom rail. As flexible alternatives are developed, the amount of input energy could be increased by integrating additional cells to the fabric surface.

While the heat generated by transmitting power through the blinds should be safe, its origin is from wasted power. Shortening the length of the transmitting conductors or lowering system resistance could reduce this power loss. This could be achieved by integrating thicker wires or more wires into the transmission system or moving the solar panels to a location that is closer to the mounted electronics.

The friction brake that keeps the shade from slipping down costs the motor twice as much power as necessary when raising the blind. An alternative braking mechanism could reduce power consumption and increase system run-time.

Switching to a lithium battery system would increase complexity, but would reduce the self discharge losses.

One of the reasons a rather complicated model was needed to simulate the system was the direct connection between the solar cell and the battery. Integrating a peak power tracker would force the system to produce its maximum power at all times. This would eliminate the dependency of solar current on the battery voltage. Additionally, this would improve overall power extraction by ensuring the solar array is always

operating at its optimal point.

Additional accuracy could be integrated into the battery system by using more advanced models, particularly for the battery. A true empirical model would use several measurements to develop an accurate model of the battery in different operating conditions. This, coupled with a finer simulation resolution could produce improved results. The impact of modeling the system with an electrochemical model could also be investigated.

Bibliography

[1] General Electric and Accenture, "Industrial internet insights report for 2015," Tech. Rep., 2014.

[2] J. Bradley, J. Barbier, and D. Handler, "Embracing the internet of everything to capture your share of 14.4 trillion," Cisco, white paper, 2013.

[3] W. O'Brien, K. Kapsis, and A. Athienitis, "Manually-operated window shade patterns in office buildings: A critical review," *Buildings and Environment*, vol. 60, pp. 319–338, 2013.

[4] J. Rabaey, M. Ammer, J. da Silva, D. Patel, and S. Roundy, "PicoRadio supports ad hoc ultra-low power wireless networking," *Computer*, pp. 42–48, 2000.

[5] J. W. Callister, *Material Science and Engineering*, 7th ed. John Wiley & Sons, 2007.

[6] A. Kitai, *Principles of Solar Cells, LEDs and Diodes: The role of the PN junction.* Wiley, 2011.

[7] B. Streetman and S. Banerjee, *Solid State Electronic Devices*, 6th ed. PHI Learning Private Limited, 2009.

[8] M. Pagliaro, R. Ciriminna, and G. Palmisano, "Flexible solar cells," *ChemSusChem*, vol. 1, pp. 880–891, 2008.

[9] T. Chen, L. Qiu, Z. Yang, and H. Peng, "Novel solar cells in a wire format," *Chem Soc Review*, vol. 42, pp. 5031–5041, 2013.

[10] R. He, T. Day, M. Krishnamurthi, J. Sparks, P. Sazio, V. Gopalan, and J. Badding, "Silicon p-i-n junction fibers," *Advanced Materials*, vol. 25, pp. 1461–1467, 2013.

[11] J. Cubas, S. Pindado, and M. Victoria, "On the analytical approach for modeling photovoltaic systems behavior," *Journal of Power Sources*, vol. 247, pp. 467–474, September 2014.

[12] M. de Blas, J. Torres, E. Preito, and A. Garcia, "Selecting a suitable model for characterizing photovoltaic devices," *Renewable Energy*, vol. 25, pp. 371–380, 2002.

[13] A. Jordehi, "Parameter estimation of solar photovoltaic (PV) cells: a review," *Renewable and Sustainable Energy Reviews*, vol. 61, pp. 354–371, 2016.

[14] Cardinal Glass Industries, "Technical glass guide," Tech. Rep., 2014.

[15] NREL. Reference solar spectral irradiance: air mass 1.5. [accessed May 31 2016]. [Online]. Available: http://rredc.nrel.gov/solar/spectra/am1.5/

[16] K. Bouzidi, M. Chegaar, and A. Bouhemadou, "Solar cell parameters evaluation considering the series and shunt resistance," *Solar Energy Materials & Solar Cells*, 2007.

[17] L. Kates, "Motorized window shade system," US Patent 7 389 806B2, 2008.

[18] I. Rowlands, B. Kemery, and I. Beausoleil-Morrison, "Optimal solar-PV tilt angle and asimuth: an ontario (canada) case study," *Energy Policy*, vol. 39, pp. 1397–1409, 2011.

[19] S. Beringer, H. Schilke, I. Lohse, and G. Sechmeye, "Case study showing that the tilt angle of photovoltaic plants is nearly irrelevant," *Solar Energy*, vol. 85, pp. 470–476, 2011.

[20] G. Qiu and S. Riffat, "Optimum tilt angle of solar collectors and its impact on performance," *Internation Journal of Ambient Energy*, vol. 24, pp. 13–20, 2003.

[21] M. Fetcenko and J. Koch, *Linden's Handbook of Batteries*, 4th ed. McGraw-Hill Professional, 2011, ch. 22: Nickel-Metal Hydride Batteries.

[22] L. Hao, Z. Yi, C. Li, X. Li, W. Yuxiu, and G. Yan, "Development and characterization of flexible heating fabric based on conductive filaments," *Measurement*, vol. 45, pp. 1855–1865, 2012.

[23] D. Herrington and S. Meacham, *Handbook of Electronic Tables and Formulas*, 4th ed. Indianapolis: Howard W. Sams & Co., Inc, 1973.

[24] *NEC 2005*, National Fire Protection Agency Std.

[25] M. Davies and T. Schmitz, *System Dynamics for Mechanical Engineers*. New York: Springer Science+Business, 2015.

[26] R. Alagirusamy, J. Eichoff, T. Gries, and S. Jockenhoevel, "Coating of conductive

yarns for electro-textile applications," *The Journal of The Textile Institute*, vol. 104, no. 3, pp. 270–277, 2012.

[27] E. Post, M. Orth, P. Russo, and N. Gershenfeld, "E-broidery: design and fabrication of textile-based computing," *IBM Systems Journal*, 2000.

[28] L. Li, W. Au, Y. Li, K. Wan, W. Chung, and K. Wong, "A novel design method for an intelligent clothing based on garment design and knitting technology," *Textile Research Journal*, 2009.

[29] D. Marculescu, R. Marculescu, N. Zamora, P. Stanley-Marbell, P. Khosla, S. Park, S. Jayaraman, S. Jung, C. Lauterbach, W. Weber, T. Kirstein., D. Cottet, J. Grzyb, F. Troster, M. Jones, T. Martin, and Z. Nakad, "Electronic textiles: a platform for pervasive computing," *Proceedings of the IEEE*, 2003.

[30] K. Cherenack and L. van Pieterson, "Smart textiles: challenges and opportunities," *Journal of Applied Physics*, vol. 112, no. 091301, pp. 1–14, 2012.

[31] S. Park and S. Jay, "Smart textiles: wearable electronic systems," *MRS Bulletin*, pp. 585–591, 2003.

[32] M. Ismail, A. Ammar, and M. El-Okeily, "Heat transfer through textile fabrics: mathematical model," *Applied Mathematical Modelling*, vol. 12, pp. 434–440, 1988.

[33] L. Hes, M. D. Araujo, and V. Djulay, "Effect of mutual bonding of textile layers on thermal insulation and thermal contact properties of fabric assemblies," *Textile Research Journal*, vol. 66, no. 4, pp. 245–250, 1996.

[34] P. Lizak and S. Mojumdar, "Thermal properties of textile fabrics," *Journal of Thermal Analysis and Calorimetry*, vol. 112, pp. 1095–1100, 2013.

[35] *Standard Test Method for Thermal Transmittance of Textile Materials*, ASTM Std. D 1518-85, 2003.

[36] Z. Abdel-Rehim, M. Saad, M. Shakankery, and I. Hanafy, "Textile fabric as thermal insulators," *AUTEX Research Journal*, vol. 6, no. 3, pp. 148–161, 2006.

[37] D. Bhattacharjee and V. Kothari, "Measurement of thermal resistance of woven fabrics in natural and forced convections," *Research Journal of Textile and Apparel*, vol. 12, no. 2, pp. 39–49, 2008.

[38] S. Hamdani, P. Potluri, and A. Fernando, "Thermo-mechanical behaviour of textile heating fabric based on silver coated polymeric yarn," *Materials*, vol. 6, pp. 1072–1089, 2013.

[39] H. Sezgin, S. Bahadir, Y. Boke, and F. Kalaoglu, "Thermal analysis of e-textile structures using full-factorial experimental design method," *Journal of Inustrial Textiles*, pp. 1–13, 2014.

[40] D. Giancoli, *Physics for Scientists & Engineers with Modern Physics*. Pearson Prentice Hall, 2009.

[41] D. Gerling, *Electrical Machines, Mathematical Fundamentals of Machine Topologies*. Springer, 2015.

[42] D. Linden and T. Reddy, *Linden's Handbook of Batteries*, 4th ed. McGraw-Hill Professional, 2011, ch. 1: Basic Concepts.

[43] I. Arasaratnam, J. Tjong, and R. Ahmed, "Battery management system in Bayesian paradigm: part I: SOC estimation," in *Transportation Electrification Conference and Expo (ITEC)*, 2014.

[44] M. Thele, O. Bohlen, D. Sauer, and E. Karden, "Development of a voltage-behaviour model for NiMH batteries using an impedance-based modeling concept," *Journal of Power Sources*, vol. 175, pp. 635–643, 2008.

[45] S. Santhanagopalan and R. White, *Linden's Handbook of Batteries*. McGraw-Hill Professional, 2011, ch. 6: Mathematical modelling of batteries.

[46] S. Moore and P. Schneider, "A review of cell equalization method for lithium ion and lithium polymer battery systems," *SAE Technical Paper*, no. 2001-01-0959, 2001.

[47] *Nickel Metal Hydride Handbook and Application Manual*, Energizer Std. NiMH02.01, 2010.

[48] M. Verbrugge and E. Tate, "Adaptive state of charge algorithm for nickel metal hydride batteries including hysteresis phenomena," *Journal of Power Sources*, vol. 126, pp. 236–249, 2004.

[49] A. Alajmi and J. Wright, "Selecting the most efficient genetic algorithm sets in solving unconstrained building optimization problem," *Internation Journal of Sustainable Built Environment*, vol. 3, pp. 18–26, 2014.

[50] Silvaco International, *ATLAS User's Manual*, 2004.

[51] M. Green, "Self-consistent optical parameters of intrinsic silicon at 300 K including temperature coefficients," *Solar Energy Materials & Solar Cells*, vol. 92, no. 11, pp. 1305–1310, 2008.

[52] Silvaco International. (2016) solarex02.in : Amorphous silicon with defects. [accessed Aug 23 2016]. [Online]. Available: http://www.silvaco.com/examples/tcad/section44/example2/

[53] Z. Holman, A. Descoeudres, L. Barraud, F. Fernandez, J. Seif, S. D. Wolf, and C. Ballif, "Current losses at the front of silicon heterojunction solar cells," *IEEE Journal of Photovoltaics*, vol. 2, no. 1, pp. 7–15, 2012.

[54] J. Taylor, *An introduction to error analysis*. University Science Books, 1997.

[55] Maxim Integrated, "Curve fitting the error of a bandgap-based digital temperature sensor," Application Note, 2002.

[56] Rincon-Mora, *Analog IC Design with Low-Dropout Regulators*, 2nd ed. McGraw-Hill Professional, 2014.

[57] ChaN. (2014). [Online]. Available: http://elm-chan.org/fsw/ff/00index_p.html

[58] *XBee Wi-Fi Module -S6B*, Digi International Std., March 2014.

[59] Wi-Fi Alliance. (2006, March) WPA2 Security Now Mandatory for Wi-Fi Certified Products. [Online]. Available: http://www.wi-fi.org/news-events/newsroom/wpa2-security-now-mandatory-for-wi-fi-certified-products

Appendix A

Cylindrical p-i-n Solar Cell Simulations

A.1 Model

Recently, novel, radially-symmetric p-i-n structures of polycrystalline silicon have been fabricated and tested as photovoltaic cells. Initial results from work by He et al. indicate that these devices can generate electrical current and can be physically deformed [10]. The investigated device has n-type and p-type regions doped to approximately the same concentration of 10^{20} cm^{-3}. The intrinsic region (i-region) is not intentionally doped but the devices have displayed slight n-type behaviour equivalent to doping at a level of 10^{16} cm^{-3}.

An ideal, simplified model is illustrated in Figure A.1 (a) that implements the same doping profile and semiconductor geometry as described by [10]. The contacting is simplified by defining the anode as a ring surrounding the n-type outer shell of the device while the cathode is modeled as a contact in the device's core. The real

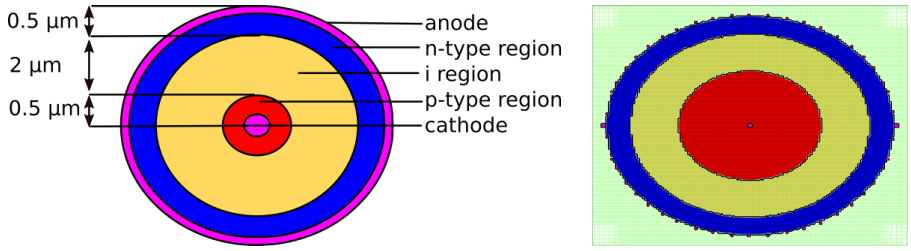

(a) (b)

Figure A.1: (a) Ideal model. (b) Simplified model analyzed using Silvaco ATLAS.

device does not have contacting along its entire length, but rather at the ends of the cylindrical column. By allowing charges to be collected in the center and edge, this model predicts the maximum efficiency since charge carriers do not recombine while traveling in the z direction to contacting electrodes. The effects of majority carrier diffusion and photocurrent collection at the electrodes are ignored by assuming that contacts behave as ohmic contacts that are transparent and perfectly conducting.

This modeled structure was simulated with ATLAS version 5.10.2.R. Software limitations necessitated some geometric simplifications that are shown in Figure A.1 (b). This software version is not capable of defining radial grids, rather a unique cross-section must be defined on a rectangular grid. To approximate a circle, a series of strips 0.05 µm wide were defined to approximate circular curvature. Three concentric, circular areas were defined using this method to approximate the p-i-n cross section of the device. ATLAS is limited to 50 rectangular electrodes making a continuous outer anode impossible. Instead, 48 small electrodes were evenly distributed along the structure's perimeter in direct contact with the n-type region and a 49th electrode is specified in the center of the structure to act as the cathode.

A.2 Simulation Setup

The behavior of this structure was investigated with different material quality. Monocrystalline silicon was modeled with the software defaults. Grain boundaries in polycrystalline silicon introduce defect states in the band structure. These defect states can be modeled with an exponential taper at the edge of the band and deep level states modeled with a Gaussian distribution as specified in [50]. This model is referred to as the high quality polycrystalline (HQP) because it uses default values found in Silvaco. A second, low quality polycrystalline (LQP), was simulated using the low charge carrier mobilities of 30 $cm^2V^{-1}s^{-1}$ for electrons and 2 $cm^2V^{-1}s^{-1}$ for holes that were reported in [10]. All crystalline models used data taken from [51] to model the wavelength specific index of refraction and absorption coefficients.

Amorphous, hydrogenated silicon (a-Si:H) was also modeled. This structure implemented the same defect states as polycrystalline models but includes additional changes to carrier mobilities, band density of states and bandgap as specified in [52]. The wavelength dependent optical characteristics (index of refraction and absorption spectra) were modeled using data from [53].

The photogeneration of these devices was evaluated using ray tracing. To speed evaluation, the AM1.5 spectrum was approximated with ten wavelengths of lights evenly spaced from 0.1 µm to 1.1 µm with relative intensities interpolated from the actual AM1.5 spectrum. Band gap narrowing due to high dopant concentrations, Shockley-Read-Hall recombination, and Auger recombination were modeled to consider all likely forms of losses. All physical models implemented Fermi-Dirac statistics to ensure accuracy instead of using approximate Boltzmann statistics.

The effectiveness of the conversion of light to electricity was evaluated by generating an IV curve. After ray tracing determined photogenerated charges, the terminal voltage was swept through a series of values. At each bias, the amount of current at the terminal was simulated and recorded. This procedure generated the structure's predicted IV curve.

A.3 Baseline Simulation

The purpose of the LQP simulation was to model the experimental device but as Figure A.2 (a) shows, the results predict enhanced voltage and current characteristics. This improved performance is consistent with the previously discussed assumptions and simplifications. The simulation assumed ideal contacts that run along the length of the device and it did not consider the contacting losses that are present in the real device. In the simulation, charges only have to travel the short micron distance between radial electrodes when the true device may have path lengths that are millimeters long. This long distance could increase the probability of recombination. The band structure and absorption spectra of this device were based on literature parameters that can approximate the behaviour but may not match it exactly.

Comparing the relative difference between similar models can provide useful information on how changing different factors can improve or reduce device efficiency. The IV curves for the monocrystalline, HQP and a-Si:H cells are shown in Figure A.2 (b) where it is easy to see that these different devices have improved performance. While the amorphous simulation predicts a comparable current to LQP, the large band gap gives the device a higher voltage characteristic. HQP and monocrystalline have enhanced voltage and current performance highlighting the benefit that can be

achieved by improving the quality of the material.

A.4 Effect of Doping

The simulations were repeated for each type of material when the doping concentrations of the p-type core and n-type sheath were varied. The maximum simulated power point is plotted against the exponentially varying dopant concentration in Figure A.3. All crystalline simulations exhibited similar behaviour, the presence of a local maximum. This can be explained by the interaction of two competing effects. Integrating more dopants causes the devices to have a larger built-in electric field that is more capable of separating EHP. Too many impurities introduce an excessive number of recombination centers preventing the separated current from being extracted by an external circuit. These simulations could be refined to determine the optimal level of impurities to introduce to the structure in order to optimize performance of crystalline cylindrical solar cells.

A local maximum is not observed in the a-Si:H simulation results in Figure A.3 (a). Even at degenerate levels of doping, the efficiency of the device appears to improve. The a-Si:H model has the most defective band structure of the simulated structures. A possible explanation is that the addition of extra dopants provided negligible additional recombination sites relative to the existing defects. In this situation, additional dopants only improved the ability of the device to separate EHP without creating additional recombination centers.

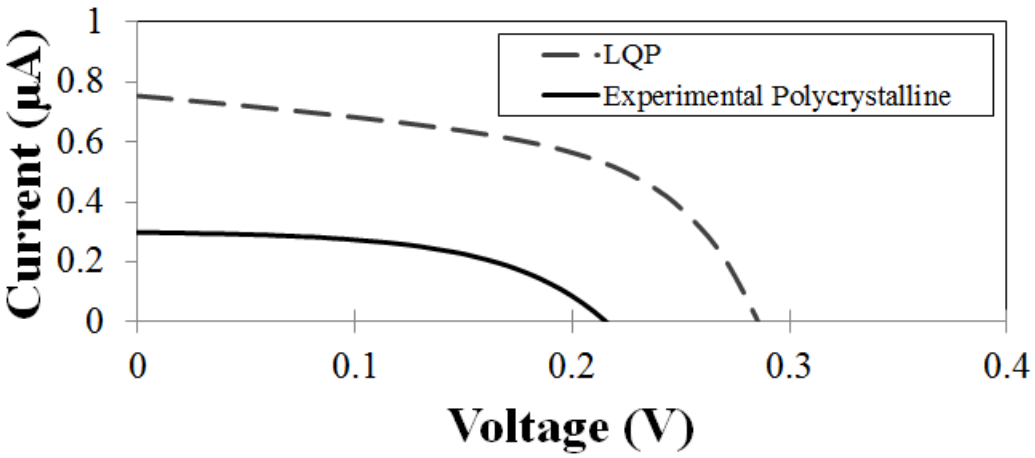

(a)

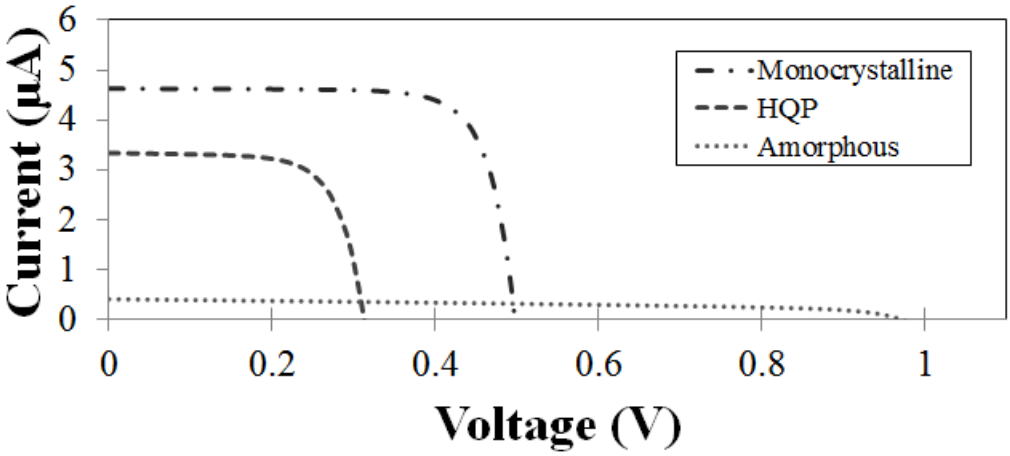

(b)

Figure A.2: (a) Photoresponse of the experimental solar thread described in [10] compared to the LQP simulation. (b) Idealized simulations for Amorphous, HQP and monocrystalline structures.

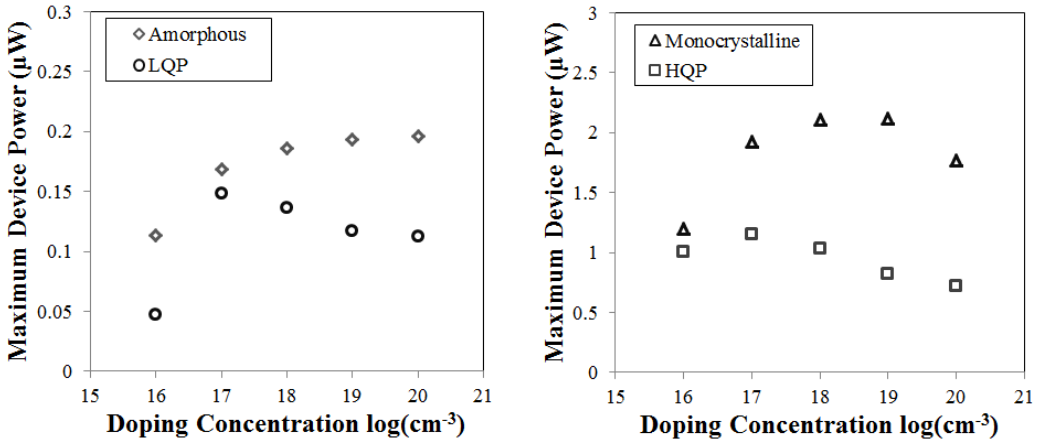

(a) (b)

Figure A.3: The effect of doping n-type and p-type regions of the p-i-n structure. For clarity of scales the results were plotted on two figures. Subfigure (a) shows the low quality devices with poor efficiency while (b) shows the higher power devices.

A.5 Effect of Geometry

The effect of intrinsic region width was explored. For this simulation, the overall device diameter of 6 µm was held constant and the width of the intrinsic ring, centered at a radius of 1.5 µm, was varied. The doping concentrations were maintained at the levels described in [10]. The impact of this change on efficiency is plotted in the two trends in Figure A.4.

Monocrystalline devices exhibit a strongly favorable response to an increased intrinsic region. Visual inspection of the device cross section in Figure A.5 shows that recombination dominates in the p-type core and n-type sheath. By shrinking these regions in favour of a larger i-region, the overall recombination rate is decreased and the extracted charges are increased.

The HQP simulation results display a local maximum. Unlike the monocrystalline simulation, Figure A.5 shows that recombination is prevalent in the i-region,

likely because polycrystalline has a more defective band structure. As the i-region is widened, the overall device recombination rate does not always decrease as it does in the monocrystalline simulation. This can be seen by comparing the wide i-region HQP device in Figure A.5 (d) to the monocrystalline device with the same geometry in Figure A.5 (b). Within the i-region, there is significantly more recombination in the HQP structure than the monocrystalline structure.

Both a-Si:H and LQP simulations showed interesting behaviour. The device with the smallest intrinsic region generated the most power. Visual inspection of Figure A.6 shows that recombination is particularly strong in the highly doped exterior n-type sheath. Recombination is low where the built in electric field (E_{field}) is strong; typically just outside of the p-type core. Devices with large p-type cores have a large cross sectional area with a strong electric field and therefore a large area where recombination is low. This simulation implies that low quality devices may benefit from an over-sized core with a small intrinsic gap.

A.6 Additional Efficiency Improvements

The diagrams in Figures A.5 and A.6 indicate that the majority of the recombination effects occur in the external sheath of the device. Hole mobility is consistently lower than electron mobility, yet minority holes are generated when light is absorbed in the n-type sheath. By reversing the order of the p-i-n device and having the sheath made of p-type material, absorbed photons will produce minority electrons that should be easier to separate due to their improved mobility. If this is true, it would be expected to improve the performance of the amorphous device considerably because this material has a high absorption coefficient and likely absorbs photons at

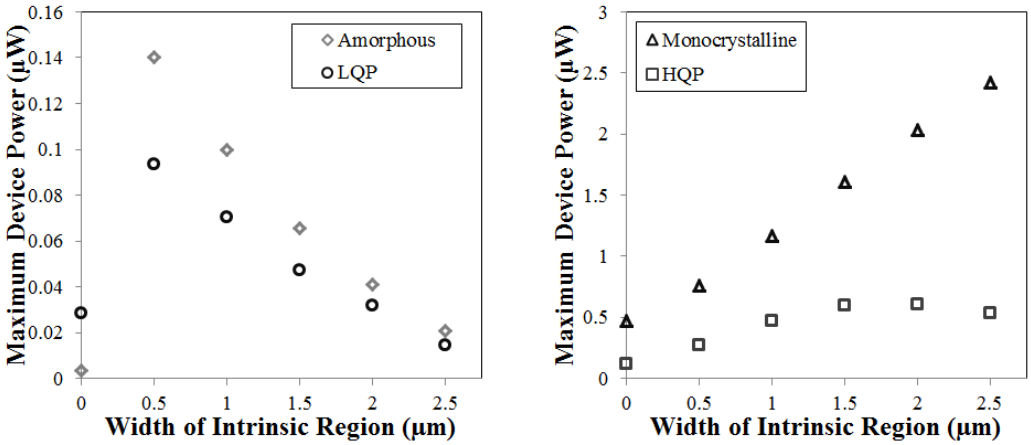

Figure A.4: Effect of modifying the width of the intrinsic region of the p-i-n structure. For clarity of scales the results were plotted on two figures. Subfigure (a) shows the low quality devices with poor efficiency while (b) shows the higher power devices.

a very shallow depth.

Switching the order of the device to a p-type sheath and n-type core could improve the cross-sectional area with a strong E_{field}. Since the model assumes that the i-region is slightly n-type, the strongest E_{field} is observed at the interface between the p-type region and the i-region. The boundary between sheath and i-region has a larger radius than the boundary between core and i-region. If the sheath were p-type, it would have a larger cross-sectional area with a strong E_{field}which could lead to reduced overall recombination in devices made of low quality materials.

A.7 Efficiency

The maximum simulated efficiency observed was 4.0% for the large-gap monocrystalline structure. Current experimental devices do not approach this scale of efficiency value.

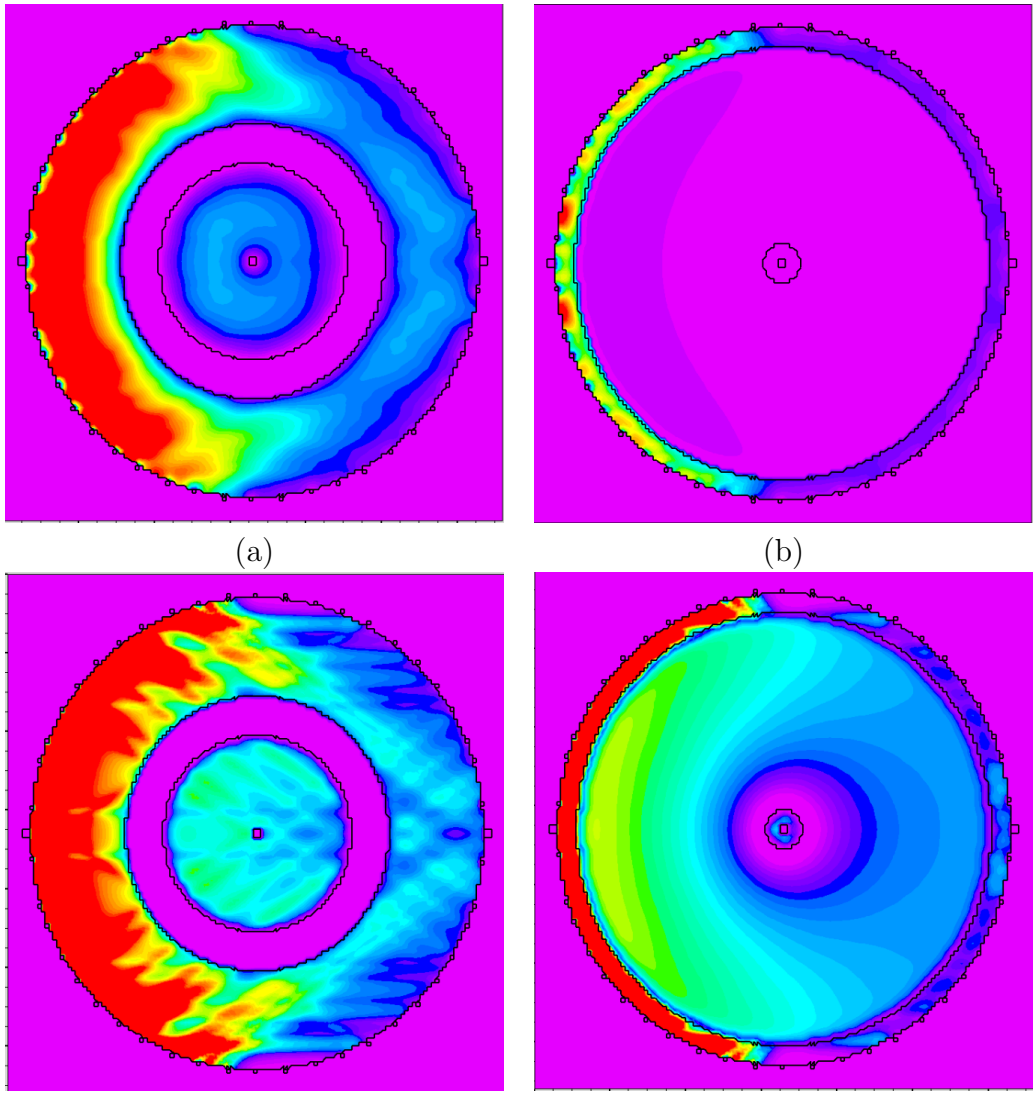

Figure A.5: Colour map representation of recombination where warm colours indicate high levels of recombination, cool colours indicate less recombination and pink regions have no recombination. The structures are as follows: (a) narrow i-region monocrystalline, (b) wide i-region monocrystalline, (c) narrow i-region HQP and (d) wide i-region HQP.

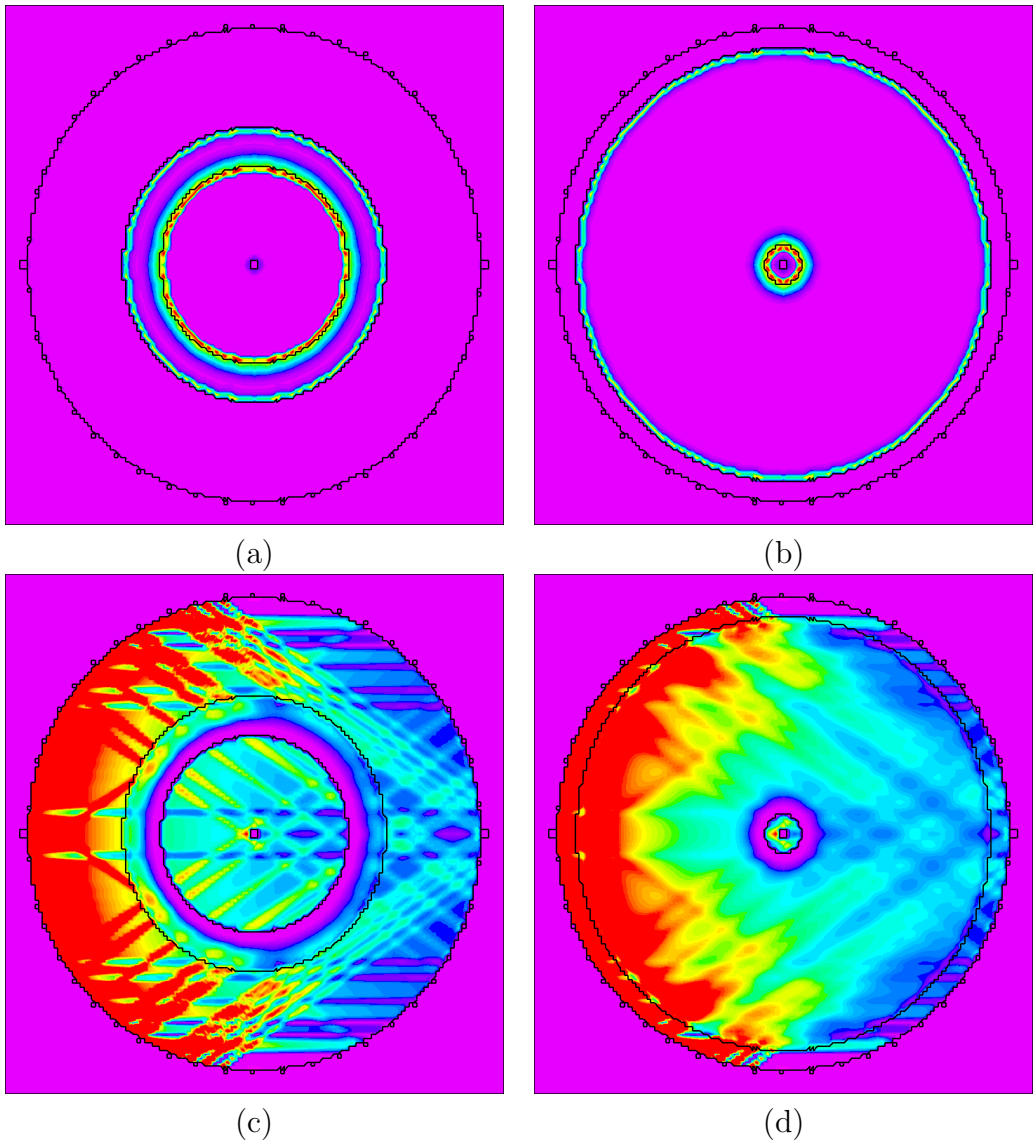

Figure A.6: Colour maps showing the relationship between built in electric field and recombination in the LQP structure in the short circuit condition. Warm colours indicate a strong E_{field} or high rate of recombination while cooler colours represent a weak E_{field} or low recombination. The diagrams depict: (a) small i-region E_{field}, (b) large i-region E_{field}, (c) small i-region recombination and (d) large i-region recombination.

Appendix B

Sample Calculations and Uncertainty Propagation

B.1 Error Propagation

Uncertainty measurements are discussed in detail in [54]. The uncertainty in function f is denoted by δf while the uncertainty of an individual variable x_i is denoted by δx_i. The fractional uncertainty of parameter is a value denoted by $\delta x_i / x_i$. After discussing error propagation techniques, this appendix provides sample calculations and uncertainty calculations for values discussed in this thesis.

By convention, error values are communicated using a single significant figure. An exception to this rule is when the first digit of error is 1 because rounding can lose notable accuracy. For example a value with an error of 1.4 would overstate the accuracy by 40% if it was rounded to 1. The calculations in this section often carry excessive significant figures as they may be used in subsequent calculations and omitting this accuracy can lead to rounding errors.

B.1.1 Simple Propagation

For simple addition and subtraction calculations, the uncertainty can be determined by adding the absolute uncertainties of each parameter in the summation. The error of the addition (B.1) is shown in (B.2).

$$f = \sum_{i=1}^{n} x_i \tag{B.1}$$

$$\delta f = \sum_{i=1}^{n} \delta x_i \tag{B.2}$$

For simple multiplication and division operations, the uncertainty is propagated by adding the fractional uncertainties. The error of the function (B.3) is shown in (B.4).

$$f = \prod_{i=1}^{n} x_i \tag{B.3}$$

$$\frac{\delta f}{f} = \sum_{i=1}^{n} \frac{\delta x_i}{x_i} \tag{B.4}$$

B.1.2 General Propagation

For a complicated function $f(x_1, x_2, ..., x_n)$, where all variables have independent errors, equation (B.5) can be used. The previous methods (B.2) and (B.4) may be quicker, but they also tend to overstate a function's uncertainty when the sources of error are independent. For complex relations and independent errors, equation (B.5) is used.

$$\delta f = \sqrt{\sum_{i=1}^{n} (\frac{df}{dx_i})^2 \delta x_i^2} \tag{B.5}$$

If the variables have related errors and the function is too complicated to apply the simple multiplication or addition propagation techniques, the error can be approximated with (B.6).

$$\delta f = \sum_{i=1}^{n} (\frac{df}{dx_i}) \delta x_i \tag{B.6}$$

B.1.3 Repeated Measurement

Some measurements have poorly defined error. A poorly calibrated measurement device or an external source of measurement noise may necessitate a method for the experimenter to independently evaluate error. This can be accomplished by repeating the measurement N times to get a dataset of measured values x_i with a mean measurement $\bar{x}$. Assuming the source of noise is Gaussian in nature, the standard deviation σ of the dataset can convey certainty. The expression $\bar{x} \pm \sigma$ describes the region where 63% of measured values have fallen. Increasing this region to $\bar{x} \pm 2\sigma$ captures 95% of the measured data. This bound can be calculated using (B.7). This value of δx can be propagated through functions using the methods discussed previously.

$$\delta x = 2\sigma = 2 \cdot \sqrt{\frac{1}{N-1} \Sigma_i^N (x_i - \bar{x})^2} \tag{B.7}$$

B.1.4 Method of Least Squares

A set of noisy data can be fit to a line of form $y = Ax + B$ using the method of least squares. The complete derivation of this method is included in [54] but the final equations are summarized here. These formulas apply to a dataset of N datapoints in the form of (x_k, y_k).

$$\Delta = N \sum x^2 - (\sum x)^2 \tag{B.8}$$

$$A = \frac{\sum x^2 \sum y - \sum x \sum xy}{\Delta} \tag{B.9}$$

$$B = \frac{N \sum xy - \sum x \sum y}{\Delta} \tag{B.10}$$

The standard deviation of the error of the fit can be evaluated using (B.11).

$$\sigma_y = \sqrt{\frac{1}{N-2} \sum_k^N (y_k - A - Bx_k)^2} \tag{B.11}$$

This value σ_y can be used to determine the standard deviation of the fit model parameters A and B. Recall two standard deviations are necessary for 95% confidence.

$$\delta A = 2\sigma_A = 2\sigma_y \sqrt{\frac{\sum x^2}{\Delta}} \tag{B.12}$$

$$\delta B = 2\sigma_B = 2\sigma_y \sqrt{\frac{N}{\Delta}} \tag{B.13}$$

B.2 Window Light Attenuation

B.2.1 Analytical Evaluation of Window's Impact on Performance

In this work, attenuation was evaluated by comparing the change in photocurrent produced by a solar cell when placed outside compared to being mounted inside a window. This can be calculated by considering the product of the available photon flux $\Phi_{ph}(\lambda)$ and the solar cell's external quantum efficiency $EQE(\lambda)$ across a reasonable range of wavelengths λ as shown in (B.15). The photon flux through the window can be calculated by taking the AM1.5 spectrum's spectrum, Φ_{AM} and multiplying it by the transmission coefficient function of the window $\gamma_w(\lambda)$.

$$\beta = \frac{G_{inside}}{G_{outside}} = \frac{I_{ph,inside}}{I_{ph,outside}} \tag{B.14}$$

$$G = \sum^{\lambda} \Phi_{ph}(\lambda) \cdot EQE(\lambda) \tag{B.15}$$

$$\beta = \frac{G_{AM}}{G_{window}} = \frac{\sum^{\lambda} \Phi_{ph,AM}(\lambda) \cdot EQE(\lambda)}{\sum^{\lambda} \Phi_{ph,AM}(\lambda) \cdot \gamma_w \cdot EQE(\lambda)} \tag{B.16}$$

For this calculation, the AM1.5 spectrum and the window transmission factors were taken from industrial sources with the assumption that they are highly accurate. The main source of error stems from the EQE trend that was obtained through visual inspection of the datasheet graph included in Appendix E. Each value was estimated with an absolute error of ± 0.05 % photons converted.

Table B.1: Parameters needed for sample calculation of n_c and δn_c at wavelength 700 nm that is transmitted through an LOE180 window (window 1).

Variable	Value
λ	700 nm
Φ_{AM}	1.28 W/m^2
EQE(700)	0.95 ± 0.05 %
$\gamma(700)$	0.7371 %

Equation (B.15) was evaluated in an Excel spreadsheet. The spreadsheet discretized the spectrum according to the data in the National Renewable Energy Lab (NREL) AM1.5 spectrum. The transmission spectrum and EQE trends were more coarsely spaced and so they were linearly interpolated. A value for G due to each discrete wavelength was calculated and then this series was summed to find a total G rate. It is not feasible to include the entire summation here, instead a single calculation for G(700nm) is included in (B.19) using sample data from Table B.1. Since the error for G originates from a single variable, the application of either the simple multiplication rule (B.4) or the general independent rule (B.5) will yield the same error propagation formula (B.18).

$$G_{700} = \Phi_{AM}(700) \cdot \frac{\lambda}{hc} \cdot \gamma_w \cdot EQE(\lambda) \tag{B.17}$$

$$\delta G_{700} = \Phi_{AM} \cdot \frac{\lambda}{hc} \cdot \gamma_w \cdot \delta_{EQE} \tag{B.18}$$

$$G_{700} = 3.17 \times 10^{18} \pm 1.66 \times 10^{17} \tag{B.19}$$

Table B.2: Best guess and upper/lower bounds of G.

Interfering Medium	Converted Photons	Absolute Error	Relative Error
Unattenuated	2.337×10^{21}	1.17×10^{20}	0.0502
Window 1	1.588×10^{21}	7.96×10^{19}	0.0501
Window 1	1.112×10^{21}	5.56×10^{19}	0.0500
Window 1	7.567×10^{20}	3.78×10^{19}	0.0499

The converted photon values must be summed across the entire spectrum of available light. Since some of the discrete absolute errors may be dependent on the same uncertainty, error propagation can be achieved using (B.2). The total values of G for the different windows as well as the summed error are displayed in the Table B.2.

The transmission coefficient β can be calculated by taking the ratio of converted photons between each window and the unattenuated case. These errors are related because they are based on the EQE calculation. The simple multiplication rule is applied to ensure an accurate error estimate. The data from Table B.2 is used in a sample calculation in (B.20).

$$\beta_{w1} = \frac{3.74 \times 10^{20} \pm 5\%}{5.48 \times 10^{20} \pm 5\%} = 0.68 \pm 11\% = 0.68 \pm 0.09 \tag{B.20}$$

B.2.2 Analytical Evaluation of Screen's Impact on Performance

Unlike windows that selectively transmit light, a bug screen does not discriminate and evenly shades the AM1.5 spectrum. This sample calculation shows how the area blocked by the screen was evaluated. A diagram of the shaded setup is illustrated in Figure B.1.

The unit cell's length L_{us} is not directly measurable using vernier calipers. It can

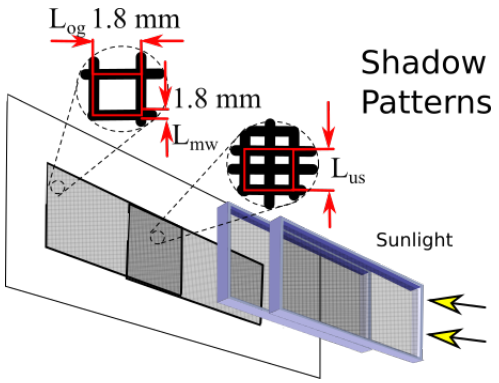

Figure B.1: Shading patterns produced by the screen.

Variable	Value
L_{og}	1.8 ± 0.05
L_{mw}	0.3 ± 0.05

Table B.3: Parameters used in screen attenuation calculations.

be determined by measuring the outer grid length L_{og}, and subtracting the width of the mesh web L_{mw} as shown in (B.21). The parameters L_{og} and L_{mw} are shown in Table B.3. The next sections consider the area using L_{us} then convert the expression to a function of L_{og} and L_{mw} so that the error calculation can be performed independently.

$$L_{us} = L_{og} - L_{mw} = 1.8 - 0.3 = 1.5 \tag{B.21}$$

B.2.2.1 Single Grid Pattern

For the single screen, the unshaded area A_{uss} area was calculated using data from Table B.3 and the following equation:

$$A_{uss} = \frac{(L_{us} - L_{mw})^2}{L_{us}^2} = \frac{(L_{og} - 2L_{mw})^2}{(L_{og} - L_{mw})^2} = 0.64 \tag{B.22}$$

Error propagation can be accomplished using the form of (B.22) that omits δL_{us}, and propagating the independent errors.

$$\begin{aligned} \delta A_{uss} &= \sqrt{[\frac{2L_{mw}(L_{og}-2L_{mw})}{(L_{og}-L_{mw})^3}]^2\delta L_{og}^2 + [\frac{-2L_{og}(L_{og}-2L_{mw})}{(L_{og}-L_{mw})^3}]^2\delta L_{mw}^2} \\ &= 0.06 \end{aligned} \tag{B.23}$$

B.2.2.2 Double Grid Pattern

The following formula was used to calculate the unattenuated area A_{usd} for the double grid pattern:

$$A_{usd} = \frac{4(\frac{1}{2}L_{us}-L_{mw})^2}{L_{us}^2} = \frac{(L_{og}-3L_{mw})^2}{(L_{og}-L_{mw})^2} = 0.36 \tag{B.24}$$

Error propagation can be accomplished using the form of (B.24) that omits δL_{us}.

$$\begin{aligned} \delta A_{usd} &= \sqrt{[\frac{4L_{mw}(L_{og}-3L_{mw})}{(L_{og}-L_{mw})^3}]^2\delta L_{og}^2 + [\frac{-4L_{og}(L_{og}-3L_{mw})}{(L_{og}-L_{mw})^3}]^2\delta L_{mw}} \\ &= 0.10 \end{aligned} \tag{B.25}$$

B.2.3 Experimental Evaluation of Media's Impact on Performance

Bouzidi's method, outlined in Appendix C, was used to fit the five parameter model (B.26) to IV curve measurements that were taken from a solar cell illuminated by a solar simulator. A solar cell's photocurrent I_{ph} is dependent on irradiance.

By comparing the photocurrent of a solar cell in direct light $I_{ph_{unattenuated}}$ and an attenuated spectrum through a medium $I_{ph_{attenuated}}$an attenuation factor β can be solved.

$$I = I_{ph} - I_d - I_{sh} = I_{ph} - I_s(\exp\frac{(V + R_s I)}{nk_t} - 1) - \frac{(V_t + R_s I)}{R_{sh}} \tag{B.26}$$

$$\beta = \frac{I_{ph_{attenuated}}}{I_{ph_{unattenuated}}} \tag{B.27}$$

Error propagation through Bouzidi's method is tricky due to the prevalence of matrix operations. Simplifications were made to make error propagation reasonable. Within Bouzidi's method, I_{ph} is calculated using using the following formula:

$$I_{ph} = \frac{I_{pA}}{1 - G_A R_s} \tag{B.28}$$

G_A and I_{pA} are defined in Appendix C and can be solved by fitting a line of form $y = A + Bx$ to the measured IV curve data within the voltage range -0.1 V to 0.1 V. The fit can be determined using (B.9) and (B.10). Once solved, I_{pa}=A and G_A=B. R_s is calculated through other matrix calculations.

For the datasets evaluated, the product $G_A R_s$ is always less than 10^{-3} and (B.28) can be approximated by (B.29).

$$I_{ph} \approx I_{pA} \tag{B.29}$$

For error propagation, it is assumed that the majority of the error contribution

stems from the error of the I_{pA} parameter. Since I_{pA} is fit using least squares error, it's error can be propagated using (B.13). Due to the large amount of data required to complete this summation, no sample calculations are provided here. Instead the calculated value of I_{pa} and the error stemming from the least squares method are included in Tables B.4 and B.5.

While the variance of the dataset has been calculated to be quite tight, using this value would conflict with the known accuracy of the Keithly 2400 sourcemeter that took the measurements. The error of current measurements from the sourcemeter is reported to be 0.055% of the reading plus an additional 6 μA. A column is used in Tables B.4 and B.5 to show what the uncertainty of the equipment is. To be conservative, the uncertainty of the equipment measurement was used for error propagation.

To calculate attenuation, the ratio between I_{pa} for the attenuated window and the unattenuated case must be taken. To be conservative, these errors were considered dependent and rule (B.4) was applied to carry the error.

$$\beta_{window1} = \frac{0.0318770}{0.0442405} = 0.720539 \tag{B.30}$$

$$\delta\beta_{window1} = 0.720539\left(\frac{3.03 \times 10^{-5}}{0.0442405} + \frac{2.35 \times 10^{-5}}{0.0318770}\right) = 0.00102 \tag{B.31}$$

B.3 Temperature Gradient

Thermometers monitored the change in temperature within the e-textile system and also in the ambient environment. The absolute measurements were converted

Table B.4: Calculated photogenerated current and associated standard deviation for the first set of irradiance tests (windows). All units are Amps.

Case	$I_{ph} \approx I_{pA}$	δI_{ph} from least squares	δI_{ph} from equipment
Unattenuated	0.0442405	1.26×10^{-5}	3.03×10^{-5}
Window 1	0.0318770	7.92×10^{-6}	2.35×10^{-5}
Window 2	0.0218075	5.60×10^{-6}	1.80×10^{-5}
Window 3	0.0147208	4.26×10^{-6}	1.41×10^{-5}

Table B.5: Calculated photogenerated current and associated absolute error for the first set of irradiance tests (screen). All units are Amps.

Case	$I_{ph} \approx I_{pA}$	δI_{ph} from least squares	δI_{ph} from equipment
Unattenuated	0.0440719	9.34×10^{-6}	3.02×10^{-5}
Single Screen Pattern	0.0266391	5.14×10^{-6}	2.07×10^{-5}
Double Screen Pattern	0.0140312	3.12×10^{-6}	1.37×10^{-5}

into temperature gradients between the thermal system and the environment, and error was propagated through this conversion.

Band-gap based thermometers follow a quadratic error characteristic [55]. As temperature varies, the amount the absolute temperature is over or under measured varies quadratically. This effect is noticeable over the thermometer's total operating region ($-55°C$ to $125°C$). Over small temperature ranges like the ones observed in this test (which only varied by $5°C$), the measurement error can be assumed to be a consistent, systematic error in the measurement of absolute temperature. This systematic error in absolute temperature measurements is observed in Figure B.2 where the thermometers reported a temperature difference between the A, E and control locations despite the fact that the system is known to have started at the same initial temperature. The analysis technique used in this chapter is not dependent on absolute temperature changes, but rather the relative change in temperature. This source of error is removed when the relative temperature difference ΔT is calculated.

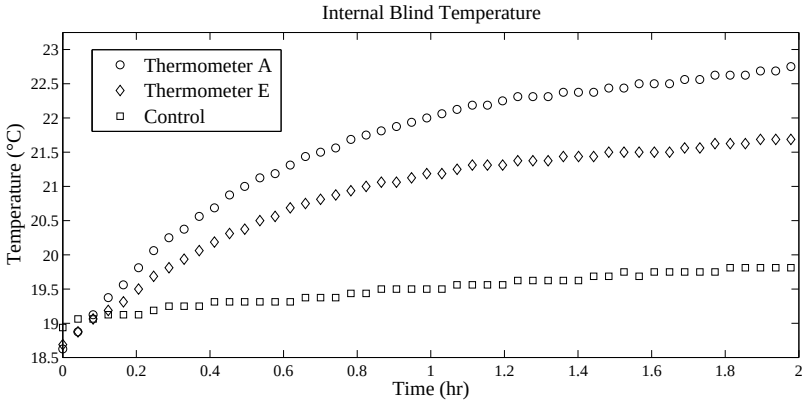

Figure B.2: Raw temperature measurements of different thermometers in the thermal system. They report different initial temperatures.

The remaining error of this measurement is caused by the discretization of the temperature measurements. Each thermometer can resolve temperature measurements in increments of 0.0625 °C, meaning each measurement has an accuracy of half this increment, ±0.03125°C.

Each ΔT measurement was calculated using (B.32) where T_m is the temperature at the measuring thermometer while T_c is the temperature at the control thermometer that is not embedded in the e-textile unit. Since the error stems from the discretization of temperature measurements at different times and two different thermometers, they are combined using the general form of the independent errors (B.5).

$$\Delta T(t) = (T_m(t) - T_c(t)) - (T_m(0) - T_c(0)) \tag{B.32}$$

$$\delta_{\Delta T} = \delta_T \sqrt{4} = 2 \cdot 0.03125 = 0.06 \tag{B.33}$$

Table B.6: Mean OCV measurement with error

Measurement	Symbol	Mean Measurement and error	Units
Motor Terminal Voltage	V_t	8.477 ± 0.2997	V
Encoder Period	T_{enc}	$(44.16 \pm 1.734) \times 10^{-6}$	s

B.4 Motor Model

B.4.1 Open Circuit Voltage Test

The open circuit voltage (OCV) test is described in Chapter 6.3.1. By spinning a motor's rotor and measuring both the rotational speed ω and the terminal voltage V_t a parameter k_U can be calculated to relate the two in (B.34). The rotational speed was measured using the motor's built in encoder which outputs a signal with period T.

The voltage and period measurements were noisy. The error on these measurements were calculated by evaluating the variance of the measurement with (B.7) rather than propagating measurement accuracy of the data acquisition (DAQ) systems. The mean measurement and its statistical error is shown in Table B.6.

The calculation is shown here. Measurement error was propagated using the general form for independent variables (B.5).

$$k_U = \omega T_{enc} = \frac{360}{2\pi} V_t T_{enc} = 0.0214 \tag{B.34}$$

$$\delta k_U = \frac{360}{2\pi} \sqrt{T_{enc}^2 \delta V_t^2 + V_t^2 \delta T_{enc}^2} = 0.0011 \tag{B.35}$$

Table B.7: Mean SCT measurement with error

Test	Symbol	Mean Measurement	Units
Series Resistance Voltage	V_I	0.1973 ± 0.01253	V
Encoder Period	T_{enc}	$(12.64 \pm 1.050) \times 10^{-5}$	s

B.4.2 Short Circuit Test

The short circuit test (SCT) is described in Chapter 6.3.2. By spinning a motor's rotor, shorting the terminals and measuring the rotation speed and output current, the internal resistance can be calculated. This experiment used measurements from the encoder's period T_{enc} and placed the terminal voltage V_t across a series resistor, R_I to measure the current. R_I was rated at 1 Ω and its datasheet reports an error of 0.01 Ω. Measurements of V_I and T_{enc} were repeated several times as they were noisy. Equation (B.7) was used to evaluate the error of the noisy measurement. The motor's internal resistance is calculated with (B.36) using data from Table B.7. Errors from these measurements were independent and were propagated through the application (B.5). The expression for this measurement's error is (B.37).

$$R_A = \frac{2\pi k_U R_I}{360 T_{enc} \cdot V_I} - R_I = 14.01 \tag{B.36}$$

$$\begin{aligned} \delta k_U \quad &= \Big((\frac{2\pi R_i}{360})^2 [(\frac{1}{T_{enc} V_I})^2 \delta k_U^2 + (\frac{-k_U}{T_{enc}^2 V_I})^2 \delta {T_{enc}}^2 + (\frac{-k_U}{T_{enc} V_I^2})^2 \delta V_I^2] \\ &+ (\frac{2\pi k_U}{360 T_{enc} \cdot V_I} - 1)^2 \delta {R_I}^2 \Big)^{\frac{1}{2}} \end{aligned} \tag{B.37}$$

$$= 1.765 \tag{B.38}$$

Table B.8: Mean Power measurement with error

Test	Symbol	Mean Measurement	Units
Motor Terminal Voltage	V_T	11.86 ± 0.07718	V
Encoder Period	T_{enc}	$(360.8 \pm 5.177) \times 10^{-7}$	s
Voltage Across R_I	V_I	0.1277 ± 0.07729	V

B.4.3 Power Test

This test was run by allowing the DC motor to spin freely while monitoring the current flowing in, the motor terminal voltage and the encoder period. The voltage V_I across a current measuring resistor R_I, was measured and used to determine the armature current I_A. The motor's rotational speed was evaluated using the period of an optical encoder's output signal. A resistor of 1 Ω and datasheet error of 0.01 Ω was used for R_I. The measurements of V_I, V_t and T_{enc} were repeated many times and (B.7) was used to evaluate the error of that noisy measurement. The mean and error for these variables are included in Table B.8. Errors are independent and propagated with (B.5). The formula to propagate the error is shown in (B.40).

$$k_\tau = \frac{V_T - I_A R_A}{\omega} = \frac{360 T_{enc}}{2\pi}(V_T - \frac{V_I R_A}{R_I}) = 0.02080 \tag{B.39}$$

$$\begin{aligned} \delta k_\tau &= \sqrt{\Sigma_{i=1}^{n}(\frac{dk_\tau}{dx}\delta x_i)^2} \\ &= \frac{360}{2\pi} \cdot \\ &\sqrt{(V_T - \frac{V_I R_A}{R_I})^2 \delta T_{enc}^2 + (T_{enc}^2)\delta V_T^2 + \frac{T_{enc}}{R_I^2}^2 [(-R_A)^2 \delta V_I^2 + (-V_I)^2 \delta R_A^2 + (\frac{V_I R_A}{R_I})^2 \delta R_I^2]} \\ &= 0.0023 \end{aligned} \tag{B.40}$$

Table B.9: Mean baseline test measurement with error

Parameter	Symbol	Mean Measurement	Units
Raising Blinds Terminal Voltage	V_{TR}	12.08 ± 0.09546	V
Raising Blinds Encoder Period	T_{encR}	$(58.93 \pm 8.073) \times 10^{-6}$	s
Raising Blinds Voltage Across R_I	V_{IR}	0.4909 ± 0.1320	V
Lowering Blinds Terminal Voltage	V_{TL}	12.10 ± 0.1021	V
Lowering Blinds Encoder Period	T_{encL}	$(32.37 \pm 1.211) \times 10^{-6}$	s
Lowering Blinds Voltage Across R_I	V_{IL}	0.06097 ± 0.07764	V

B.4.4 Baseline Test

Current, voltage and encoder output from the motor were monitored as the motor raised and lowered the fully assembled blind prototype. The results from the baseline test are summarized in the Table B.9. The same 1 Ω current monitoring resistor R_I (with 1% error) was employed to determine current flowing into the motor. The measurements of V_I, V_t and T_{enc} were repeated 50 times and (B.7) was used to evaluate the error of that noisy measurement.

Using the baseline test measurements, the motor's terminal voltage and accuracy is predicted in equations (B.41) through (B.44). The predicted operating voltages are consistent with measured results.

$$V_t = \frac{V_I}{R_I} R_A + k_U \frac{2\pi}{360 T_{enc}} \tag{B.41}$$

$$\delta V_t = \sqrt{(\frac{V_I}{R_I})^2 \delta R_A^2 + (\frac{R_A}{R_I})^2 \delta V_I^2 + (\frac{-V_R}{R_I^2} R_A)^2 \delta R_I^2 + (\frac{2\pi}{360 T_{enc}})^2 \delta k_U^2 + (\frac{-2\pi k_U}{360 T_{enc}^2})^2 \delta T_{enc}^2} \tag{B.42}$$

$$V_{TR} = 13.23 \pm 2.246 = 13 \pm 2V \tag{B.43}$$

$$V_{TL} = 12.42 \pm 1.325 = 12 \pm 1V \tag{B.44}$$

The torque used while raising and lowering the blinds are calculated next. In equation (B.45), the motor torque is calculated and transformed according to the gear ratio, $g_r = (139 + \frac{184}{1221})$, of the orbital gear set.

$$\tau = k_\tau I_A g_r \tag{B.45}$$

$$\delta\tau = g_r \sqrt{(\frac{V_I}{R_I})^2 \delta k_\tau^2 + (\frac{k_\tau}{R_I})^2 \delta V_I^2 + (-\frac{k_\tau V_T}{R_I^2})^2 \delta R_I^2} \tag{B.46}$$

$$\tau_R = k_\tau \frac{V_{IR}}{R_I}(139 + \frac{184}{1221}) = 1.422 \pm 0.5419 \ Nm = 14.50 \pm 5.53 \ kgcm \tag{B.47}$$

$$\tau_L = k_\tau \frac{V_{IL}}{R_I}(139 + \frac{184}{1221}) = 0.1766 \pm 0.4169 \ Nm = 1.801 \pm 4.252 \ kgcm \tag{B.48}$$

B.4.5 Efficiency Calculations

If the friction brake were omitted in the design of the proposed prototype, the motor would still be required to provide a minimum amount of torque in order to lift the bottom rail. This minimum torque can be determined by considering the weight

Table B.10: Relevant parameters for the efficiency calculations.

Test	Symbol	Mean Measurement	Units
Bottom Rail Approximate Weight	m_B	1.5 ± 0.5	kg
Diameter of blinds	D_B	$(55 \pm 15) \times 10^{-3}$	m
Current to overcome built in friction	$I_{\tau\_builtin}$	0.1277 ± 0.07729	A
Measured current to raise blinds	I_{IR}	0.4909 ± 0.1320	A

of the bottom rail and the diameter of the top rail. These values are included in Table B.10 and used to calculate the minimum torque in (B.49). The errors calculating this ideal torque are independent and are propagated using (B.5) as shown in (B.50).

$$\tau_{raise\_ideal} = 0.5 m_B g D_B = 0.4047 \pm 0.1743 Nm \tag{B.49}$$

$$\delta\tau_{raise\_ideal} = 0.5 g \sqrt{(M_B)^2 \delta D_B^2 + (D_B)^2 \delta M_B^2} \tag{B.50}$$

To calculate the current needed by the motor to raise the blinds the torque of the DC motor before going into the gear set must be calculated. This requires scaling the torque according to the gear set's gear ratio $g_r = (139 + \frac{184}{1221})$.

Along with providing enough torque to raise the blinds, the motor must provide enough torque to overcome its built in friction. The motor's armature mounting introduces a source of friction and the series orbital gearset also has friction. This was observed in the previously discussed power test where the motor was running without any load on the armature, yet it still consumed current $I_{\tau\_builtin}$ of about 130 mA. To calculate the current needed by the motor while raising the blinds I_{raise_ideal} in the idealized case, it is necessary to add $I_{\tau\_builtin}$ as shown in (B.51). $I_{\tau\_builtin}$ is

used to calculate k_τ, therefore these parameters are dependent. A combination of (B.2) and (B.5) were used to evaluate the error in (B.52).

$$I_{raise\_ideal} = \frac{\tau_{raise}}{k_\tau g_r} + I_{\tau\_builtin} = 0.2674 \pm 0.1277\ A = 0.27 \pm 0.14\ A \tag{B.51}$$

$$\delta I_{raise\_ideal} = \sqrt{(\frac{1}{k_\tau g_r})^2[\delta\tau^2_{raise} + (\frac{-\tau_{raise}}{k_\tau})^2\delta k^2_\tau]} + \delta I_{\tau\_builtin} \tag{B.52}$$

In this prototype, the operating voltage of the motor is irrelevant because a voltage regulator ensures the system operates at 12V. The rotating speed of the motor will stay consistent and the current will vary as mechanical power varies. Efficiency improvements can be calculated by only considering the change in current.

$$\%improvement = pct = \frac{I_{IR} - I_{raise\_ideal}}{I_{IR}} \times 100 = 46\% \tag{B.53}$$

The error propagation for this value is shown below. While the uncertainty of this process is still high, it still illustrates that there is significant power savings that can be expected by removing the waste friction.

$$\delta_{pct} = \sqrt{(\frac{1}{I_{IR}})^2\delta I^2_{raise\_ideal} + (\frac{I_{raise\_ideal}}{I^2_{IR}})\delta I^2_{IR}} = 32\% \tag{B.54}$$

B.5 Battery capacity measurement

The process outlined in Chapter 7.3.3.1 was used to determine the battery's charge capacity. A labVIEW program sent commands to a BK Precision 8500 Variable DC Load (VDCL) and monitored the current from the battery. The capacity measurement was taken by summing the product of the current measurement and the time between measurements.

$$C_{bat} = \sum I_{measured} \cdot \Delta t \tag{B.55}$$

The uncertainty of the VDCL's current measurement is 3 mA $\pm$ 0.001% of measurement. To be conservative, errors were considered dependent. Errors were evaluated using (B.4) for the product $I_{measured} \cdot \Delta t$ and (B.2) for the summation. There are too many datapoints to include a sample summation. A sample product calculation is included using the data from Table B.11.

$$I_{measured} \cdot \Delta t = 0.352As = 9.77 \times 10^{-5} Ahr \tag{B.56}$$

$$\delta(I_{measured} \cdot \Delta t) = \frac{\delta I_{measured}}{I_{measured}} \times (I_{measured} \cdot \Delta t) = 1.27 \times 10^{-3} As = 3.53 \times 10^{-5} Ahr \tag{B.57}$$

When summed, the final value is 2.35 ± 0.03 Ahr.

Table B.11: Relevant parameters for the battery capacity calculations.

Parameter	Symbol	Mean Measurement	Units
Bottom Rail Approximate Weight	$I_{measured}$	1.149 ± 0.00415	A
Diameter of blinds	Δt	0.306	s

Appendix C

Bouzidi's Method

A discussion on the solar cell five-parameter, equivalent circuit model is provided in Chapter 2.1.4. This model considers a solar cell as the equivalent circuit in Figure C.1. The output current I_t of this structure is the photocurrent I_{ph} less the amount of current flowing through the parallel diode I_d and shunt resistance I_{sh}. This can be quantified with the expression (C.1).

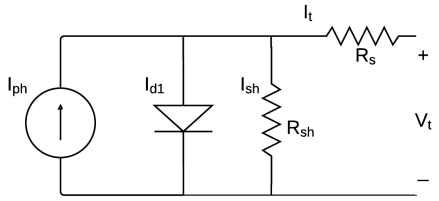

Figure C.1: Photovoltaic solar cell equivalent circuit [11].

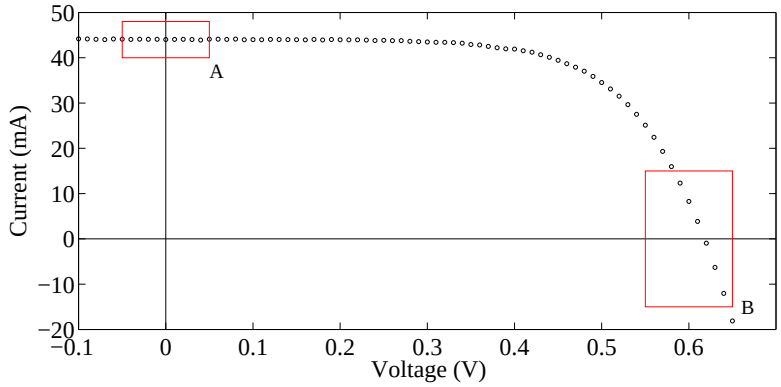

Figure C.2: Sample IV curve data taken from a solar cell. The box A highlights where I_{sh} dominates behaviour and the box B highlights where I_d dominates behaviour.

$$\begin{aligned} I_t &= I_{ph} - I_d - I_{sh} \\ &= I_{ph} - I_s(\exp\frac{q(V_t + R_s I_t)}{nk_bT} - 1) - \frac{(V_t + R_s I_t)}{R_{sh}} \\ &= I_{ph} - I_s(\exp\frac{(V_t + R_s I_t)}{nV_{th}} - 1) - \frac{(V_t + R_s I_t)}{R_{sh}} \end{aligned} \tag{C.1}$$

This performance can be observed by illuminating a solar cell and sweeping through a series of different terminal biases to get a sample dataset such as the dataset shown in Figure C.2. Bouzidi, Chegaar and Bouhemadou present a method of fitting the five parameters in the equivalent-circuit model to a set of IV curve data [16].

The process starts by defining several substitutions (C.2) through (C.5).

$$G_{sh} = 1/R_{sh} \tag{C.2}$$

$$I_{pA} = \frac{I_{ph}}{1 + G_{sh}R_s} \tag{C.3}$$

$$I_0 = \frac{I_s}{1 + G_{sh}R_s} \tag{C.4}$$

$$G_A = \frac{G_{sh}}{1 + G_{sh}R_s} \tag{C.5}$$

When these values are substituted into (C.1) a new form (C.6) is arranged:

$$I_t = I_{pA} - I_0[\exp(\frac{1}{nV_{th}}(V_t + I_tR_s)) - 1] - G_AV_t \tag{C.6}$$

During low voltage operation, the linear portion of (C.6) dominates as shown in box A of Figure C.2.

$$I_t = I_{pA} - G_AV_t \tag{C.7}$$

Data near the beginning of the trend can be used to solve for I_{pA} and G_A using a basic linear fit. The least squares method of line fitting is discussed in [54] and summarized in Appendix B. Knowing these parameters, an expression can be determined to evaluate the corrected current I_c that will be used in further substitutions.

$$I_c = I_t + G_AV_t \tag{C.8}$$

Consider device operation in forward bias near the open circuit voltage; box B in Figure C.2. At high bias level, the exponential term can be simplified by $(\exp\frac{(V_t+R_sI_t)}{nV_{th}} - 1) \approx (\exp\frac{(V_t+R_sI_t)}{nV_{th}})$. Rearranging the principle model equation to

solve for the corrected current yields (C.6).

$$I_c = I_{pA} - I_0[\exp(\frac{1}{nV_{th}}(V_t + I_t R_s))] \tag{C.9}$$

A method to evaluate R_s, I_o and n is possible by rearranging (C.9) to solve for V_t.

$$V_t = nV_{th}\ln(\frac{I_{pA}}{I_0}) + nV_{th}\ln(1 - \frac{I_c}{I_{pA}}) - R_s I_t \tag{C.10}$$

In the common form, this expression is:

$$f(I_t) = C_0 + C_1 I_t + C_2 \ln(1 - \frac{I_c}{I_{pA}}) \tag{C.11}$$

Using a least squares method of fitting the parameters C_0, C_1 and C_2 to the measured data forms the following system:

$$C_1 \sum_{i=1}^{N} I_{ti}^2 + C_2 \sum_{i=1}^{N} I_{ti}\ln(1 - \frac{I_{ci}}{I_{pA}}) + C_0 \sum_{i=1}^{N} I_{ti} = \sum_{i=1}^{N} I_{ti} V_i \tag{C.12}$$

$$C_1 \sum_{i=1}^{N} I_{ti} + C_2 \sum_{i=1}^{N} \ln(1 - \frac{I_{ci}}{I_{pA}}) + C_0 N = \sum_{i=1}^{N} V_i \tag{C.13}$$

$$C_1 \sum_{i=1}^{N} I_{ti}\ln(1 - \frac{I_{ci}}{I_{pA}}) + C_2 \sum_{i=1}^{N} \ln^2(1 - \frac{I_{ci}}{I_{pA}}) + C_0 \sum_{i=1}^{N} \ln(1 - \frac{I_{ci}}{I_{pA}}) = \sum_{i=1}^{N} V_i \ln(1 - \frac{I_{ci}}{I_{pA}}) \tag{C.14}$$

This system can be solved using Kramer's rule or by using a computational tool

like MATLAB. With the best estimates of C_0, C_1 and C_2, parameters for the solar cell model can be determined with the following:

$$R_s = -C_1 \tag{C.15}$$

$$n = \frac{C_2}{V_{th}} \tag{C.16}$$

$$I_0 = I_{pA} \exp(-C_0/C_2) \tag{C.17}$$

$$G_{sh} = \frac{G_A}{1 - G_A R_s} \tag{C.18}$$

$$I_{ph} = \frac{I_{pA}}{1 - G_A R_s} \tag{C.19}$$

$$I_s = \frac{I_0}{1 - G_A R_s} \tag{C.20}$$

Appendix D

Prototype Design Documentation

D.1 Design Objectives

The goals of this design exercise were to design a device that is capable of operating a roller blind autonomously. Additionally, the device must operate with energy neutrality, meaning its power consumption can be supplied from the energy production of a built in energy harvesting system.

This thesis discussed the design of the prototype's power system but omitted other design work. In particular, the thesis did not discuss: the design choices, how to recreate the prototype or its communication systems. This appendix describes in detail the design and construction of the prototype blind.

D.2 Design Overview

A motorized blind was designed and built to use a compact and simple solar energy harvesting system that is capable of sustaining continuous operation. A conventional

roller blind was modified to introduce automatic functionality. Key features of the original blind (fabric, mounting brackets, top cylinder) were maintained to ensure it behaves in a similar fashion to a non-motorized counterpart. Additional electronics were integrated to make the system capable of autonomous operation.

To keep track of all components, a principled design methodology was followed to reduce the complexity The design was modularized into design sectors of related components. Secotors are denoted as S_x where x is the unique identifying number of the sector. The identifying numbers were assigned according to the order that they sectors connected electrically and mechanically, S_x connects only to S_{x-1} and S_{x+1}. The exception to this rule are S_5 and S_6 which must have an additional electrical connection to the auxiliary electronics in S_8. The physical location of all sectors in the prototype is shown in Figure D.1, their electrical connections are shown in Figure D.2 and a brief description of each sector is included in Table D.1.

The original roller blind came with a bottom rail that functions to keep the fabric flat and smooth. This piece was redesigned to hold a wall adapter jack (S_1) for a backup charge and the solar array (S_2) for energy harvesting.

All other electronics (S_4-S_9) were inserted into the top of the blind, hidden from view. This was accomplished by using thin electrical components, including a thin DC motor and orbital gear set. Conventionally, the motor's exterior body stays stationary while the rotor spins. In this prototype however, the stator is fastened to the top cylinder and the rotor is connected to the wall. When energized, the rotor applies a force to the stationary wall forcing the stator and the rest of the top blind to rotate.

The energy harvesting system and the control electronics are located in opposite ends of the prototype, separated by the blind fabric. This textile was redesigned

with embedded wires capable of transmitting power between the two sections and is called S_3. This design requires little additional space, and allows the blinds to harvest their own power and to be recharged by inserting a DC power supply into the easily accessible bottom rail.

D.3 Prototype Operation

The unit is operated through a boot-up sequence where the user inserts a configured secure digital (SD) card. The SD card provides the blinds with the information they require it needs to boot such as which direction they must spin to move the fabric up or down or what the Wi-Fi network and password is. The prototype will operate on its own power, periodically check-ing its schedule by connecting to a server through the local Wi-Fi network. The user can update this schedule by accessing website from any device with a web browser. If the user would prefer an immediate change, they can pull the bead chain or press the button box in S_9 to send commands to the control electronics. LEDs and an emergency stop switch are mounted at the end of the top cylinder in S_8 where they are visible and accessible.

D.4 Sector Design

D.4.1 Sector 1: Wall Adapter Input

This component is a PCB that is designed to fit within the bottom rail and have a barrel jack that is capable of interfacing with an external wall adapter. Power from this component is conducted to the electronics in the top cylinder through the

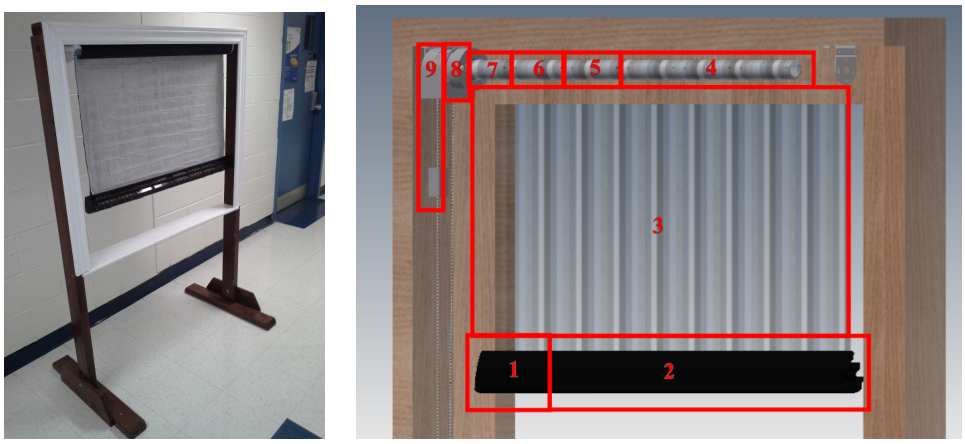

(a) (b)

Figure D.1: (a) Photo of the assembled prototype in a mock window stand (outside view). (b) Computer aided design (CAD) model of the assembly from the inside. Red overlay indicates a separate sectors. Note that the blinds and top cylinder are made transparent in (b) to make the embedded electronics enclosures more clear.

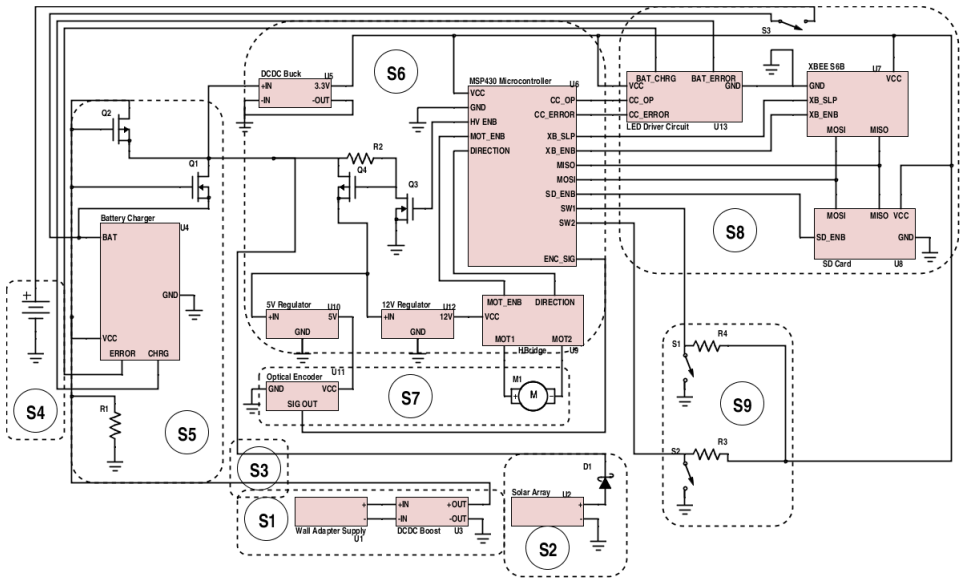

Figure D.2: Overview of the electrical systems. The prototype sectors are shown by the dashed rectangles and labeled with the solid circles S1-S9. Pink block represent electrical networks, and solid black lines show how these networks and the sectors themselves are connected in this design.

Module Number	Sector Description
1	Power Adapter Input. Power from a wall adapter is accepted and boosted to 30 V to limit copper losses.
2	Bottom rail with solar modules mounted at optimal angle.
3	Blind fabric with embedded conductive wires.
4	Battery pack.
5	Battery charging PCB and emergency-stop. The circuit can be broken here to stop operation if necessary.
6	Control circuitry responsible for preparing messages, controlling motor, keeping track of time and buffering voltage.
7	Motor, gear set and optical encoder.
8	Peripheral electronics. Wi-Fi is mounted here to avoid signal attenuation, SD card is accepted here so that user can inset it and LEDs are located here to be visible to user.
9	Roller Clutch. Must transfer a user's manual input into blind motion. Button box is integrated so that user can send signals to control circuit.

Table D.1: Description of all sectors.

wired blind. A XTW-SY-8 DCDC converter was also installed in this sector to boost the input voltage to 30 V. As long as the external wall adapter supplies power at a lower voltage, the DCDC converter can boost it to 30 V, this makes the design flexible and able to accept power from many adapters An additional advantage to the integration of this component is that the higher voltage reduces I^2R losses associated with conducting electricity through the wired textile. The boosted voltage of 30 V was chosen as it was the highest voltage that can be used in the system without operating outside the recommended range of the other circuit components.

D.4.2 Energy Sectors (S_2-S_4)

The design of the bottom rail (S_2), the electronic blind (S_3) and the battery pack (S_4) are discussed in Chapter 4.2 as they pertain directly to energy systems that are discussed in the thesis. This chapter should be referenced for details on the design of these sectors.

D.4.3 Sector 5: Battery Charging PCB and E-Stop

This sector was originally designed just for the the battery charging PCB. The detail drawings for this section are shown in Appendix D.7.2. This PCB is designed around an LTC4011 IC which can control an external power source to recharge a series stack NIMH battery pack. A switching network on the PCB is designed to ensure the load (S_6-S_9) receives continuous power flow. When an external power source is connected, the battery is disconnected from the load as it is recharged and the external supply is used to power the load. This PCB also connects the positive terminal of the solar array to the battery pack allowing a trickle charge. The battery

pack's blocking diode protects the solar array from being damaged when an external supply is connected.

After assembling this sector, it was realized that there was no emergency stop (E-stop). This is necessary for a prototype. A perfboard circuit was designed and assembled that routes power from the battery through a switch mounted in the peripheral electronics (S_8).

D.4.4 Sector 6: Control Circuit

D.4.4.1 Load Power System

Different components within the blinds electronics require different voltages. All components that are always powered require 3.3 V. The motor and its controller require 12 V to operate and the optical encoder requires 5 V. The supplied power voltage will fall between the range of 10.9 V and 30 V (from the battery pack that is almost dead to the AC Adapter). There are two main, economical mechanisms that can be used to switch between DC voltages:

1. Linear voltage regulators take a high voltage and linearly modulate the conductance of the path of the power to get the correct output voltage. This means they act as a series variable resistor, whose resistance varies according to the current that passes through them so that the output voltage is stable. These devices require the input voltage to be higher than the regulated voltage. By passing power through a series resistor, they waste power as heat [56].

2. Switched converters use an analogue or digital switching circuit to temporarily store energy in a medium (capacitors or inductors). By switching at the correct

frequency, the voltage of the output can be controlled. This mechanism can be used to raise (boost) or lower (buck) the output voltage relative to the input. Since power is temporarily stored, these devices are typically more efficient that voltage regulators, however the necessity for large capacitors and inductors can increase the size of these devices [56].

Conserving energy is the number one priority in this application to extend the life of the device and better utilize available solar power. Second to that concern is space. The electronics that are always powered consume more energy over the course of a day in standby, so a DCDC buck converter (DSN2596 step down converter) was chosen to supply these loads. The 5 V and 12 V signals were generated by linear voltage regulators in order to fit all the components on a single PCB. To minimize power loss, a switching circuit was designed to ensure they are only turned on when the motor is running.

D.4.4.2 Microcontroller Selection

The selected microcontroller had to have: compatible voltages to other system components (the Wi-Fi chip, XBee S6B has a voltage of 3-3.6 while the optical encoder operates at 5 V), an easy programming interface and a dip construction for modular prototyping. The Texas Instruments (TI) MSP430 programmed using a TI launchpad meets these requirements. It operates at the lower range of voltage (such as the XBee), and a voltage divider can be used to read signals from the encoder. TI's code composer suite and Energia package provide simple coding and debugging. This microcontroller is available in dip.

D.4.4.3 PCB Design

The design documentation for this sector is shown in Appendix D.7.3. This board was designed to be thin and narrow and to fit within the tight enclosure space. It has several connectors including two 1x8 header plugs that send signals through a ribbon cable to the peripheral circuit (S_8). This is necessary because the microcontroller located on this board coordinates the electronics that are mounted on the peripheral circuit S_8.

D.4.5 Sector 7: Motor Assembly

D.4.5.1 Motor Selection

Considering an initial estimate of the bottom rail weight and radius of the top cylinder, the required torque was calculated to be: 0.2943 Nm. After constructing the demo, an actual weight measurement was taken and the blind was found to weigh 1.4 kg and the radius with some fabric wrapped around the blind was measured as 2.6 cm. This was used to update the torque calculation to 0.357 Nm.

Conventional permanent magnet brushed DC motors are high speed with low torque. Adding a gearbox can change the rotation to a lower speed with a higher torque. Initially a Phidgets 3263E_0 was sourced because it has dimensions appropriate to fit inside the top rail, its input voltage and current were within the ability of the battery pack, the built in orbital gear set provided adequate torque (0.304 Nm) the assumed load and its stall torque (1.78 Nm) is significantly higher than what is required. This product also came with a built-in optical encoder.

Initial tests in the prototype were unsuccessful. An additional source of friction was introduced to prevent the blinds from slipping when not in use which means

the motor must provide more torque to raise the blinds. A Phidgets 3264E_0 motor proved to have enough torque to operate the prototype. This is the same as the previous motor but has an orbital gear set with a larger gear ratio, increasing its rated torque (rated torque 0.833 Nm, stall torque 4.9 Nm).

D.4.5.2 Mechanical Mating

The rotor mates with a rigid axle. The torque provided by the motor pushes along the rotor, but since the rotor is mated with a rigid axle, the motor body rotates.

There are two challenges with this design:

1. Mating the rotor with an anchored axle to push against.
2. Mating the motor body to the rest of the blinds so that the blinds move with the motor.

A 3D printed part was made that slips onto the motor's rotor and uses its flat to become locked in place and is further secured with an 8-32 screw. This part is referred to as the motor axle adapter and is specified in Figure D.60. This printed adapter is bonded to a 0.25" steel axle rod (specified in Figure D.61) using the same mechanism.

The motor body is fastened to to the blinds through a separate 3D printed part called the motor bracket which is specified in Figure D.59. This part has holes made in it that allow M3 screws to fasten it to the front plate of the motor. The piece has been designed with grooves that mate with the extruded tabs of the top rail so when the motor and it rotate, so does the top cylinder. This piece is designed with a hole through the center so that it rotates with the motor while without rubbing against the stationary rotor.

The motor is mated to its enclosure through a custom built friction clamp made from steel strapping. This friction clamp also holds tension on the ribbon cable to reduce mechanical wear on the cable as it is inserted or removed.

D.4.6 Sector 8: Peripheral Electronics

All electronics that need external access or must be accessible to the user are mounted here. This includes the slot to install the SD card and the E-stop button that disconnects the battery from the load circuitry. Components that send signals requiring minimal attenuation are located here such as the Wi-Fi chip whose RF signal would be blocked if placed in the aluminum top rail, and the LEDs whose light must be visible by the user. Finally the connections to the button box in S_9 are also included in this component.

D.4.6.1 Wi-Fi

Wi-Fi (IEEE 802.11) was chosen to act as the system's communication protocol. Conventional motorized blind prototypes use proprietary protocols that require the installation of a networking box to coordinate the devices. For example, Somfy products use a custom radio application that requires a hub be plugged into the user's home router. Hunter Douglas PowerView operates with a hub and signal boosters installed throughout the house. By connecting the blind unit directly to the home Wi-Fi network, these additional components can be avoided. An XBee S6B was chosen as the component to provide this networking capability.

D.4.6.2 LED communication

Three colour (red, green and blue) RGB LEDs were used so that messages could be conveyed to the user by illuminating different colours. The enclosure was assembled out of clear PLA so that the LEDs would be visible from the outside. The list of signals are included in Table D.2.

D.4.6.3 SD Slot

A method of programming the blinds was needed and an SD card were chosen to convey the extra information. There are several reasons for this choice:

- SD cards have a slim profile.
- They can be easily programmed from many PCs that have SD card readers built in.
- They can be read from the MSP430 with a readily available library (PetiteFS).
- They operate within 2.7 V and 3.6 V and are compatible with the MSP430.

D.4.7 Sector 9: Roller Clutch

Either by pressing a button or by pulling the beaded chain, this is the sector the user interacts with to move the blind's position. This assembly has a few other technical purposes. An anchored axle runs through this part to provide a stationary reference for the motor to push against. The assembly of this component introduces a variable amount of friction to prevent the blinds from slipping.

This assembly accomplished these goals through a unique manufacturing mechanism. The enclosure was divided into slices that could easily be fabricated using

a 3D printer. This is necessary because the available 3D printer is incapable of assembling a complicated part with all the required cavities. Additionally, this stacked manufacturing method allows access to individual cavities so that moving gears can be installed. The entire assembly is shown in Figure D.47.

The button box is a simple box with a cavity for some simple electrical buttons. Signals from the buttons are relayed to the peripheral circuit through a ribbon cable. The ribbon cable winds and unwinds around the wire wheel in Figure D.49. This wheel is placed in a cavity between clutch case B and C and is designed to be wide enough for the ribbon cable to be completely wrapped.

The beaded chain from the original mechanical blind is used. The gear in Figure D.50 was designed so that the beads would fit into its grooves and linear pulling would be translated into rotation.

The wire wheel, beaded chain gear and the electronics wheel (the peripheral electronics), must all rotate at the same time. The clutch is designed with space so that two screws can be inserted into all of these components and keep them rotationally locked.

D.5 Software Design

Software was designed and coded to gather information, and operate the prototype. The design of this code merits discussion.

D.5.1 Configuration Assistant

An SD card provides the data needed for the microcontroller to bootup. A program was written to prompt the user for relevant information. This program is called the configuration assistant.

This application was coded using Java because it is commonly available software that is supported on many devices. It also has strong support for graphical user interfaces (GUI) that are easy to navigate.

D.5.1.1 Graphical User Interface Design

The design of the GUI was based on installation wizards commonly used in the Microsoft Windows environment. It operates by displaying a window of static dimensions on the screen and presenting the user with a sequence of prompts. Each prompt contains a single step that the user completes and the user can navigate between prompts by clicking buttons labeled "next" or "back" located in the bottom right corner.

The order of the prompts is shown in Figure D.3 (a). Basic geometry information is obtained so that the blinds can raise and lower without damaging the unit. The user is given the choice to have blinds that connect to the internet and receive remote schedule and timing updates, or they can choose to not give network information if Wi-Fi is not available. The user also has an option to program a schedule directly into the blinds on bootup. For each prompt, visuals are implemented to aid in user comprehension, making it easier for the user to understand the questions and interact with the program. Some examples of how these graphics help are shown in Figure D.3 (b) and (c).

Colour	Message
Yellow	SD Card is being read at the start of the program
Green	Motor is being operated, encoder is measuring motor movement or XBee communication
Blue	Battery is being charged
Solid Red	Error charging battery
Flashing Red	Error with control circuit

Table D.2: List of messages relayed through the LED colour circuit.

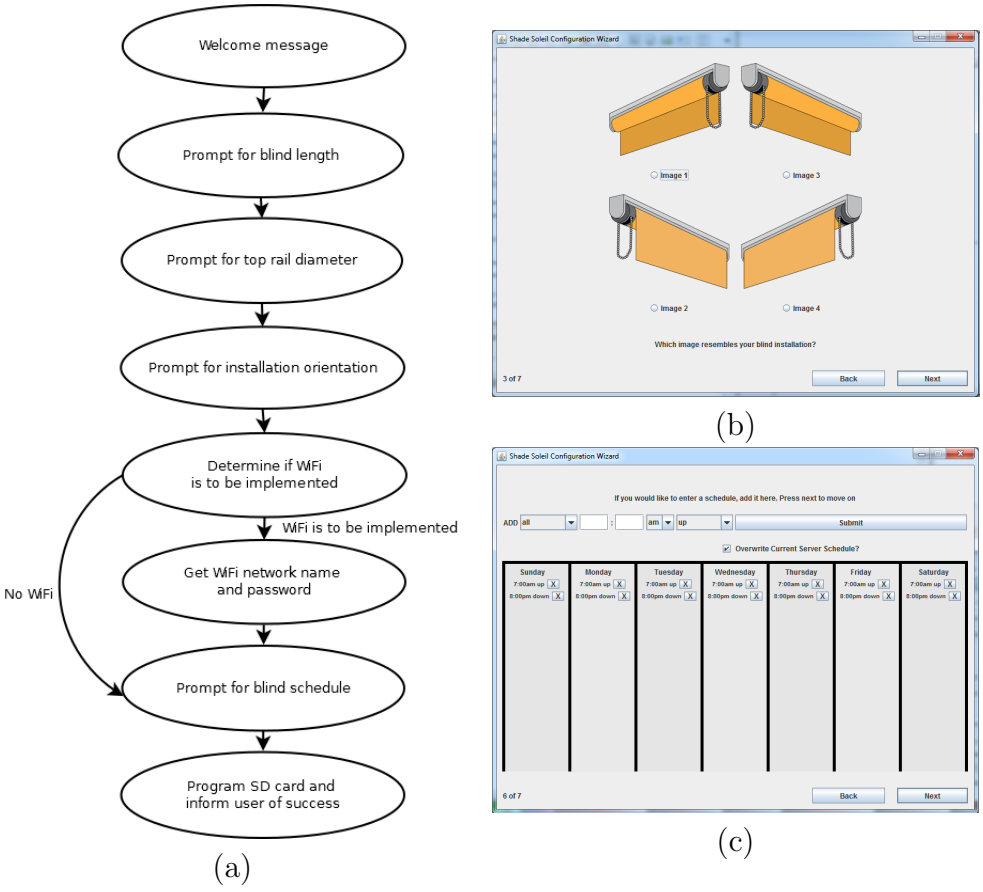

Figure D.3: (a) Flowchart illustrating the order of prompts in the configuration wizard. (b) An example prompt that shows how the configuration assistant collects information on the installation in order to determine which direction to spin the motor. (c) An example prompt showing how the user can manually enter a schedule on the configuration assistant.

D.5.1.2 File Transfer

The program saves the collected information to a file called config.txt on the SD card. The bytes in this file are reserved in specific blocks as illustrated in Figure D.4. Table D.3 describes the purpose, formatting and and example of each block. The size of each block is chosen based on a reasonable worst case length for each field. If a field is too long or is unused (for example the Wi-Fi password if the user elected to leave the blinds disconnected from the internet), the extra space is padded with zeros. A final challenge in this field is the timing of a disconnected blinds. As the SD card has no internal timing mechanism, it is assumed that the user will take 1-2 minutes to remove the SD card from their computer and install it in the blind unit. Just before the configuration assistant writes the config.txt, it reads the current hour and minute from the computer and adds an extra 2 minutes. When the blinds boot up, they will read byte block F and assume that is the current time until they can connect to the internet and get the real time.

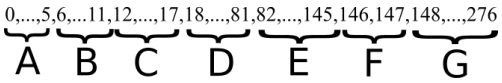

Figure D.4: Bytes inside of the config.txt file used to program the microcontroller. Each number represents a numbered byte within the file. Groups of bytes are labeled in a "byte block" that is described in detail in Table D.3.

Byte Block	Description
A	ASCII representation of blind length in mm. Leading zeros are ignored. For example: 0x00 0x00 0x00 0x00 0x39 0x30 0x30 represents 900 mm.
B	ASCII representation of blind top rail diameter in mm. Leading zeros are ignored. For example: 0x00 0x00 0x00 0x00 0x00 0x37 0x30 represents 70 mm.
C	ASCII representation for motor direction vector. Leading zeros are ignored. For example: 0x00 0x00 0x00 0x00 0x00 0x00 0x31 represents one of the two possible vectors
D	ASCII representation for WiFi network name. Leading zeros are ignored. For example: 0x00 0x00 ... 0x00 0x57 0x69 0x46 0x69 represents the network name "WiFi"
E	ASCII representation for WiFi password string. Leading zeros are ignored. For example: 0x00 0x00 ... 0x00 0x57 0x69 0x46 0x69 0x70 0x61 0x73 0x73 represents the network name "WiFipass"
F	Binary representation of microcontroller local timestamp (number of minutes since midnight, Sunday). For example: 0x02 0xD0 would represent a timestamp of 720 minutes. This corresponds to noon on Sunday.
G	This is the microcontroller schedule. It holds information on the last time the schedule was updated, repetitive scheduled events and individual events. The actual format of this schedule is discussed in the control circuit scheduler documentation.

Table D.3: Detailed description of all byte blocks as displayed in Figure D.4.

D.5.2 Microcontroller Code

Basic code for the MSP430 was initially developed using the TI Energia sketchpad which uses the same simple programming syntax as Arduino Wiring. As more complex functions and debugging capabilities were needed, the code was imported into TI Code Composer Suite (CCS). CCS offers advanced debugging capabilities such as the ability to step through lines of code and view memory as the microcontroller runs. CCS also supports complicated data structures like objects and open source function libraries.

As the code was imported into CCS, it was modularized according to function. This was accomplished by building objects with unique attributes and methods that could be called by other objects. As the microcontroller fundamentally operates in an imperative format, a main loop cycles through each object giving them the opportunity to respond to interrupts or timing events. Objects were grouped into two categories. Driver objects directly interact with output pins for specific functions such as operating external LEDs or communicating over Wi-Fi. Administrator objects keep track of timing events and direct drivers to operate when appropriate.

The MSP430 has limited memory resources. One programming challenge was memory overflow. The device has 512 bytes of flash RAM, and running over that limit causes undesirable behavior. Certain coding conventions were not followed in order to meet the memory constraints. For example, driver objects refer to the MSP430 pins through preprocessor constants rather than private variables. Likewise, the SD driver and the Wi-Fi driver share message buffer space in a coordinated fashion.

D.5.2.1 Hardware Considerations

All driver objects interact with specific control pins that are connected to external components. The PCB documentation in Section D.7 can be referenced for more details on hardware connections. In general, voltage inputs to each pin are held at a constant value using a pull-up or pull-down resistor based on the pin's application. Small 0.1 μF capacitors are added in parallel to the pullup resistors on the switch inputs to debounce the signal and prevent the microcontroller from detecting several false events. A voltage divider is connected to the encoder input to lower the encoder's 5 V signal to a safe 3.3 V signal.

D.5.2.2 LED Driver

The LED driver object controls the signals going to an LED driving circuit in the peripheral circuit. When the object asserts a low signal, a switching circuit sends power to the LEDs to turn them on. The microcontroller can only interact with two LEDs, the red and green LEDs (blue is reserved for charging). It can turn either LED on or both at the same time. It may also interact with the schedule administrator object to keep track of time. It uses this reading to flash the LED at a frequency of 1 Hz. Due to the possibility of multiple interactions occurring at the same time (for example the motor and XBee both attempt to operate the LEDs), there is a small level of control used in this object through a lock function. The LEDs can be "locked" and will ignore all future prompts to change the LED colour until the driver is "unlocked". This feature is useful for internet communication where the response time is unknown and the LEDs must be kept lit to indicate ongoing communication.

D.5.2.3 SD Driver

The SD driver uses an external library called petite FAT file system (pfatfs) [57] to read the SD card. When initiated, the driver checks to see if an SD card's CS pin is high indicating that an SD card is present. If this signal is not present, or if this signal is grounded, the microcontroller assumes there is no SD card installed or it has been removed. Without the SD card present, the device assumes its external configuration has been changed and shuts down to prevent damage. This shutdown is accomplished by restarting the MSP430's watchdog timer and allowing the circuit to timeout.

When the SD card is read, the code will read a chunk of bytes corresponding to the groups labeled in Figure D.4 and convert it into a useful form. The SD driver passes this information on to the relevent objects, for example the Wi-Fi password is sent to the XBee driver.

D.5.2.4 Motor Driver

This driver controls motor operation. It tracks blind height using a state variable that is configured on bootup. When the SD card is read, information on the blind height and the direction of spin is written to the motor driver. The motor driver will not operate the motor until the SD card has been read to avoid spinning the prototype in the wrong direction.

This object keeps track of the motor's height through interrupts received by its encoder pin. The interrupt service routine is designed to respond quickly without overloading the microcontroller. When an interrupt is detected, the motor driver is not loaded, instead a globally accessible counter is incremented. When the motor

driver is called from the main loop it checks the counter and uses its value to update its own state variable tracking height. Should the state variable exceed a maximum value or run below 0, the motor is turned off. The encoder is left alone for a few seconds after the motor is shut down in order to keep track of the blinds if they slip down after the motor is deactivated.

The motor can be told to go up or down through two mechanisms, the button box, or a scheduled event. If the blinds were raising or lowering according to schedule, and the user decided they didn't like this, they would indicate their desire to change direction by pressing a button. Therefore, the direct method of input has precedence over scheduled events. When the motor driver is sent a signal to raise or lower, there is an associated priority. Scheduled events have a lower priority than events that are directed by the user. Additional, when the user inputs a signal using the button box, they can press the button twice within a span of half a second to indicate that they want the motor to completely raise or lower the blinds. This option is faster than forcing the user to wait and hold a button down as the blinds completely raise or lower.

D.5.2.5 XBee Driver

Communication with the XBee occurs along the SPI lines and messages must be configured according to the XBee's frame based application programming interface (API) [58]. Functions have been developed that allow the microcontroller to set the Wi-Fi network and password, set the XBee to sleep and transmit messages to the raspberry pi server. When the microcontroller needs to send information, an administrator object will fill one of the shared memory buffers with the correct characters

that the python server application will recognize. This buffer is passed to the XBee which tacks on a header and a tail to make the message recognizable to the XBee. When messages are not being sent, the microcontroller sets the XBee to sleep. Due to an unknown bug, the XBee doesn't immediately fall asleep unless a software restart command is issued. There are a series of delays introduced in the code using the delay_cycle function. This is to give time after a message is sent for the XBee to process and respond. It is possible that the XBee could send a message and experience an extended delay before receiving an internet response. Rather than freeze the program while waiting for the response, control is returned to the main program allowing the blinds to control other system operations such as motor events. When the main loop returns control to the XBee driver, it will check and handle any messages that have been received in the interim. The driver tracks how long it has been waiting for a response and will eventually give up and return an error because it is possible for the server or network to go down.

D.5.2.6 Object Administrator

This object contains static references to all other objects and shared buffers. The static declaration tells the code to define variable space that is common regardless of how many objects are defined. In this code, no actual object administrator is ever initialized because only the static fields are referenced. On system boot-up, all other administrator or driver objects must copy a reference to itself into the correct static field so that other objects may send it a message.

D.5.2.7 Client Administrator

This Administrator ensures that the client responsibilities of the communication protocol outlined in Chapter D.5.3.5 are followed. It prepares messages according to this custom communication protocol, sends the messages to the XBee which prepares them into packets that can be sent over the internet. The Client Administrator maintains a state variable keeping track of what messages have been sent and how to process the server response. If too many failed communications occur, it goes into an error state where it modifies the schedule to lower the frequency that internet messages are attempted to save power and it flashes a red LED to communicate the error.

D.5.2.8 Schedule Administrator

This administrator maintains the schedule, the current time and initializes events when they are required. The schedule is maintained in the microcontroller's flash memory (registers 0x1040-0x10C0). In the event that the blinds lose power, the schedule data in the flash memory will not be lost. Storing the schedule here also prevents the data from being saved in the stack which has limited free space. The microcontroller tracks time using its internal digitally controlled oscillator clock with interrupts being generated at a frequency of 490 Hz. The microcontroller counts these interrupts to keep track of the number of minutes since midnight on Sunday. Every Sunday, the timer is rolled back to 0. If the time drifts by more than a minute, it will be corrected the next time the microcontroller communicates with the server.

The registers are divided into several blocks with different purposes to ensure that the blinds can operate reliably and demonstrate different methods of scheduling

events. The first four words (registers 0x1040-0x1047) are reserved for the Unix timestamp of the last schedule update. If the blinds have three different schedules, one in the server, one loaded in the memory and one on the SD card, it can refer to the Unix timestamp to determine which schedule is the most recent. The next 26 words (registers 0x1048-0x1080) are reserved for repetitive events. A repetitive event requires 2 words, the bits are used according to Figure D.5 and Table D.4. The last chunk of registers (0x1080-0x10BF) are reserved for unique events. The use of the bit chunks is changed and is described in Table D.5.

On bootup, a schedule is read from the SD card and loaded into the memory. As the other objects in the microcontroller communicate with the server, they can request to modify the schedule in this administrator object. Whenever the schedule is rewritten, the microcontroller will force the first repetitive event to be a Wi-Fi message event, overwriting whatever was there previously. It will operate every 5-minutes unless there is a communication error at which point it will change to once an hour.

Whenever the timestamp counter is incremented, the microcontroller will check if an event is scheduled to happen. If so, it will direct the appropriate driver or administrator object to run the event. Once completing this task, the schedule administrator will search the flash memory for the next soonest event.

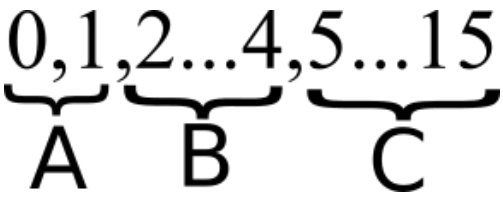

Figure D.5: Byte order of repetitive events.

Table D.4: Description of the byte groups illustrated in Figure D.5 when referring to the repetitive memory storage.

Byte Group	Description
A	The first two bytes represent the type of event. 0b00 is null, 0b01 is a Wi-Fi check-in, 0b10 is blind lower event and 0b11 is blind raise event.
B	The next three bytes are a code representing the frequency of the event. In the current code, 0b111 represents an event that occurs every day, 0b110 is an event that only occurs on weekdays (not weekends), 0b010 is an hourly event, 0b001 is every five minutes and 0b000 occurs every minute. All other patterns do not have an assigned frequency.
C	The remaining 11 bits are used to represent an event offset. If a motordown event is to occur every day at 7:00pm, the offset would be 0d1140 or 0b10001110100.

Table D.5: Description of the byte groups illustrated in Figure D.5 when referring to the non-repetitive memory storage.

Byte Group	Description
A	The first two bytes represent the type of event. 0b00 is null, 0b01 is a Wi-Fi check-in, 0b10 is blind lower event and 0b11 is blind raise event.
B and C	The remaining bits are reserved to represent the minute since midnight on Sunday that the even is scheduled to occur.

D.5.3 Raspberry Pi Server

One of the goals of this project was to provide the user with a method of updating their schedule from a web portal. In order to describe how this was accomplished, the basics of internet communication must be summarized. There are three fundamental components of the Internet:

1. A client that requests information.

2. A network through which data is exchanged.

3. A server that provides information.

These roles are not strict. When doing online banking for example, a server can ask the client to provide information that is used to validate their identity. By providing instructions on how to draw the webpage in the user's browser, and populating it with the user's data such as their account balance, the server would provide the majority of the information.

For this project, there are two unique clients. The user can use their personal computer to login to a website and provide updates to their blinds' schedule and the blinds themselves must also be able to request the updated schedule from the server. As it is the standard supported by the Wi-Fi Alliance, it is assumed that the user has access to a wireless network encrypted using WPA2 [59]. This section will discuss the design of the server computer that allows a user to load a webpage on their browser and allows the blinds to receive updated schedules.

D.5.3.1 Design Choices

A Raspberry Pi with Raspbian Wheezy installed and configured with packages needed for a server (MySQL, SCP, RDP, Apache) was available at the start of this project. While it cannot handle the volume of traffic expected at a server bank, it can communicate effectively with the few clients that might connect while a demonstration is happening. The computer was assigned a permanent McMaster IP (130.113.54.158), which the URL "www.shadesoleil.mcmaster.ca" is directed to. It was configured to receive traffic from sources outside of McMaster's local campus. When not in use, the Pi is turned off to prevent malicious traffic. Programming of all active server programs are completed by logging into the Raspberry Pi using Window's remote desktop connection.

Several programming languages are used together for the webpage. HTML is used to outline the position of text, links and other images when a web browser navigates to it. Javascript is used to specify interaction on the client-side (typing characters, sending scheduled events to the server). PHP is used for server side interaction (accessing information from the database, issuing cookies). Rather than use a programming environment, code was written in a notepad++ and tested by loading webpages.

All scheduled information on the server is stored in a MySQL database. This database was configured using the default terminal application included with the installation of Raspbian Wheezy.

In order to communicate with the blinds, Python was chosen. It is a versatile language with easy byte manipulation. The Python code was written using the default IDLE environment. Initial testing was performed by writing a test Python client

before moving to test packets sent from the microcontroller circuit.

D.5.3.2 Webpage GUI design

The purpose of the webpage is to demonstrate functionality rather than aesthetics. Only four webpages are accessible and the way a user would navigate between them is illustrated in Figure D.6. The server ensures that only the true owner may access their blinds by requiring a user name and login. Figure D.7 shows a sample webpage following a successful login.

The web portal was constructed in a modular fashion. Shared javascript functions were written in a single file. A uniform formatting style was maintained throughout the document by using a Cascading Style Sheets (CSS) file.

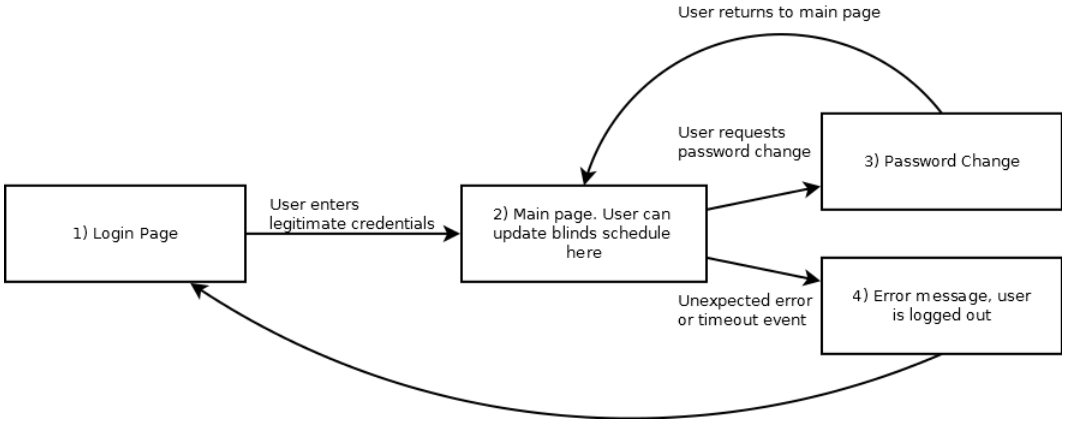

Figure D.6: Flowchart illustrating how a user would navigate between available web pages.

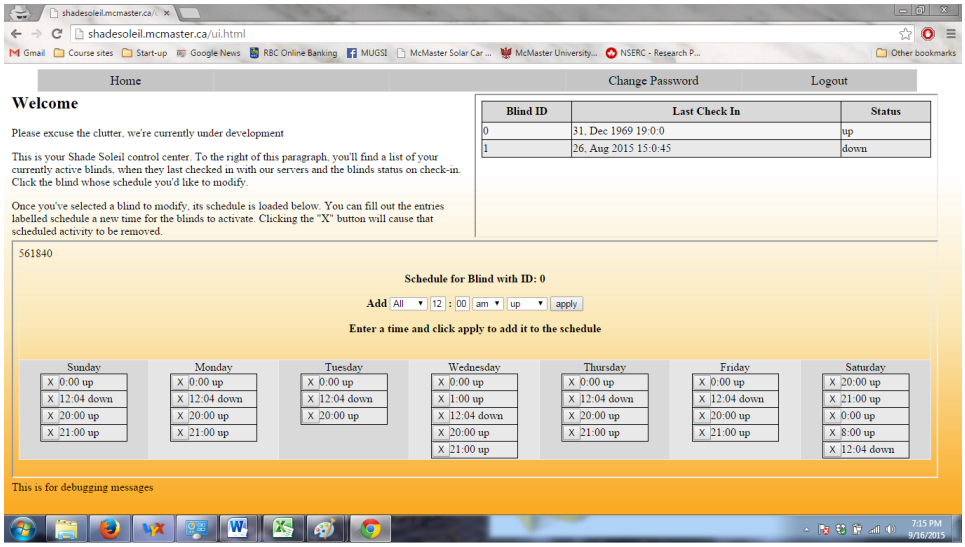

Figure D.7: Screenshot of the main page a user would access (number 2 in Figure D.7). The top left of the screen provides an explanation on how to use the page. The top right is a list of available blind units, sometimes referred to as the unit viewer. The bottom is the schedule for an individual blind, this section of the screen is sometimes called the schedule viewer.

D.5.3.3 Client-Server Interaction, Web Portal

When a user loads a webpage in their browser, they are really connecting to a server and loading graphics according to an HTML file stored on the server. Javascript can be embedded in the HTML file that will provide instructions to the client computer to do actions. The server could send an HTML file that displays a calculator and Javascript could tell the client what mathematical operations are to be performed when different buttons are pressed. Javascript forces the computing to be on the client computer, not the server.

In some cases, the server needs to do computing. For example, the server could access specific information from an internal database. PHP: Hypertext Preprocessor (PHP) can instruct the server to run instructions to access the requested information and send it back to the client. MySQL is used to store data in this server. PHP can also be used to load a small temporary file onto the client called a cookie that contains extra information.

The client and server computers must be able to send messages between each other, and they must do so in a way that the user's Javascript and the server's PHP will understand. When the user indicates an action is to be taken, Javascript initiates a message to the listening PHP script using a $_POST array. This array will pass a request string so that the PHP script will know what the client is asking for, any other variables that are needed to process this request are also passed along. When multiple variables are being returned from the PHP server, they must be packaged using the JSON format. Figure D.8 shows which programs are used on which side of the communication, in a general sense.

For this website, a communication protocol was developed, where the client will

initiate a message by sending a variable called “req” with an attached string. The PHP script checks the client’s cookie to ensure the session is still valid then responds with a specific action. Table D.6 summarizes the possible requests the client can make to the server. An example of the messages passed in a complete user interaction on the website is shown in Figure D.9.

Table D.6: List of possible requests and actions.

Request String	Description	Parameters	Response Variables	Finishing Action
add_item	Add a specific scheduled event in a given blinds' schedule	Blind ID number (int), time of event (int), up/down (int)	"OK"	Add the item to the schedule viewer
add_many _items	Add a specific event at the same time, every day of the week to one blinds' schedule	Blind ID number (int), time of event (int), up/down (int)	"OK"	Add all the items to the schedule viewer
delete_item	Delete a specific scheduled event in a given blinds' schedule	Blind ID number (int), time of event (int)	"OK"	Remove the specific event from the schedule viewer
logout	Terminate the user's session	None	"OK"	Remove session cookie and redirect user to end page
schedule	Request all scheduled events for one blind unit	Blind ID number (integer)	An array of scheduled events (response encoded in microcontroller schedule format)	Populate the schedule viewer with this information
status _dump	Request blind ID, last communication time and up/down state for all blinds owned by user	None	An array of info including the blinds owned by the user, blind ID, last communication time and up/down status	Populate the unit viewer with this information
update_ password	Update the user's password in the database	Old password (string), new password (string)	"OK" if successful or a string explaining the user's error	Load a message informing user of successful change or the encountered error
verify_pwd	On login, ask the server to check the validity of password	Username (string), password (string)	"OK" if accepted. If not, an error string is sent	If credentials are valid, the main webportal is loaded. If not, the error message is shown

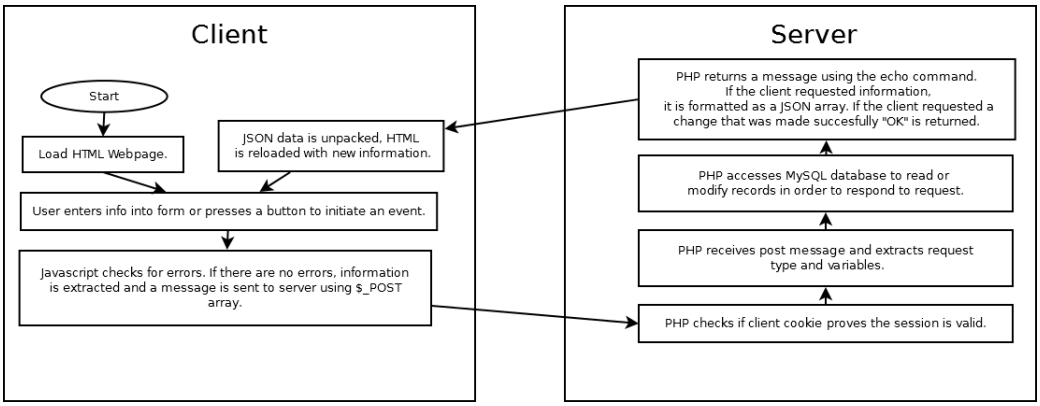

Figure D.8: The general flow of the webportal. Interaction is cyclic and hinges on user input. Once a user presses a button, javascript analyses data, sends it to the server where php prepares a response. Java unpacks the response and redraws the HTML page while waiting for user input.

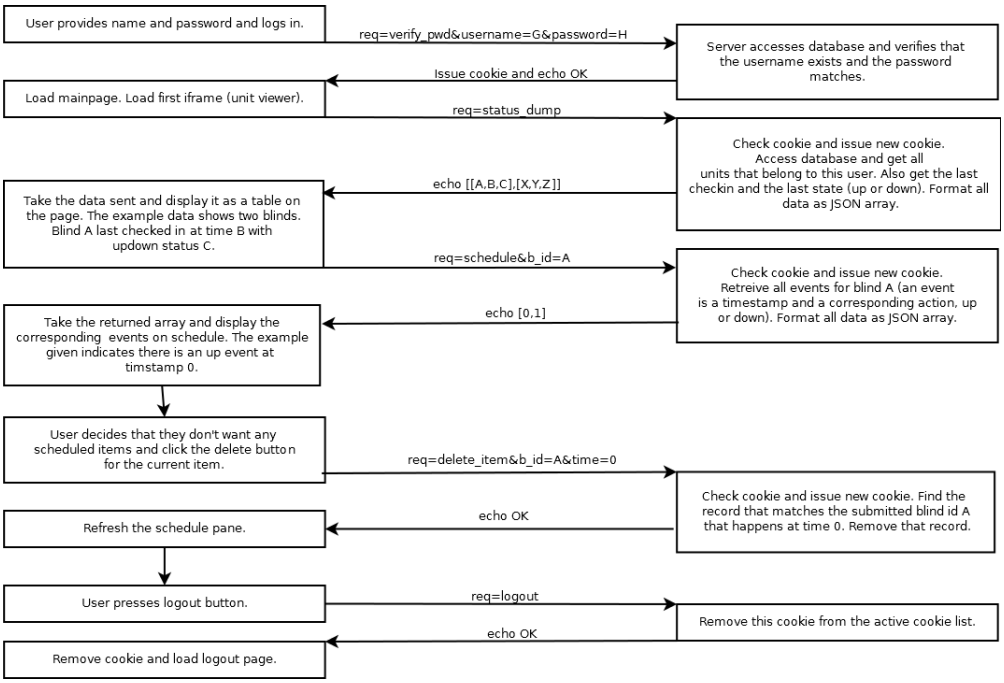

Figure D.9: An example of a client server interaction diagram. In this image, a user logs into the web portal, views a schedule, removes a scheduled item and logs out.

D.5.3.4 Client-Client Interaction, Web Portal

The main webpage shown in Figure D.7 is a main HTML web page with two embedded web pages (the unit viewer and the schedule viewer) made using iframe labels. The unit viewer displays all units owned by the user and the schedule viewer displays the schedule for a single unit. When the user clicks a different blind in the unit viewer, the corresponding schedule must be displayed in the schedule viewer. Since these two iframes are independent processes, they must pass a message between each other. On a mouse click event in the unit viewer, a javascript function launches and uses the postmessage function to send a message to schedule viewer. The schedule viewer has a listener that waits for a message sent from the same website (filtering out malicious messages) and responds by loading the requested schedule. This interaction is done on the client-side only.

D.5.3.5 Client-Server Interaction, Blinds

The blinds must be able to communicate with the server to get notified of changes to their schedule. The standard languages and methodologies of a personal computer (HTML, Javascript, PHP) are not appropriate for this case because the blinds do not display a graphical web page with embedded links. For the blinds, the goals are to:

1. Develop a protocol that can run in parallel with the web page.
2. Design the protocol to exchange small lightweight messages that can be processed on the MSP430's limited memory.
3. Design the protocol to minimize power consumption of the blinds.
4. Design the protocol to work given a user's home network situation.

Because of python's simple TCP and IP functions, its decent development environment and its ability to manipulate individual bytes, it was chosen to program the server program to address objectives 1 and 2. The protocol was designed to run in short bursts every few minutes to address issues 3 and 4. These short bursts mean the control circuit radio in the blinds is usually turned off, saving power. The short bursts are initiated by the blinds. Since the blinds create the connection with the server, the user's router or modem's built in firewalls will not filter out the traffic. These firewalls can prevent the server from pushing data on the blinds.

The short bursts have been designed to convey only the necessary information. Figure D.10 illustrates the length of a packet and the order in which bytes are grouped while Table D.7 describes the purpose of each byte group. This protocol was designed for future use and expansion, for example, a full word is reserved for blind IDs allowing for 65536 units before serial numbers will run out. The types of actions that can be specified by this communication protocol are discussed in Table D.8 while the python server program that responds to these requests is summarized by the flowchart in Figure D.11.

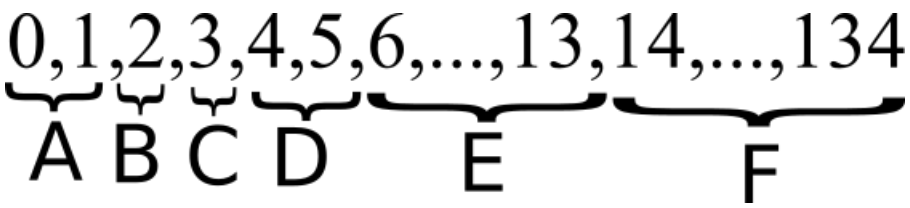

Figure D.10: Bytes in a messages exchanged between the Pi server and blinds' client program. The numbers represent byte number. Bytes are grouped together based on what they represent and are discussed in the following table.

Table D.7: Description of the byte groups illustrated in Figure. D.10

Byte Group	Description
A	The first two bytes are reserved for the blind's serial number to identify what unit is sending the request.
B	The third byte is used to describe the message. It is referred to as request type.
C	The forth byte is for blind height index. This byte is currently not supported, but the intention is to convey information about how high or low the blinds are currently.
D	The fifth and sixth byte are reserved to convey the local timestamp to the blinds. The MSP430 uses its internal crystal which has limited accuracy. This byte group is used to allow the blinds to correct their timestamp to within $\pm$ 1 minute.
E	This is the UNIX timestamp of the last time the blinds were updated. This value is used by the server to determine if the blind's schedule is outdated or not.
F	The remaining 122 bytes are optional and are used to convey the rest of the schedule. The blinds will send their schedule on bootup if the server is outdated, otherwise the server will send a new schedule to the blinds if it has been updated recently. This byte is not included for standard check-in messages.

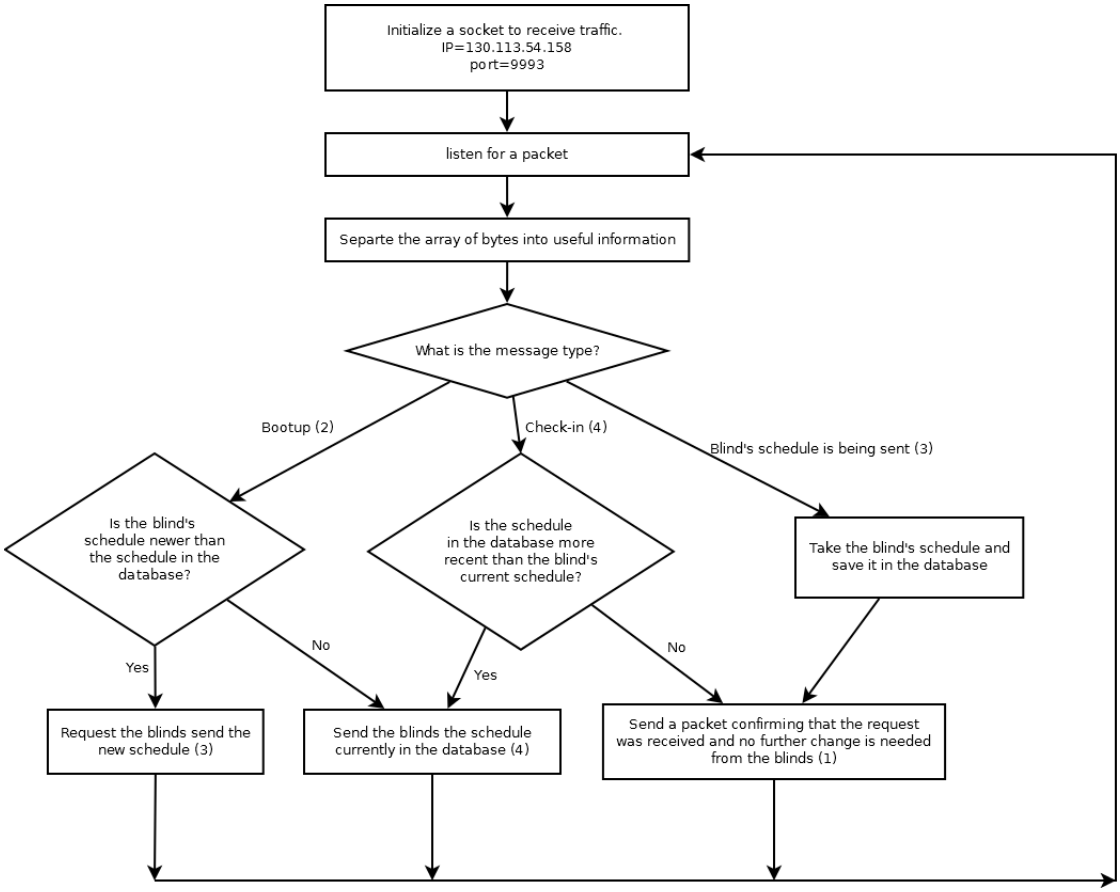

Figure D.11: Decision process taken by the python server based on the messages it receives from the blinds.

Table D.8: All possible request bytes and their meaning when sent from either the client or the server.

Request Byte Value	Meaning when sent from Blinds	Meaning when sent from server
1	The blinds are asking the server if there is a new schedule	The blinds are acknowledging that they received the blind's previous message.
2	The blinds have just been booted up. If there was a schedule on the SD card, they send the Unix timestamp for when that schedule was last updated.	N/A
3	The blinds acknowledge the server's request to send a new schedule. This message includes the updated schedule.	The server has just received a bootup message, and the timestamp indicates the blind's schedule is more recent. This code requests the blinds send the new schedule.
4	N/A	The blinds have just send a check-in message (request byte=1). The schedule has been modified. This message includes the new schedule.

D.6 Assembly Instructions

D.6.1 Assembly Introduction Notes

This section include step-by-step sequential instructions on how to build the motorized blind prototype that was studied in this thesis. It is recommended that prior to assembling the entire unit, the electronics are assembled, connected and tested for functionality because it can take significant effort to debug individual circuit boards once the unit is assembled.

D.6.2 Materials

A bill of materials (BOM) is included for each step of the assembly instructions as well as for the PCB assembly instructions in Section D.7

D.6.3 Preparation

1. Manufacture and assemble the PCBs according to the documentations in Appendix D.7.

2. 3D print a single copy of all components in Appendix D.9.1 to D.9.4. The exception is bottom rail part A (print 10 of these) and bottom rail part B (print 11 of these). The electronics wheel should be printed from clear PLA.

3. Purchase a roller blind unit. The top cylinder for the unit must be at least 5 cm (2") for the control electronics to fit. For this particular prototype, the blind was 889 mm (35") wide and 1752.6 mm (69") long. Remove the existing bottom rail.

4. Set all components aside until later.

D.6.4 Solar Stack

Table D.9: BOM for solar array.

Description	Quantity Information
Foam block of appropriate dimensions (consider modifying baseboard).	In excess of 180 mm (71")
SLMD121H08 solar modules	16
RA 13V1 schottky diodes	20
Assorted wire	1

For this project, the four solar stacks for energy harvesting were previously built by an undergraduate research assistant. They were built according to the diagrams in Section D.8.

1. Cut down the foam block to four 45 cm (17.75") pieces. Mill the block to the dimensions in Figure D.39.

2. Lay five diodes in the narrow deep trench of the holder. Lay four solar modules in the wide and shallow trench. Solder the diodes and modules according to Figure D.38.

Figure D.12: Two completed solar stacks.

D.6.5 Bottom Rail

Table D.10: BOM for Bottom Rail.

Description	Quantity Information
6/32 1.25” screws	24
6/32 nuts	24
Assembled PCB S1	1
Assembled solar stacks	4
Bottom Rail A	10
Bottom Rail B	11
Bottom Rail A non-PCB end piece	1
Bottom Rail A PCB end piece	1
Bottom Rail B non-PCB end piece	1
Bottom Rail B PCB end piece	1
Wire twist connectors	In excess of 3

1. Install PCB S1 into Bottom Rail Piece Part A, the PCB side. Connect the

headers leaving the PCB to thick wire (16 AWG or thicker). See Figure D.13 (a).

2. All bottom rail back pieces have two hexagonal cutout shapes (visible in Figure D.41). These structures is designed to have 6-32 captive nuts placed. Place the nuts into the holes and secure with hot glue.

3. Attach copper tape and wire to the three bottom rail A and three bottom rail B pieces. Each A-B pair will form a bottom rail crimp connector that will conduct power from the bottom rail to the e-textile. See Figure D.13 (b).

4. Build two halves of the bottom rail. Start by assembling the two end cap and end cap back pieces. Then alternately slide A and B components to build the half stacks. Make sure that the conductive parts from the previous step are paired together in A-B pairs and are spaced evenly throughout the bottom rail.

5. This half stack is long enough to install the previously manufactured solar stacks. Slide these into place securing with hot glue and pull wires into the hollow rail cavity. Secure the individual bottom rail pieces by screwing 6-32 screws from the bottom rail component A and into the captive nut of the corresponding bottom rail B. Don't tighten too much yet (they will be tightened when securing to the fabric in a later step). See Figure D.13 (c) and (d).

6. Wire all ground connections together using twist connectors. This consists of a ground to each of the four solar arrays, the PCB S1 and one of the bottom rail connectors. Make sure that the conductive bottom rail is chosen to mate with the e-textile bus that is specified to be ground. See Figure D.13 (d).

7. Use twist connectors to wire the positive end of the PCB to a different bottom rail connector. Makes sure this bottom rail connector is chosen so that it connects to the e-textile's positive bus.

8. Use twist connectors to wire the positive end of the solar array to the third bottom rail connector. Makes sure this bottom rail connector is chosen so that it connects to the e-textile's solar positive bus (the center bus).

9. Connect the two half stacks together.

10. Completed assembly pictured in Figure D.13 (e). Set it aside until later.

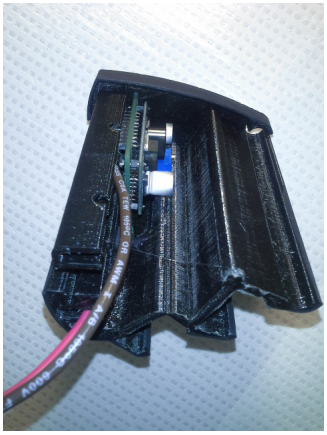

(a)

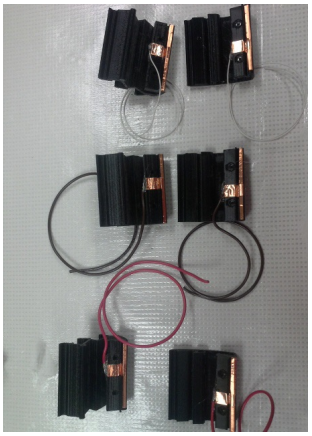

(b)

(c)

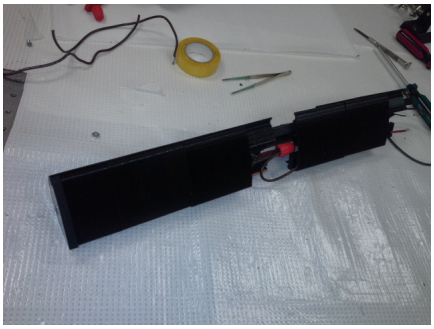

(d)

(e)

Figure D.13: Images to help guide assembly of bottom rail.

D.6.6 Electronic Blind Textile

Table D.11: BOM for electronic blind textile.

Description	Quantity Information
Roller Blind Unit. Ensure top cylinder is at least 5 cm (2") wide.	1
Unwoven backing material.	Match dimensions of blind fabric
Heat'n Bond	Enough to lay several strips along width of blind
34 AWG magnet wire	500 g
3M 1181 Copper Tape	1 roll
Hirose DF1B male connector (pins and enclosure)	1

1. Using 34 AWG magnet wire lay 600 wires in parallel along the length of the blind. Masking tape may be needed to temporarily secure the wires in place. See Figure D.14 (a).

2. Strip insulation off the ends of the wires using an open flame. Do this step in a well ventilated area.

3. Fold copper tape across the exposed ends to form a parallel circuit. Connect 250 wires on each sides and the center 100 wires.

4. Lay strips of heat'n bond perpendicular to the wires across the entire length of the fabric. Place a sheet of unwoven cotton backing material with matching dimensions across the blind. Apply heat using a clothes iron to secure. See Figure D.14 (b).

5. Solder a wire to each of the copper busses near the top of the e-textile. Bring these wires together in a crimp connector, for this project the Hirose DF1B family was used. See Figure D.14 (c).

6. Set aside until later.

(a) (b) (c)

Figure D.14: Images to help guide assembly of electronic textile.

D.6.7 Button Box

Table D.12: BOM for Button Box.

Description	Quantity Information
Standard spacing (2.54mm, 0.1") perfboard	25.4x 12.7 mm (1" x 0.5")
D6R00 F1 LFS pushbutton	2
3x1 ribbon cable	In excess of 91.4cm (3')
Button Box Back (3D printed)	1
Button Box Front (3D printed)	1
Male headers (1x2)	2
3mm x 6mm screws	6
Original roller blind's beaded chain	1

1. Solder each push button to a small perfboard. Place the assembled electronics into the Button box front, securing with 3x6 mm screws and hot glue. This may require additional holes to be drilled into the 3D printed button box front

piece.

2. Solder a wire to connect the grounds of both buttons.

3. Cut the ribbon cable to an appropriate length. In this prototype a minimum of 91.4 cm (3') was used, however this length may need to be adjusted according to the length of the roller blind. Ensure it is long enough that it will be able to wind and unwind in the roller clutch without any issues.

4. Solder one end of the ribbon cable to the appropriate ends of the circuitry in the button box. In particular, one lead must connect to the ground, the other leads must connect to the other terminals of each push button. The assembled circuitry is shown in Figure D.15 (a).

5. Slide the original roller blind's beaded chain into the grooves of the front button box. Slide the button box backing piece onto the assembly to secure the beaded chain in place. Secure with two 3x6 mm screws on the sides. The assembled unit is shown in Figure D.15 (b).

6. At the other end of the ribbon cable, solder the header connectors. Each connector should have a connection to the shared ground and to a different button pin on the ribbon cable.

7. Set aside until later.

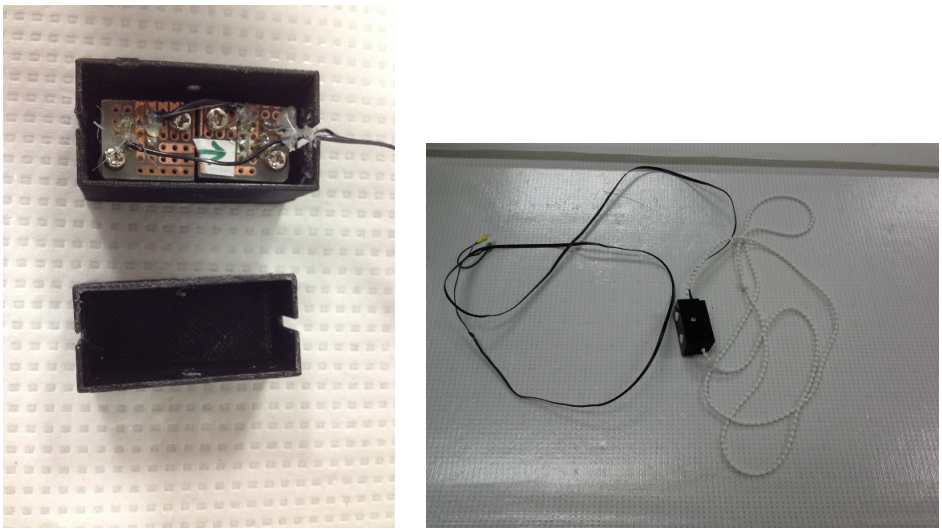

(a) (b)

Figure D.15: Images illustrating the assembly of the Electronics wheel.

D.6.8 Circuit Tube

Table D.13: BOM for circuit tube.

Description	Quantity Information
IPS SCH 40 PVC pipe	In excess of 838.2mm (33")
Energizer NH15 1.2V AA NIMH rechargeable batteries	12
Battery holder BH14AAL	3
NXRT15XV103FA1B040 thermistor	1
Pelco 16031 Colloidal Silver Liquid	Very small dab
1.1" diameter solid plastic rod	In excess of 152.5 mm (6")
Hirose DF1B 2x3 Male Connector (pins and enclosure)	6
Hirose DF1B 2x3 Female Connector (pins and enclosure)	3
Hirose DF1B-6DP-2.5DS(01) connector	1
Hirose DF1BZ-8P-2.5DSA connector	1
Standard spacing (2.54mm, 0.1") perfboard	25.4x 12.7 mm (1" x 0.5")
Assembled PCB S5	1
Parallel 8 line ribbon cable	In excess of 1067 mm (42")
Hirose DF1B 1x8 Male Connector (pins and enclosure)	4
Assembled PCB S6	1
TI MSP430	1
TI launchpad	1
Phidgets 3264E_1 - 12V/8.4Kg-cm/28RPM 139:1 DC Gear Motor w/Encoder	1
1/4" steel rod	In excess of 80 mm (3.13")
Motor Axle Adapter (3D printed Part)	1
8-32 set screws	2
Motor Electronics Wheel adapter (3D printed Part)	1
3x6 mm screws	4
Steel Strapping	In excess of 152.5 mm (6")
6-32 0.5" nut and bolt set	1
6-32 1/4" flathead screws	22

1. Cut PVC pipe into six 140 mm (5.5") pieces as drawn in Figure D.63. Milling

the grooves shown in Figure D.63 may not be necessary. These grooves originally were meant to bind the enclosure to the top cylinder. Different blind products have different shapes and may require different groove patterns.

2. Machine six interconnects according to the specifications shown in Figure D.64. This purpose of this piece is to mechanically connect two adjacent enclosures as shown in the exploded diagram in Figure D.62). To ensure that the holes in both pieces lined up, the connector was inserted into the enclosure and a hole was drilled and while they were inserted. This guaranteed a fit. The holes are tapped for 6-32 1/4" flathead screws.

3. Battery Pack Assembly. Install four NIMH batteries in each of the three battery holders. Each battery pack must go in one of the 5.5" PVC pipe enclosure, this may require the cavity to be widened slightly. Add wires and 6 pin Hirose DF1B connectors to each of the battery holders according to the wiring diagram in Figure D.16. An NTC thermistor is bonded to the external surface of one of the batteries using a small dab of colloidal silver paste.

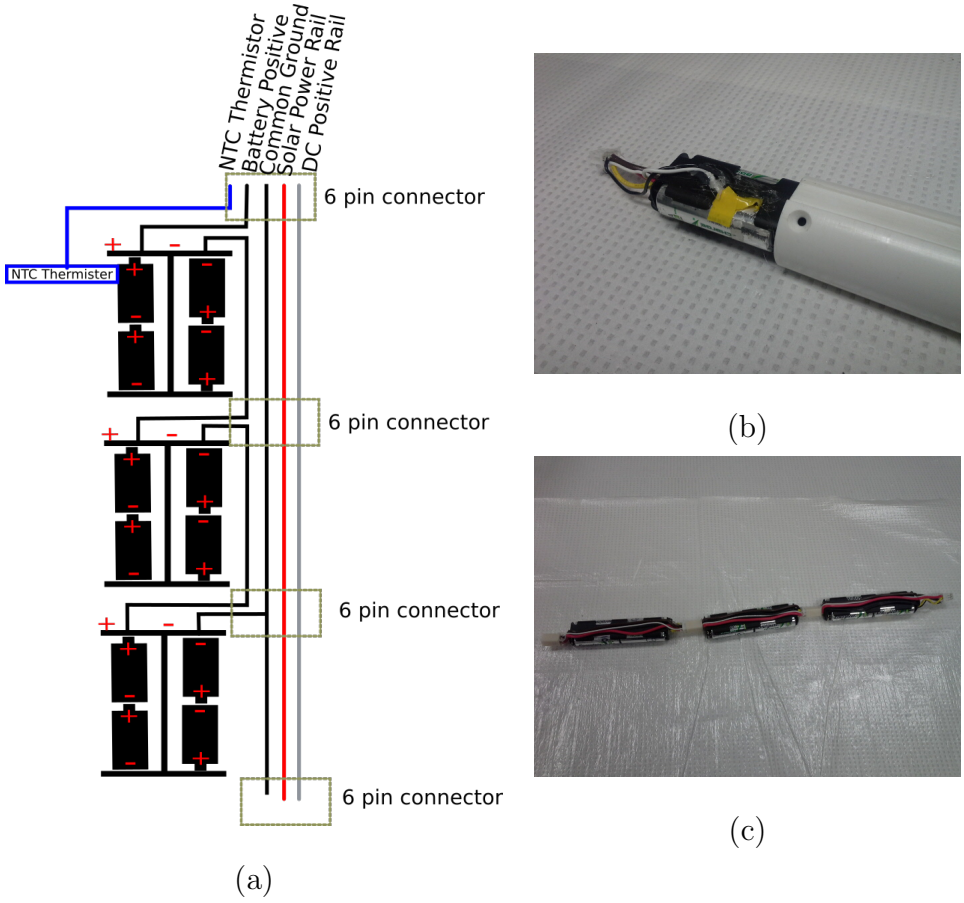

Figure D.16: (a) Wiring diagram of the battery pack. (b) Example battery pack with NTC thermistor secured to battery and pack partially inserted into enclosure. (c) Assembled battery pack connected to each other but outside of their enclosures.

4. E-stop functionality was not included in the PCB design, and is added through a manually designed perfboard circuit. Using perfboard, solder a Hirose DF1B-6DP-2.5DS(01) connector, a Hirose DF1B-6DP-2.5DS(01) connector and use wires to solder a standard Hirose DF1B 2x3 Male Connector as shown in Figure D.17 (a). Route the pins from the female connector to the male connector according to Figure D.17 (b). Basically all pins are routed without interruption except for the batter positive connection. This gets routed through the 8

pin connector and sent to a mechanical switch mounted in an accessible location allowing the batteries to be manually disconnected from the prototype if necessary.

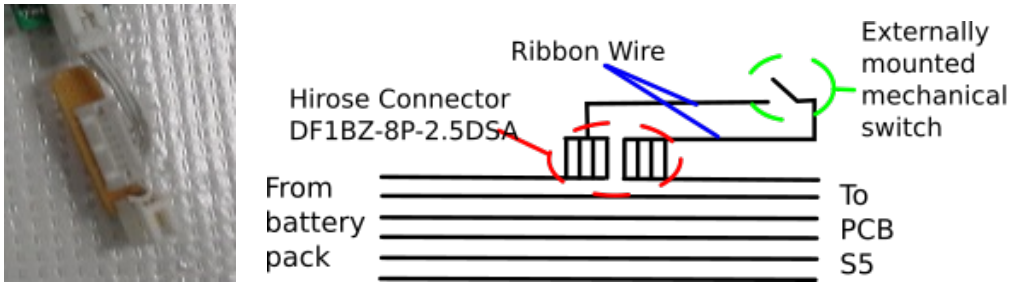

(a) (b)

Figure D.17: (a) Image of the assembled Estop circuit. (b) Wiring diagram of the Estop circuit.

5. Ribbon Cable. In the previous step, a circuit was made that routes the battery power through a switch. This switch is not assembled in these steps, but is located in an accessible location outside the top cylinder. To route that line, a cable is needed. parallel 8 line ribbon cable was used. Prepare a length of this cable that is long enough to reach from this circuit to the outside of the top cylinder (about 457.2 mm or 18" long). Crimp the metal pins and assemble a 1x8 connector on either end of the cable. The cable is shown in Figure D.18 (a).

6. The ribbon cable connects to the Estop perfboard and runs along the outside of the electronics enclosure. Mill a hole large enough in an enclosure so that the ribbon cable can be inserted and plugged into the perfboard. The modified enclosure is shown in Figure D.18 (a).

7. Connect the PCB S5 to the perfboard circuit. Insert the assembly into the enclosure and plug the ribbon cable through the enclosure hole to the perfboard circuit. The assembled circuitry, ribbon cable and modified enclosure are pictured in Figure D.18 (a). The installation of the ribbon cable to the perfboard is shown in Figure D.18 (b).

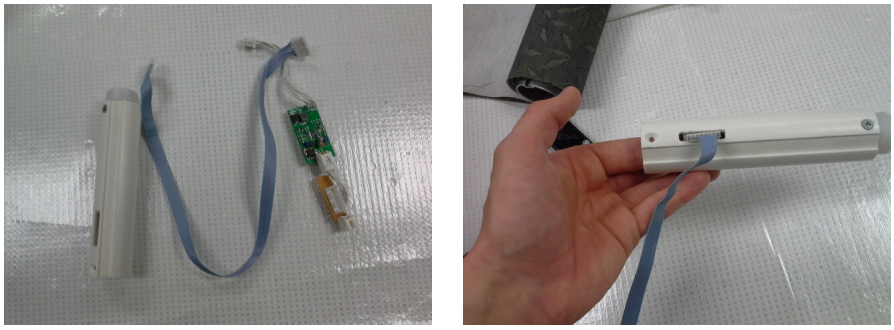

(a) (b)

Figure D.18: (a) Wiring diagram of the Estop circuit. (b) Image of the physically assembled Estop circuit.

8. Control Circuit S6. The PCB S6 requires a connection to the external mounted electronics through a parallel ribbon cable. Cut two lengths of 8 parallel line ribbon cable to a about 305 mm (12"). On one end, each ribbon cable will have a single 1x8 Hirose male connectors that are capable of plugging into the PCB S6. On the other end the ribbon cables are joined in a 2x8 Hirose male connector capable of connecting to PCB S8. Ensure that the wires correctly connect the pins in PCB S6 and S8. The built cable is shown in Figure D.19.

9. The ribbon cables two individual leads connect to PCB S6 and run along the outside of the electronics enclosure. Mill a hole large enough in the enclosure so that the ribbon cable can be inserted and plugged into the PCB (milled enclosure pictured in Figure D.19).

10. Use Code Composer studio and a connection to a TI Launchpad to program an MSP430 with the code in the attached code directory titled “1 MSP430 Program”. Once loaded, insert the microcontroller into the 2x8 DIP socket in PCB S6.

11. Insert the circuit board S6 into its enclosure. The electronics enclosure may need to be widened, or parts of the circuitboard (like the plastic enclosure for the 8 pin connector) may need to be filed or cut to make it fit. Plug the two individual ribbon wire leads into the PCB.

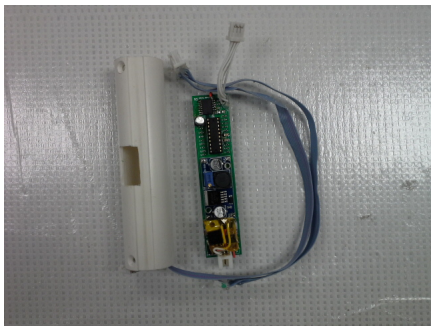

Figure D.19: Enclosure, wires and assembled S6.

12. The motor is connected to PCB S6 which provides it with power and reads the encoder. The motor comes with a small 5 wire ribbon cable to connect the encoder. It has two metal terminals to power the motor. Solder wires to the motor terminals and cut the encoder wire to an appropriate length, about 152.5 mm (6”). Crimp the ends of these wires into a Female Hirose 2x3 connector. Ensure that the wires are in the correct order so that they match the corresponding pins from PCB S6. The cable assembly on the motor is shown in Figure D.20 (a).

13. The motor enclosure may need adapting. For this particular prototype, the enclosure was widened to fit the gear box and a hole with drilled with the mill to allow clearance for the encoder electrical connection.

14. The motor must be able to push against an anchored axle in order to rotate the blinds. Use a saw to cut the steel rod to 80 mm (3.13") as shown in Figure D.61 to make the axle. Use a file to add a flat on one end of the axle.

15. Insert the flat end of the axle into the axle adapter (figure D.60), and the other end into the motor's rotor. The dimensions of the adapter are quite tight, so this process may need force (it may need to be hammered on). Screw two 8-32 set screws into the axle adapter to complete the fit. The 3D printed part is soft enough that the process of screwing the set screws will tap the holes.

16. Insert the motor axle assembly into its enclosure a shown in Figure Figure D.20 (b).

17. Connect the electronics wheel adapter to the motor. Fasten it using four 3x6 mm screws. See Figure D.20 (c).

Figure D.20: (a) Wired motor. (b) Motor inserted into electronics enclosure. (c) Electronics wheel adapter secured to motor with M3 screws.

18. At this stage, the following enclosures have been assembled:

    (a) Three battery pack enclosures (comprising S_4).

    (b) E-stop and battery charging PCB in enclosure (S_5).

    (c) Control circuit PCB S6 enclosure (S_6).

    (d) Motor Enclosure. (S_7).

19. Each enclosure connects with a male/female Hirose connector to its adjacent block. Make these connections in a sequential order. Fasten the tube using 6-32 flat head screws and the previously built enclosure connectors.

20. Run the ribbon cables from the E-STop and PCB S6 flat against the enclosure body to the end of the tube where the motor electronics wheel adapter are located. Form the metal strapping into a C structure and wrap around the motor electronics wheel adapter. Tighten with 6-32 not and bolt to secure the

adapter to the plastic enclosure and to prevent the ribbon cable from moving. This assembly is pictured in Figure D.21 (a).

21. The entire control circuit tube is shown in Figure D.21 (b).

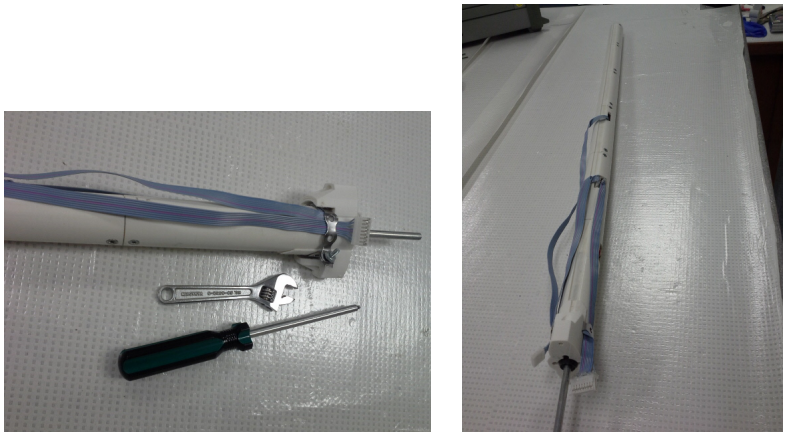

(a) (b)

Figure D.21: (a) Final assembly of motor adapter as well as the tools needed.(b) The assembled circuit tube.

D.6.9 Electronics Wheel

Table D.14: BOM for electronics wheel.

Description	Quantity Information
Assembled circuit tube	1
Electronics wheel (3D printed part)	1
DF1BZ-8P-2.5DSA 1x8 Hirose connector	1
6-32 3/4" screws	2
GPB023B05BR mechanical switch button	1
4x1 ribbon cables	In excess of 304.8 mm (12")
WP154A4SUREQBFZGW RGB LED	3
Standard 2.54 mm (0.1") headers	12
Assembled PCB S8	1
XBee S6B	1
XBee USB adapter	1
electronics wheel lid	1
washers	Potentially a few

1. E-stop button. Install the GPB023B05BR mechanical switch button into the 12.7 mm (0.5") hole of the electronics wheel, secure using the included bolt. Install the 1x8 Hirose connector in the adjacent 12.70 x 22.86 mm (0.5" x 0.9") hole, secure with hot glue. Wire one terminal of the push button to the first four pins of the 1x8 connector, and wire the push button's other terminal to the remaining four pins. When switched off, this button will disconnect the battery

from the rest of the prototype circuitry. See Figure D.22 (a).

2. Install the LEDs. Cut 4x1 parallel ribbon cable into 102 mm (4") strips. On one end, wire each of the four ribbon wires to a different terminal of the RGB LEDs. On the other end, solder the wire to a 1x4 set of male headers. There are three inset holes of diameter 5.59 mm (0.2"). Push an LED into each one of the three holes. Just a note, the electronics wheel must be fabricated from clear PLA for the light of the LEDs to be visible. See Figure D.22 (a).

3. Configure XBee S6B. Go to the Digi website (the manufacturer of XBee) and download their software XCTU. Plug the XBee into the usb adapter and connect to the computer. Using XCTU, update the firmware to version 2021. Test that the XBee component is good by attempting to connect it to a router using the XCTU interface. Set the IP setting of the XBee to TCP. Set destination port to 9993 (or whatever port the python server is listening on). Set AP setting to API Mode Without Escapes (1). Set D2 to SPI_SCLK (1). Set D3 to SPI Slave Select (1). Set D4 to SPI Mosi (1). Disable DIO7 (0). Set P2 to SPI Miso (1) set SM to Pin sleep (1). Set EE to WPA2 (2).

4. Assemble PCB S8. Install the configured XBee in the female headers provided on the PCB as shown in Figure D.22 (b). On top of the XBee, the assembled SD adapter PCB is inserted. This is also pictured in Figure D.22 (b).

5. Install assembled PCB S8. Take the previously assembled PCB S8 assembly and slide it into the electronics wheel as shown in Figure D.22 (c). The SD Card slot and the 2x8 connector should line up with the remaining open rectangular holes. Plug LED wires into PCB S8, make sure that the grounds are connected

properly.

6. It is time to connect the electronics wheel to the control circuit tube. Mate the motor electronics wheel adapter to the flat face of the electronics wheel as pictured in Figure D.22 (d). This requires inserting the axle through the electronics wheel as shown in previously discussed images. Plug in the ribbon cables to the corresponding housings. Use 6-32 3/4 screws to fasten the electronics wheel to the motor adapter. Depending on clearances, washers may be needed to separate the two systems.

7. The electronics wheel lid is noted, but not secured yet.

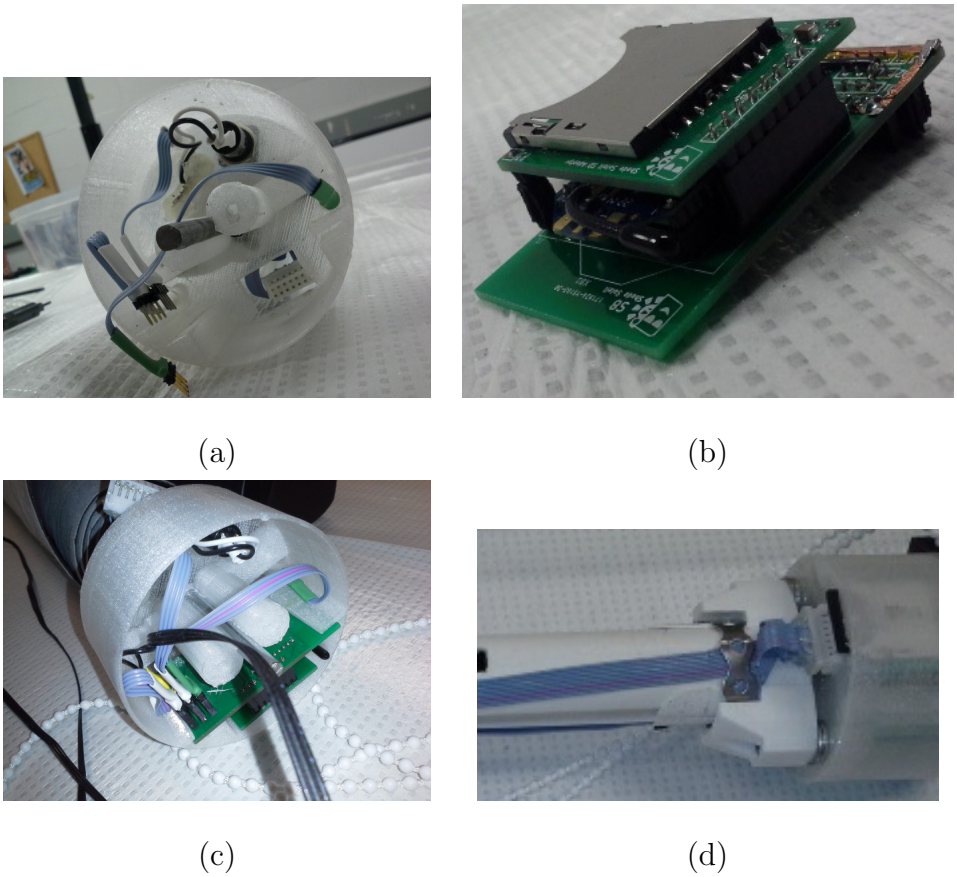

(a) (b)

(c) (d)

Figure D.22: Images illustrating the assembly of the Electronics wheel.

D.6.10 Roller Clutch

Table D.15: BOM for roller clutch.

Description	Quantity Information
Circuit tube and electronics wheel assembly	1
Button box assembly	1
Roller clutch enclosure A	1
Roller clutch enclosure B	1
Roller clutch enclosure C	1
Roller clutch enclosure D	1
Roller clutch button box wheel	1
Roller clutch beaded chain gear	1
Roller clutch axle adapter structure	1
6-32 nuts	3
1 1/4” 6-32 screw	2
8-32 set screw	1
3/4” 6-32 screw	3

1. In Roller clutch enclosure D, there are three hexagonal insets. Insert three 6-32 nuts into these insets and secure with hot glue.

2. One of the purposes of the clutch is to relay signals from the button box to the rotating control circuit. This means that the ribbon cable must have a way

of being wound and unwound while maintaining an electrical connection to the rest of the prototype's circuitry. The first step to accomplishing this goal is to thread the headers of the button box's ribbon cable through the center holes of the clutch enclosure C, the beaded chain gear, roller clutch enclosure D and then the electronics wheel lid (in that order) as shown in Figure D.23 (a).

3. The headers are now through the electronics wheel lid. Insert them into the corresponding switch input female headers of PCB S8 as shown in Figure D.23 (b). If the ribbon cable was made too long, extra slack can be bundled here and stuffed into the electronics wheel.

4. Line up the electronics wheel lid, clutch case D and the beaded chain gear along the motor axle. Press these components tightly together to ensure the axle is long enough to reach through the remainder of the clutch. Drape the beaded chain between clutch D and the beaded chain gear. The results of this step are illustrated in Figure D.23 (c).

5. Sandwich the beaded chain gear assembly between clutch case D and clutch case C. Install the ribbon cable wheel and wrap the ribbon around the wheel as pictured in Figure D.23 (d).

6. The point of this assembly is to ensure that the button box, the beaded chain and the motorized blind move to the same height when the roller blind is activated. Each of the wire wheel, beaded chain gear, the electronics wheel lid, and the electronics wheel have a set of two holes that are 9.53 mm (0.38") away from the axle center. A 2" 6-32 screw can be screwed from the wire wheel through the holes of the wire wheel, electronics lid and into the electronics wheel itself.

The screws tap the holes in the electronics wheel, but captive nuts can also be inserted if desired (using the hexagonal cutouts in the electronics wheel). Once installed, these three components are locked to rotate with each other. Figure D.23 (d) shows the screws being inserted in the wire wheel.

7. Clutch case B is slotted into the structure to keep the wire wheel in place.

8. At this stage, the remaining axle length should be quite short. Insert the axle into the circular cutout of the Roller clutch axle adapter structure. Use an 8-32 set screw to secure the structure to the axle. This step is illustrated in Figure D.23 (e).

9. Place clutch case A over the axle adapter and secure all clutch case components in place using three 3/4" 6-32 screws. To set the friction brake, screw the top 6-32 screw until it digs through the roller clutch into the electronics wheel lid (you can also substitute a longer screw if necessary).

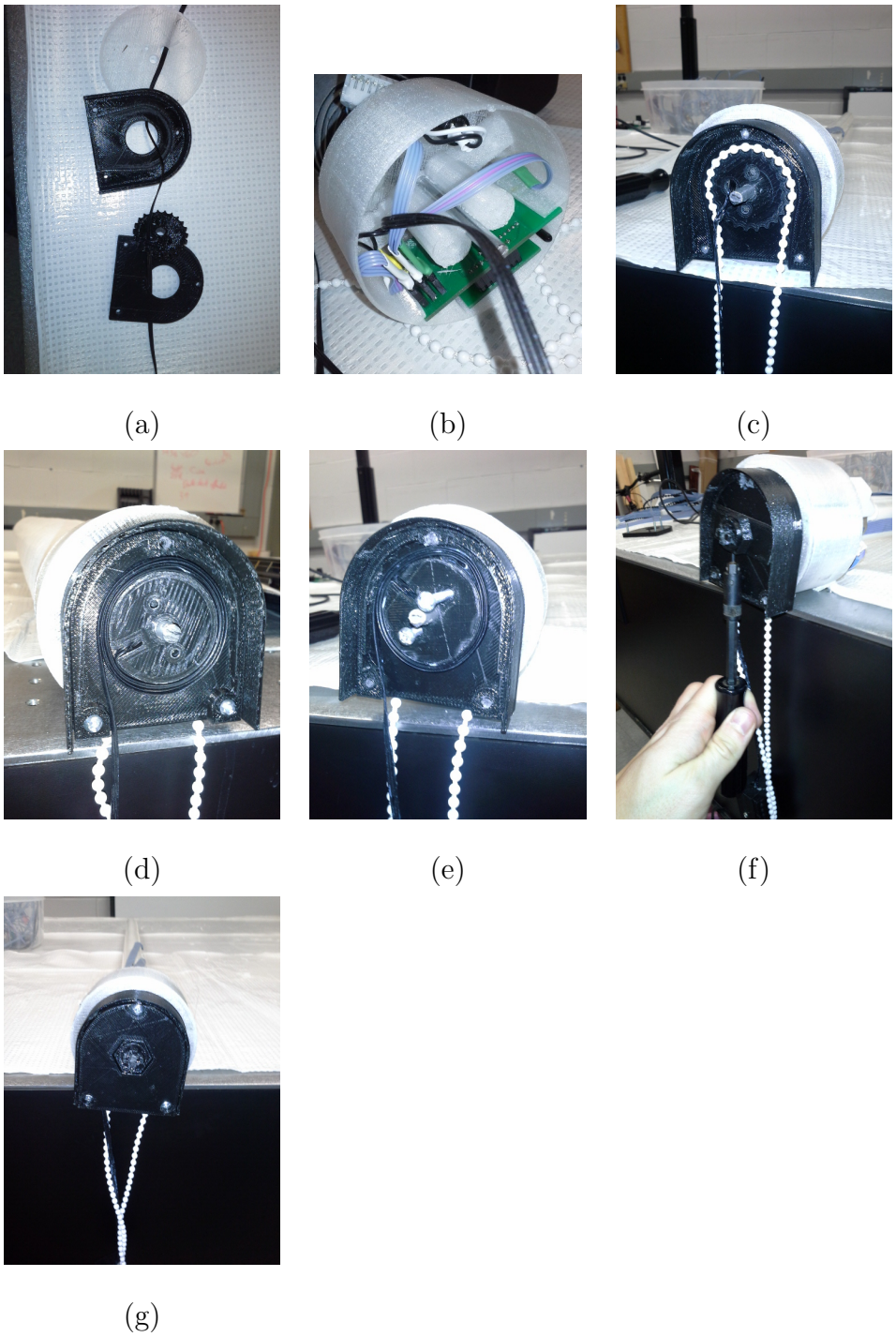

(a) (b) (c)

(d) (e) (f)

(g)

Figure D.23: Images illustrating the assembly of the roller clutch.

D.6.11 Entire Prototype Assembly

Table D.16: BOM for final assembly.

Description	Quantity Information
Circuit tube and clutch assembly	1
Electronic textile blind	1
Bottom Rail Assembly	1
Flexible 0.2" wide plastic tubing	length of bottom rail
Raspberry Pi	1
Minimum 8Gb SD card	1
Smaller capacity SD card	1
CUI ETSA240270UD-P5P-SZ 24V 60W Desktop Adapter	1
Top cylinder mounting insert	1

1. Tuck a loop of the wired blind into the top circular cavity of the bottom rail. Push the flexible plastic tubing through the fabric to ensure it is secure. This step is shown in Figure D.24 (a).

2. Loop the fabric down under the bottom rail to the clamping teeth. Insert the metal tabbing into the clamping teeth and tighten the bottom rail screws. At this point, double check the conductive teeth of the bottom rail make a connection with the correct e-textile bus. This action is illustrated in Figure D.24 (b). Tape the remaining fabric flat against the bottom rail so it blends in.

3. At the top of the blind, insert the control circuit tube and clutch assembly into the top cylinder. Be careful not to damage the ribbon cable that runs on the

outside of the control circuit enclosure and could rub against the inside of the metal cylinder. This action is illustrated in Figure D.24 (c).

4. At the opposite end of the top cylinder, there is a 2x3 connector to connect the terminals of the wired blind to the control circuit tube. Plug this into the connector at the end of the battery pack.

5. Find the top cylinder mounting insert that came with the original blind unit. Insert this unit into the opposite end of the motorized blind from the roller clutch.

6. The unit is now ready to be mounted in a window as shown in Figure D.24 (d).

7. The wall adapter can be plugged into the bottom rail to recharge the unit as shown in Figure D.24 (e).

8. For full network ability, a server must be assembled and be running. A new server can be built and the programs discussed in Table D.22 items 3-6 can be modified and installed. All code should be reviewed, in particular, references to the IP address may need to be updated and a MySQL database that is compatible with the PHP code may need to be written.

9. A small capacity SD card can be loaded with the Java program discussed in Table D.22 item 2. This allows the user to configure the prototype (which direction is up/down, what is the local Wi-Fi password etc.). The wizard that is installed in this Java program must be run to make the configuration file necessary for the prototype to start.

(a)

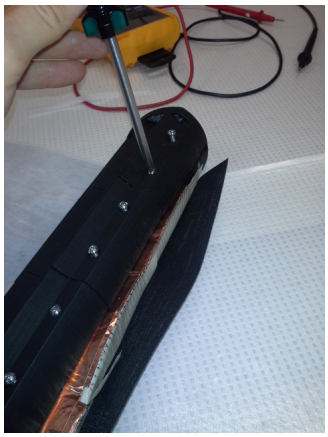

(b)

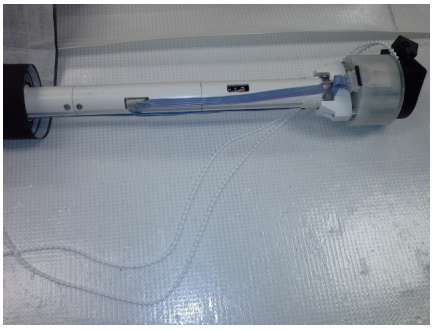

(c)

(d)

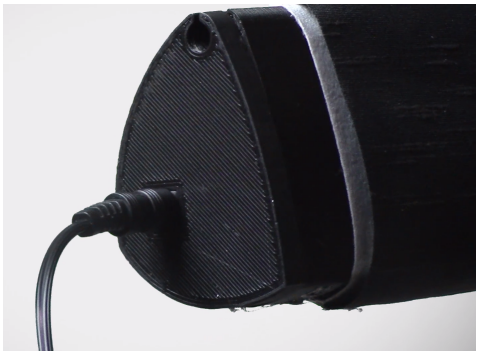

(e)

Figure D.24: Images illustrating the assembly of the prototype.

D.7 PCB Diagrams

D.7.1 S1: Power Adapter Input

Table D.17: BOM for PCB in Sector 1.

Label	Part Number	Footprint	Description
CON1	PJ-037A	Barrel Jack	Barrel Jack
P1, P2	PREC040SAAN-RC	10x2.54 mm	Male headers
U1	XTW-SY- 8	Custom	DCDC converter

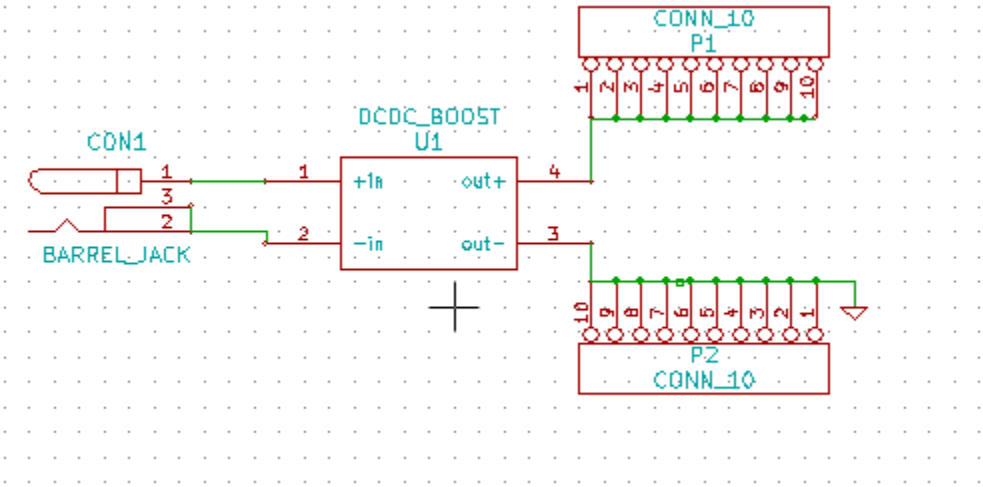

Figure D.25: Schematic diagram for the PCB in Sector 1. This PCB accepts power from an AC adapter and boosts the voltage.

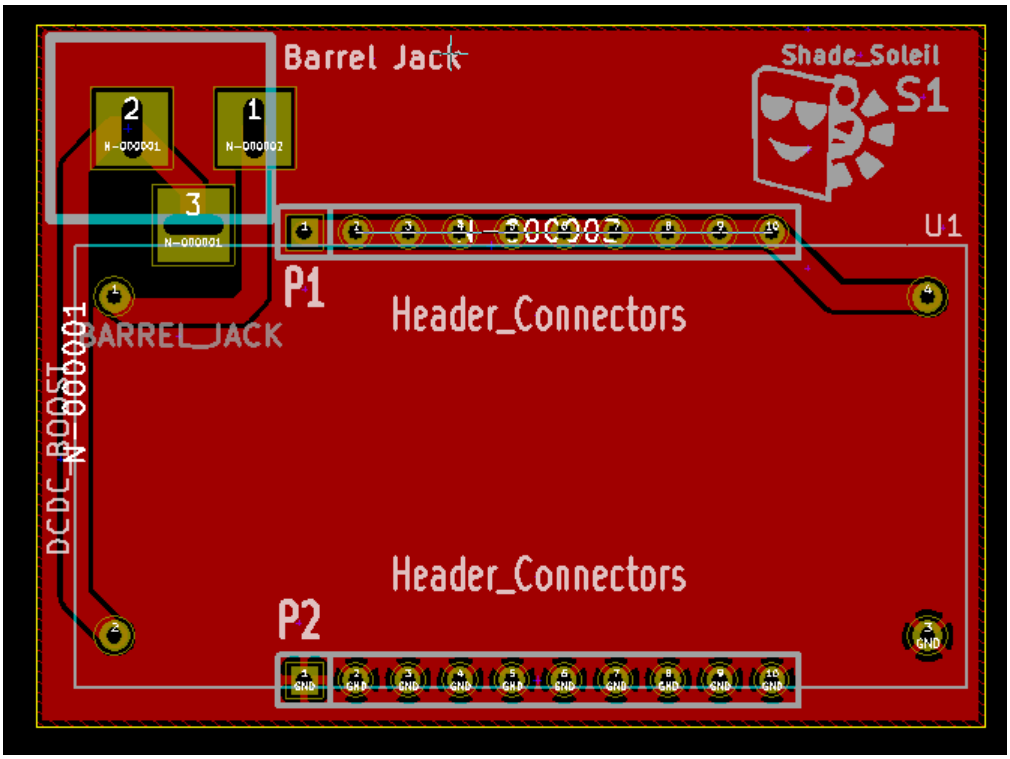

Figure D.26: Top PCB layout for the PCB in Sector 1. There are no bottom traces on this PCB. This board is 34.5x46.5 mm (1.36"x1.83").

D.7.2 S5: Battery Charger

Table D.18: BOM for PCB in Sector 5.

Label	Part Number	Footprint	Description
C1, C5	TMK316F106ZL-T	SM1206	10 μF
C2	CC1206KRX7R9BB103	SM1206	10 nF
C3, C4	C1206C104K3RACTU	SM1206	100 nF
D1, D2	B340-13-F	DO-21AA(SMB)	Schottky Diode
L1	74437349100	Custom	10 μH
P1	NA	3x2 2.54 mm	6 pin sector connector
P2	NA	3x2 2.54 mm	6 pin sector connector
Q1	fds6975	SO8E	P-FET
Q2	fdc658ap	SOT23_6	P-FET
Q3	SI1470DH	SOT23_6	N-FET
R1	MCT06030C2002FP500	SM0603	20 kΩ
R2, R3, R4	ERJ-3EKF4992V	SM0603	50 kΩ
R5	ERJ-3EKF9761V	SM0603	9.76 kΩ
R7	RC0603FR-0726K7L	SM0603	26.7 kΩ
R8	RC0603FR-07187RL	SM0603	187 Ω
R9	MCR03ERTF1103	SM0603	110 kΩ
R10	ERJ-3GEYJ103V	SM0603	10 kΩ
R11	CSR0603FK50L0	SM0603	0.05 Ω
U1	LTC4011	Custom	Battery Charging IC

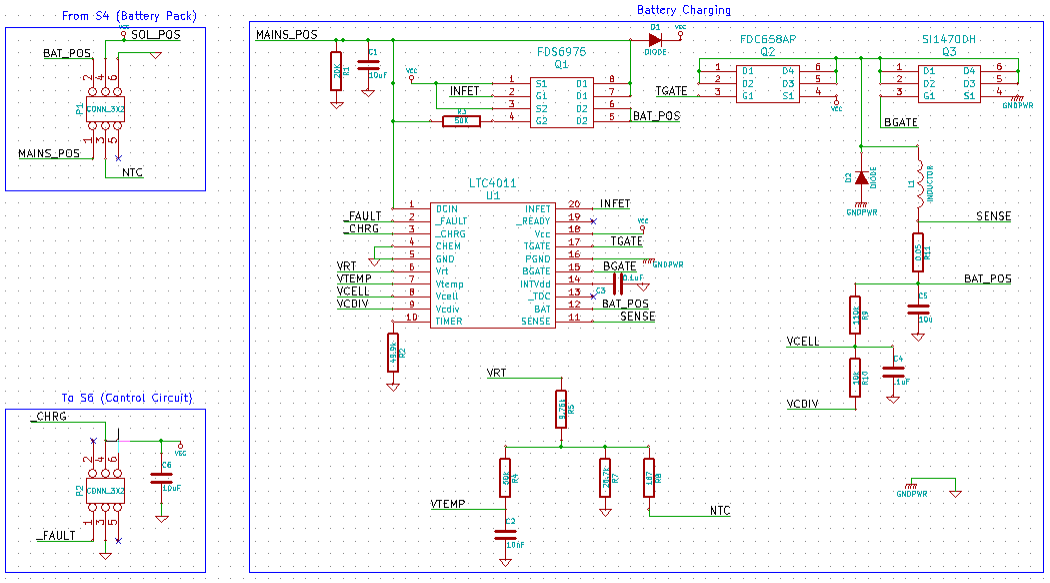

Figure D.27: Schematic diagram for the PCB in Sector 5. This PCB charges the battery and ensure the load is always powered.

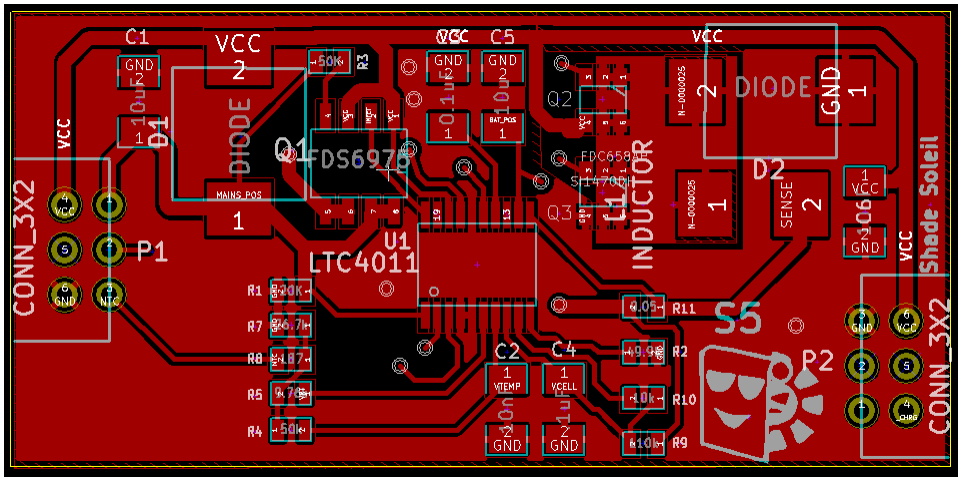

Figure D.28: Top layout of PCB S5. This board is 25.4x52.6 mm (1"x2.07").

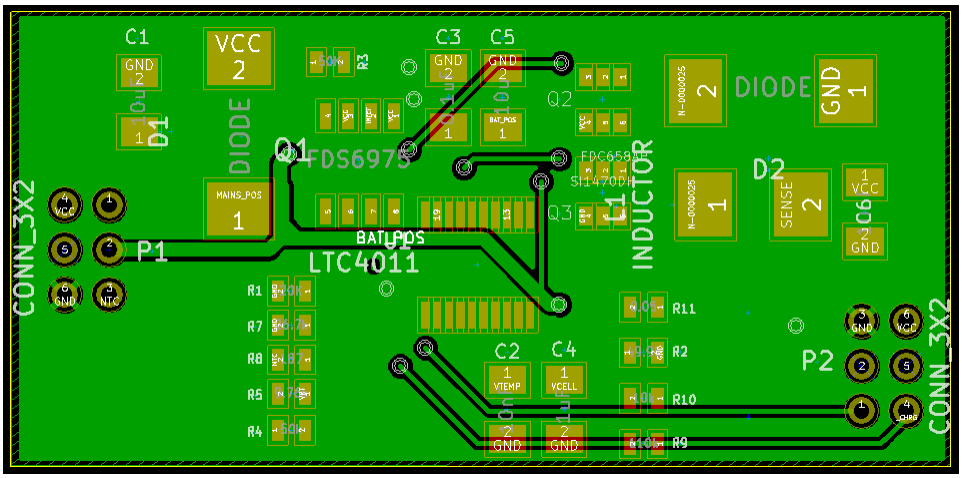

Figure D.29: Bottom layout of PCB S5.

D.7.3 S6: Control Circuit

Table D.19: BOM for PCB in Sector 5.

Label	Part Number	Footprint	Description
C1, C2	102R18W101KV4E	SM1206	100 pF
C3	TMK316F106ZL-T	SM1206	10 µF
C4	UWT1V470MCL1GS	Custom	47 µF
P1	NA	3x2 2.54 mm	6 pin sector connector
P2	NA	1x8 2.54 mm	8 pin sector connector
P3	NA	3x2 2.54 mm	6 pin sector connector
P4	NA	1x8 2.54 mm	8 pin sector connector
Q1	IRML6344TRPBF	SOT23	N-FET
Q2	DMP3098L-7	SOT23	P-FET
R1, R3, R18	ERJ-3GEYJ104V	SM0603	100 kΩ
R2, R4-R17, R19	ERJ-3EKF4992V	SM0603	50 kΩ
U1	DSN2596	Custom	DCDC Buck Converter
U2	LT1086CT-12#PBF	TO-220	12 V Regulator
U3	IFX7805ABTFATMA1	TO-252	5 V Regulator
U4	ED20DT	DIP-20	Socket for microcontroller
U5	A4973SLBTR-T	SOIC-16	H-Bridge

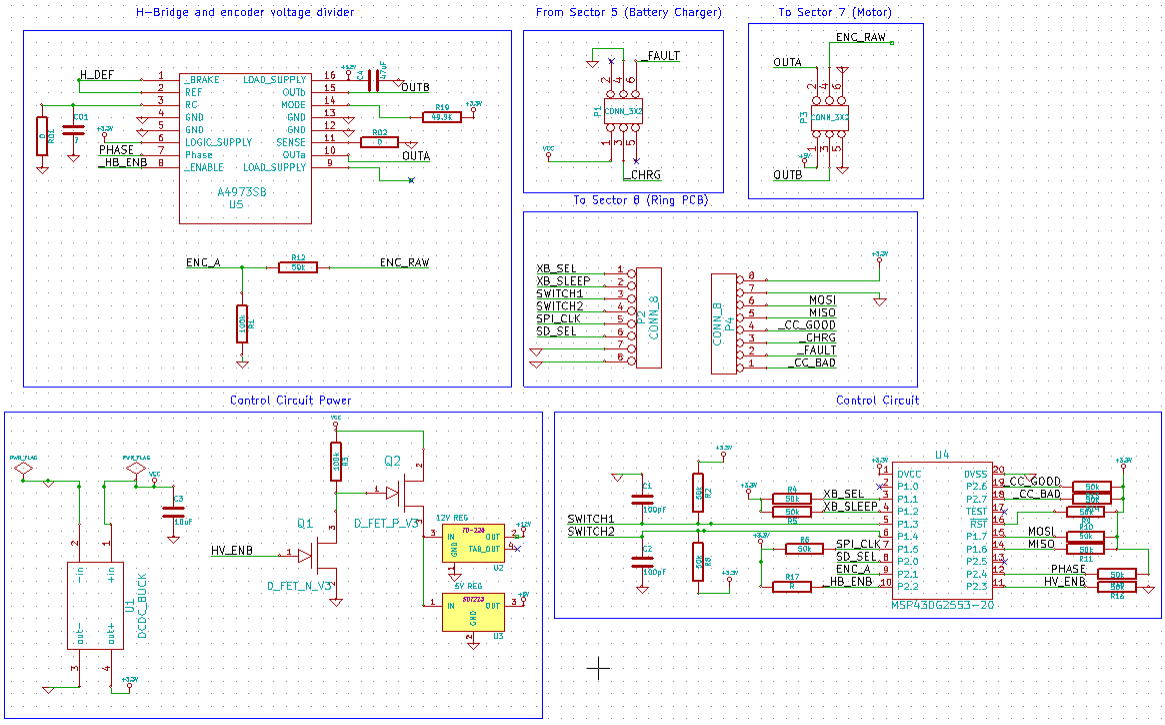

Figure D.30: Schematic diagram for the PCB in Sector 5. This PCB provides stable voltages for low powered electronics, has the microcontroller to keep track of operation and the motor controlling electronics. Connection CO1, RO1 and RO2 are optional components.

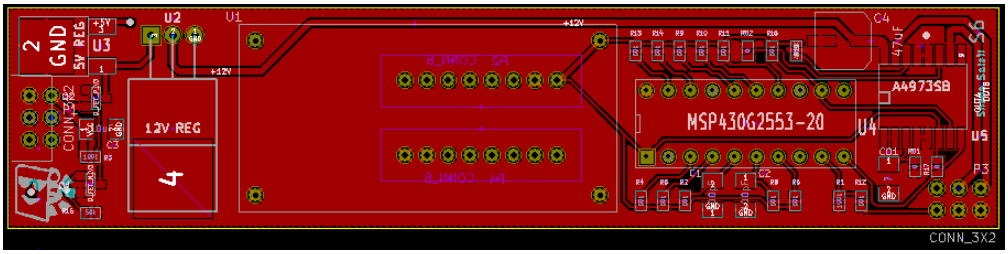

Figure D.31: Top layout for PCB S6. This board is 25.4x114.3 mm (x1"x4.5").

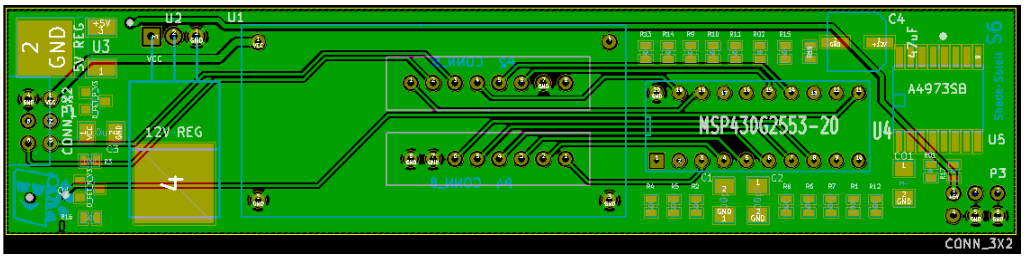

Figure D.32: Bottom layout for PCB S6.

D.7.4 S8: Peripheral Electronics

Table D.20: BOM for PCB in Sector 8.

Label	Part Number	Footprint	Description
C1	TMK316F106ZL-T	SM1206	10 µF
C2	C1206C104K3RACTU	SM1206	100 nF
D1, D2, D3	929974-01-36-RK	1x4 2.54 mm	Female header LED Connector
J1	929974-01-36-RK	Custom	Set of female headers. Interface with custom SD adapter
P1-P2	929974-01-36-RK	1x2 2.54 mm	Female header connector for button box switches
P3	DF1B-16DP-2.5DS(01)	2x8 2.54 mm	Connector to S6
Q1, Q2, Q3, Q4	DMP3098L-7	SOT23	P-FET
R1, R2, R8, R13-R16	ERJ-3EKF4992V	SM0603	50 kΩ
R3-R5,	RMCF0603JT39R0	SM0603	40 Ω
R6, R7, R9-R12	RC0603JR-07120RL	SM0603	120 Ω
XB1	NPPN101BFCN-RC	Custom	Two 1x20 2 mm Female headers for plug-in Wi-Fi chip

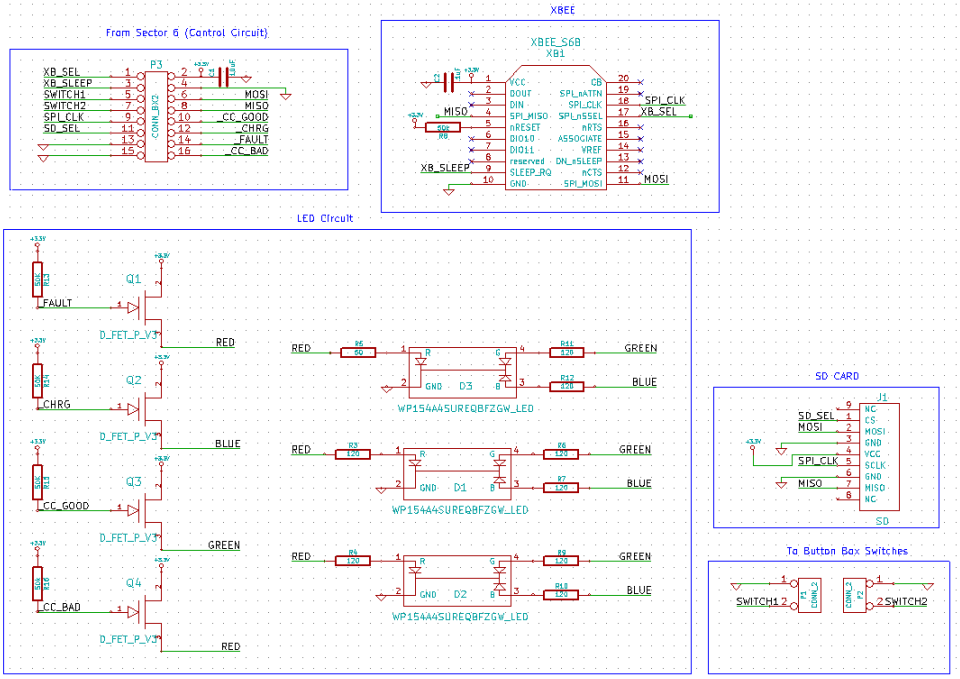

Figure D.33: Schematic diagram for the PCB in Sector 8. This PCB connects electronics that need peripheral access like: the XBee IC, LEDs, SD card slot and connections to the button box.

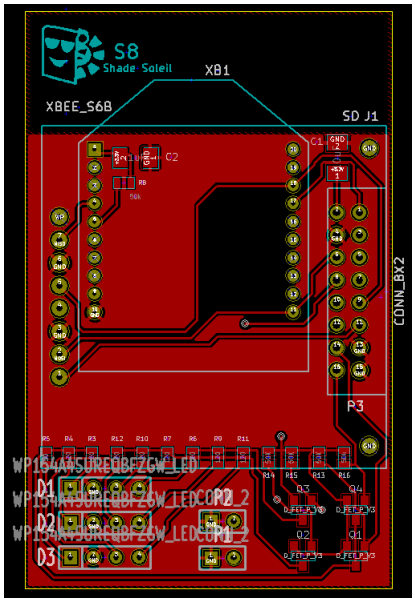

Figure D.34: Top layout for PCB S6. This board is 40.8x64.3 mm (1.605"x2.53").

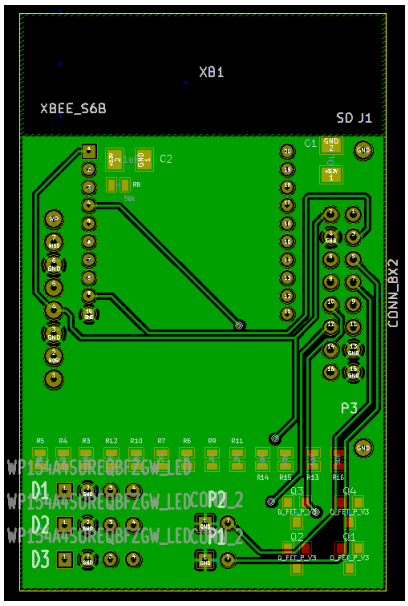

Figure D.35: Bottom layout for PCB S6.

D.7.5 SD Card Adapter

Table D.21: BOM for SD card adapter PCB.

Label	Part Number	Footprint	Description
C1	TMK316F106ZL-T	SM1206	10 µF
J1	101-00313-68-02	Custom	SD Socket
P1	PREC040SAAN-RC	1x8 2.54mm	Headers to interface with S8
P2-P3	PREC040SAAN-RC	1x1 2.54 mm	Headers to interface with S8
R1-R2	ERJ-3EKF4992V	SM0603	50 kΩ

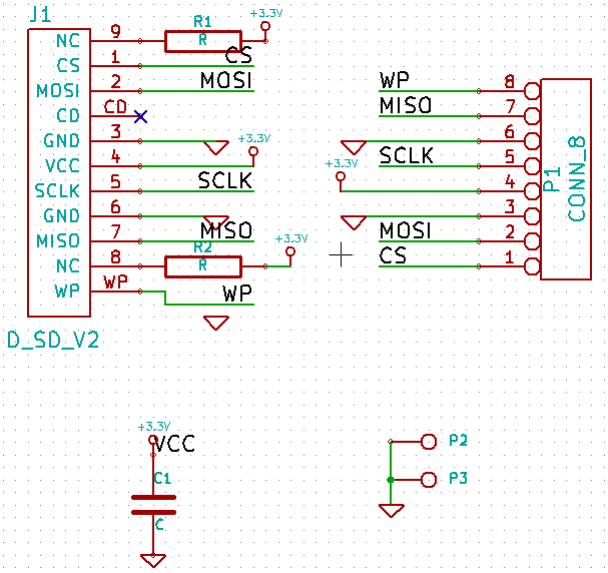

Figure D.36: Schematic diagram for the SD Card Adapter PCB (which is used in PCB S8).

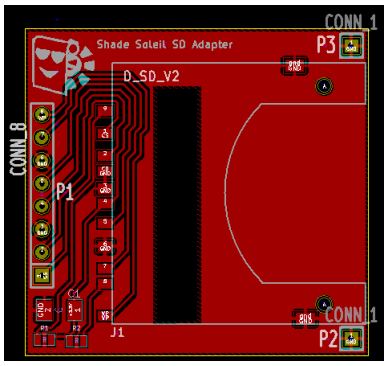

Figure D.37: Top PCB layout SD Card Adapter. This board is 10.2x11.8 mm (0.4"x0.465").

D.8 Solar Array Drawings

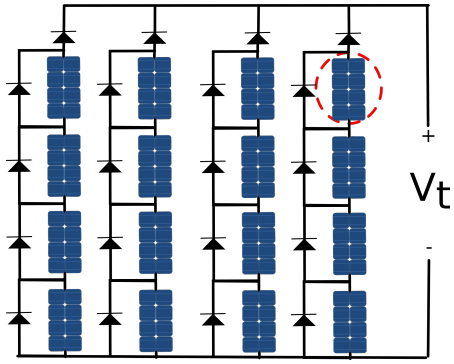

Figure D.38: Solar array circuit diagram.

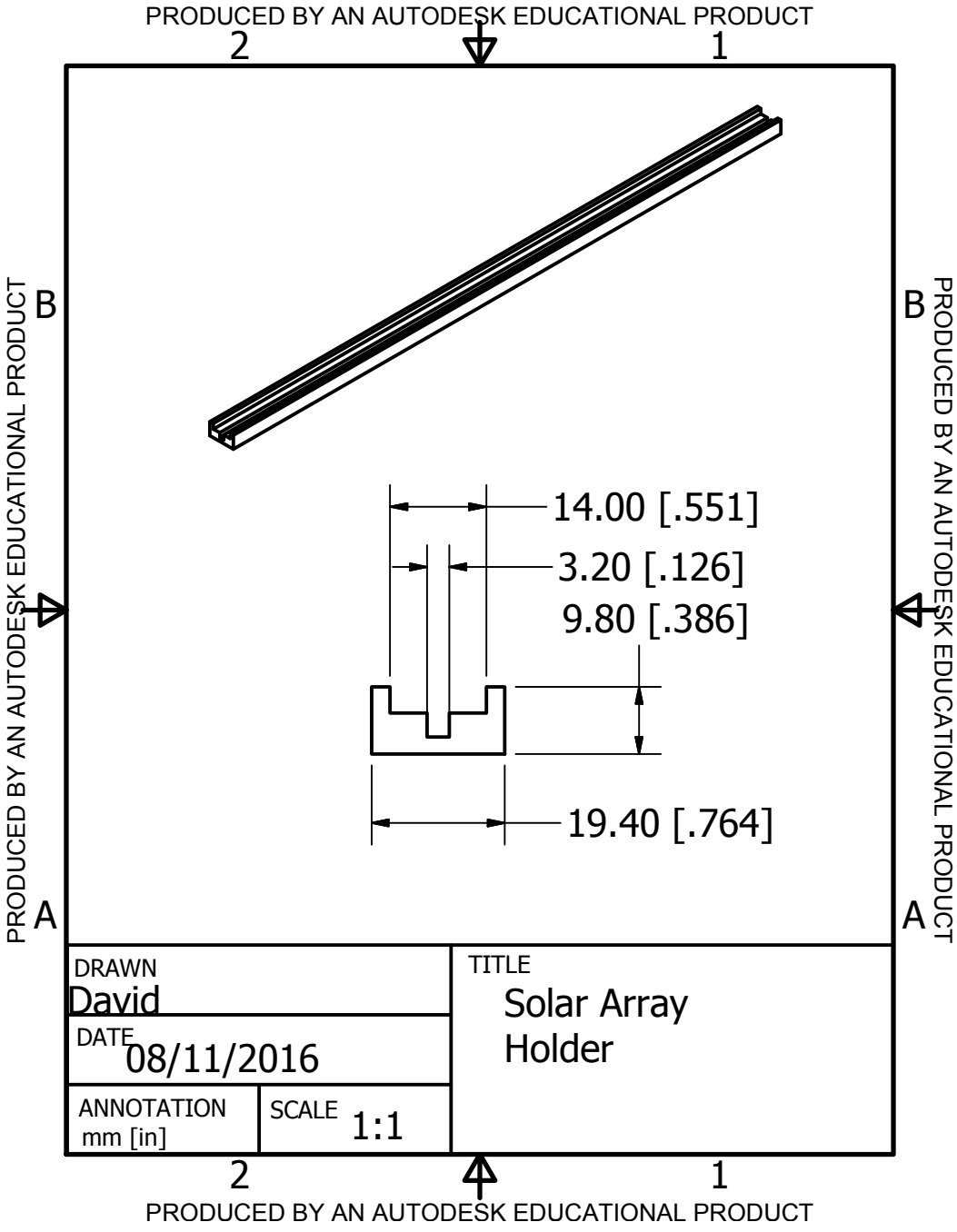

Figure D.39: Solar stack circuit holder. This profile is 45 cm (17.75") long.

D.9 Mechanical Drawings

D.9.1 Bottom Rail

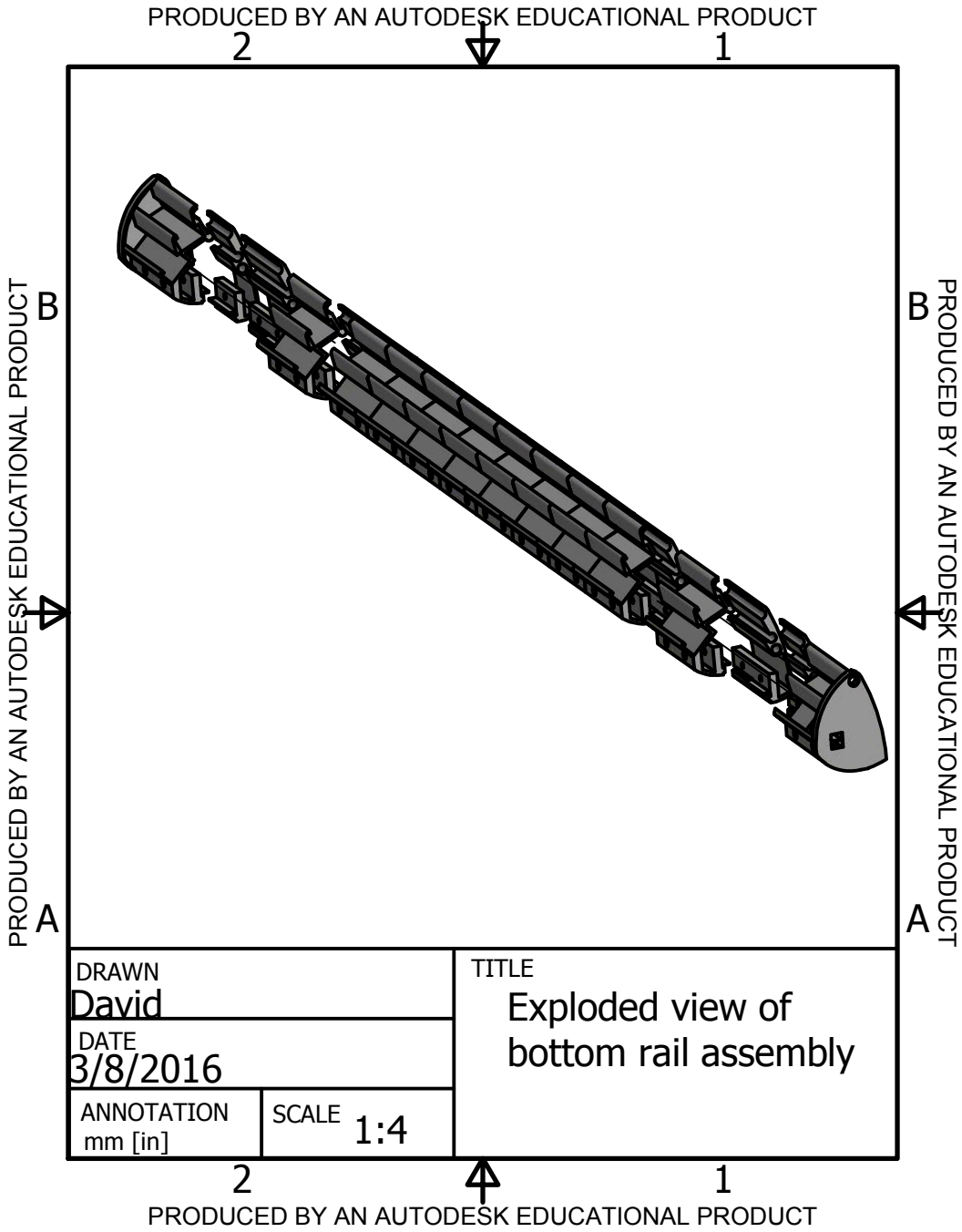

Figure D.40: Exploded view of the 3D printed bottom rail. This assembly is fastened with 1.25" 6-32 screws inserted in the front side and into a captive nut on the backside.

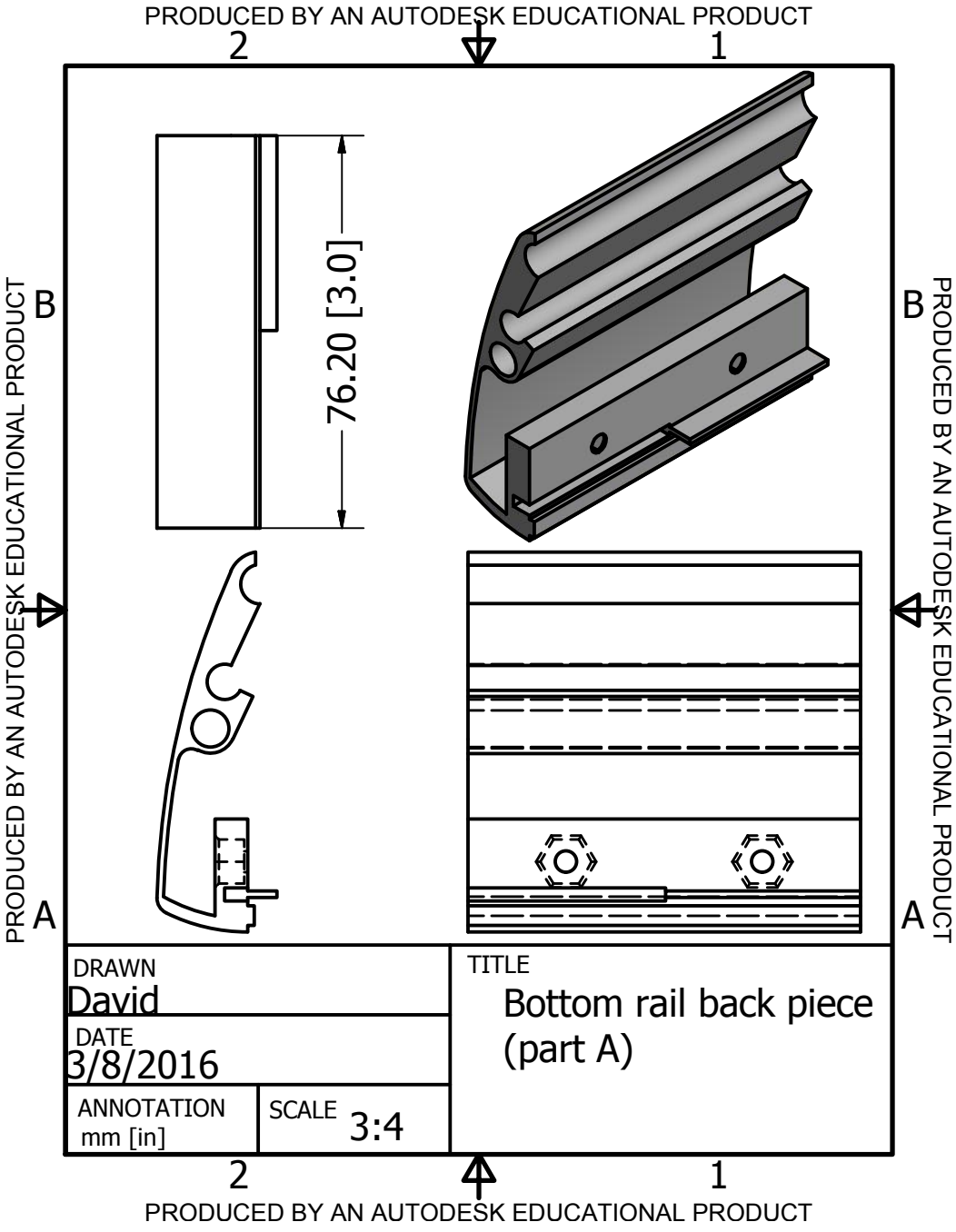

Figure D.41: Mechanical drawing for the back piece of the bottom rail.

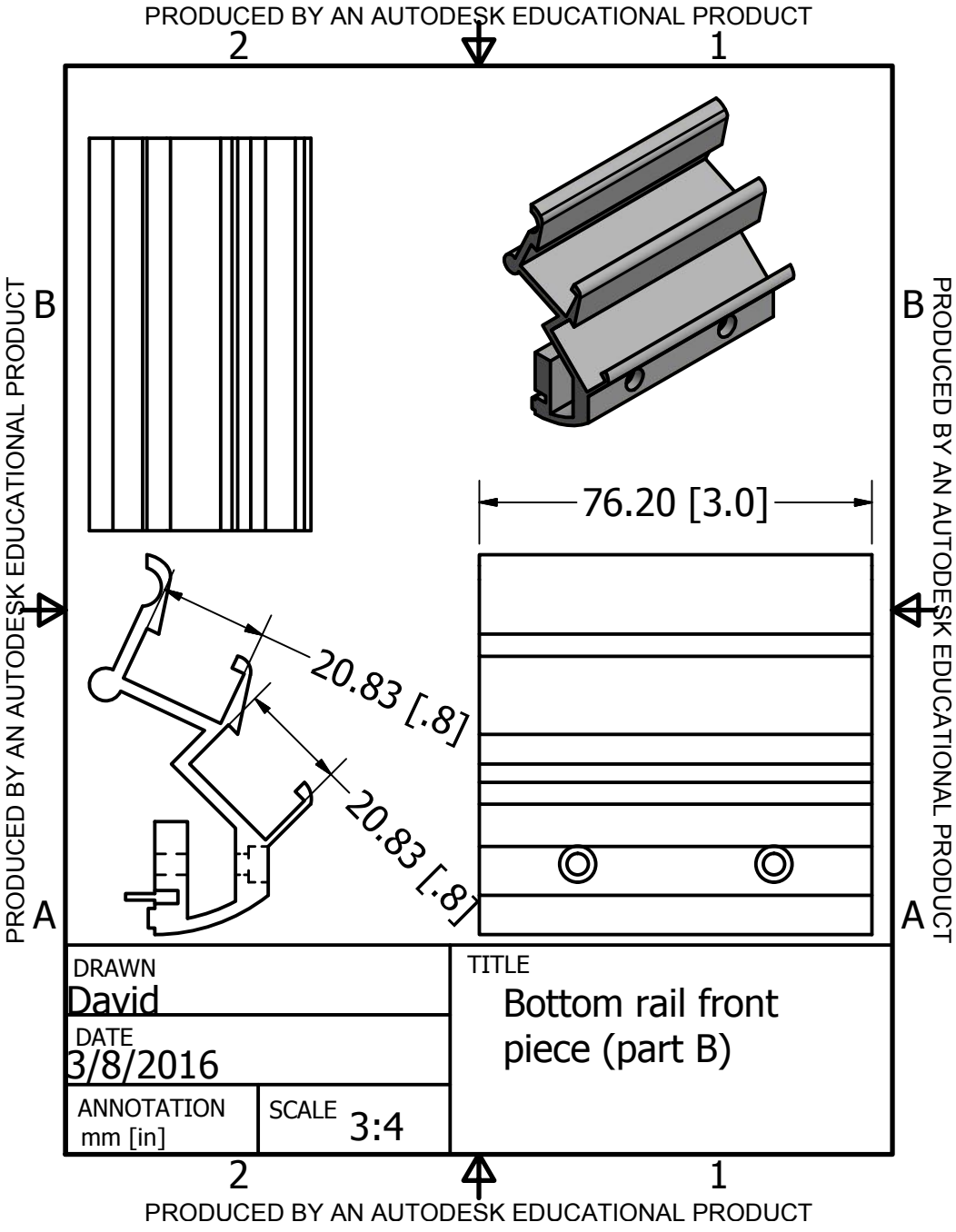

Figure D.42: Mechanical drawing for the front piece of the bottom rail.

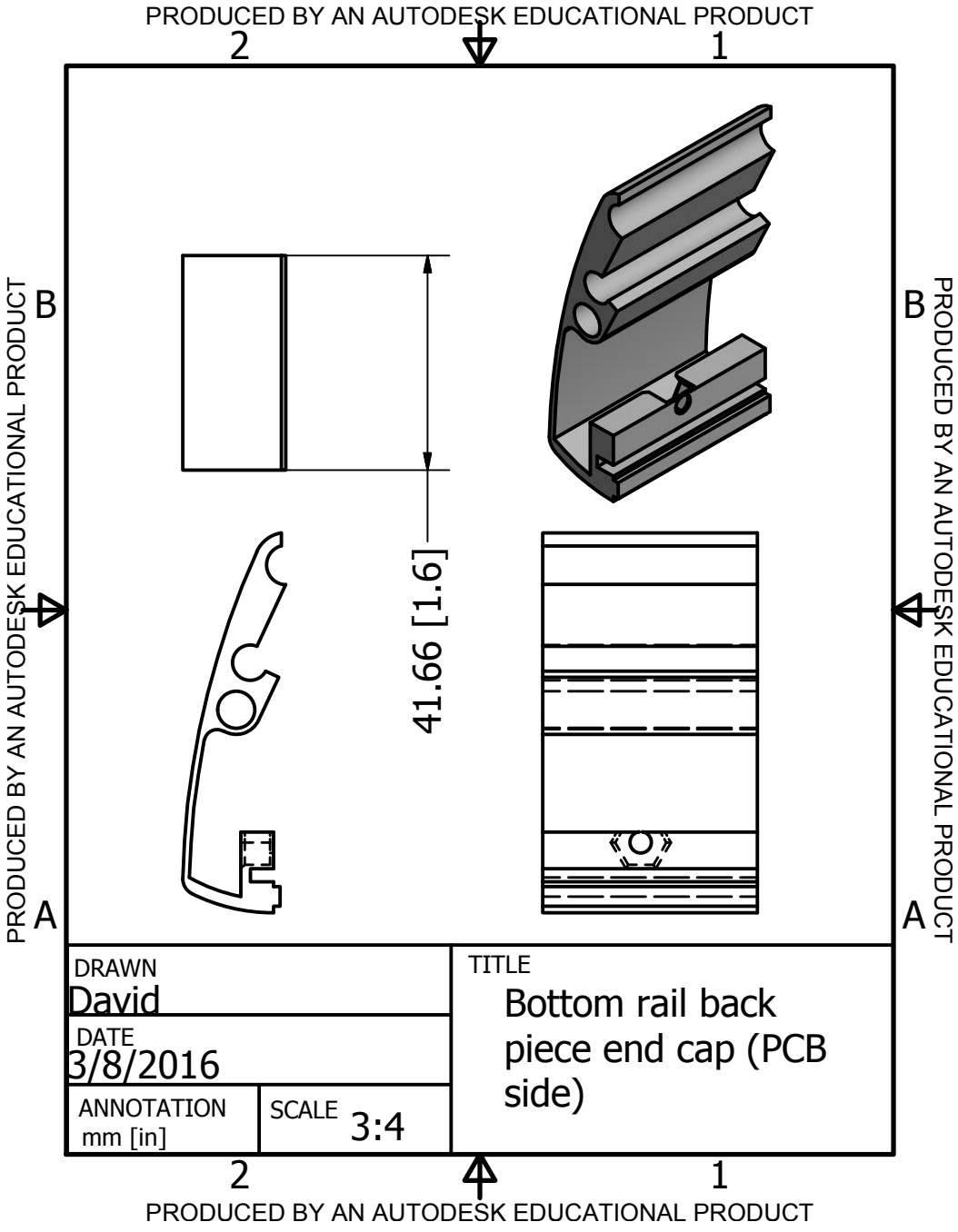

Figure D.43: Mechanical drawing for the back piece end cap for the side of the bottom rail that does accept wall adapter power.

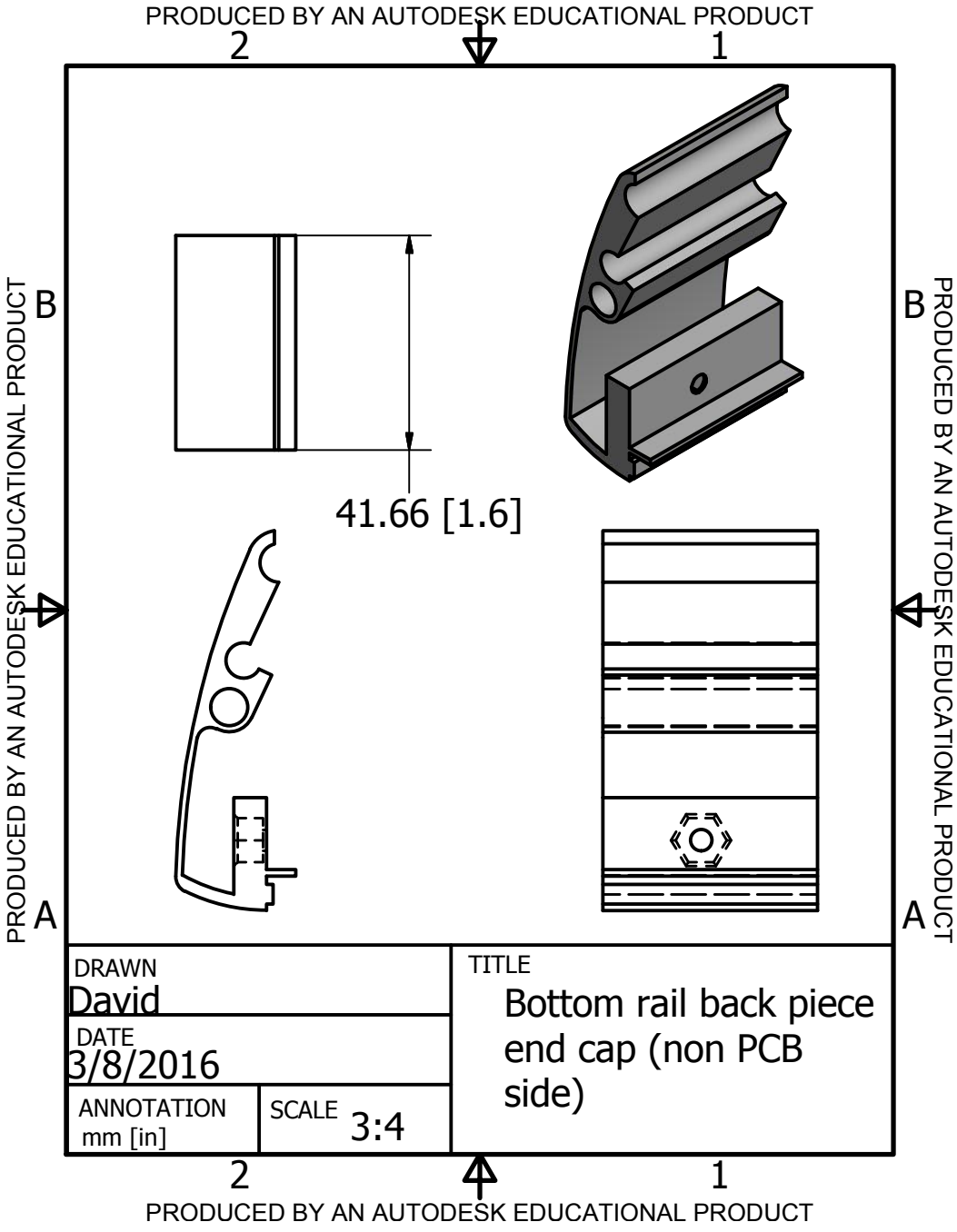

Figure D.44: Mechanical drawing for the back piece end cap for the side of the bottom rail that does not accept wall adapter power.

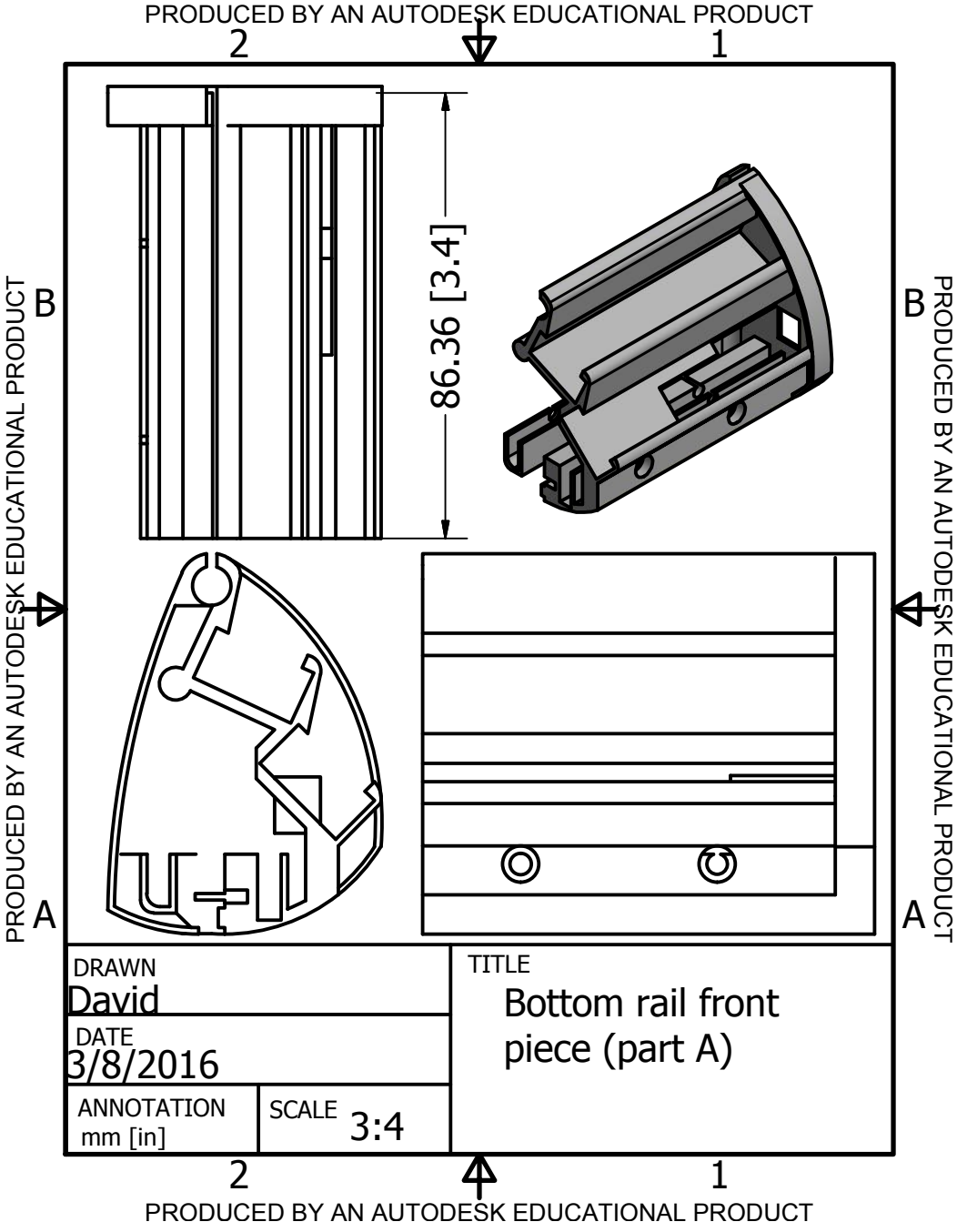

Figure D.45: Mechanical drawing for the front piece of the bottom rail for the side that accepts wall adapter power and requires additional clearance for a PCB.

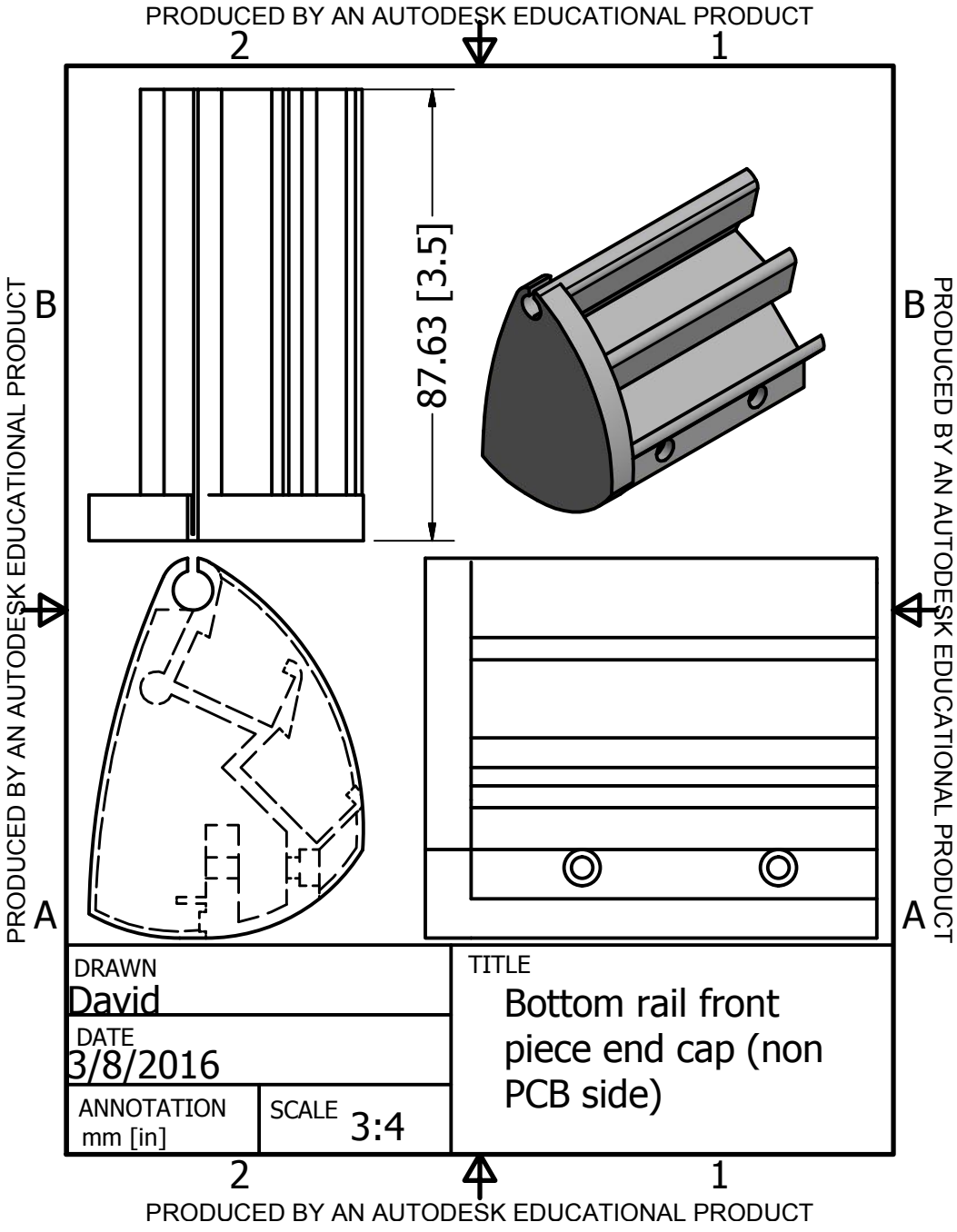

Figure D.46: Mechanical drawing for the front piece of the bottom rail for the side of the bottom rail that does not accept wall adapter power.

D.9.2 Roller Clutch

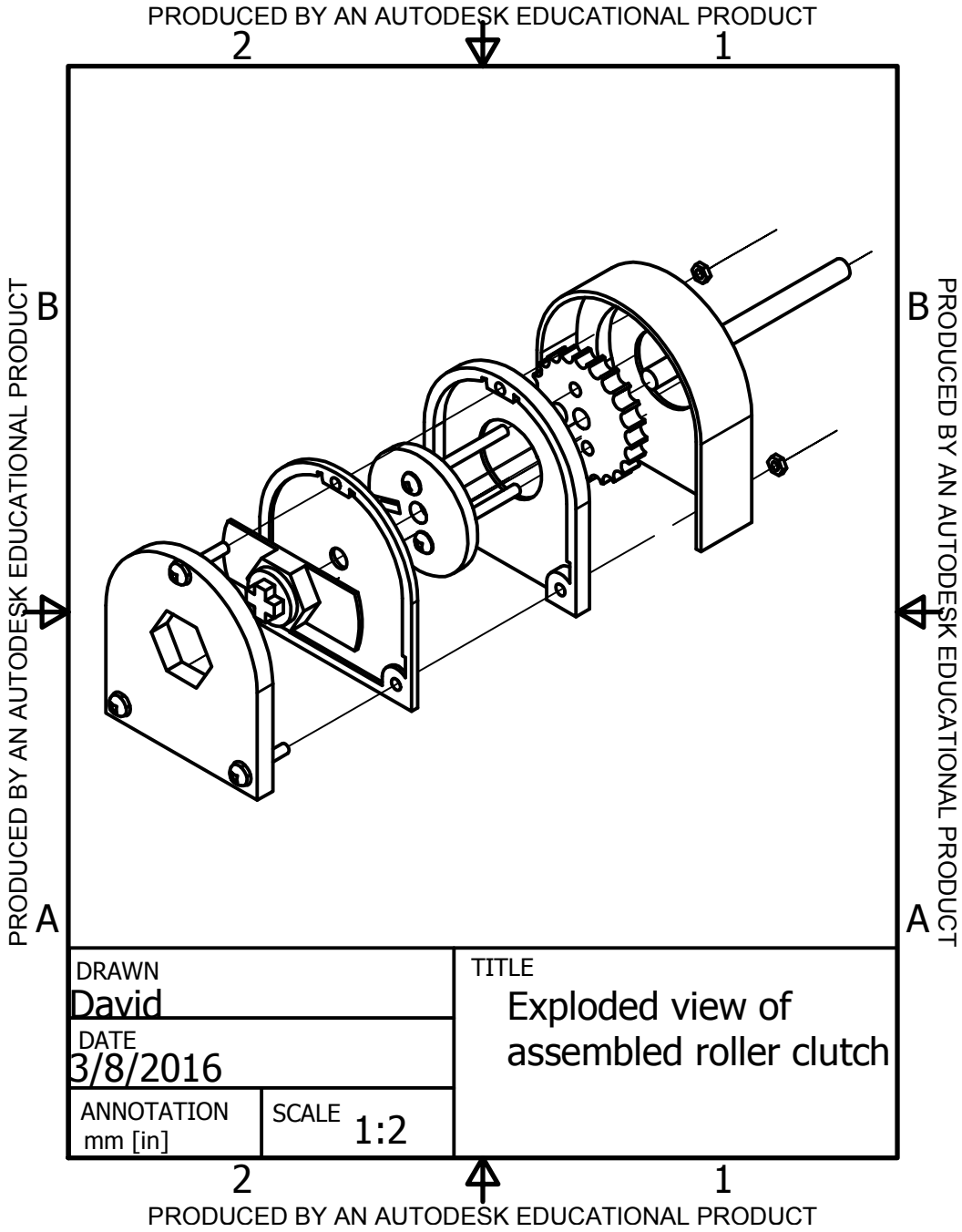

Figure D.47: Exploded view of the roller clutch. The enclosure layers are fastened with three 3/4" 6-32 screws and captive nuts. An axle is anchored with the axle adapter. The wire wheel and gear are linked with two long 6-32 screws but rotate around the axle.

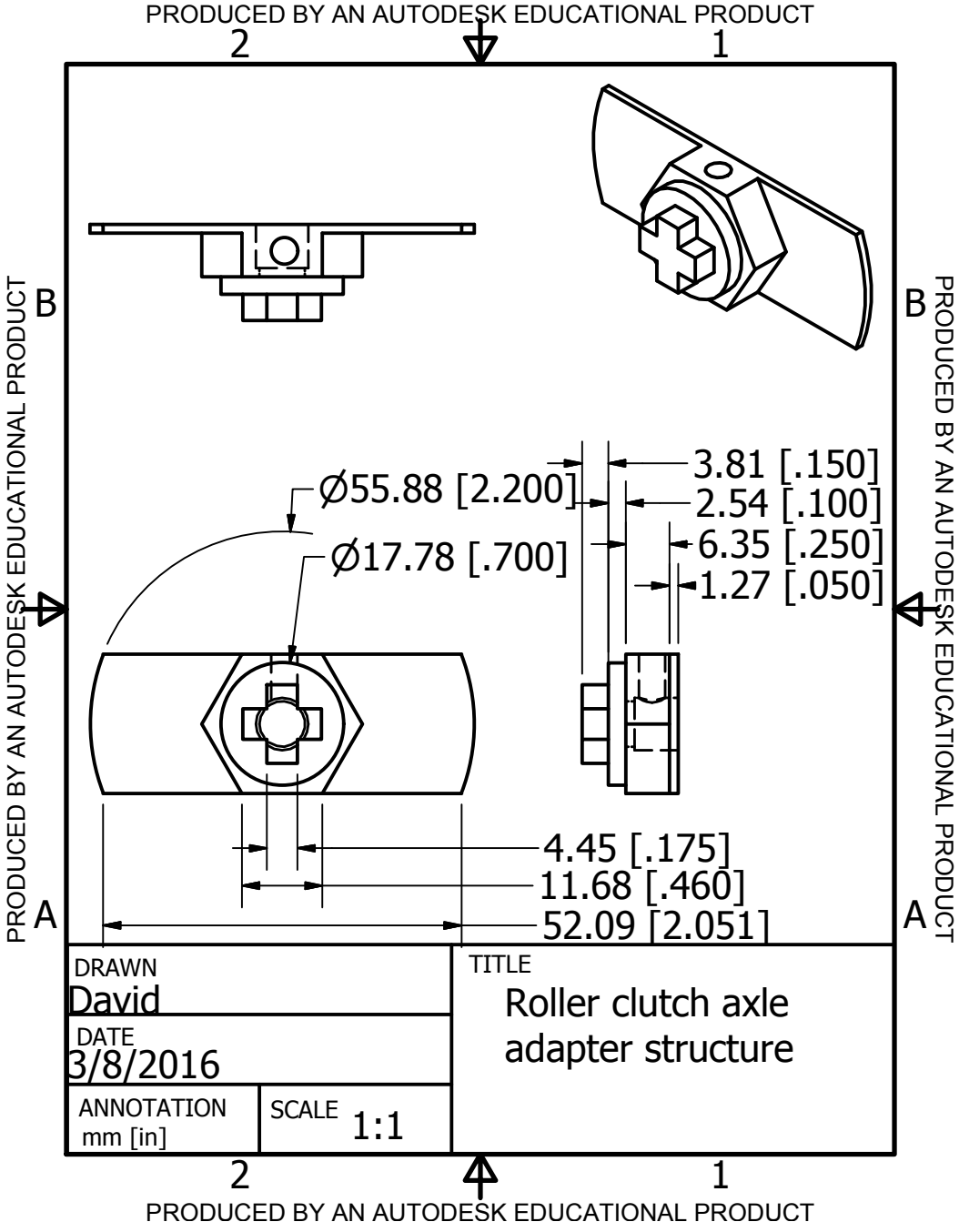

Figure D.48: Mechanical drawing for the axle adapter. This piece secures an axle to blind mounting bracket. This provides a central axis for the blind to rotate around and forces the rotor of the motor to be stationary so the stator rotates.

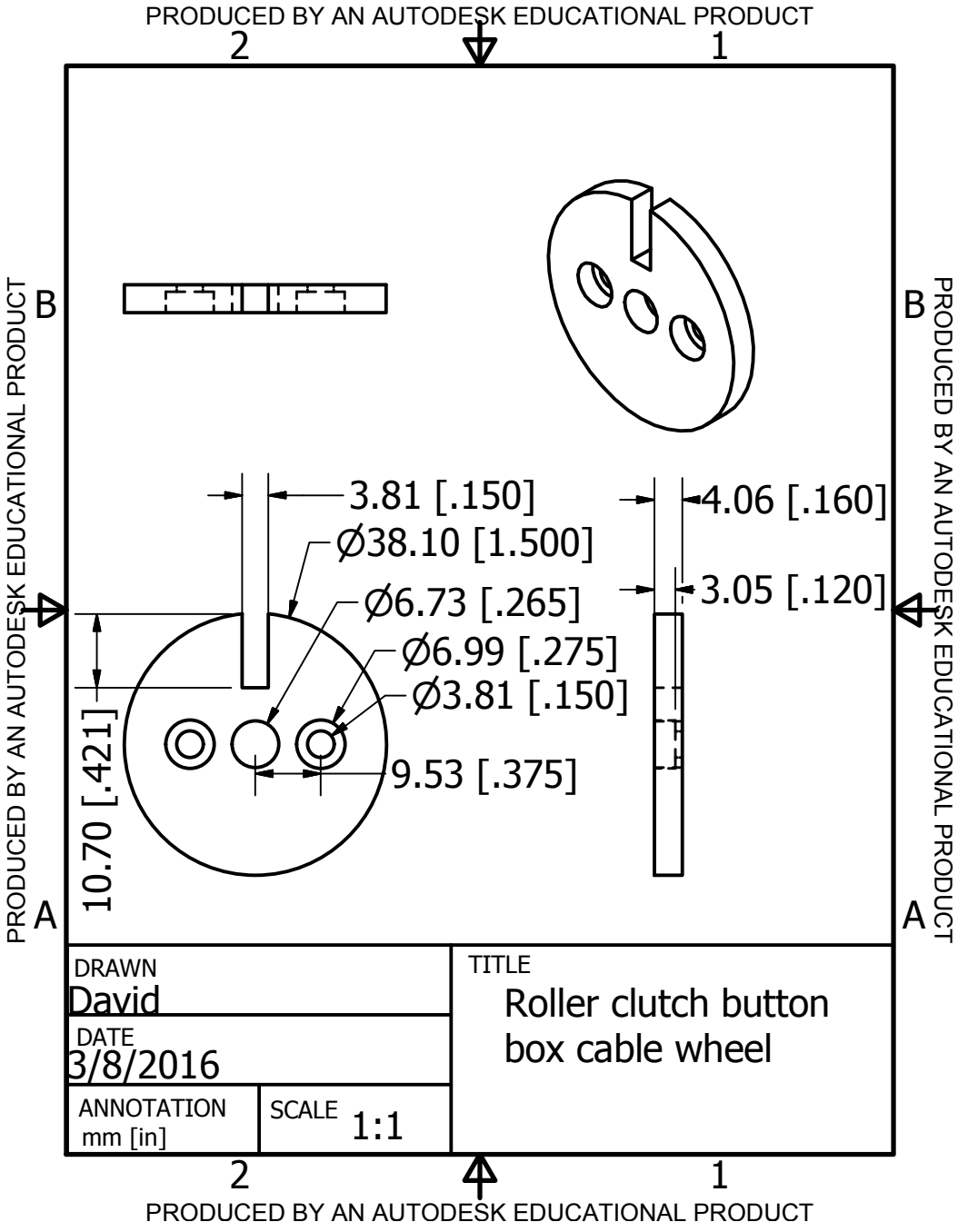

Figure D.49: Two 2" 6-32 screws connect in this wheel to the blind assembly forcing this wheel to rotate with the blinds. This wheel wraps and unwraps the ribbon cable that connects to button box.

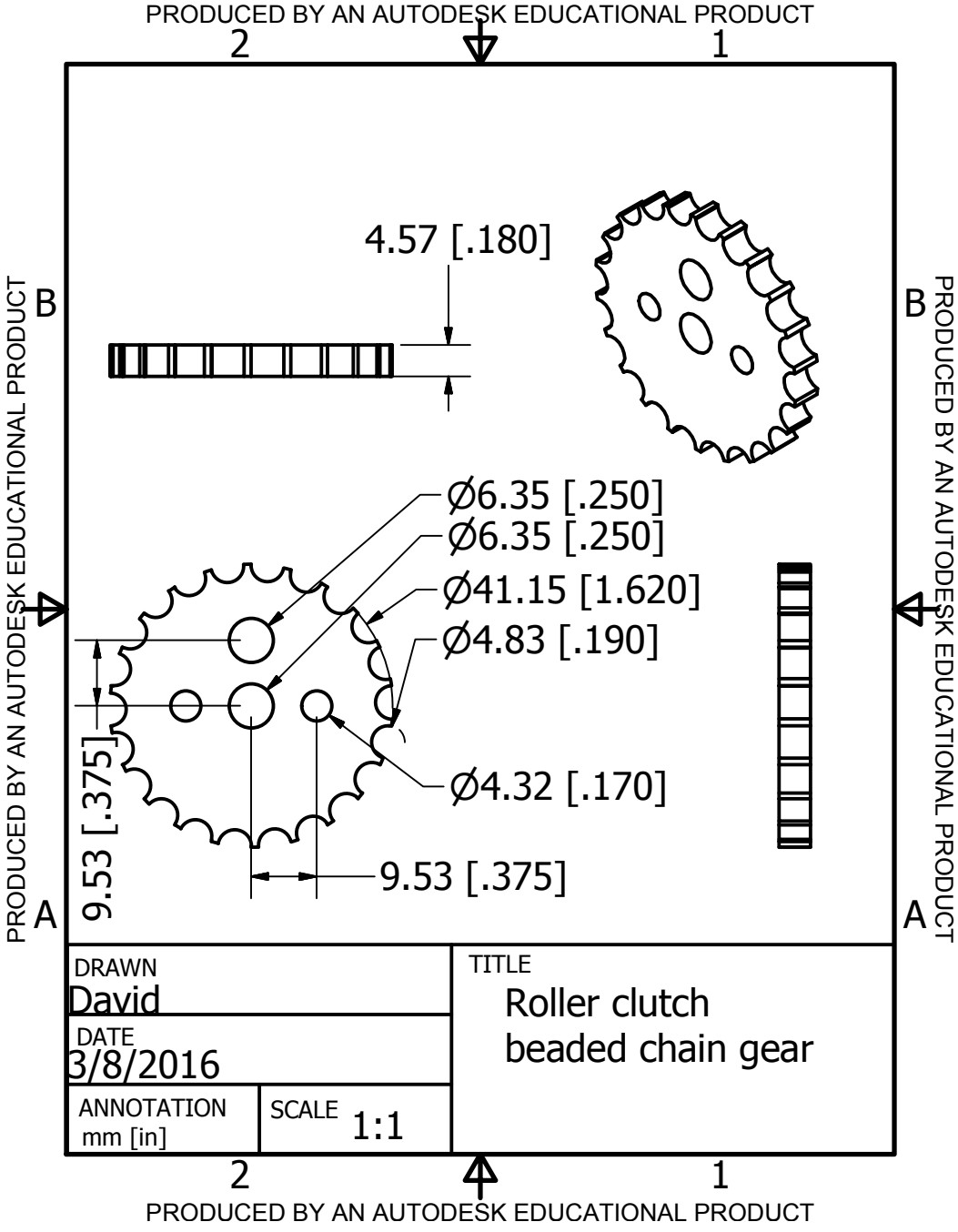

Figure D.50: This wheel mates with a commercial window blind's beaded chain. Two long 6-32 screw connects through this wheel to the rest of rotating components of the blind assembly. When the beaded chain is moved, so will the entire window blind assembly.

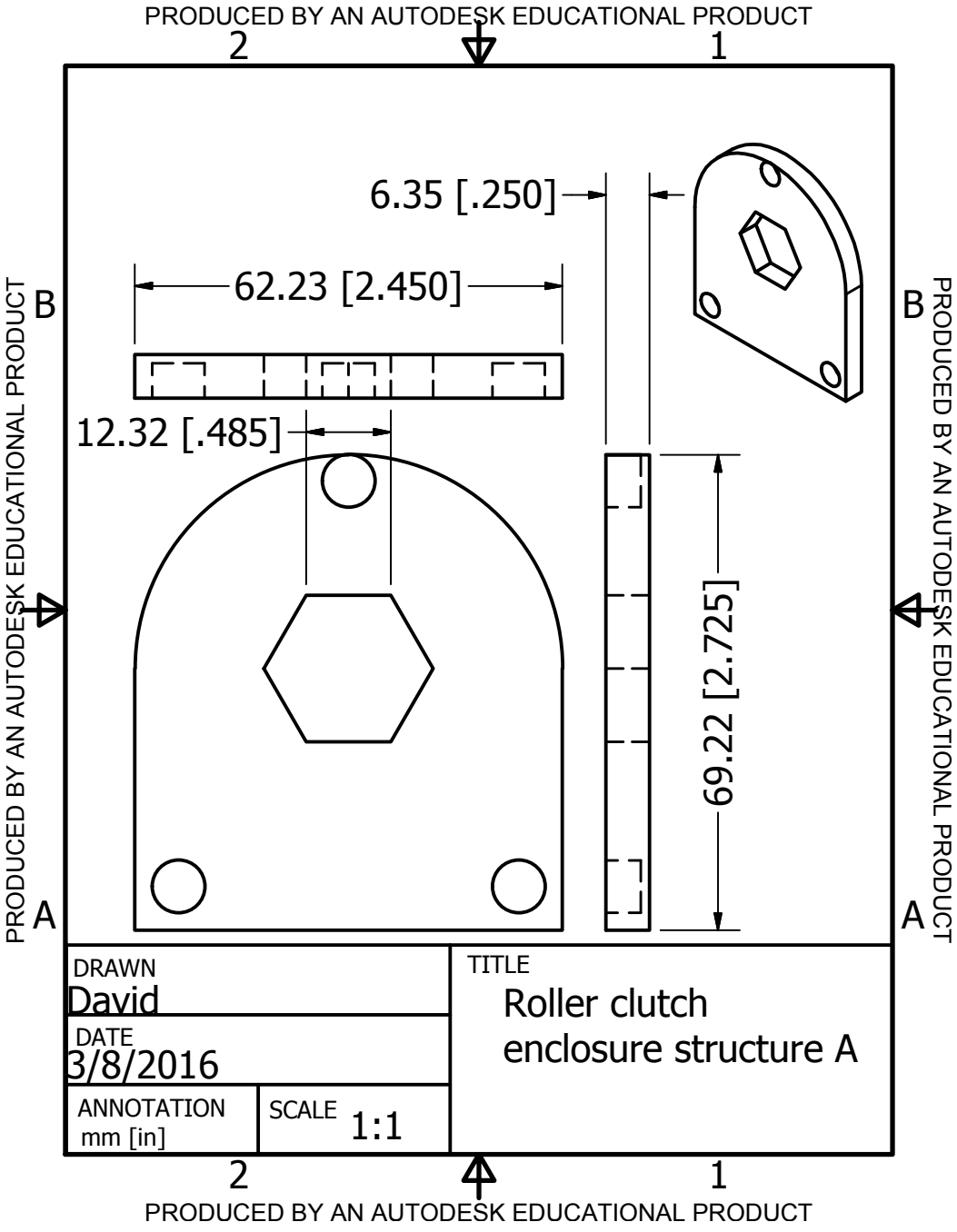

Figure D.51: Mechanical drawing for enclosure layer A.

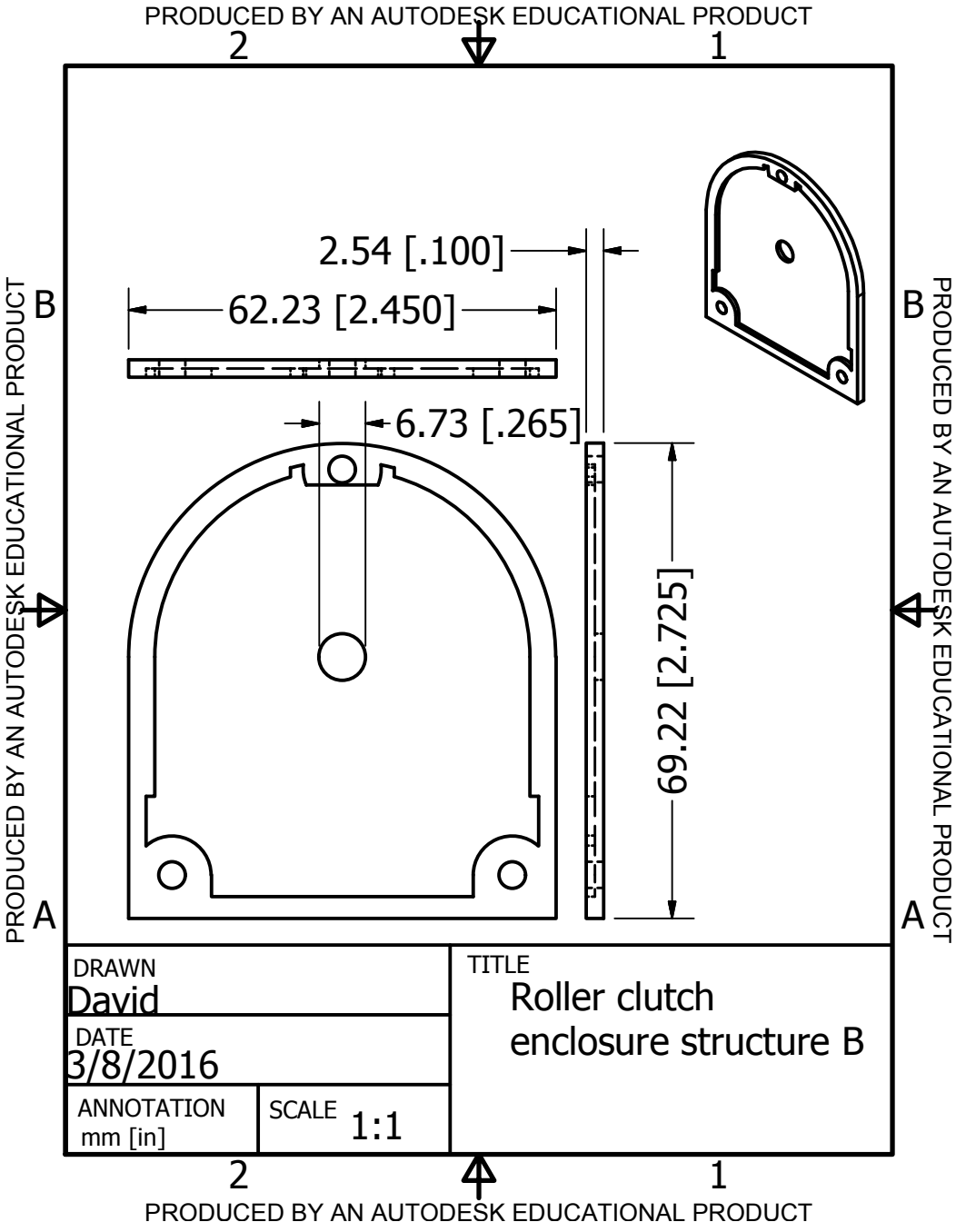

Figure D.52: Mechanical drawing for enclosure layer B.

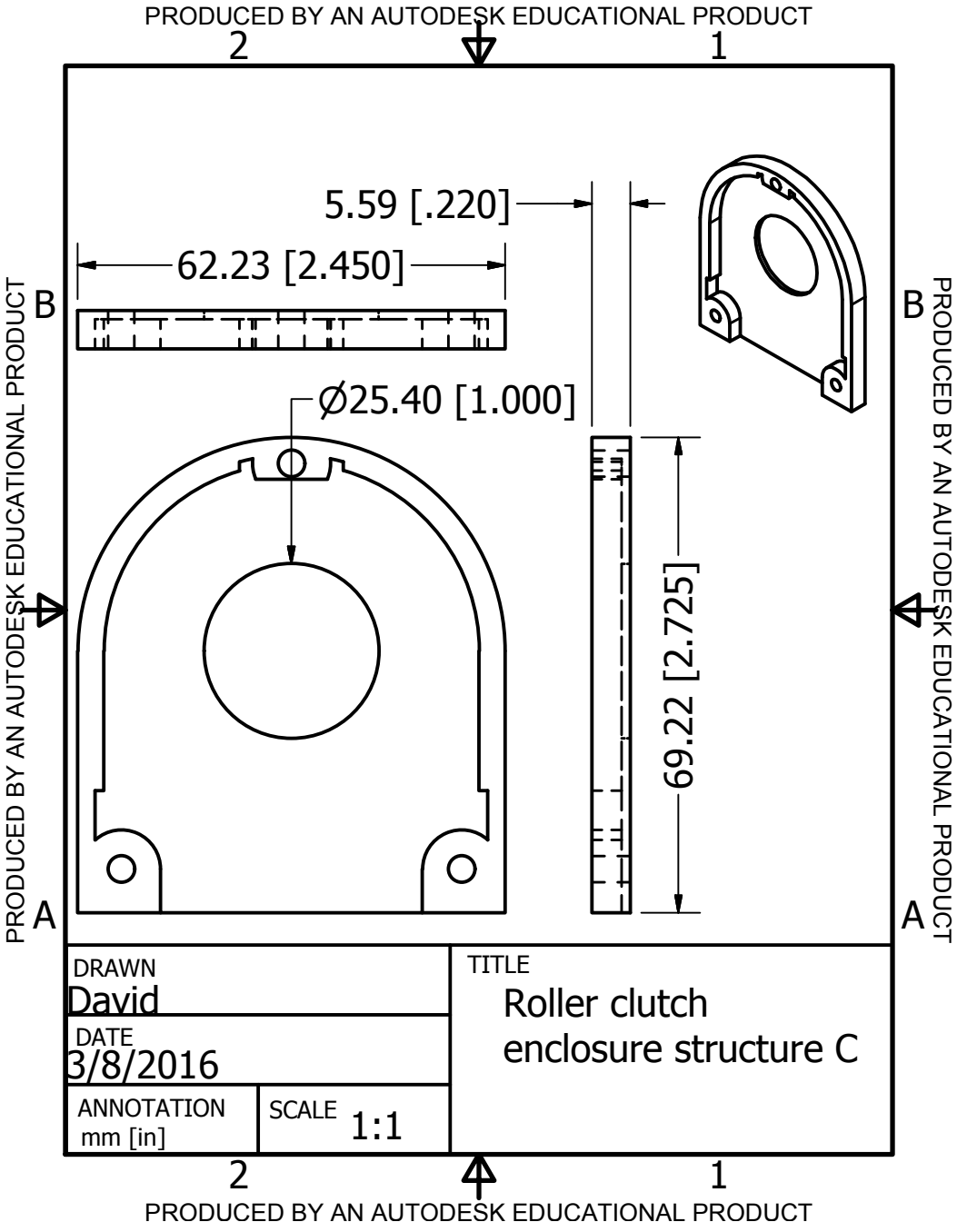

Figure D.53: Mechanical drawing for enclosure layer C.

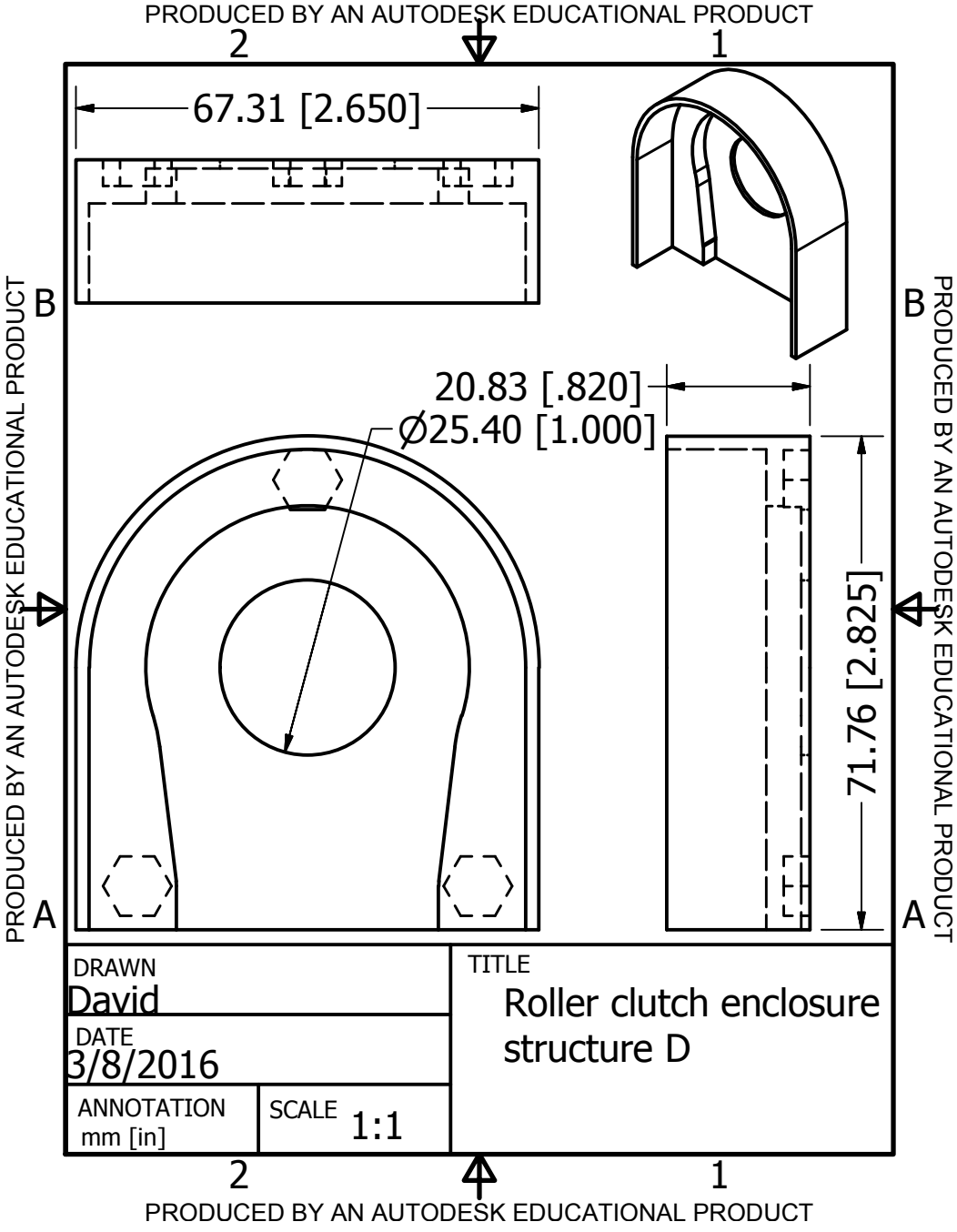

Figure D.54: Mechanical drawing for enclosure layer D.

D.9.3 Button Box

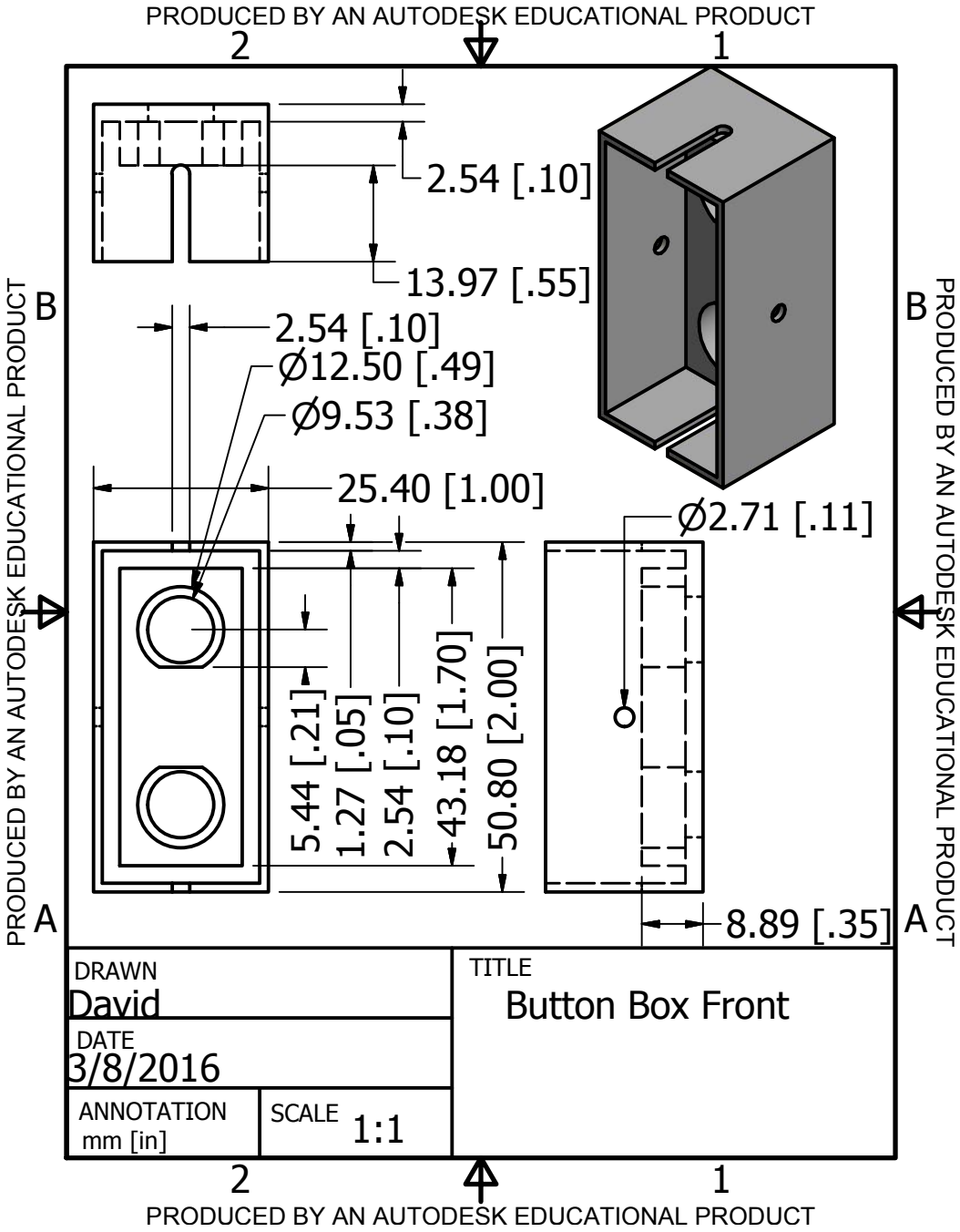

Figure D.55: Mechanical drawing for the back piece of the bottom rail for the side that accepts wall adapter power and requires additional clearance for a PCB.

D.9.4 Electronics Wheel 3D printed

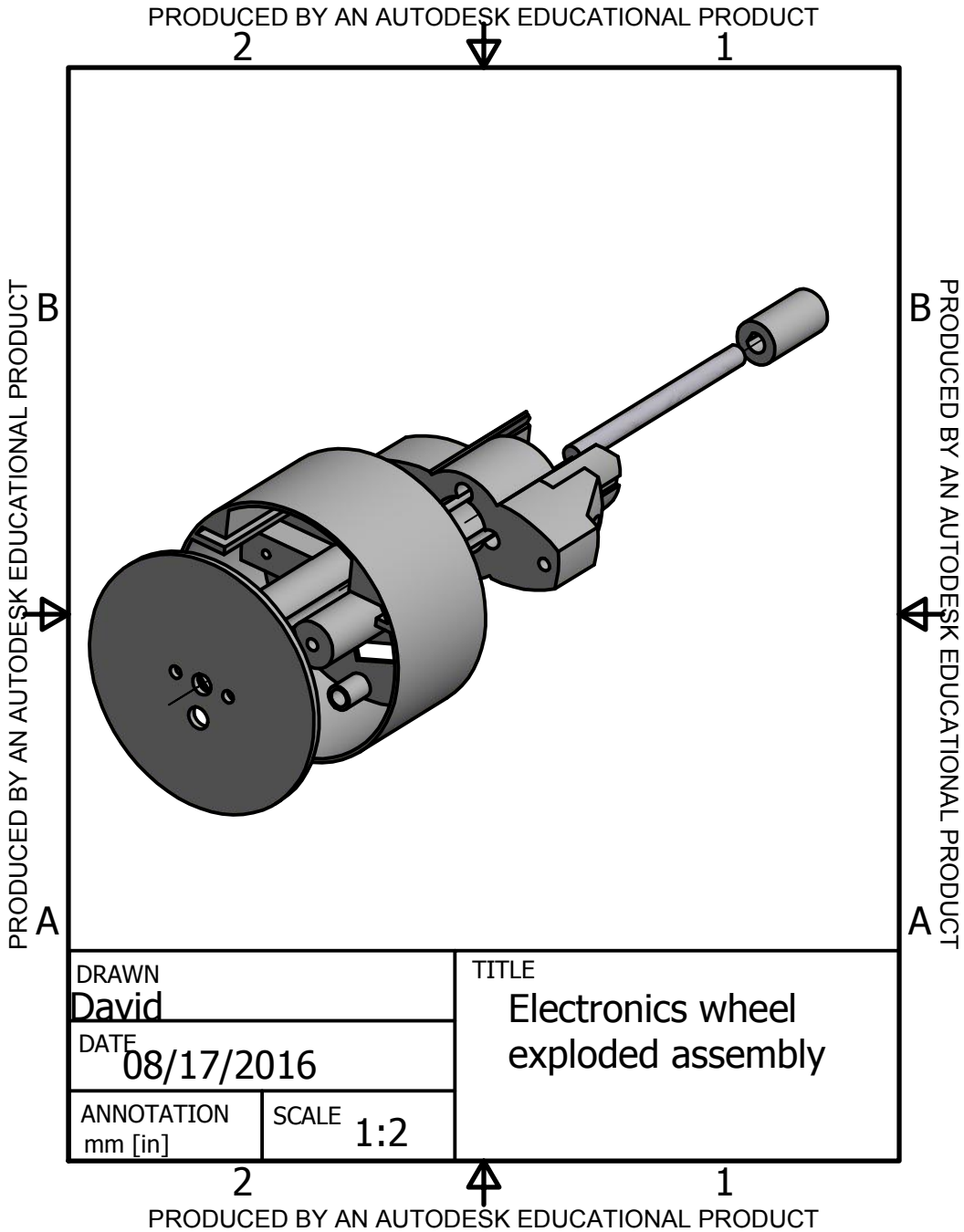

Figure D.56: Exploded view illustrating how the electronics wheel is assembled. 6-32 screws fasten this wheel to the rotating components in the roller clutch. M3 screws connect the motor adapter to the motor. The rotor adapter is secured using 8-32 set screws (not pictured).

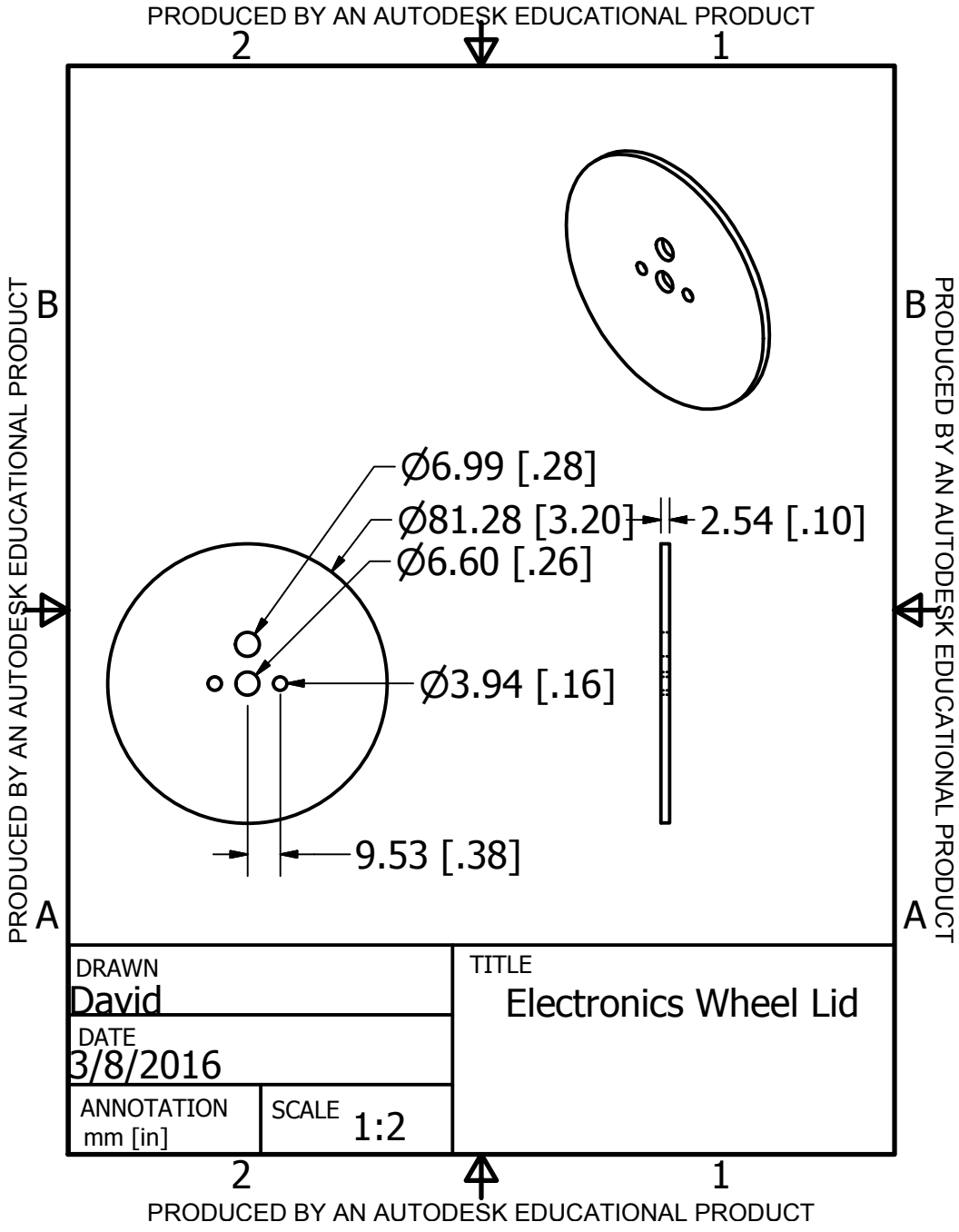

Figure D.57: Mechanical drawing for lid of electronics wheel. The two 9.53 mm holes are clearance for 6-32 screws that rotationally lock the electronics wheel to the rotating components in the roller clutch. The 6.99 mm hole is so that the ribbon cable from the button box can be inserted into the enclosure. The central hole is to pivot around the axle.

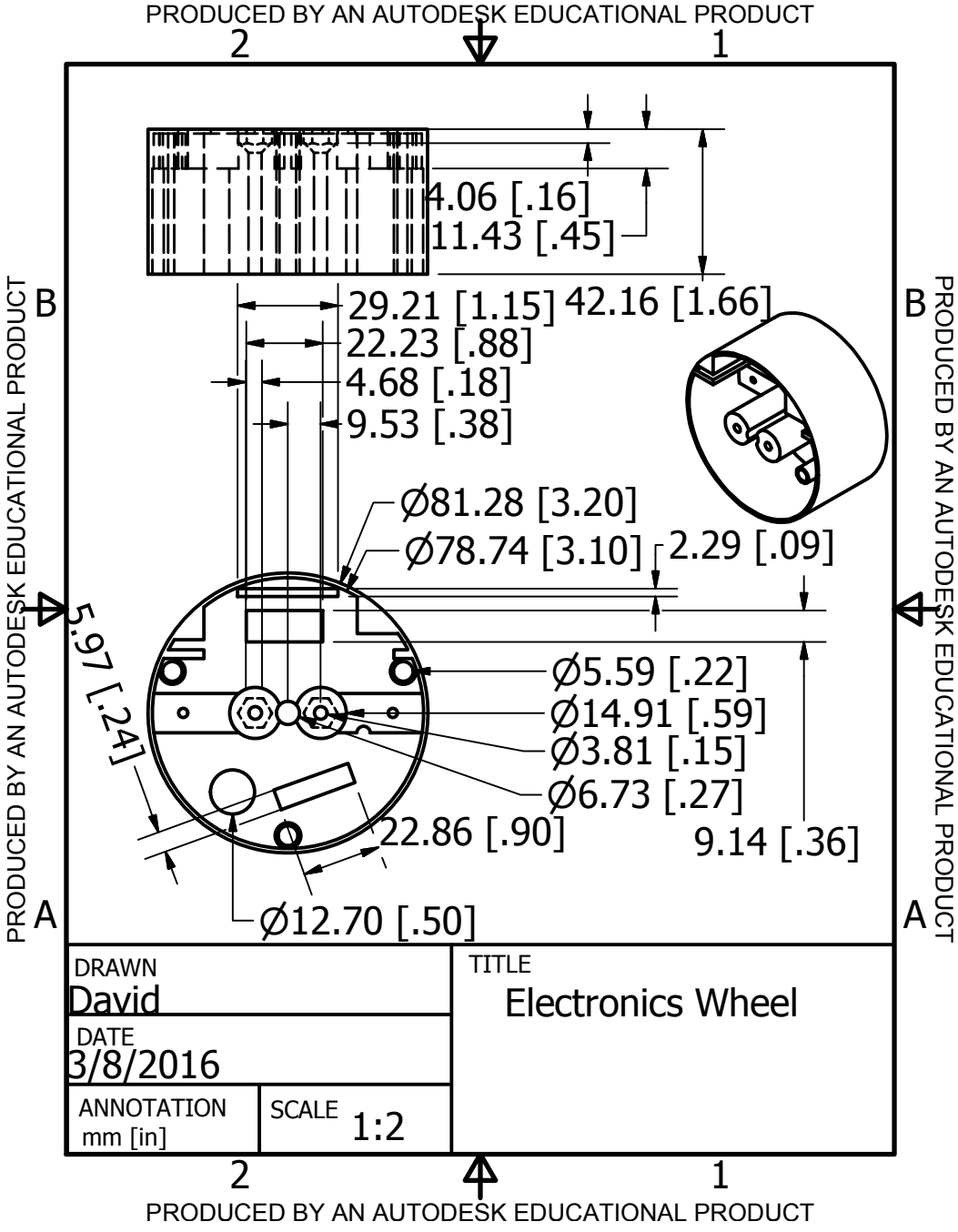

Figure D.58: Mechanical drawing for the electronics wheel. Electronics that need external access are mounted in this wheel. There are several features of note in this feature that are explained in the assembly instructions.

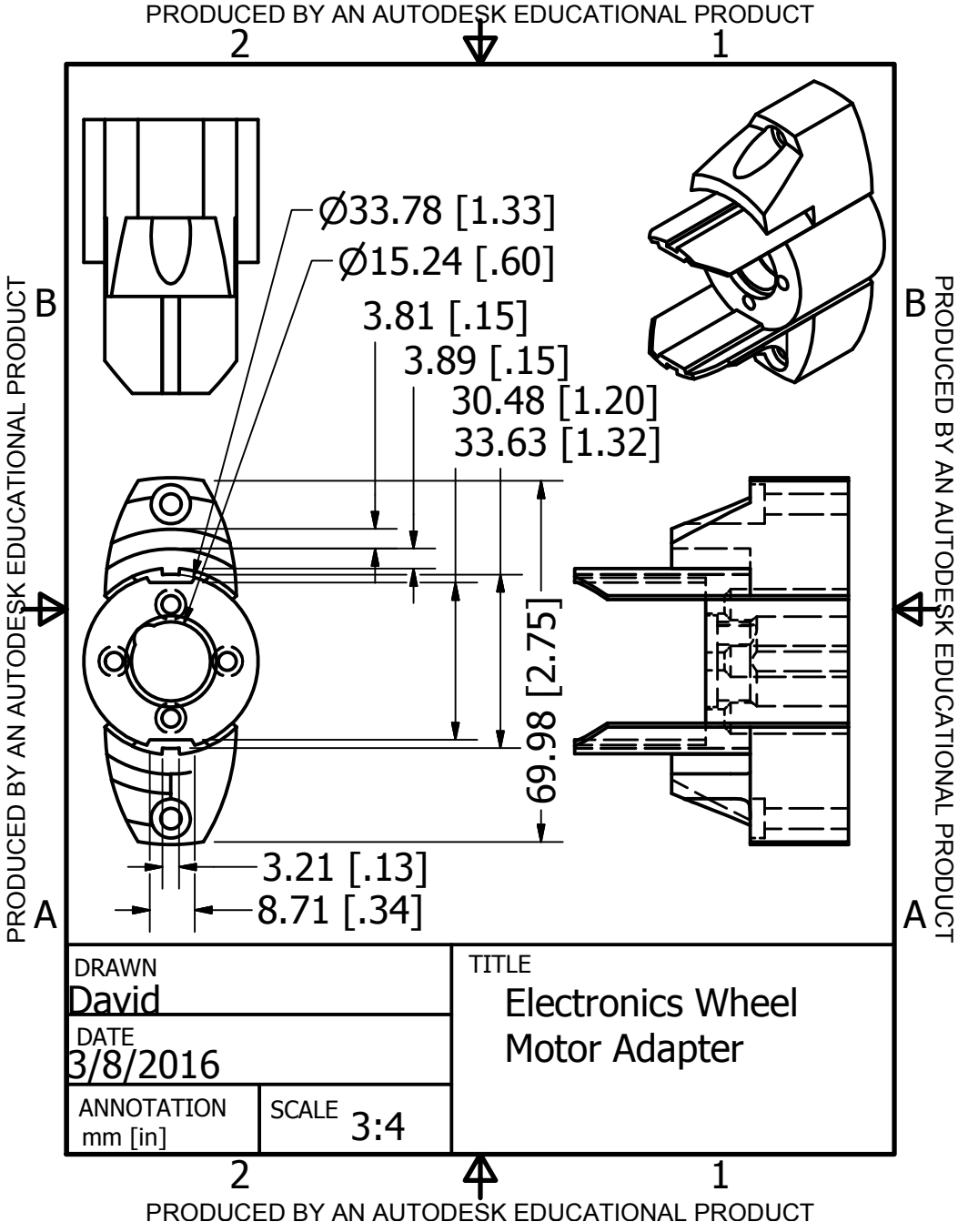

Figure D.59: Mechanical drawing for the electronics wheel motor adapter. This piece is screwed into the motor with four M3 screws and screws into the electronics wheel with two 0.75" 6-32 screws. The grooves in this piece ensure the window blind assembly also rotates while providing clearance for the ribbon cable that connects this PCB to the internal electronics. Steel strapping is needed to secure this piece to the motor.

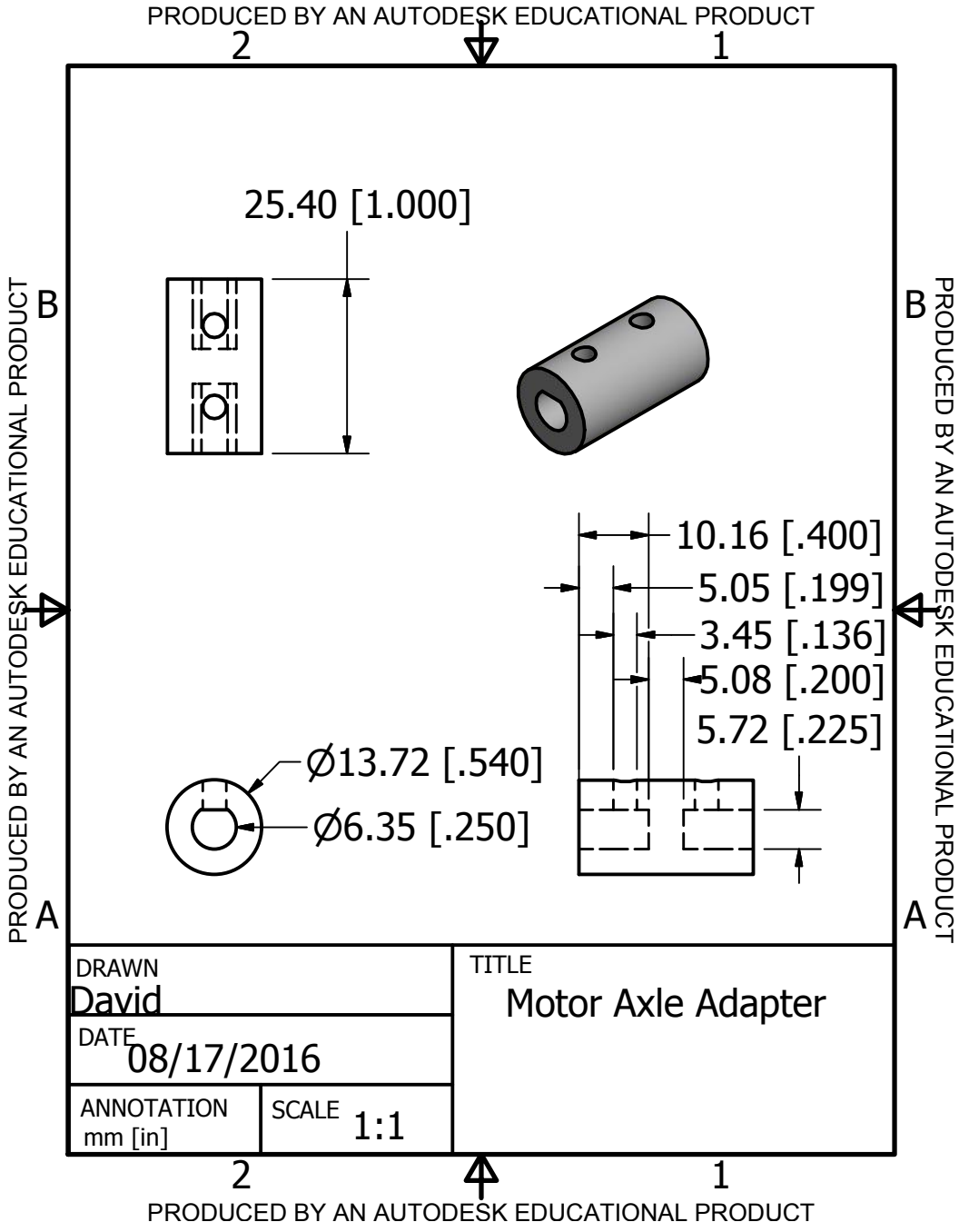

Figure D.60: Mechanical drawing for the electronics wheel motor-axle adapter. This piece is screwed onto the motor's rotor and the assembly's axle using two 8-32 set screws.

D.9.5 Electronics Wheel 3D machined

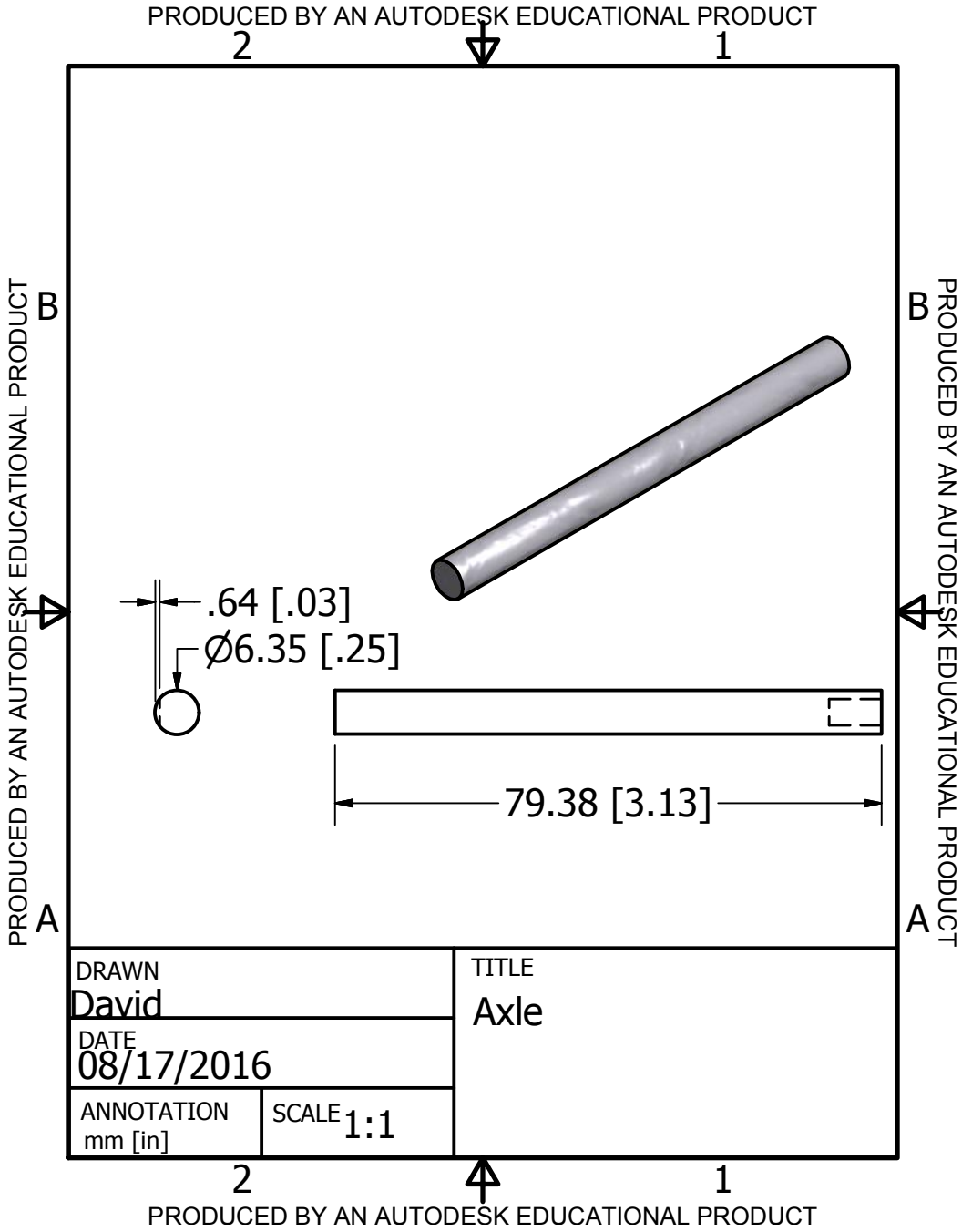

Figure D.61: Mechanical drawing for the electronics wheel axle. This axle provides an anchor for the motor to push against and rotate the blind unit. A flat is added using a file.

D.9.6 Electronics Enclosure

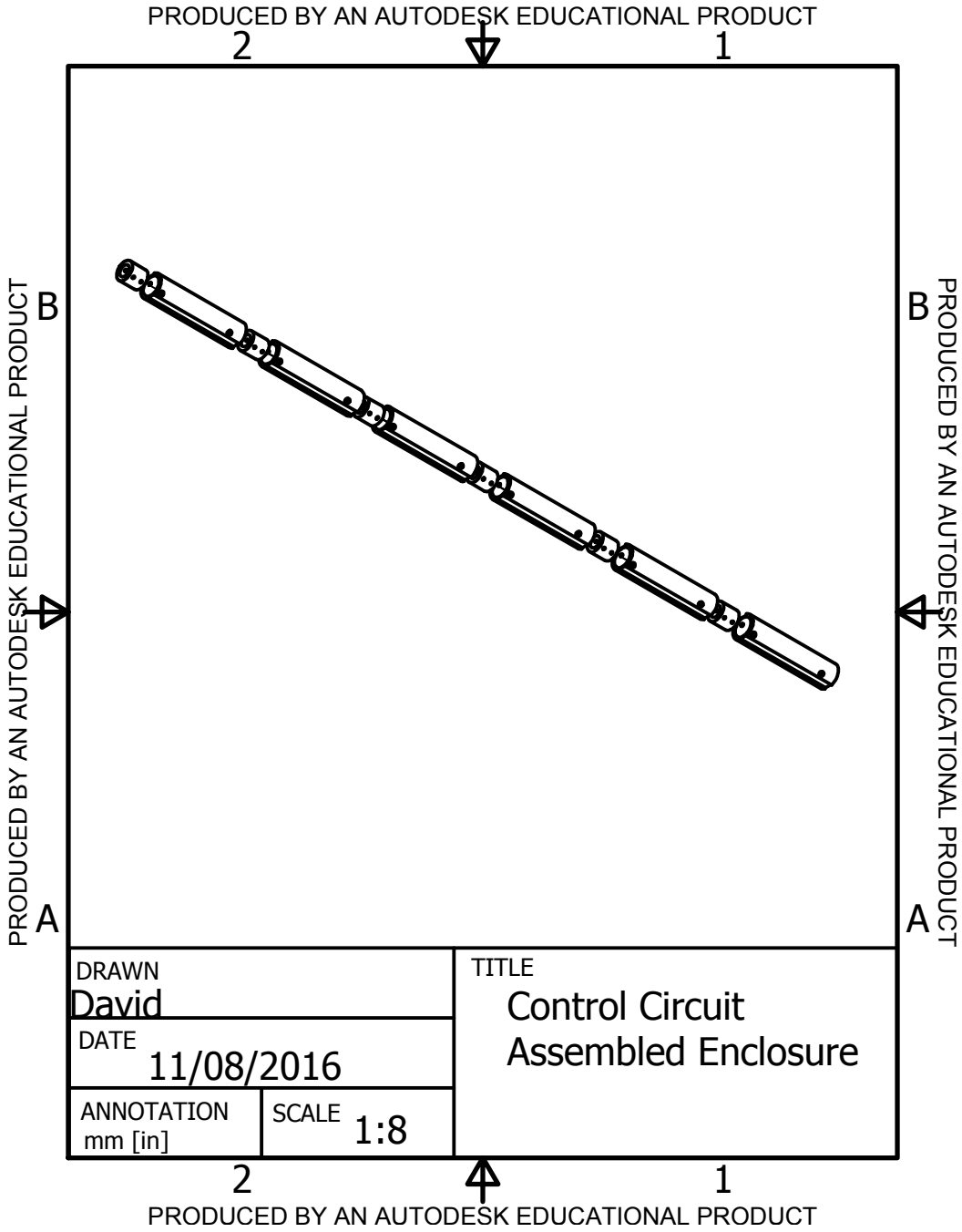

Figure D.62: All the control circuit enclosures are secured by being screwed into connectors. Various electronics are inserted into these component's cavities.

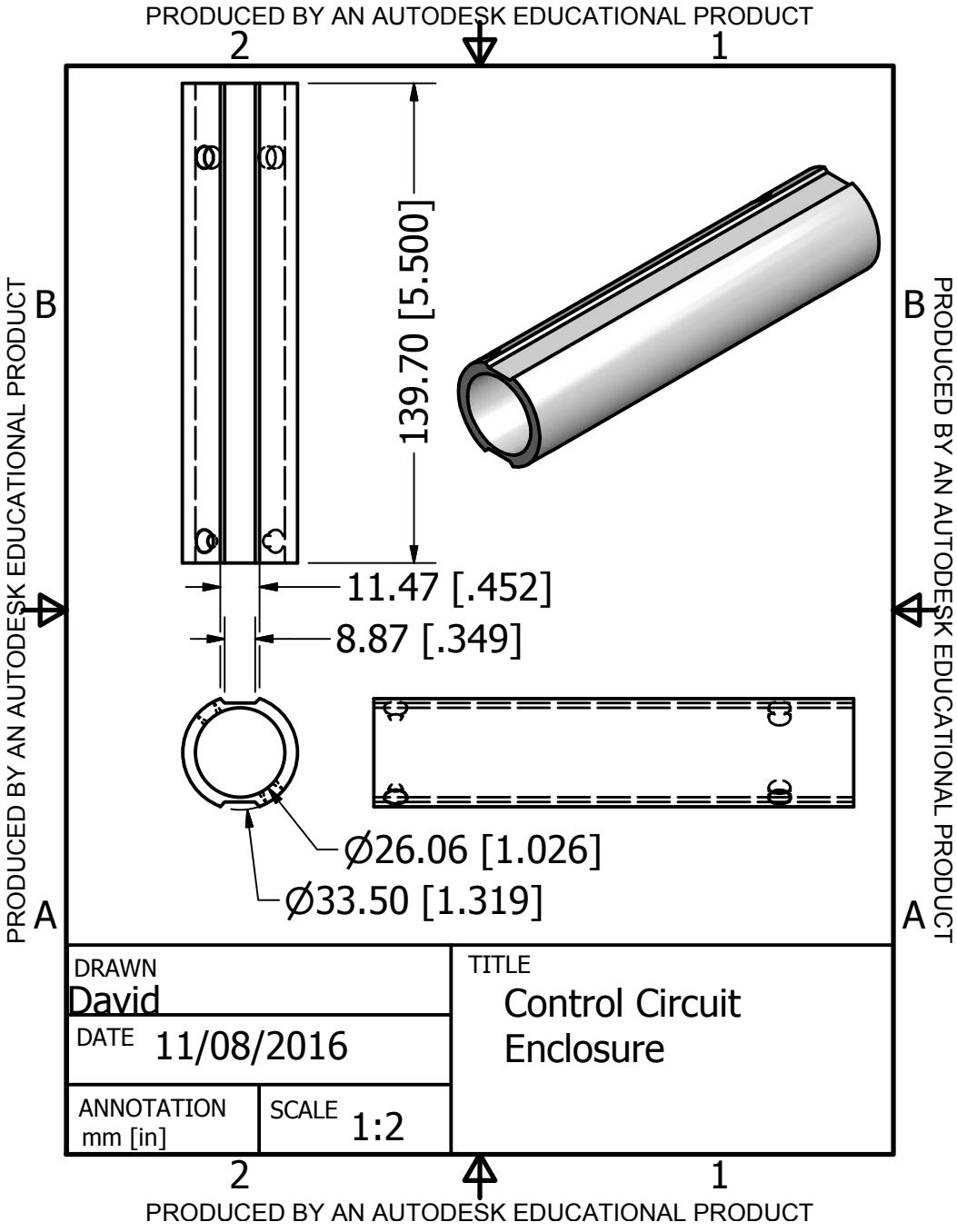

Figure D.63: Electrical Enclosure for control circuits.

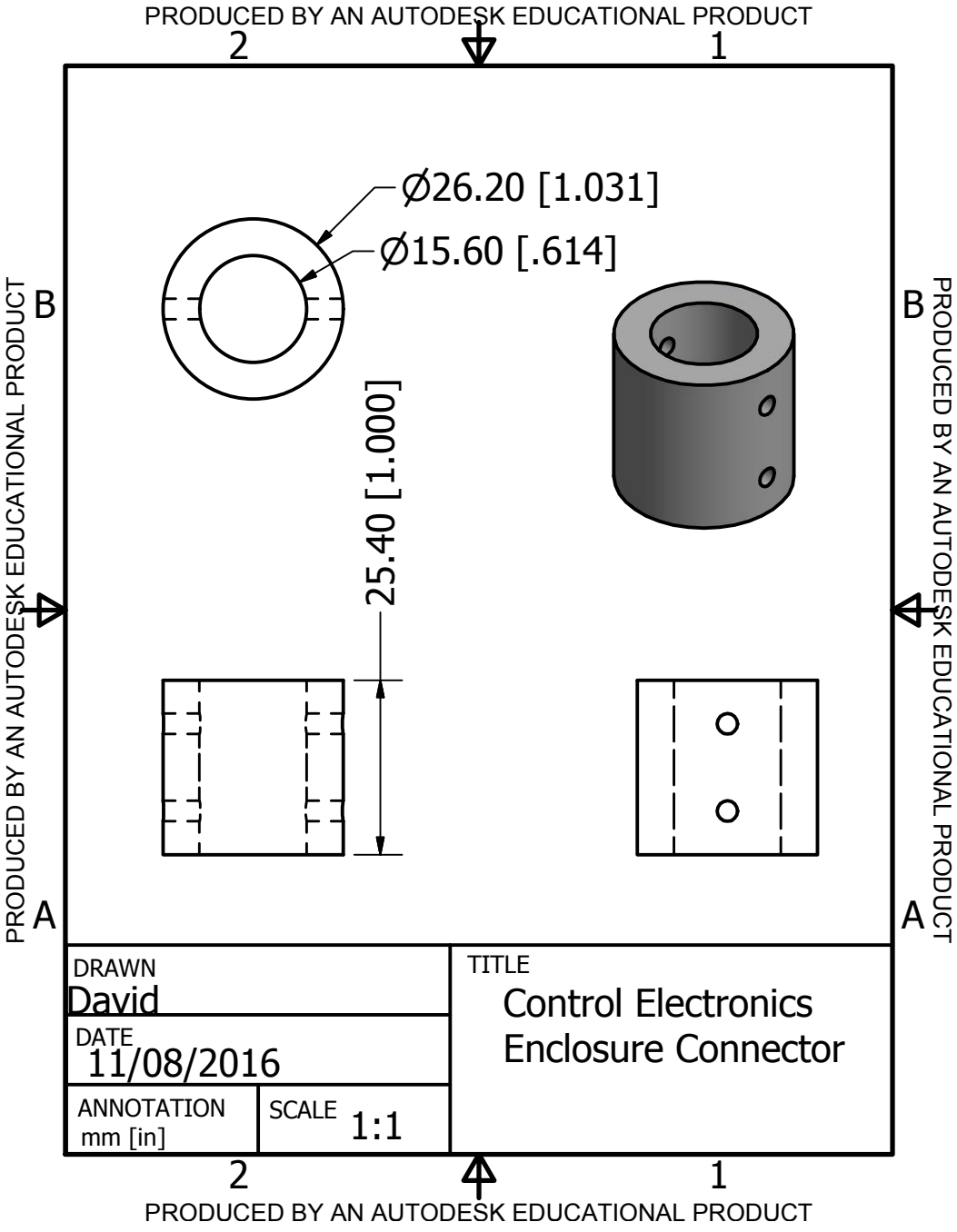

Figure D.64: Connector for enclosures.

D.10 Software Directory

Many code files were written in order to make the prototype functional. Directly inserting the code into this Appendix would take excessive space and require formatting the code to make it legible rather than functional. Instead a code directory titled "Prototype Software Directory" was submitted with this thesis. This Appendix serves to document the files contained in the directory and what programming environment is needed to edit and make the files.

Table D.22: Description of the code files included with Thesis submission.

Folder Name	Language	Programming Environment	Description
1 MSP430 Program	C++	Code Composer Studio 6.0.1	These code files are compiled and flashed on the MSP430 so that it can successfully operate the control circuit.
2 Java Configuration Assistant	Java	Eclipse 4.5.0	This includes all code and image files needed to create the configuration assistant. The compiled code is placed on the prototype's SD card.
3 Server Website	HTML and CSS	Leafpad 0.8.15.1 (Text Editor)	These were written on a text editor and placed in the www directory of a web server running Raspbian v7. They are used to define how the website is shown to a user on a web browser.
4 Website Client Side Interaction	Javascript	Leafpad 0.8.15.1 (Text Editor)	The one file included in this directory defines several interactive components that are processed on the user's web browser.
5 Website Server Side Interaction	PHP	Leafpad 0.8.15.1 (Text Editor)	The one file included in this directory defines several interactive components of the server's website that are processed by the server.
6 Blind Prototype's Server	Python	Idle 2.7.3	This file must be opened and run in order for the system to be fully operational. It listens for requests from the physical prototype and provides it with scheduling information.

Appendix E

Solar Cell Datasheet

The solar cells used in the prototype are IXOLAR KXOB22-12X1L SolarBIT. They were purchased in a series string of 8 cells in the IXOLAR product SLMD121H08. This Appendix includes some relevant datasheet tables and figures for the SolarBIT product.

Table E.1: Defining solar cell performance parameters.

Part Number	Open Circuit Voltage [V]	Short Circuit Current [mA]	Typ. Voltage @ P_{mpp} [V]	Typ. Current @ P_{mpp} [mA]
KXOB22-12X1L	0.63	50.0	0.50	44.6

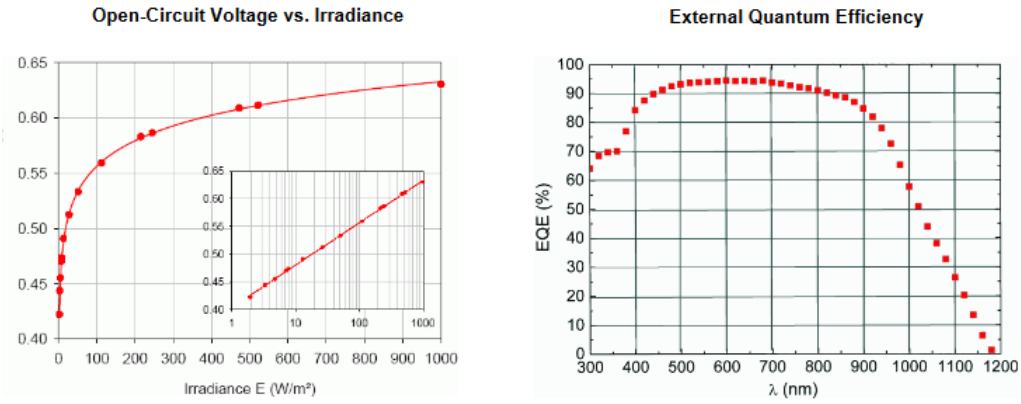

(a) (b)

Figure E.1: Trends used while analyzing this system (a) is the variation of the solar cell's V_{oc} as a function of impinging irradiance while (b) is the EQE of the solar cell.